Durham E-Theses

Diagenesis & Reservoir Quality of the Middle Bakken Formation

BRODIE, MARK,WILLIAM

How to cite:

BRODIE, MARK,WILLIAM (2016) *Diagenesis & Reservoir Quality of the Middle Bakken Formation*, Durham theses, Durham University. Available at Durham E-Theses Online: http://etheses.dur.ac.uk/11716/

Use policy

This work is licensed under a Creative Commons Attribution Non-commercial No Derivatives 2.0 UK: England & Wales (CC BY-NC-ND)

Academic Support Office, Durham University, University Office, Old Elvet, Durham DH1 3HP
e-mail: e-theses.admin@dur.ac.uk Tel: +44 0191 334 6107
http://etheses.dur.ac.uk

Diagenesis & Reservoir Quality of the Middle Bakken Formation

Mark Brodie

A thesis submitted to Durham University in partial fulfilment of the requirements for the degree of Doctor of Philosophy in the Faculty of Science

Department of Earth Sciences
Durham University

June 2016

Declaration

Originality

I hereby certify that the work described in this thesis is my own, except where otherwise acknowledged and has not been submitted previously for a degree at this, or any other University.

Copyright

The copyright of this thesis rests with the author and is made available under a Creative Commons Attribution Non-Commercial No Derivatives licence. Researchers are free to copy, distribute or transmit the thesis on the condition that they attribute it, that they do not use it for commercial purposes and that they do not alter, transform or build upon it. For any reuse or redistribution, researchers must make clear to others the licence terms of this work.

Mark Brodie

Acknowledgements

Submitting a PhD is not just a personal endeavour; but one achieved by a team, most of whom do not elect to be part of the project but have very kindly come along with me.

First and foremost, I would like to extend my unreserved gratitude to my supervisor Professor Andrew Aplin. A man of seemingly endless patience and someone who has always made time for me. Without Andy I would not have submitted this work. Thank you!

My family, whom most definitely did not elect to be part of this; my latest venture. Notable thanks go to my parents who have in their own unique ways supported me. From those formative fossil-hunting walks to watching endless re-runs of 'Tomorrows World'; they sparked my interest in the natural world! During this project; their belief in me, spurred me on, even when I doubted myself; thankyou.

Thanks go to my sponsor, Statoil and their team of geoscientists without which my work would not have been possible. I am very grateful for the help and advice you have given me during this project. My thanks go to Andrew Cavanagh, Beatriz Garcia-Fresca, Eric Radjef, Matt Dawson and Phil Ringrose. Particular mention must go to Nick Drenzek who helped me drive the project in its infancy. I would also like to make special mention to Bruce Hart who helped in so many ways and offered continuity as a go-to throughout the project. Thank you!

Thank you must also go to Ian Chaplain, who has helped me in many ways, far beyond sample preparation. A 'go to' for my latest idea, he always offered me sound advice and a helping hand. I am very grateful; thanks Ian!

Many thanks go to my friends; many from different areas of my life, you have a played an important part in keeping my sanity. There really are too many to name. A special 'thank you' must go to Helen. It has been surprising how we have shared this venture; its trials and tribulations but in very different fields - thank you! We never did agree who won the bet, did we?

Away from Durham, I must thank the team at the University of Wisconsin-Madison SIMS laboratory; Ian, John, Maciej, Koukie, Noriko and Jim. Thank you for one of the most memorable experiences of my PhD; if one of the most exhausting of weeks. It was a privilege to work with you.

A special mention must also go to Dr Ed 'Eddie' Anderson, my Geology teacher from sixth form college. He gave me my first formal introduction to geology and his infectious enthusiasm, grew my passion for Geology! Thanks Ed!

I have met many inspirational people, many of whom are not named here and many I wish I had got to know better, but all of whom I wish to thank. There have been so many people who have offered help, advice and the not-so-occasional coffee throughout what has unquestionably been the most exciting but without question the most challenging adventure I have been on so far. Thank you!

Abstract

The largest continuous oil accumulation ever assessed by the USGS, the Bakken Formation in the Williston Basin, USA, is a tight oil resource with low recovery factors. Increasing the recovery factors from tight hydrocarbon formation has significant economic implications.

In this study we show that the effects of diagenesis have significantly affected the reservoir quality of the middle Bakken Formation. Diagenetic processes in the middle Bakken are complex and vary across several scales. Early carbonate cementation exerts the primary control on porosity loss in the middle Bakken. Detailed petrographic examination by electron microscopy reveals multiple textural phases of calcite and dolomite, each of which contributes to changes in the reservoir quality. Cementation by calcite and dolomite has resulted in the low porosity and low permeability in the middle Bakken. Depositional facies have been defined within the middle Bakken. Cementation by carbonate minerals exert a key control on reservoir quality at scales below that of a facies.

Porosity in the middle Bakken varies from ~2-10%. Low pressure nitrogen gas sorption experiments show this is composed of pores which are small; predominantly mesoporous in size. Mercury intrusion experiments show pores in the middle Bakken typically have pore throats with radii <100 nm and low pressure nitrogen gas sorption analysis shows pore bodies are <135 nm in size. A significant component of porosity forms as intragranular pores, predominantly in quartz, calcite and dolomite.

Previous studies have struggled to unravel the timing and history of porosity-occluding carbonate cement due to its exceptionally fine-grained nature. We have taken a novel approach, using both sequential acid dissolution and in-situ Secondary Ion Mass Spectrometry (SIMS), to determine the carbon and oxygen isotope composition of individual carbonate phases. Coupled with grain-scale compositional analysis by SEM-WDS we show that diagenetic dolomite formed at 5-64°C by replacement of early calcite cement in low temperature, near surface ocean conditions at temperartures of 8-51°C. The results of this PhD show that multi-stage carbonate diagenesis has destroyed, preserved and created porosity in the middle member of the Bakken Formation.

Contents

List of Figures

List of Tables

Chapter 1

Introduction

Background

The Bakken Formation in the Williston Basin, USA, (Figure 1.1), is a tight oil resource. Tight oil resources are defined as those with very low permeability, typically <10mD (Bjørlykke, 2010). In recent years such resources have made international headlines due to rapid technological advances, including horizontal drilling and hydraulic fracturing, which have begun to unlock these hydrocarbon reservoirs. Resources, for which hydraulic fracturing techniques are required in order to produce oil at economic rates are commonly referred to as 'unconventional'. Until recently, the Bakken was viewed as a marginal conventional resource due to its generally low permeability. The 'boom in Bakken production, began around 2008 as these new technologies began to make an impact (Brandt, 2014). For efficient production to occur and to be sustained an improved understanding on the key controls on reservoir quality are required.

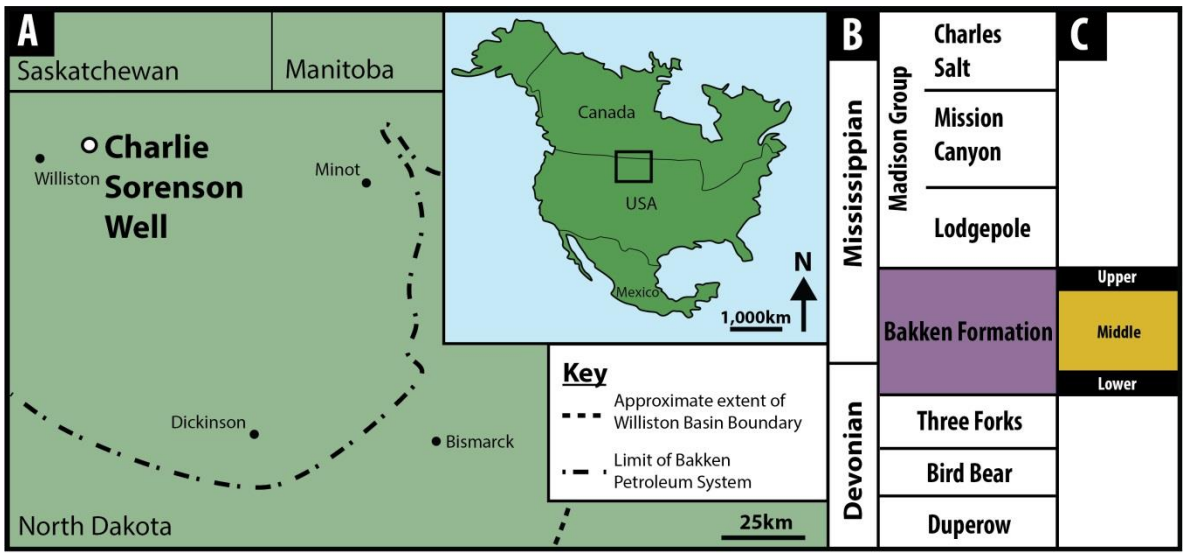

Figure 1.1 - a) Map showing the limits of the Williston Basin and Bakken Formation. Inset is a map of North America. b) Stratigraphic column showing the relative position of the Bakken Formation. c) Schematic section showing the three main members of the Bakken.

The name 'Bakken Formation' was first formally defined and described by Nordquist in 1953 from strata identified in Amerada Petroleum Corporation H. O. Bakken No. 1 deep test well. Prior to this the Bakken was known by several names including the Exshaw, Englewood and Kinderhook (Angulo & Buatois, 2011). Broadly, the Bakken is divided into three stratigraphic members; Upper, Middle and Lower. The upper and lower members are broadly similar and can be described as fissile, pyritic, organic rich shales. The upper

and lower Bakken are the source rocks for the Bakken hydrocarbon system. The middle Bakken member is the reservoir unit and is composed of a series of cemented, fine grained sandstones, siltstones and carbonates (Figure 1.1c).

The Bakken was most likely deposited in a shallow epicontinental sea. Since deposition the Bakken in this area is thought to have been buried to a maximum depth of 3900m and reached a maximum temperature of ~130°C (Kuhn et al., 2012). Given the apparent observed lateral homogeneity, it is assumed that the conditions of deposition must be having been similar over a large area (for a detailed outline see Chapter 2).

Over the last decade, hundreds of wells have been drilled into the Bakken in search of oil. Many have been successful, some world class; however, many have also been unsuccessful. The variability in success has been attributed to the vertical heterogeneity of the formation both in lithology and microstructure; and its reservoir quality (Sorenson & Terneus, 2008). This is true of other hydrocarbon settings around the world. The quality of a reservoir is one of the important uncertainties in wildcat drilling (Wilson, 1994).

A critical issue is still the pathways by which hydrocarbon fluids move from the pore system to the fracture system, and which geological processes exert the primary controls on the nature of the pore system: the reservoir quality. A greater understanding of the geological and diagenetic controls on pore systems and therefore permeability should ultimately result in higher hydrocarbon recoveries.

Producibility in hydrocarbon systems is a function of both porosity and permeability (reservoir quality) (e.g. Katz & Thompson, 1986). Porosity in the middle Bakken has predominantly been measured by wireline log measurements at low measurement resolution (e.g. Cramer, 1991; Kreis et al., 2006; Sonnenberg & Pramudito, 2009). More recently some works have tried to perform detailed pore scale characterisation studies (e.g. Sonnenberg & Pramudito, 2009). For example Li et al. (2015), relate pore character to lithological controls indicating the identification of pore-facies and pore-mineral as a key step in rock typing and the identification of more producible regions, sometimes referred to as 'sweet-spots'. Differences in lithological characteristics are a product of both depositional and diagenetic processeses.

Diagenesis is a group of processes which occur after deposition of the sediment, resulting in the physical, chemical and biological change of the sediment (Worden & Burley, 2003; Nichols, 2009). The principle suite of tools used to investigate diagenesis is petrographic analysis (e.g. Schmidt, 1979; Bjørlykke, 1983; Wilkinson & Haszeldine, 1996; Aplin et al., 2003; Nguyen et al., 2013). Specific studies of diagenesis in the Bakken have been conducted previously (e.g. Last & Edwards, 1991; Pitman et al., 2001; Ferdous, 2001; Karasinksi, 2006); however, none of these studies have been conducted on wells close to this study, nor is there much agreement in the order of which diagenetic events occurred or the complexity of the effects of diagenesis in the middle Bakken. Far more work has focussed on the over and underlying Bakken shales (e.g. Breit et al., 1992; Schieber, 1998; Price et al., 2011). In this study we seek to show how diagenetic processes have changed the original Bakken sediment with the aim of understanding the control, diagenesis exerted had on the pore systems of the middle Bakken.

Previous workers have shown that carbonate cementation has effected the reservoir quality of the middle Bakken. Very little work has been conducted to characterise these minerals, this is most likely due to the very fine grained nature of the carbonate phases, particularly dolomite. In order to investigate these fien grained carbonate phases further we apply an integrated grain-scale approach, using both secondary ion mass spectrometry (SIMS) and scanning electron microscopy - wavelength dispersive spectroscopy (SEM-WDS) we are able to make analyses of individual crystals to ~10 µm. This combination of grain scale techniques is unique in the study of diagenesis in the middle Bakken and uncommon in diagenetic studies generally. By doing so, the aim is to better understand the timing and temperature at which these phases formed to help us to better understand where the diagenetic history of these carbonate phases, from which we aim to deduce the effect these minerals had on the primary, depositional porosity.

Aims

This project aims to investigate the interplay between lithology, diagenesis and porosity in the middle Bakken. To do this, different facies within the core will be analysed from those identified in the facies classification described by Simenson, (2010). The aim is to identify and quantify diagenetic minerals, and to define the diagenetic controls on the micro-structure of the middle Bakken member. The project also seeks to quantify the pore systems and the morphology of these systems in the middle member. The effect of diagenesis can then be quantified.

The project seeks to answer the following questions:

1) How are the diagenetic products related to the initial mineralogy of the facies?
2) What is the relationship between facies and pore systems?
3) What is the effect of diagenesis on the morphology of pore systems in each facies?
4) What are the critical scales of heterogeneity within the middle Bakken formation?

Layout of the Thesis

Chapter 2 provides the geological context; the regional geology of the Bakken Formation and the overlying and underlying units. The chapter also offers a literature review of previous work on the Bakken petroleum system.

Chapter 3 details the diagenesis of the middle Bakken, identifying the key events in its geological history. This chapter provides a broad, full and complete view of diagenesis obtained principally from petrographic tools. This forms the basis for more detailed analysis of the carbonate cements in chapter 5.

Chapter 4 outlines the character of middle Bakken pore systems. In this chapter we make detailed measurements of individual pores and their respective features from the nanometre-scale upwards. This chapter seeks to relate the pore features identified and measured to the lithological and diagenetic observations made in Chapter 3.

Chapter 5 principally deals with carbonate cementation in the middle Bakken, seeking to unravel the processes which formed the different carbonate phases identified in chapter 3. This is primarily achieved using geochemical techniques.

Chapter 6 is a summary of the chapters in this thesis and seeks to synthesise the findings in order to answer the aims outlined above. This chapter also outlines proposals for future work which have arisen during the course of writing this thesis.

References

Angulo, S. & Buatois, L. (2011). Petrophysical characterization of sedimentary facies from the Upper Devonian–Lower Mississippian Bakken Formation in the Williston Basin, southeastern Saskatchewan. Canada: Summary of Investigations, 2011-2014.

Aplin, A. C., Matenaar, I. F. & van der Pluijm, B. (2003). Influence of mechanical compaction and chemical diagenesis on the microfabric and fluid flow properties of Gulf of Mexico mudstones. Journal of Geochemical Exploration 78, p. 449-451.

Bjørlykke, K., 1983. Diagenetic reactions in sandstones. In Sediment diagenesis. Springer Netherlands, p. 169-213.

Bjørlykke, 2011. Petroleum geoscience: From sedimentary environments to rock physics. Springer, p. 508.

Brandt, C. M. (2014). Impact of the Bakken Oil Boom on Employment and Wages in North Dakota. Undergraduate Economic Review 10, p.12.

Breit, V., Stright Jr, D. & Dozzo, J. (1992). Reservoir characterization of the Bakken shale from modeling of horizontal well production interference data. SPE Rocky Mountain Regional Meeting: Society of Petroleum Engineers.

Cramer, D. D. (1991). Stimulation Treatments in the Bakken Formation: Implications for Horizontal Completions. Montana Geological Society: 1991 Guidebook to Geology and Horizontal Drilling of the Bakken Formation, p. 117 – 140.

Ferdous. (2001). Regional sedimentology and diagensis of the Middle Bakken Member: implications for reservoir rock distribution in southern Saskatchewan. Unpublished thesis, Department of Geological Sciences: University of Saskatchewan, p. 467.

Karasinski, D. R. (2006). Sedimentology and Hydrocarbon Potential of the Devonian Three Forks and Mississippian Bakken Formations, Sinclair Area, Southeast Saskatchewan-southwest Manitoba. Masters Thesis. University of Manitoba (Canada).

Katz, A. & Thompson, A. (1986). Quantitative prediction of permeability in porous rock. Physical review B 34, p. 8179 - 8188.

Kreis, K., Costa, A. & Osadetz, K. (2006). Hydrocarbon potential of Bakken and Torquay formations, southeastern Saskatchewan. Saskatchewan and Northern Plains Oil & Gas Symposium 2006, Saskatchewan Geological Society Special Publication 19, p. 118 - 137.

Kuhn, P. P., di Primio, R., Hill, R., Lawrence, J. R. & Horsfield, B. (2012). Three-dimensional modeling study of the low-permeability petroleum system of the Bakken Formation. AAPG Bulletin 96, p. 1867-1897.

Last, W. & Edwards, W. (1991). Petrology of the Middle Bakken Member in the Daly Field, southwestern Manitoba. Williston Basin Symposium, p. 64-69.

Li, H., Dawson, M., Hart, B. & Radjef, E. (2015). Characterizing the Middle Bakken: Laboratory Measurement of Middle Bakken Properties. Unconventional Resources Technology Conference (URTEC).

Nguyen, B. T., Jones, S. J., Goulty, N. R., Middleton, A. J., Grant, N., Ferguson, A. & Bowen, L. (2013). The role of fluid pressure and diagenetic cements for porosity preservation in Triassic fluvial reservoirs of the Central Graben, North Sea. AAPG Bulletin 97, p. 1273-1302.

Nordquist, J. W. (1953). Mississippian stratigraphy of northern Montana. Billings Geological Society: Guidebook:: Montana Geological Society, p. 68-82.

Pitman, J. K., Price, L. C. & LeFever, J. A. (2001). Diagenesis and fracture development in the Bakken Formation, Williston Basin: Implications for reservoir quality in the middle member: US Department of the Interior, US Geological Survey.

Pitman, J. K., Price, L. C. & LeFever, J. A. (2001). Diagenesis and fracture development in the Bakken Formation, Williston Basin: Implications for reservoir quality in the middle member: US Department of the Interior, US Geological Survey Professional Paper 1653.

Price, L.C., Ging, T., Daws, T., Love, A., Pawlewicz, M. and Anders, D., (2011). Organic metamorphism in the Mississippian-Devonian Bakken shale North Dakota portion of the Williston basin. The Bakken-Three Forks Petroleum System in the Williston Basin, 2011. p. 438 - 489.

Schieber, J. (1998). Developing a sequence stratigraphic framework for the Late Devonian Chattanooga Shale of the south-eastern USA: relevance for the Bakken Shale. Williston Basin Symposium, p. 58 – 68.

Schmidt, V., 1979. The role of secondary porosity in the course of sandstone diagenesis. SEPM Special Publication No. 26, p. 175 - 207.

Simenson, A. (2010). Depositional facies and petrophysical analysis of the Bakken Formation. Parshall Field, Mountrail County, North Dakota: Master's Thesis, Colorado School of Mines, Golden, Colorado.

Sonnenberg, S. A. & Pramudito, A. (2009). Petroleum geology of the giant Elm Coulee field, Williston Basin. AAPG Bulletin 93, p. 1127-1153.

Sorensen, J.A. and Terneus, J.R. (2008). Evaluation of key factors affecting successful oil production in the Bakken formation, North Dakota. Technology status assessment. Energy and Environmental Research Center, Grand Forks, ND. Report submitted to US Department of Energy.

Wilkinson, M. & Haszeldine, S. (1996). Aluminium loss during sandstone diagenesis. Journal of the Geological Society 153, p. 657-660.

Wilson, M. (1994). Reservoir Quality Assessment and Prediction in Clastic Rocks, SEPM Short Course 30. SEPM (Society for Sedimentary Geology), Tulsa, Okla.

Worden, R. H. & Burley, S. D. (2009). Sandstone Diagenesis: The Evolution of Sand to Stone. Sandstone Diagenesis: Blackwell Publishing Ltd., p.1-44.

Chapter 2

Regional Geology & the Bakken Petroleum System

Tectonic Setting

The Williston basin is an ellipsoidal, intra-cratonic basin (Carlson & Anderson, 1965; Anna et al., 2010; Pollastro et al., 2011). The basin developed on the North American craton and along the south-western edge of the Canadian Shield (Meissner, 1978). The basin occupies parts of Montana, North Dakota and South Dakota in the USA and parts of Saskatchewan and Manitoba in Canada covering an area of ~770,000 km^2, Figure 2.1.

The basin is generally regarded as structurally simple due to its almost complete stratigraphic section, simple, small displacement faults and low wavelength folding (Webster, 1984; Meissner, 1991). The main macro-scale tectonic features in the Williston are the Neeson anticline in the North West of the basin (Carlson & Anderson, 1965), the Cedar Creek anticline which extends into south western North Dakota (Carlson & Anderson, 1965), the Brockton-Froid-Fromberg fault zone and the Colorado-Wyoming lineament, Figure 2.1.

These two Archean shear fault systems fault systems (the Brockton-Froid-Fromberg fault zone and the Colorado-Wyoming lineament) created a topographic low between the two faults, which is thought to have defined the Williston Basin (Gerhard & Anderson, 1988) (Figure 2.1). In the late Ordovician [~495 Ma] this topographic low began to infill with sediment (Pollastro et al., 2011). In total more than 5,000 m of sediment preserved in the basin centre (Peterson and MacCary, 1987) since deposition begun in the early Palaeozoic.

The basin sediments have been folded into a series of North and North-west trending anticlines, Figure 2.1 (Gerhard, 1982). It is these structural features that form the main oil traps of the basin. The Nesson anticline was initiated in the Cambrian (Pollastro et al., 2011). It is a north-south trending structure. Research has shown it is not simply one fold but in fact a series of smaller domes and anticlines along a trend which extends for around 105 km (Carlson, 1960). The Cedar Creek anticline is an elongate, north-west trending fold, approximately 160 km long found in eastern Montana (Strickland, 1954). The Cedar Creek anticline is an asymmetric fold with a westerly facing steep side (Strickland, 1954). It is one a long, narrow structure. The Billings anticline, or Billings Nose area as it is often referred to, is a gentle, northward plunging, anticlinal nose (Breig, 1988).

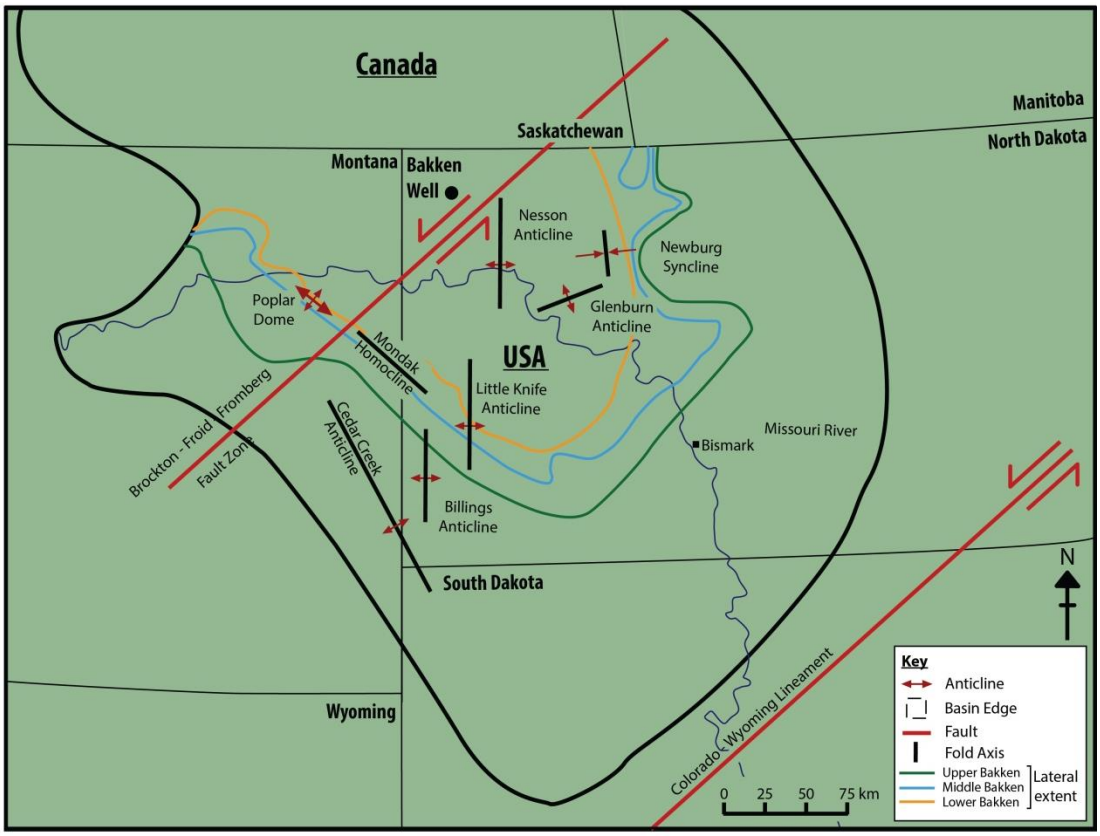

Figure 2.1 - Main structures of the Williston Basin. The approximate location of the Bakken-Sorenson well is shown. After Webster (1984); Bachu et al. (1988); Anna et al. (2010); Pollastro et al. (2010) and Sorenson et al. (2010).

Stratigraphy

Macro-Scale

The Williston basin is composed of Phanerozoic sedimentary rocks overlying Precambrian crystalline rocks, which are mostly meta-igneous and meta-sedimentary in nature (Burwash et al., 2008) (Figure 2.2). The first sediment was deposited in the Williston basin in the Cambrian, however it wasn't until the Ordovician when basin filling commenced. Between the Cambrian and the Tertiary, in excess of 4,900 m of sediment was deposited (Pollastro et al., 2011).

The first sequence stratigraphic model of the Williston basin was proposed by Sloss (1963), in which sedimentation in the Williston was proposed to have occurred in a series of cycles (Figure 2.2 & 2.3). Dating of the Bakken Formation was done using conodonts in work first conducted by Hayes (1985), see also page X.

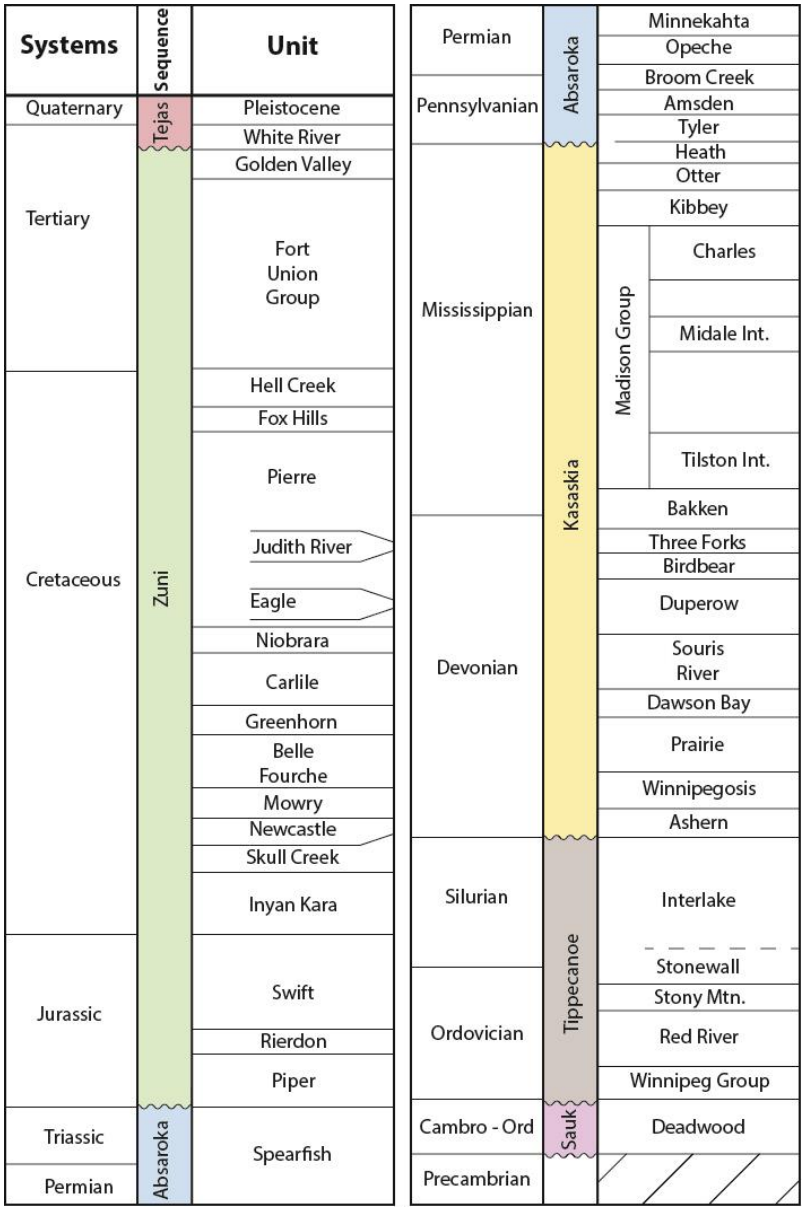

Figure 2.2 - Stratigraphic column of the Williston Basin, showing the Devonian-Mississippian Bakken Formation. After Gerhard et al., (1982) & Webster (1984).

1) The first of the 6 cycles of sedimentation is the Sauk, (Sloss, 1963). Sediments of the Sauk were deposited between the Cambrian to Lower Ordovician, deposited unconformably on Precambrian basement rocks (Sloss, 1963). These sediments vary from conglomerates at the base to argillaceous carbonate in the middle section to red sandstones in the upper beds (Gerhard et al., 1982).

2) The Sauk is overlain by the Tippecanoe sequence which represents the start of the Ordovician sedimentation (Sloss, 1963). Sediments of the Tippecanoe lie unconformably

over the Sauk. These sediments are predominantly composed of sandstones and shales in the lower section and carbonates in the upper part of the sequence (Gerhard et al., 1982). Tippecanoe sedimentation ended at the end of Silurian (Sloss, 1963).

3) Overlying these rocks are the sediments of the Kasaskia, for which deposition commenced in the Devonian. The rocks of the Kasakia sequence are mostly shelf and reef carbonates with some siliclastic sediments.

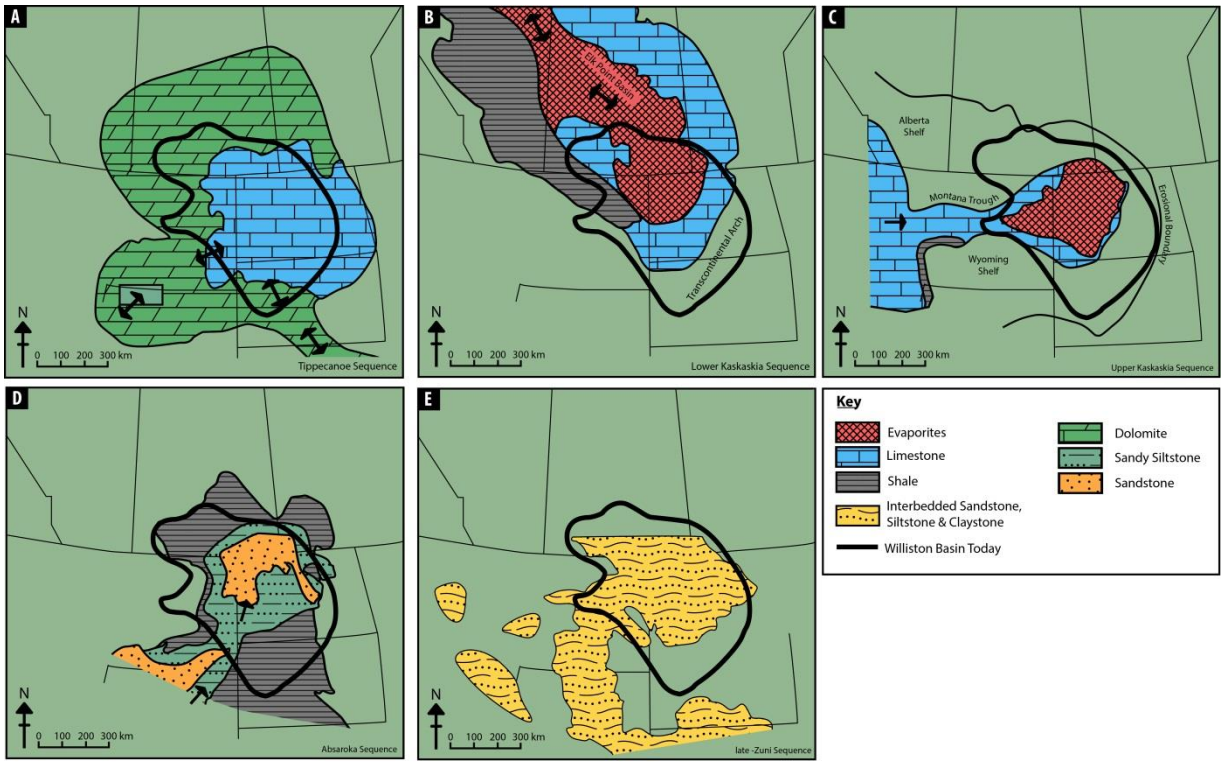

Figure 2.3 - Sequential maps for the time periods of key changes to basin sedimentation, showing source direction of sediment and lateral extent of deposition. A) Tippecanoe sequence B) Lower Kasaskia Sequence C) Upper Kasaskia sequence D) Absoroka sequence E) Late Zuni sequence. After Gerhard et al. (1982) and Peterson & MacCary (1987).

4) During a period of widespread uplift during the Late Carboniferous (Pennsylvanian) deposition of the Absoroka sequence commenced. Composed predominantly of siliclastics, it has minor dolostone, evaporite and limestone components (Gerhard et al., 1982).

5) Following this, the Zuni sequence was deposited during the Jurassic to Tertiary period (Sloss, 1963). In the lower section the Zuni is composed of shallow marine clastics and

carbonates, with the upper part composed of terrestrial sediments and a minor component of volcanic sediments (Gerhard et al., 1982).

6) The final sequence of the sedimentary succession is the Tejas (Sloss, 1963). This cycle was deposited during the Tertiary until Recent time. The Tejas is predominantly composed of terrestrial sediments mostly of glacial origin (Gerhard et al., 1982).

The Bakken Formation, Three Forks Formation and Lodgepole Limestone

The focus of this study is the Bakken Formation. The Bakken occurs directly below the Madison Group the Three Forks Formation (Figure 2.4).

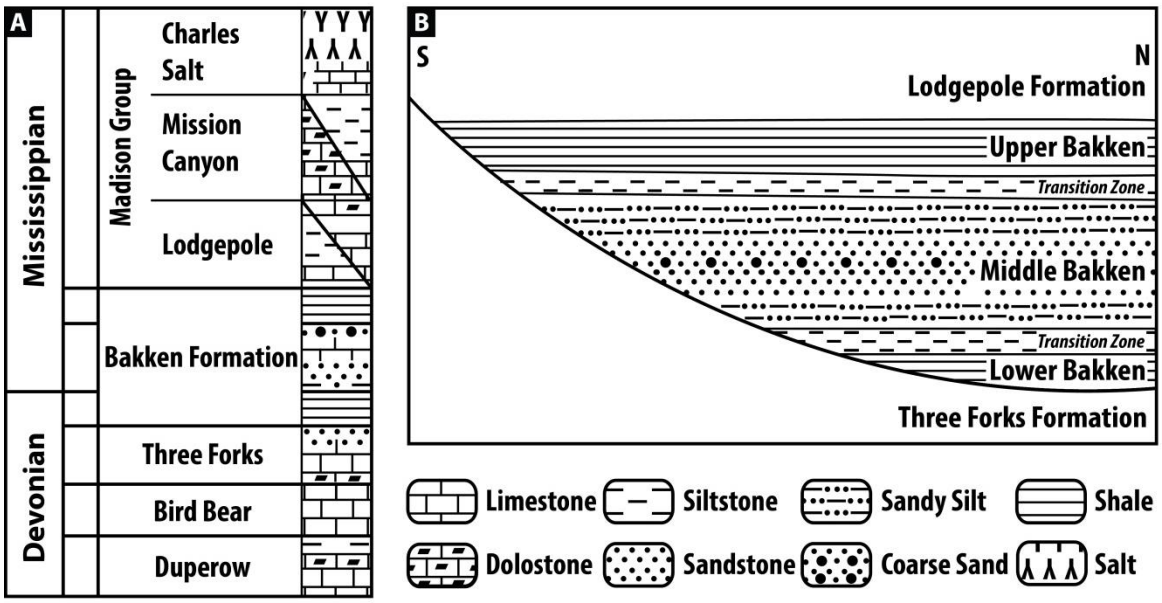

Figure 2.4 - a) Stratigraphic column of the Devonian-Mississippian strata overlying and underlying the Bakken Formation. b) Schematic cross-section showing the Bakken with detail of the stratigraphic heterogeneity and the unconformable relationship between the Three Forks Formation and the Lower Bakken. After Ostadhassan (2013).

The Madison group is a much thicker unit, predominantly composed of carbonates, which was deposited between the upper most Devonian and lower most Mississippian. The Bakken is one of several partially stratigraphically equivalent formations (Meissner, 1978). The stratigraphic position of the Bakken is well known; the Three Forks Formation underlies the Bakken with the Lodgepole Formation directly above (Holland et al., 1987) (Figure 2.4).

Bakken Formation

The Bakken unconformably overlies the Three Forks formation. The first formal definition of the Bakken Formation was made by Nordquist (1953) from strata studied in the Amerada Petroleum Corporation-H. O. Bakken No 1 deep test well in Williams County, North Dakota. He identified three distinct members within the Bakken: the upper, middle and lower members. The upper and lower members are broadly similar and can be described as fissile, pyritic, organic-rich shales.

The middle Bakken is a complex, heterogeneous unit of siltstone, sandstone, dolomite and calcite. Since this first formal definition the lithology of the Bakken, the unit has been studied extensively (Smith and Bustin, 2000; Pitman et al., 2001; Stasiuk & Fowler, 2004; Angulo & Buatois, 2010). Many workers have sought to divide the middle Bakken into different facies based on its geological characteristics, including lithology and palaeontology (Christopher, 1961; Le Fever & Le Fever, 1991; Smith & Bustin, 2000; Ferdous, 2001; Pitman, 2001; Le Fever et al., 2011; Canter et al., 2009; Kohlruss & Nickel, 2009; Angulo & Buatois, 2010; Angster, 2010; Simenson, 2010; Angulo & Buatois, 2011).

One of the defining components used in facies differentiation in the middle Bakken is paleontological evidence. The earliest body of work focussing on the palaeontology of the Bakken was by Hayes (1985) who looked at Conodonts in an attempt to determine the age and thermal maturity of the Bakken. Similar studies were conducted by Thrasher (1985), Huber (1986) and Karma (1991). Most recently in the Master's thesis of Simenson (2010), the Bakken was divided into the five facies which will be used in this study (Figure 2.5). These definitions are used primarily as they combine lithological and palaeontological data and present a workable number of associations for the sample size of this study. Furthermore, the Bakken-Sorrenson core was first logged using these facies, thus providing the most reliable record of the lithology of the core.

The five facies designations depict the change in depositional environment from argillaceous, bioturbated siltstones and sandstones deposited in the low shore face (facies B) to un-bioturbated sandstones and siltstones of low-mid shore face (facies C), to argillaceous sandstones which had deformed (facies D1) and calcite cemented sandstones (facies D2) of the mid shore face to bioturbated siltstones and sandstones of the low shore face and storm deposit (facies E).

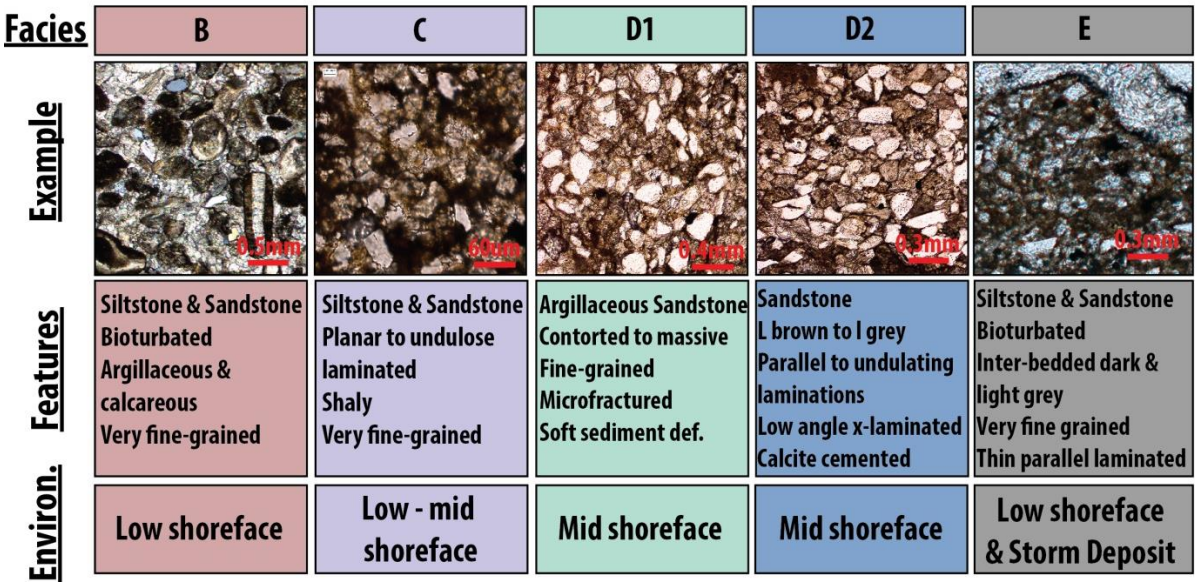

Figure 2.5 - Summary of the facies associations proposed by Simmenson (2010) and used in this thesis. 'Environ.' - the interpreted depositional environment.

A much broader biostratigraphic study was undertaken by Thrasher in 1987. In this study, over 500 macrofossils were analysed from the Bakken, and more than 50 taxa were identified. Of these, Brachiopods were found to be the most abundant fossils. Other macro-fossils included corals, gastropods, pelecypods, trilobites and trace fossils. These paleontological observations were used to extend and refine the biozones by Holland et al., (1987). The most recent study of the palaeontology of the Bakken was conducted in 2012 by Angulo & Buatois, who used trace fossils to develop new paleo-environmental interpretations. Using ichnotaxa they identified a restricted embayment in the middle Bakken which they suggest has major implications for both exploration and production. Locally, the presence of an embayment facies with good reservoir quality would present a high quality oil prospect, whereas in a more regional context a fully marine facies is likely to present a larger hydrocarbon target Angulo & Buatois (2012).

The upper and lower Bakken shales are regarded as laterally continuous almost completely across the basin, with only minor exceptions (Hayes, 1985). Several depositional models for the Bakken shales have been proposed including an offshore marine environment with and without a layered water column, a marine swamp with restricted circulation, and a stagnant marginal marine lagoonal environment (McCabe, 1959; Christopher, 1961; Webster, 1984; Pitman et al., 2001). The present consensus is that

the shales formed in an offshore marine environment during periods of sea-level rise (Webster, 1984; Le Fever & Le Fever, 1991; Smith, 1996). Anaerobic bottom-water conditions are indicated by the presence of pyrite, rare benthic fauna and high organic matter content (Pitman et al., 2001).

The upper and lower Bakken shales make identification of the Bakken Formation easy, particularly in wireline logs due to several characteristic responses on gamma-ray, sonic, resistivity and neutron traces. On gamma ray logs, the Bakken shales exhibit anomalously high gamma-ray radioactivity (>200API). On sonic logs, the Bakken has an anomalously low yet highly variable sonic velocity (high transit time of 80-120 microsec/ft.) (Murray, 1968 and Meissner, 1978). It is however challenging to resolve from seismic data due to its relatively thin nature and the comparatively low resolution of seismic techniques (Southcott & Harper, 2014).

Three Forks Formation

Unconformably underlying the Bakken is the Devonian Three Forks Formation. The Three Forks is approximately 50 m in thickness and is composed of interbedded siltstones and shales which have been highly dolomitised (Sandberg & Hammond, 1958). In some of the silty zones, conglomeritic dolomite clasts and pebbles have been observed. At the base of the formation is a thinly layered bed of anhydrite (Meissner, 1978). The unit can be broken down into three facies: a massive to chaotically bedded dolostone, inter-bedded dolostone with green mudstones and the Sanish sand, a bioturbated dolostone to sandstone (Sonnenberg et al., 2011).

The Sanish sand occurs at the top of the formation; it is a sandy zone which is 3-4 m in thickness which occurs erratically and inconsistently at the top of the Three Forks Formation. In several fields this is a productive unit (Meissner, 1978); some workers are of the view that the Sanish sand should be included in the Bakken (Sonnenberg et al., 2011).

The Three Forks Formation is thought to have been deposited in shallow marine environments (Lower Three Forks) during a period of transgression, which resulted in the deposition of terrestrial sediments of the Upper Three Forks Formation (Berry, 1943).

Lodgepole Limestone

Overlying the Bakken is the Lodgepole Formation which is the basal unit of the Mississippian Madison group (Meissner, 1978). The Lodgepole formation reaches a maximum thickness of 275 m in the centre of the basin in McKenzie County (Heck, 1978). The lower section of the Lodgepole is composed of dark grey lime mudstone interbedded with dark grey calcareous shales and minor amounts of chert and anhydrite (Meissner, 1978; Le Fever & Le Fever, 1991).

A localised heterogeneity observed in the Billings, Dunn, McKenzie and Mountrail Counties is the 'False Bakken' (Le Fever & Le Fever, 1991). This is a thin black shale and organic-rich limestone (Le Fever & Le Fever, 1991). The false Bakken is separated from the Upper Bakken by a medium-grey to brownish-grey, dense pelmatozoan limestone (Le Fever & Le Fever, 1991).

The Lodgepole is thought to have been deposited in a subtidal, open marine environment across a shallow ramp. The presence of an open-marine fauna suggests that the bottom waters were well oxygenated and of normal salinity (Jenks, 1972; Young & Rosenthal, 1991).

Stratigraphic Context

Deposited as part of the Kasaskia sequence the Bakken was deposited between the Upper Devonian to Early Carboniferous (Mississippian). The Bakken is one of several (partially) stratigraphically equivalent formations including the Exshaw-Banff Formation (Alberta, Canada), Sappington Member of the Three Forks Formation (Montana, USA), Leatham Formation (Utah & Idaho, USA), Leatham Member) of the Pilot Shale (Utah & Nevada, USA), Cottonwood Canyon Member of Lodgepole Limestone (Montana,USA) and the Englewood Formation (South Dakota, USA) (Meissner, 1978 and Hayes, 1985).

At the start of sedimentation in the Late Devonian, a phase of major uplift was concluding along the transcontinental arch, tilting the Williston basin northward. This tectonic event removed the main connection to the open ocean, resulting in more restricted conditions leading to the deposition of organic-rich shale of the Lower Bakken.

The Bakken represents the first major input of clastic material into the Williston basin since the Late Sauk and Early Tippecanoe. Clastic input into the basin reduced as sea level

dropped, at which time the Mississippian Lodgepole Limestone was deposited. It was during the Lodgepole deposition in the early Mississippian that the basin returned to its more circular form, reminiscent of its shape during the Tippecanoe period. During this period of structural adjustment, a narrow marine connection, the Montana Trough was formed, connecting the basin to the Cordilleran Sea and the depositional centre was returned to North Dakota.

Bakken Petroleum System

Production History

Hydrocarbon exploration and production in the Bakken has occurred in three main cycles. The first dates back to the first commercial discovery of oil in the Bakken which is thought to have occurred in 1951 by Amerada Petroleum. In 1953 the Antelope Field was discovered by Standard Oil and Gas, in a vertical well, penetrating the Bakken and Sanish sands of the Upper Three Forks Formation. Production in this area has largely been reliant on steeply dipping, naturally occurring fractures on the anticline (Figure 2.6). Soon after, Shell Oil made a further discovery in 1961, identifying the Elkhorn Ranch Field in the Billings Nose area (Figure 2.6). During this cycle a total of 44 wells were drilled in the Antelope field in the 1950's and 60's.

In 1978 Meissner published a paper describing a region of intense fracturing fairway along the flexure of the Antelope fold (Silver, 2013) (Figure 2.1). This generated renewed interest and boosted drilling in the Bakken formation, with production from both the upper and lower Bakken shale (Jarvie, 2012).

After these initial periods of interest in the Bakken, exploration proceeded slowly due to the generally low permeability of the formation (Le Fever, 1991). A third cycle of success in the Bakken was triggered by the development of unconventional drilling technologies including horizontal drilling and hydraulic fracturing (Le Fever & Le Fever, 1991 and Breit & Dozzo, 1992). The first horizontal well to be drilled in the Bakken was completed by Meridian Oil Incorporated, in 1987, which drilled into the Upper Bakken Shale in the Bakken Fairway.

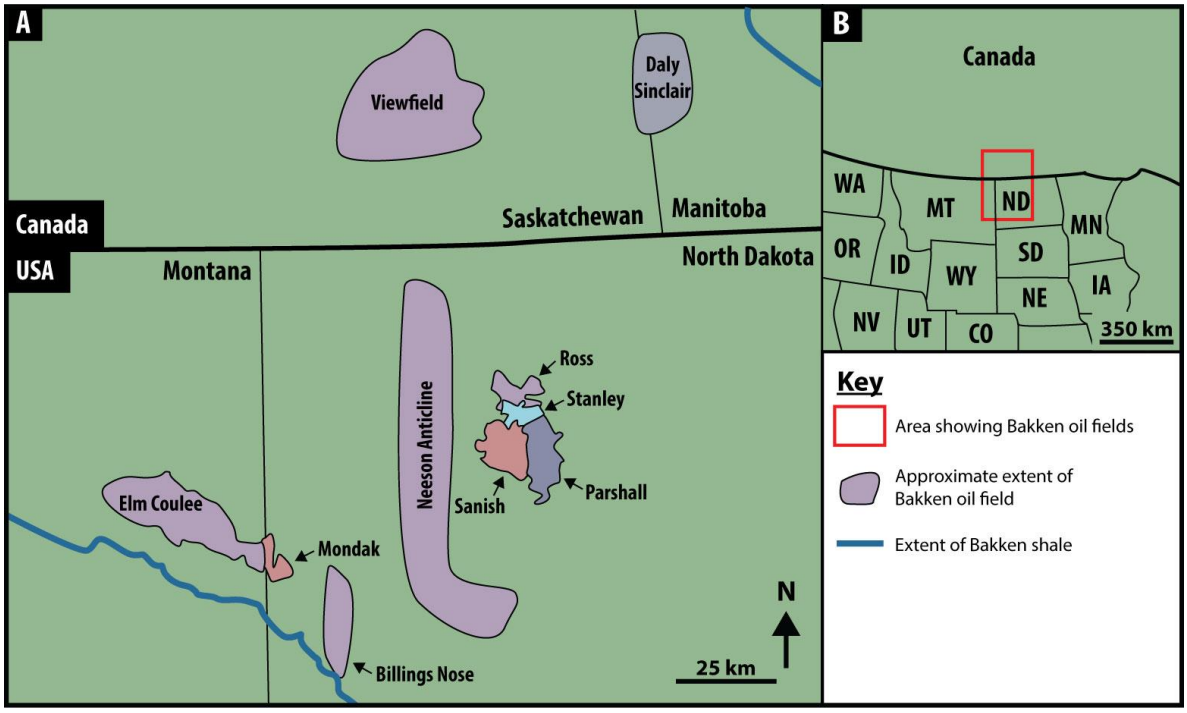

Figure 2.6 - Map of the main Bakken oil fields in northern USA and southern Canada. After EIA (2011).

In the early 1990s the application of hydraulic fracturing technology improved with increasing use in horizontal wells of the Bakken. In 1995, Dick Findley, an independent geologist, developed the 'sleeping giant' theory, suggesting it may be possible to produce oil from the Middle Bakken Member (Jarvie, 2012). The Elm Coulee Field was discovered in 1996, partly due to Dick Findley's work (Jarvie, 2012). From Findley's work the first horizontal well was drilled into the middle Bakken. By the late 90's multi-stage fracturing was conducted routinely in the Bakken Formation. Since then Bakken production has continued unabated. More recently in 2011, a 40-stage hydraulic fracturing and well-treatment workflow was conducted in the Bakken by Baker Hughes; at that time this was the largest number of fracturing stages conducted in a fracturing sleeve-packer system.

In December 2015, the North Dakota Department of Mineral Resources reported production from the Bakken and Three Forks petroleum system of 33.98 million barrels extracted from 10,373 wells. The U.S. Energy Information Administration report specific Bakken production is showing a gentle decline (from~1.2 million barrels a day in January 2015 to ~1.14 million barrels a day in January 2016). This is most likely due to a reduction in global oil price and not thought to be a reflection of geological controls on production.

Burial History & Oil Generation

For oil to form within a basin, the rocks must be rich in organic matter and experience exposure to sufficiently high enough temperature to transform the organic matter into petroleum. The shales of the Bakken formation are rich in organic carbon with a Total Organic Carbon (TOC) composition as high as 20% (Smith & Bustin, 2000).

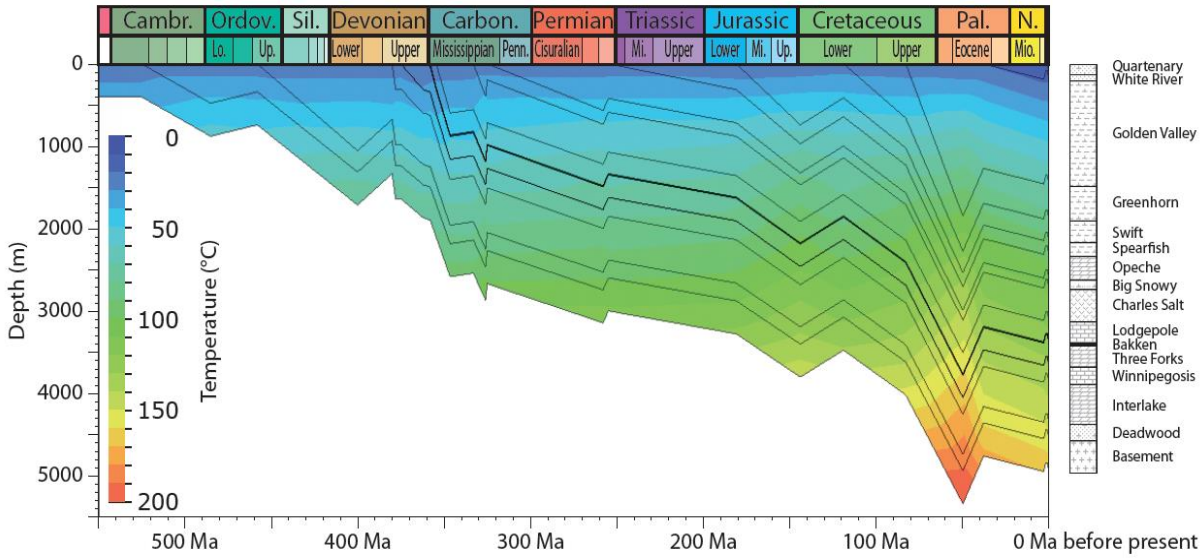

Figure 2.7 - Burial history of the Williston Basin developed for the basin centre in North Dakota (see Figure 2.1 for location). The temperature through time is overlain. Cambr - Cambrian, Ordov - Ordovician, Sil - Silurian, Carbon - Carboniferous, Pal - Paleogene, N - Neogene, Up - Upper, Mi - Middle, Lo - Lower, Penn - Pennsylvanian, Mio - Miocene. From Kuhn, (2012).

The Bakken is thought to have reached early 'oil window' conditions (~100°C) in North Dakota, during the Upper Cretaceous, and peak oil generation (~130 °C) during the mid-Paleocene (Eocene), (Figure 2.7), (Webster, 1984 and Kuhn, 2012) . Some workers have suggested that oil generation in parts of the basin continues today (Coskey and Leonard, 2009).

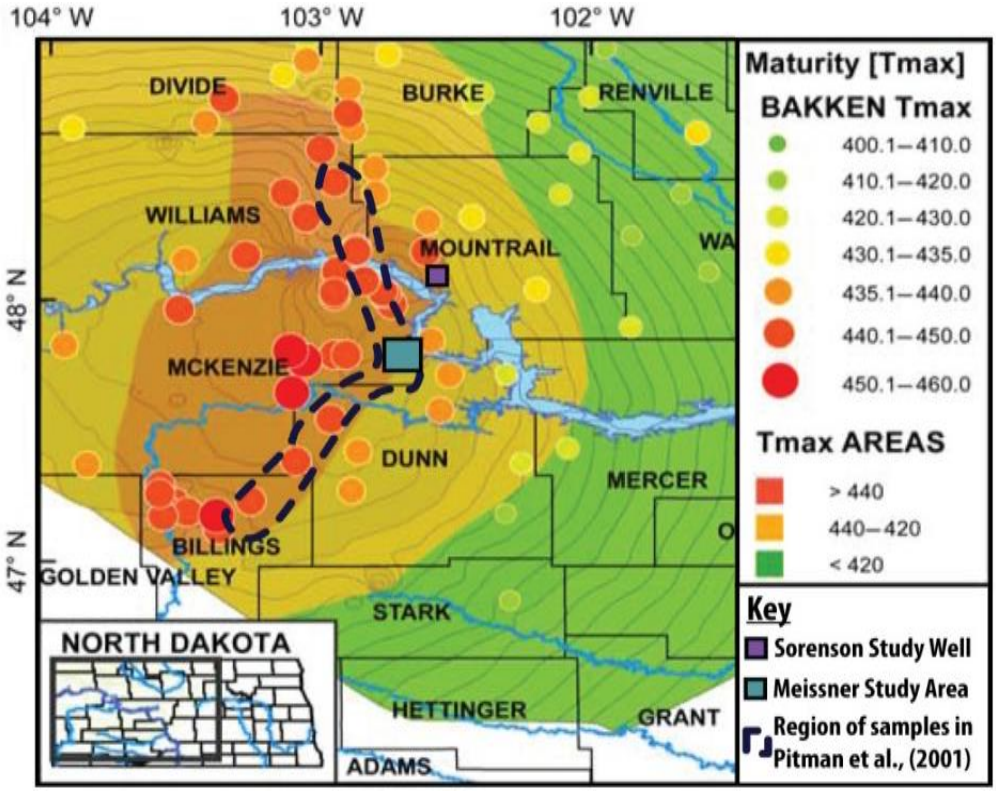

Figure 2.8 - Maturity map of organics in the middle Bakken, created from T_{max} value of the S2 peak from Rock-Eval pyrolysis, the approximate location of the Charlie-Sorrenson Bakken well is shown by the black star. Showing the approximate location of the Bakken-Sorenson well analysed in this study and the region that samples were taken from for analysis in Pitman et al., (2001). After Kuhn et al. (2010).

Paleo-reservoir temperatures have also been determined by analysis of fluid inclusions. The fluid inclusions present in fracture calcite were analysed by Pitman et al. (2001). In this study, they determined the homogenisation temperature of the inclusions to be between 110-115°C, similar to reservoir temperatures today (~125°C) (Kuhn, 2012). This suggests that the maximum paleo-burial depth was not significantly different to the depth of the Bakken today. This work is in agreement with the work of Kuhn (2012), discussed above.

Overpressure

In 1978, Meissner conducted a study of pore pressure in McKenzie County, North Dakota. They found the middle Bakken was anomalously over pressured, near to the well in this study. Overpressure occurs when the pore water pressure of sediment after burial exceeds the normal hydrostatic pressure at that depth. Generation of oil in the Bakken shales is

thought to be the source of the anomalously over pressure (Meissner, 1978), Figure 2.9. The conversion of organic matter in the Bakken to oil increases the volume of the fluid by as much as 30% (Sarg, 2012).

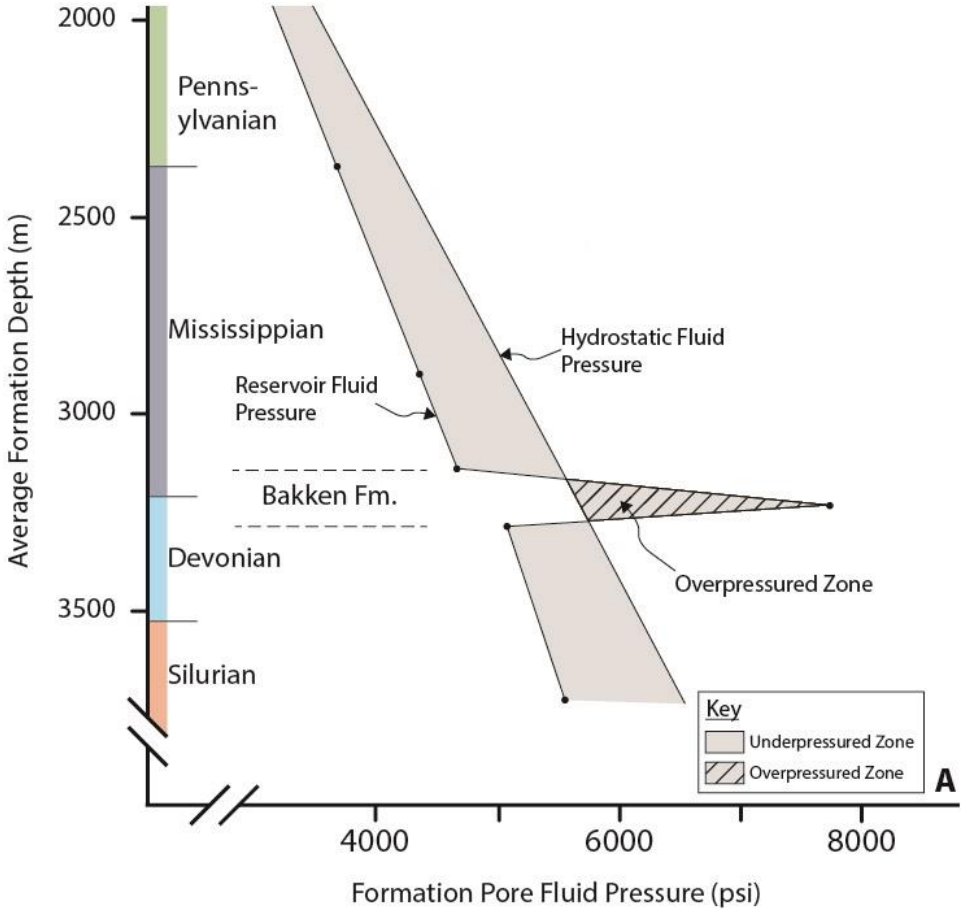

Figure 2.9 - Reservoir fluid pressure versus depth, Antelope field, Mc Kenzie County, North Dakota. Rock ages and the Bakken Formation are shown. After Meissner, 1978.

Resource Estimates

Whilst it is accepted that the Bakken shales matured sufficiently for oil to be expelled, the question of how much of this remains the Bakken Formation, is an important one. Several independent workers and the United States Geological Survey have published estimates on the size of the Bakken resource, (Figure 2.10), (Dow, 1974; Webster, 1982; Schmoker & Hester 1983; Schmoker, 1996; Price, 1999; Meissner & Banks, 2000; Flannery, 2006; Bohrer et al., 2008; USGS, 2008; Continental Resources, 2011; Mason, 2012).

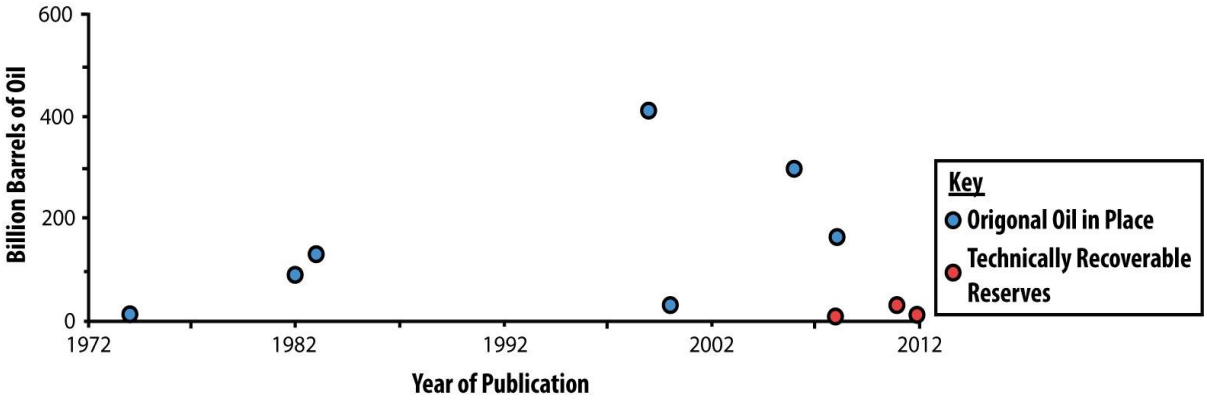

Figure 2.10 - Plot showing published estimates of OOIP (Original Oil in Place) [blue] and TRR (Technically Recoverable Reserves) [red] for the Bakken formation, shown by date of publication.

The smallest estimate came early in 1978, at this time few wells had been drilled and consequently data was very limited. Even after this early estimate, there was huge variability in the modelled estimates of OOIP. There is no clear trend between size of resource and time (Figure 2.10). The most comprehensive analysis, using the largest data set was conducted by Price in 1999. In his work, Price suggested there could be up to 503 Bbbl OOIP; the largest estimate ever proposed. The most recent estimate of technically recoverable oil was made by the USGS in 2013, in which they support their 2008 estimate of 3.65 Bbbl mean reserve (USGS, 2013).

Reservoir Quality

One of the biggest challenges to exploiting this potentially huge resource is the porosity and permeability of the reservoir: it's reservoir quality. Many studies have analysed porosity and permeability data obtained from Drill Stem Testing (DST's) (Meissner, 1978, Webster, 1984, Cramer, 1992, Ropertz & Jülich, 1994; Pitman et al., 2001). A DST is an in-situ down-hole test which is conducted after the drilling of a borehole and is used to determine the permeability, pressure and production capacity of a rock unit, over a section of the formation of several metres (Gluyas & Swarbrick, 2013). Meissner (1978) found the porosity of the middle Bakken to generally be very low, with an average porosity of ~5% and the work of Sarg, (2012) found middle Bakken permeability to average ~ 0.04 mD. Both porosity and permeability values are low when compared to

values in a conventional reservoir where one may expect the porosity and permeability to be of the order of 20-30 % and 0.1-10 mD respectively (Gluyas & Swarbrick, 2013).

Some workers have studied the pores of the Bakken on a smaller scale, from core samples. This work has primarily been conducted by Mercury Intrusion Capillary Pressure analysis (MICP), (Hunt, 1996; Ferdous, 2001; Wang et al., 2010). Most other studies using pore-scale analysis of the Bakken have focussed on the sealing capacity of the upper Bakken shales (Curtis et al., 2013 and Nagarajan, 2013).

The low porosity and permeability values determined by these earlier studies have largely been attributed to the effects of diagenesis both preserving and destroying porosity of the formation (Sonnenberg et al., 2011). Many workers have identified post-depositional processes which have occurred in the Bakken Formation (Durcharme & Murray, 1980; Kent, 1987; Last & Edwards, 1991; Pitman et al., 2001).

Currently there is very limited peer-reviewed literature on the effects of diagenesis on reservoir quality in the Bakken Formation. Early work made reference to the effects of diagenesis through the study of porosity (Meissner, 1978; Ducharme & Murray, 1980; Webster, 1984; Kent, 1987). Meissner (1978) suggests that low porosity values of the Bakken indicate fracturing is the principle reason that the formation is productive. He suggests the fractures provide the pathways for fluid flow. However, the study also highlights the importance of the marginal matrix porosity for obtaining hydrocarbon storage volume. In 1980, Ducharme and Murray concluded that the products of diagenesis varied between facies. In this study they split the middle Bakken into two facies, a lower wavy and lenticular rippled sandstone, interbedded with silty shale layers and a lower calcite cemented zone; the second facies is a fine cross-bedded sandstone with no calcite cementation. The study concluded that the precipitation of calcite cement in the lower middle Bakken facies caused the porosity to be significantly lower. However, these earliest studies described the effects of diagenesis as relatively insignificant. The only evidence of diagenesis observed was limited to grain interactions and grain rearrangement due to mechanical compaction. The suggestion that reservoir quality may be relatively poor with low porosity was postulated by Webster in 1984. Webster noted that the middle Bakken the unit is highly cemented with variable proportions of calcite and silica in all but one

facies and whilst variability exists in the presence and abundance of porosity occluding cements, Webster concludes the middle member is a marginal oil reservoir.

Whilst many of these studies propose that porosity has been destroyed by diagenetic processes, Kent (1987) suggested that diagenetic processes may also be preserving porosity. Kent proposed that the precipitation of an initially pore-occluding dolomitic cement was later dissolved, thereby restoring and potentially enhancing the pore system. The dissolution of the early diagenetic cement is thought to have been caused by upward-migrating acidic fluids, possibly related to hydrocarbon maturation (Kent, 1987).

Few studies have focussed solely on diagenesis in the Bakken. Of those which have, Last & Edwards (1991) were the first. They looked at samples from the Daly Field in Manitoba, Canada. In this study they proposed a simple paragenetic sequence based on transmitted light, SEM and XRD analysis. They identify at least 5 diagenetic stages. These are: early dolomite formation, precipitation of iron sulphide cements, partial dissolution of detrital feldspars and authigenic carbonate, the precipitation of illite and authigenic quartz, the formation of authigenic potassium feldspar, and concluded with the precipitation of anhydrite.

A second, more comprehensive study was conducted in 2001 by Pitman et al. They studied 26 samples obtained from wells penetrating the Bakken across North Dakota. They found evidence for both chemical and mechanical compaction, the degree of which corresponded to the depth of burial of the sediment. In moderately to deeply-buried sediments, they found long and concave grain contacts and stylolites, a result of chemical compaction. Authigenic phases were predominantly found in coarser-grained facies, with carbonates being the dominant cement; other authigenic phases included quartz, potassium feldspar and pyrite. Pitman et al. (2001) found no notable variations in authigenic mineral type related to changes in depositional facies or thermal maturity and burial depth. Mechanical compaction resulted in ductile deformation of grains. Secondary porosity was seen as a result of dissolution of carbonates, which Pitman et al. (2001) attributed to the generation of organic acids released during kerogen diagenesis. From these petrographic observations they developed a 12 stage paragenetic sequence.

Diagenesis of the Bakken has also been considered in a number of unpublished Masters and PhD theses (Edwards, 1993; Grover, 1996; Ferdous, 2001; Pramudito, 2008; Stroud,

2010). The study of Ferdous (2001) provides a very detailed discussion of diagenesis in the Bakken.

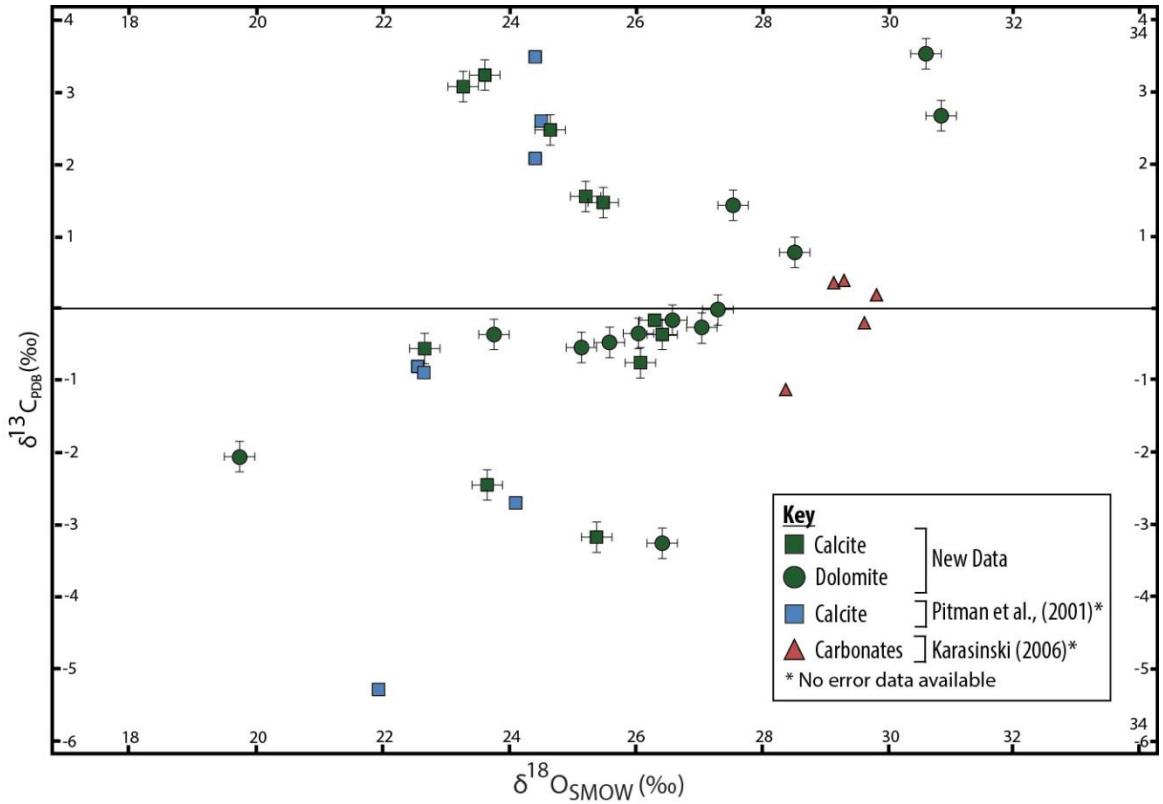

Figure 2.11 - Cross-plot showing the bulk stable isotope compositions of samples from the Bakken Formation and Three Forks Formation from previous studies, Pitman et al., (2001) and Karasinski (2006). Also shown is new bulk isotope data of Bakken samples obtained by sequential acid dissolution (discussed below). Note that the isotopic compositions are not consistent with marine dolomite derived from Late Devonian and Mississippian seawater, Karasinski (2006).

Ferdous obtained samples from the Bakken in south western Saskatchewan. He developed a comprehensive 18 stage paragenetic sequence incorporating a range of mineral phases of different forms which were then used to define different diagenetic facies and investigate the effects of these differences on the reservoir quality. The latest work in this field was by Pramudito (2008), who observed dolomite and anhydrite as mid to late diagenetic fracture fills.

Detailed analysis of the complex carbonates in the Bakken has been conducted by some workers by analysis of the stable isotopic composition of the carbonates. Pitman et al.

(2010) present $\delta^{13}C$ and $\delta^{18}O$ from 7 calcite fracture fill cements (Figure 2.11). They concluded that the calcite was derived from a marine carbonate rock with little input from organic matter. Karasinski (2006) performed bulk carbon and oxygen analysis on 5 middle Bakken samples (Figure 2.11); Karasinski identified different phases of dolomite but found it difficult to relate the isotopic data to particular formation fluids or diagenetic processes, most probably because of the limitations of bulk analyses of mixed carbonate phases and as a result suggested all 3 phases of dolomite occurred at the same time in the diagenetic sequence.

Whilst the early studies hold a general consensus that the diagenetic history of the Bakken is relatively simple (Meissner, 1978; Ducharme & Murray, 1980; Webster, 1984; Kent, 1987). Later studies suggest this may not be completely true (Pitman et al., 2001; Ferdous, 2001). Recent attempts to perform stable isotope analysis of the carbonates support this (Last & Edwards, 1991; Pitman et al., 2001; Ferdous, 2001; Pramudito, 2008). These previous provide a qualitative outline of the main diagenetic processes which have occurred in the middle Bakken and to some extent offer suggestions to potential mechanisms by which they formed. These studies do not offer a robust quantitative approach to the abundance of different phases in the middle Bakken; neither offer any specific connection between lower porosity zones and the abundance of pore occluding phases.

Conclusion

If the largest resource estimates are to be believed then there is a significant reward for improvements in understanding the lithology and pore systems of the Bakken petroleum system. Most workers hold a consensus view that the study of the reservoir quality of the Bakken will improve production in the Bakken. Ideas on the diagenetic history and its interplay with the pore systems of the Bakken are confused, unclear and disputed, providing a clear and necessary research opportunity.

References

Angster, S. (2010). Fracture Analysis of the Bakken Formation, Williston Basin: Field Studies in the Little Rocky Mountains and Big Snowy Mountains, MT, and Beartooth Mountains, WY, and 3D Seismic Data, Williston Basin. Master's Thesis. Colorado School of Mines.

Angulo, S. & Buatois, L. (2010). Sedimentary facies distribution of the Upper Devonian–Lower Mississippian Bakken Formation. Williston Basin, southeastern Saskatchewan: Implications for understanding reservoir geometry, paleogeography, and depositional history: Summary of Investigations, 2010-2014.

Angulo, S. & Buatois, L. (2011). Petrophysical characterization of sedimentary facies from the Upper Devonian–Lower Mississippian Bakken Formation in the Williston Basin, southeastern Saskatchewan. Canada: Summary of Investigations, 2011-2014.

Angulo, S. & Buatois, L. (2012). Integrating depositional models, ichnology, and sequence stratigraphy in reservoir characterization: The middle member of the Devonian–Carboniferous Bakken Formation of subsurface southeastern Saskatchewan revisited. AAPG bulletin, 96(6), p.1017-1043.

Anna, L., Pollastro, R. & Gaswirth, S. (2010). Williston Basin province—stratigraphic and structural framework to a geologic assessment of undiscovered oil and gas resources. USGS National Assessment of Oil and Gas Fact Sheet, p. 2013 – 3013.

Bachu, S. (1988). Analysis of heat transfer processes and geothermal pattern in the Alberta Basin, Canada. Journal of Geophysical Research: Solid Earth 93, p. 7767-7781.

Berry, G. W. (1943). Stratigraphy and Structure at Three Forks, Montana. Geological Society of America Bulletin 54, p. 1-30.

Bohrer, M., Fried, S., Helms, L., Hicks, B., Juenker, B., McCusker, D., Anderson, F., LeFever, J., Murphy, E., and Nordeng, S. (2008). Bakken Formation resource study project. North Dakota Department of Mineral Resources.

Breig, J. J. (1988). Mississippian Mission Canyon reservoirs of the Billings Nose, Billings County, North Dakota. Occurrence and Petrophysical Properties of Carbonate Reservoirs in the Rocky Mountain Region. Rocky Mountain Association of Geologists, Denver, Colorado, p. 357-369.

Breit, V. & Dozzo, J. (1992). Reservoir characterization of the Bakken shale from modeling of horizontal well production interference data. SPE Rocky Mountain Regional Meeting.

Burwash, R. A. M., C R; Wilson, J. (2008). Precambrian Basement Beneath the Western Canada Sedimentary Basin; in Geological Atlas of the Western Canada Sedimentary Basin, G.D. Mossop and I. Shetsen, p. 49 – 56.

Canter, L., Skinner, O. & Sonnenfeld, M. (2009). Facies and mechanical stratigraphy of the middle Bakken. Mountrail County, North Dakota, Abstract, Rocky Mountain Section of SEPM Luncheon.

Carlson, C.G., 1960, Stratigraphy of the Winnipeg and Deadwood Formations in North Dakota:North Dakota Geological Survey Bulletin 35, p. 145.

Carlson, C. G. & Anderson, S. B. (1965). Sedimentary and tectonic history of North Dakota part of Williston Basin. AAPG Bulletin 49, p. 1833-1846.

Continental Resources. (2011). Bakken field recoverable reserves. Assessment prepared by Continental Resources, Inc., Enid, Oklahoma, 14 February 2011.

Christopher, J. E. (1961). Transitional Devonian-Mississippian formations of southern Saskatchewan. Department of Mineral Resources, Petroleum and Natural Gas Branch, Geology Division, Province of Saskatchewan.

Coskey, R. & Leonard, J. (2009). Bakken Oil Accumulations – What's the Trap?: AAPG Search and Discovery Article# 90090. AAPG Annual Meeting, Denver, CO, 48.

Cramer, D. (1992). Treating-pressure analysis in the Bakken formation. Journal of petroleum technology 44, p. 20-27.

Curtis, M., Sondergeld, C. & Rai, C. (2013). Relationship between organic shale microstructure and hydrocarbon generation. Paper SPE 164540 presented at SPE Unconventional Resources Conference, Woodland, Houston, USA.

Dow, W. G. (1974). Application of oil-correlation and source-rock data to exploration in Williston basin. AAPG Bulletin 58, p. 1253-1262.

Ducharme, D. & Murray, D. L. (1980). Heavy oil occurrences of the Cactus Lake area Saskatchewan. Saskatchewan Geological Society Special Publication Number 5, p. 64 – 95.

Energy Information Administration [EIA]. (2012). Annual EnergyOutlook 2012 With Projections to 2035. Annual Report No.DOE/EIA-0383(2012, USDOE/EIA, Washington, DC (June 2012).

Ferdous. (2001). Regional sedimentology and diagensis of the Middle Bakken Member: implications for reservoir rock distribution in southern Saskatchewan. Unpublished thesis, Department of Geological Sciences: University of Saskatchewan, p. 467.

Flannery, J. K. (2006). Integrated analysis of the Bakken petroleum system, US Williston Basin. Saskatchewan Geological Society Special Publication 19, p. 138 – 145.

Gaswirth, S.B., Marra, K.R., Cook, T.A., Charpentier, R.R., Gautier, D.L., Higley, D.K., Klett, T.R., Lewan, M.D., Lillis, P.G., Schenk, C.J. and Tennyson, M.E. (2013). Assessment of undiscovered oil resources in the Bakken and Three Forks Formations, Williston Basin Province, Montana, North Dakota, and South Dakota, 2013. US Geological Survey Fact Sheet,3013(4).

Gerhard, L.C., Anderson, S.B., Lefever, J.A. and Carlson, C.G., (1982). Geological development, origin, and energy mineral resources of Williston Basin, North Dakota. AAPG Bulletin, 66(8), p.989-1020.

Gerhard, L. & Anderson, S. (1988). Geology of the Williston basin (United States portion). Sedimentary Cover; North American Craton; US Geological Society of America, The Geology of North America 2, p. 221-241.

Gluyas, J. & Swarbrick, R. (2013). Petroleum geoscience: John Wiley & Sons.

Grover, P. W. (1996). Stratigraphy and diagenesis of the Mississippian Bakken shale-Lodgepole Limestone sequence, Williston basin, North Dakota. PhD Thesis. Texas A & M University.

Hayes, M. D. (1985). Conodonts of the Bakken Formation (Devonian and Mississippian), Williston Basin, North Dakota. The Mountain Geologist, p. 64 – 77.

Heck, T. (1978). Depositional environments of the Bottineau interval (Lodgepole) in North Dakota. Montana Geological Society: Twenty-fourth Annual Conference, p. 191 – 199.

Holland Jr, F., Hayes, M., Thrasher, L. & Huber, T. (1987). Summary of the biostratigraphy of the Bakken Formation (Devonian and Mississippian) in the Williston basin, North Dakota. Williston Basin Symposium, p. 68 – 76.

Huber, T. (1986). Conodont biostratigraphy of the Bakken Formation and lower Lodgepole Formation (Devonian and Mississippian). Williston basin, North Dakota: Masters thesis, University of North Dakota, Grand Forks, North Dakota.

Hunt, J. (1996). Petroleum geology and geochemistry. Freeman, New York.

Jarvie, D. M. (2012). Shale resource systems for oil and gas: Part 2—Shale-oil resource systems. Shale reservoirs—Giant resources for the 21st century: AAPG Memoir 97, p. 89 – 119.

Jenks, S. (1972). Environment of deposition and diagenesis of the Lodgepole Formation (Mississippian), central Montana: Montana Geological Society Proceedings, 21st Annual Field Conference, p. 19-28.

Karasinski, D. R. (2006). Sedimentology and Hydrocarbon Potential of the Devonian Three Forks and Mississippian Bakken Formations, Sinclair Area, Southeast Saskatchewan-southwest Manitoba: University of Manitoba (Canada).

Karma, R. (1991). Conodonts of the Bakken Formation (Devonian-Mississippian) in Saskatchewan, northern Williston Basin. Sixth Williston Basin Symposium, p. 70 – 73.

Kent, D. M. (1987). Paleotectonic Controls on Sedimentation in the Northern Williston Basin, Saskatchewan. In: Longman, M. (ed.) Williston Basin: Anatomy of a Cratonic Oil Province. Denver: The Rocky Mountain Association of Geologists, p. 44 - 55.

Kohlruss, D. & Nickel, E. (2009). Facies analysis of the Upper Devonian-Lower Mississippian Bakken Formation, southeastern Saskatchewan. Summary of Investigations 1, 2009-2004.

Kuhn, P., Di Primio, R. & Horsfield, B. (2010). Bulk composition and phase behaviour of petroleum sourced by the Bakken Formation of the Williston Basin. Geological Society, London, Petroleum Geology Conference series: Geological Society of London, p. 1065-1077.

Kuhn, P. P. (2013). Integrated geochemistry and basin modelling study of the Bakken Formation, Williston Basin. PhD Thesis. Technische Universität Berlin, Fakultät VI - Planen Bauen Umwelt.

Kuhn, P. P., di Primio, R., Hill, R., Lawrence, J. R. & Horsfield, B. (2012). Three-dimensional modelling study of the low-permeability petroleum system of the Bakken Formation. AAPG Bulletin 96, p. 1867-1897.

Last, W. & Edwards, W. (1991). Petrology of the Middle Bakken Member in the Daly Field, southwestern Manitoba. Williston Basin Symposium, p. 64-69.

Le Fever, R. D. & Le Fever, J. A. (1991). Newburg and South Westhope Fields--USA Williston Basin, North Dakota. Stratigraphic Traps II, Treatise of Petroleum Geology, Atlas of Oil and Gas Fields: AAPG, p. 161 - 187.

Le Fever, J. A., Le Fever, R. D. & Nordeng, S. H. (2011). Revised nomenclature for the Bakken Formation (Mississippian-Devonian), North Dakota. The Bakken-Three Forks Petroleum System in the Williston Basin, p. 11 – 26.

Mason, J. (2012). Oil production potential of the North Dakota Bakken. Article accepted for publication in the Oil & Gas Journal. Feburary, 10.

McCabe, H. R. (1959). Mississippian stratigraphy of Manitoba: Manitoba: Department of Mines and Natural Resources. Mines Branch. Pub 58, p. 99.

Meissner, F. F. (1991). Petroleum Geology of the Bakken Formation Williston Basin, North Dakota and Montana. Montana Geological Society. Guidebook to Geology and Horizontal Drilling of the Bakken Formation, p. 19 – 42.

Meissner, F. F. & Banks, R. B. (2000). Computer simulation of hydrocarbon generation, migration, and accumulation under hydrodynamic conditions—Examples from the Williston and San Juan basins. USA: American Association of Petroleum Geologists Search and Discovery Article # 40179.

Murray Jr, G. H. (1968). Quantitative Fracture Study--Sanish Pool, Mckenzie County, North Dakota. AAPG Bulletin 52, p. 57-65.

Nagarajan, N. (2013). Critical role of rock and fluid-impact on reservoir performance on unconventional shale reservoirs. Unconventional Resources Technology Conference (URTEC), p. 1 – 20.

Nordquist, J. W. (1953). Mississippian stratigraphy of northern Montana. Billings Geological Society: Guidebook: Montana Geological Society, p. 68-82.

Ostadhassan, M. (2013). Geomechanics and elastic anisotropy of the Bakken Formation, Williston Basin. PhD Thesis. University of North Dakota.

Peterson, J. A. & MacCary, L. M. (1987). Regional stratigraphy and general petroleum geology of the US portion of the Williston Basin and adjacent areas. Williston Basin: Anatomy of a Cratonic Oil Province: Rocky Mountain Association of Geologists, p. 9-43.

Pitman, J. K., Price, L. C. & LeFever, J. A. (2001). Diagenesis and fracture development in the Bakken Formation, Williston Basin: Implications for reservoir quality in the middle member: US Department of the Interior, US Geological Survey Professional Paper 1653.

Pollastro, R. R., L; Cook, T. (2011). Geologic assessment of technically recoverable oil in the Devonian and Mississippian Bakken Formation. U.S. Geological Survey Williston Basin Province Assessment Team, p. 1 – 38.

Pramudito, A. (2008). Depositional facies, diagenesis, and petrophysical analysis of the Bakken Formation. Elm Coulee field, Williston Basin, Montana. Master's thesis. Colorado School of Mines.

Price, L. (1999). Origins and characteristics of the basin-centered continuous reservoir unconventional oil-resource base of the Bakken source system, Williston Basin. Energy and Environmental Research Center, University of North Dakota, Grand Forks, ND, p. 282.

Ropertz, B. & Jülich, F. (1994). Wege der primären Migration: eine Untersuchung über Porennetze, Klüfte und Kerogennetzwerke als Leitbahnen für den Kohlenwasserstoff-Transport: Forschungszentrum Jülich. PhD Thesis. RWTH Aachen University.

Sandberg, C.A. and Hammond, C.R., 1958. Devonian system in Williston Basin and central Montana. AAPG Bulletin, 42(10), p.2293-2334.

Sarg, J. F. (2012). The Bakken – An Unconventional Petroleum and Reservoir System. Technical Report. Oil & Natural Gas Technology: Colorado School of Mines, p. 64.

Schmoker, J. (1996). A resource evaluation of the Bakken Formation (Upper Devonian and Lower Mississippian) continuous oil accumulation, Williston Basin, North Dakota and Montana. Mountain Geologist 33, p. 1-10.

Schmoker, J. W. & Hester, T. C. (1983). Organic carbon in Bakken formation, United States portion of Williston basin. AAPG Bulletin 67, p. 2165-2174.

Silver, B. A. (2013). Montana Bakken Hybrid and Unconventional Plays. AAPG Search & Discovery Article #70139, p. 1- 44.

Simenson, A. (2010). Depositional facies and petrophysical analysis of the Bakken Formation. Parshall Field, Mountrail County, North Dakota: MS Thesis, Colorado School of Mines, Golden, Colorado.

Sloss, L. (1963). Sequences in the cratonic interior of North America. Geological Society of America Bulletin 74, p. 93-114.

Smith, M. G. (1996). The Bakken Formation (Late Devonian-Early Mississippian): a black shale source rock in the Williston basin. PhD Thesis. Department of Earth, Ocean & Atmospheric Sciences. Vancouver: University of British Columbia.

Smith, M. G. & Bustin, R. M. (2000). Late Devonian and early Mississippian Bakken and Exshaw black shale source rocks, Western Canada Sedimentary Basin: a sequence stratigraphic interpretation. AAPG Bulletin 84, p. 940-960.

Sonnenberg, S., Gantyno, A & Sarg, R. (2011). Petroleum Potential of the Upper Three Forks Formation, Williston Basin, USA. AAPG Annual Convention and Exhibition. Houston, Texas, USA.

Sonnenberg, S. A. & Pramudito, A. (2009). Petroleum geology of the giant Elm Coulee field, Williston Basin. AAPG Bulletin 93, p. 1127-1153.

Sorensen, J.A. and Terneus, J.R. (2008). Evaluation of key factors affecting successful oil production in the Bakken formation, North Dakota. Technology status assessment. Energy

and Environmental Research Center, Grand Forks, ND. Report submitted to US Department of Energy.

Southcott, A. and Harper, H. (2014). 3D Seismic Proves its Value in Bakken Geosteering. Unconventional Resources Technology Conference (URTEC), p. 1 - 7.

Stasiuk, L. & Fowler, M. (2004). Organic facies in Devonian and Mississippian strata of Western Canada Sedimentary Basin: relation to kerogen type, paleoenvironment, and paleogeography. Bulletin of canadian petroleum geology 52, p. 234-255.

Strickland, J. W. (1954). Cedar Creek Anticline, Eastern Montana. AAPG Bulletin 38, p. 947-948.

Stroud, J. (2010). The role of the lower Lodgepole Formation in the Bakken Petroleum System. Billings Nose, North Dakota: Master's Thesis, Colorado School of Mines, Golden, Colorado.

Thrasher, L. C. (1985). Macrofossils and biostratigraphy of the Bakken Formation (Devonian and Mississippian) in western North Dakota. Fifth International Williston Basin Symposium, p. 53 – 67.

USGS. (2008). 2008 U.S. Geological Survey petroleum resource assessment of the Bakken Formation, Williston Basin Province, Montana and North Dakota. Slide presentation prepared by the United States Geological Survey, U.S. Department of Interior, Washington, D.C., April 2008.

Wang, X., Luo, P., Er, V. & Huang, S.-S. (2010). Assessment of CO2 Flooding Potential for Bakken Formation, Saskatchewan. Canadian Unconventional Resources and International Petroleum Conference, p. 1 – 14.

Webster R. L. (1984) Petroleum source rocks and stratigraphy of the Bakken formation in North Dakota. In Hydrocarbon Source Rocks of the Greater Rocky Mountain Region, p. 57-81.

Young, H. R. & Rosenthal, L. R. (1991). Stratigraphic framework of the Mississippian Lodgepole Formation in the Virden and Daly oilfields of southwestern Manitoba. Sixth International Williston Basin Symposium, p. 113 – 122.

Chapter 3

Diagenesis

Introduction

Diagenesis is a group of processes which occur after deposition of the sediment, resulting in the physical, chemical and biological change of the sediment (Worden & Burley, 2003; Nichols, 2009). The main driving mechanisms for diagenetic reactions are temperature, pressure and pore fluid chemistry (Nichols, 2009). Diagenetic processes can significantly affect the quality of a petroleum reservoir, producibility of petroleum and is a function of the porosity and permeability of the unit (Purser, 1978; Moore & Druckman, 1981; Summa, 1995; Moore, 2001). The close relationship between diagenesis and reservoir quality are well accepted (e.g. Galloway, 1979; Loucks et al., 1984; Ehrenberg, 1990; Nichols, 2009).

The importance of understanding diagenesis and its effect on reservoir quality is demonstrated by the growth in research in this field through the 1980's and 1990's (Worden & Burley, 2003). This flurry of interest has largely been driven by the petroleum industry (Worden & Burley, 2003). In unconventional, tight, hydrocarbon systems the amount, size, distribution and connectivity of pore systems and therefore quality of the reservoir controls the hydrocarbon storage capacity and extractability of oil and gas from the reservoir (Doyen, 1988; Nelson, 2009; Curtis et al., 2010; Aguilera, 2014).
The ultimate aim of many companies was and is to predict regions within the reservoir of high porosity; sometimes referred to as 'porosity sweet-spots'. These are locations within the rock where a high quality reservoir may be found (Davies & Almon, 1981; Ajdukiewicz & Lander, 2010). More recently, with increased demand for hydrocarbons and the development of 'enhanced oil recovery' techniques, there is a drive to understand the chemical stability of authigenic minerals within a reservoir (Worden & Burley, 2003). This is particularly important as some EOR well treatments require the injection of reactive chemicals into the reservoir (Worden & Burley, 2003).

Low porosity and low permeability conventional reservoirs which are exploited for oil are referred to as 'tight-oil' plays. One of the most well-known tight-oil formations is the Bakken Formation (Yao et al., 2012). The earliest studies of the Bakken focussed on characterising the lithology of the Bakken, with only limited differentiation of detrital and diagenetic mineralogy. The first formal study of the Bakken was by Nordquist (1953), in which the Bakken was first described.

Whilst studies on the lithology of the Bakken are comprehensive both in number and detail (McCabe, 1959; Meissner, 1978; Webster, 1984; Holland et al., 1987; Smith & Bustin, 1996; Pitman et al., 2001, Angulo & Buatois, 2010), previous published work on diagenesis in the middle Bakken is limited, furthermore these studies have been conducted on samples taken from across the Williston Basin (Figure 3.1). The earliest work specifically commenting on diagenesis in the Bakken was conducted by Ducharme and Murray (1980) who analysed the middle Bakken in western Saskatchewan. They suggest that the effects of diagenesis in the middle Bakken have been limited. Ducharme and Murray find evidence of mechanical compaction which has led to ductile deformation of grains and a reduction in the pore space. They suggest carbonate cementation occurred very early in the diagenetic sequence. This was later partially dissolved and led them to suggest that all porosity in the studied well is secondary.

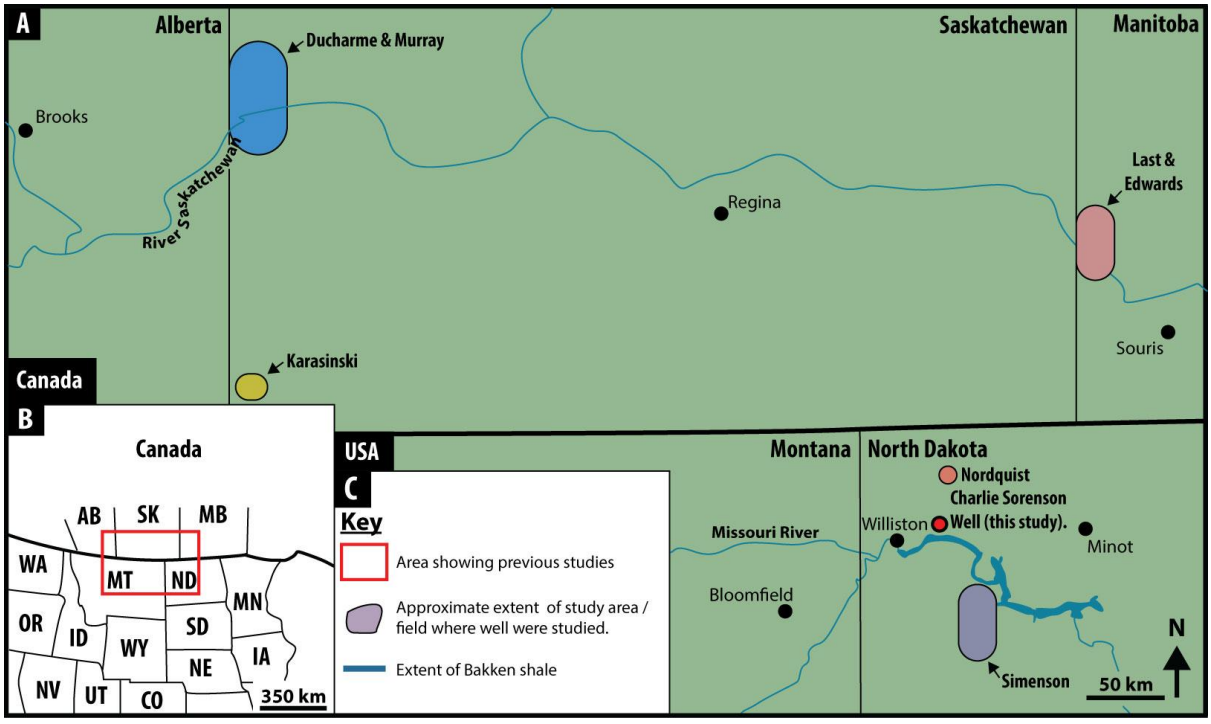

Figure 3.1 - Map showing the location of wells analysed in previous studies of diagenesis in the middle Bakken. Also plotted is the location of the Charlie Sorenson well which is the subject of this study.

The first specific and comprehensive diagenetic study of the middle Bakken was undertaken by Last and Edwards (1991) in a study of the Daly field, south western Manitoba. From thin-section and SEM examination they proposed that the middle Bakken

underwent at least 5 diagenetic stages. Pitman et al. (2010) extended these earlier conclusions, including observations of mechanical compaction, ankerite and K-feldspar overgrowths, chlorite growth and fracturing. These observations were incorporated into a paragenetic sequence of post-depositional events. The most recent, comprehensive diagenetic study is the PhD thesis of Ferdous (2001) which considered the effects of diagenesis on samples obtained from the Bakken in south western Saskatchewan. The study developed a comprehensive paragenetic sequence which was then used to define different diagenetic facies.

Summarising the findings of these earlier studies we find that the earliest workers hold a consensus view that the effects of diagenesis within the Bakken is simple, comprising between only a few diagenetic events which they postulate did not significantly affect the reservoir quality of the middle Bakken. However, these, more recent studies, (Ferdous, 2001 and Karasinski, 2006) suggest that diagenesis is complex, comprising many events and significantly affecting the reservoir quality. All of the studies do however agree that diagenesis was terminated at the onset of hydrocarbon generation. Furthermore, since the middle Bakken is a carbonate cemented siltstone, we cannot directly apply models of reservoir quality and diagenesis, drawn from either the carbonate or sandstone literature directly to the middle Bakken reservoir (Kupecz et al., 1997).

The purpose of this chapter is to assess the post-depositional history of the middle Bakken in the Charlie-Sorenson well, forming the context in which to evaluate the reservoir quality of the middle Bakken [Chapter 4] and ultimately to conclude what effect post-depositional diagenetic processes have had on the reservoir quality of the middle Bakken.

Methods

The Bakken-Sorenson core was drilled in North Dakota, close to the depocentre of the Bakken (Figure 3.1). The core was logged using the facies associations proposed in the Master's thesis of Simenson (2010). This facies scheme was developed from description of 10 cores in the Parshall Field (Figure 3.1).

Facies	Description & Characteristics (Simenson, 2010)	Depositional Environment
B	Strongly bioturbated, argillaceous and calcareous sandstones and siltstones.	Low shoreface
C	Very fine-grained siltstone and sandstone with planar to undulose laminations and shaly horizons.	Low - mid shoreface
D1	Fine-grained sandstone that has common micro-faults, micro-fractures, and slumps representing soft sediment deformation.	Mid shoreface
D2	Light brown - grey, parallel to undulating laminated, low angle cross-laminated sandstone, lacks bioturbation and highly cemented by patchy calcite. Thin, discontinuous shaly laminations. Fine grained.	Mid shoreface
E	Dark grey siltstone interbedded with a light grey, thinly parallel laminated, very fine grained, sandstone. Unit is bioturbated.	Low shoreface & storm deposits

Table 3.1 - Bakken depositional facies descriptions used to log the core and referred to as a proxy for depositional environment, after Simenson (2010).

The Simenson facies associations (Table 3.1) is one of ~25 facies schemes published for the Bakken. This scheme is used (and has continued to be used in this study) as it is concise yet highlights different depositional zones and key lithological changes within the Bakken Sorenson core at the metre scale. Samples of the middle Bakken were then selected from the full length of the Sorenson core in order to represent the full range of facies observed in the middle Bakken, Figure 3.2. A detailed core scale, lithology log with sample locations is given in Appendix 1.

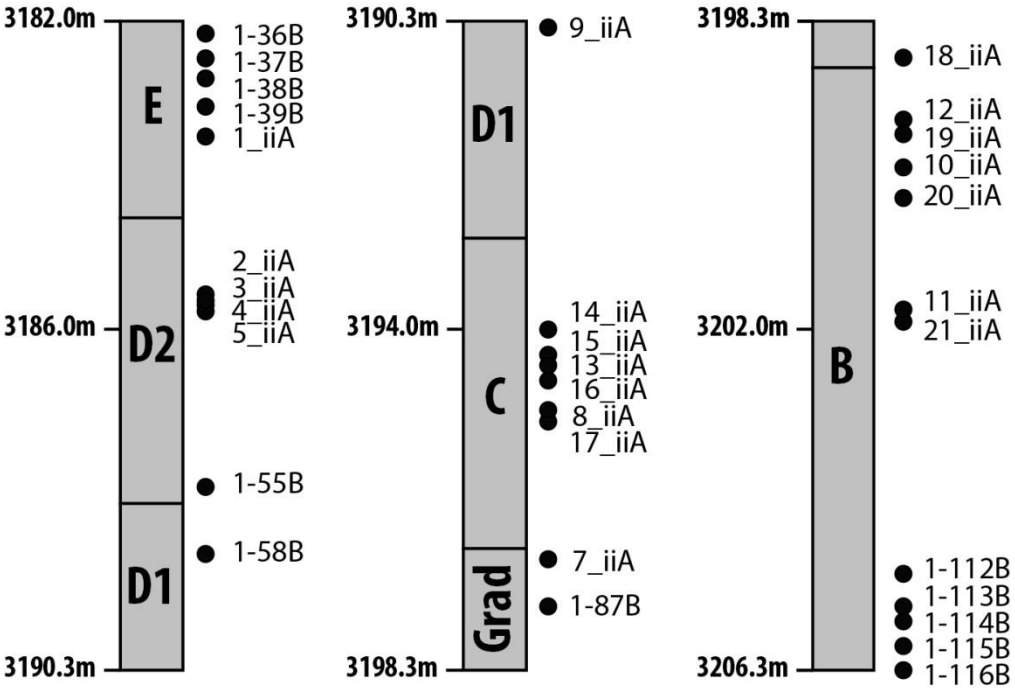

Figure 3.2 - Log of the middle Bakken, showing the relative position of the different facies

associations (grey blocks) and the samples taken (black dots), from the top of the middle Bakken (3182.0m) to the base of the middle Bakken (3206.3m), after Simenson (2013). Gradational facies (Grad) - mixed section of core showing characteristics of facies B, C, B Hart pers. comm. (2013).

In total 32 samples were analysed from the middle Bakken reservoir unit, (Appendix 2). These samples were initially taken as 1" plugs. The samples were then cut perpendicular to bedding and polished to a standard 30 µm thick, petrographic thin-section.

The thin-sections were first scanned using a Minolta Dimage Scan Elite II photographic slide scanner at a resolution of 2820dpi. This was used to identify sedimentary structures. The thin-sections were then analysed using a Leica DM2500P transmitted light petrographic microscope with a camera attached. A full rock description was made both from observations under the microscope and point counting. This included textural and mineralogical information, which sought to differentiate detrital from diagenetic mineral phases, Table 3.2. The petrographic terminology used to describe mineral grains is that defined by Folk (1980). Clay minerals and other grains too fine to be reliably identified under a transmitted light microscope were grouped and referred to as 'matrix' for the purposes of this study. Dolomite crystal textures were classified using the scheme described in Sibley & Gregg (1987). Whilst the nomenclature defined by Sibley and Gregg was proposed principally for dolomite crystals in carbonate rocks, it is very appropriate to mixed clastic-carbonate systems as it considers the grain boundary and grain size relationships of individual crystals over a range of low diagenetic temperatures similar to those experienced by the middle Bakken during burial (see Chapter 2). The grain boundary and grain size relationships are used in this scheme to infer the genetic origin of each dolomite crystal class. We do not use the popular scheme proposed by Friedman (1965) as this focusses on crystal shape alone. The merits of this classification scheme are discussed in Sibley & Gregg (1987) and Randazzo & Zachos (1984). To determine the abundance of individual dolomite and calcite phases, point counting was conducted on 27 samples with a Petroglight petrographic point counter. The data were normalised to remove minerals other than dolomite and calcite.

After transmitted light examination, all of the polished thin-sections were coated with ~25nm of carbon to prevent charging during electron microscopy. Samples were analysed using a Hitachi SU-70 High Resolution Analytical FEG SEM, which is equipped with an Oxford Instrument Energy Dispersive X-ray (EDX) system. Both Secondary Electron (SE) and Backscattered Electron (BSE) images were collected with the settings: 15-16mm WD, 15 & 20keV accelerating voltage, 2-4nA filament current and magnifications of between x300 & x10,000. Image and EDX data were analysed using INCA Energy software. The topographic information provided by SE images is useful for differentiating pores and organic material from other phases, whereas the BSE images allow differentiation of phases based on their mean atomic number. Cross-cutting relationships were used as the principle evidence for determining the relative timing of diagenetic events.

Prior to each analytical session, an elemental cobalt instrument standard was run. The standard was measured 3 times by EDX at a magnification of 5,000x and an instrument adjustment applied to correct for any variation in intensity. In addition, a suite of carbonate minerals standards (calcite, dolomite, ankerite and siderite) were also measured using SEM-WDS which gave an average accuracy of ±1.04 wt% between reported and average measured elemental composition. See Appendix 4 for a full report on accuracy and precision.

For EDX mineral and elemental mapping, 10 samples were selected to represent their respective facies. The samples chosen were those which had petrographic characteristics consistent with the facies which they represent. Petrographic-facies characteristics used were: mineral abundance, presence of bioclasts, bioturbation and lamination/sedimentary structure. For each sample, two 0.5 mm^2 sites were selected at random. Post-analysis, the selected sites were checked for any apparent bias e.g. bioclasts (no such bias was observed). Maps of elemental distribution were obtained using the SEM-EDX system for each of these sites. The settings used for the EDX elemental map collection were 300 µs dwell time, 15 kV accelerating voltage and 4nA filament current with 25 frames recorded for each area.

One of the inherent compromises is that in order for an element map to be of a large enough area to be representative a low magnification must be used, yet a higher magnification is required to resolve the finest grains component minerals in the rock

matrix. To try to minimise this compromise, the highest pixel resolution was chosen for each frame (512 x 512) at a magnification of x500, so a sufficiently large, representative area could be imaged and elementally mapped. The images and elemental map data were obtained as a series of frames which were montaged together automatically by INCA software post-acquisition.

The elemental maps were then processed using aZtec Energy software to create mineral phase maps and to determine the area of each mineral phase. For phase segmentation a boundary tolerance of 3 and grouping value of 2 were used. The grouping level combines phases of similar elemental composition. The lower the grouping value, the less merging of compositionally similar phases (aZtec, 2013). The boundary tolerance controls segmentation at the boundaries between different mineral phases. When the boundary tolerance is low, a greater number of unresolved phases will be shown (black pixels) (aZtec, 2013). These maps were binarised using ImageJ and analysed using the particle analysis tool to measure the grain size, morphology and mineral abundance. Determination of the chemistry of individual grains was conducted using Scanning Electron Microscopy-Wavelength Dispersive Spectroscopy (SEM-WDS). This was completed using an INCA Wave 700 spectrometer WDS detector attached to a Hitachi SU-70 FEG SEM. The operation was controlled by and the data processed using INCA microanalysis software.

Scanning Electron Microscopy - Cathodoluminescence (SEM-CL) was used to differentiate detrital quartz from authigenic quartz on the coated thin-sections. This method was used in preference to transmitted light microscopy as quartz overgrowths are difficult to resolve due to being in optical continuity with the host grain (Hogg et al., 1992). The SEM-CL method uses the phenomenon of luminescence. The luminescence is created by the bombardment of a mineral with a beam of electrons derived from a cathode source (Boggs & Krinsley, 2006). Detrital quartz is strongly luminescent relative to the weakly luminescent/non-luminescing authigenic quartz (Sippel, 1968). The analysis was conducted on a Gatan Mono-CL cathodoluminescence system, using Digiscan II software for spectrum imaging. We used mono-CL to produce grey-scale images rather than colour-CL, as this is much quicker at producing images where textural features are far more critical than CL wavelength (colour). We were able to observe internal structures within

individual quartz silt grains. CL images were recorded with the corresponding inline backscattered electron images.

We operated the instrument in panchromatic mode with a blue filter, using an accelerating voltage of 10kV. The samples were polished thin-sections, coated with 30-35 nm of carbon. Previous workers have found CL imaging of mixed silicate-carbonate samples to be challenging due to the significant difference in brightness between highly luminescent carbonate phases and less luminescent silicate phases (Reed & Miliken, 2003). In our initial experiments we encountered challenges associated with streaking in the image. This artefact has been observed in other studies and is thought to be due to persistence of luminescence (phosphorescence) (Marshall & Mariano, 1988 and Reed & Milliken, 2003). This artefact is caused by the simultaneous detection of light from different areas of the specimen, and occurs when the beam raster speed is slower relative to the decay time of the CL emission (Reed & Milliken, 2003). One approach to overcome this, is to use long dwell times (~3,200 µs per pixel), as implemented by Lee (2000); however even at dwell times of (~1000 µs) we found that this produced significant beam damage to the sample surface. Reed & Milliken (2003) found that acquiring images of the shorter wavelengths of CL-emissions by inserting a short wavelength (blue) filter between the mirror and photo-multiplier tube. We recognise that spectral emission information will be lost for carbonate minerals, however for the study of quartz (in this chapter), this is not a limitation; similar conclusions were drawn by Bouch (2006).

X-ray diffraction (XRD) was performed by KT GeoServices, Inc. The samples were disaggregated in a mortar and pestle. A split of each sample was then transferred to distilled water and pulverized using a McCrone micronizing mill. The powdered sample was then dried, disaggregated, and packed to form random whole-rock mounts. A separate split of each sample was dispersed in distilled water using a sonic probe. The suspensions were then size fractionated in a centrifuge to isolate clay-size (<4 micron equivalent spherical diameter) materials for a separate clay mount. The suspensions were then vacuum-deposited on nylon membrane filters to produce oriented clay mineral mounts which were attached to glass slides and exposed to ethylene glycol vapour for approximately 12 hours (Talbot, 2014, pers. comm. 24th March).

The XRD analysis was conducted using a Siemens D500 automated powder diffractometer equipped with a copper X-ray source (40 kV, 30 mA) and a scintillation X-ray detector. Both bulk and clay (<4 µm) analyses was conducted. All quantitative data (including clay mineral amounts) come from the whole rock pattern, using Whole Pattern Fitting (WPF) and Rietveld refinement methods. The detection limits differ for each individual mineral but are reported to be between 1-5 wt% (Talbot, 2014, pers. comm. 24th March, 2015). The accuracy of the analyses is dependent on the abundance of the individual phase; as the mineral abundance increases, the error decreases. For example, quartz with an abundance of 50% has a relative error of ~10% (45-55%). Pyrite with an abundance of 5% has a relative error of ~50% (2.5 to 7.5%) (Talbot, 2014, pers. comm. 2nd March, 2016).

Results

Facies

The whole core was logged at the wellsite using the facies descriptions of Simenson (2010). See Appendix 1 for the full core log, Hart pers comm (2014). The results of facies analysis show an upward change in the core from a low shoreface deposit, to a mid shoreface deposit and finally a return to a low-shoreface, Figure 3.3.

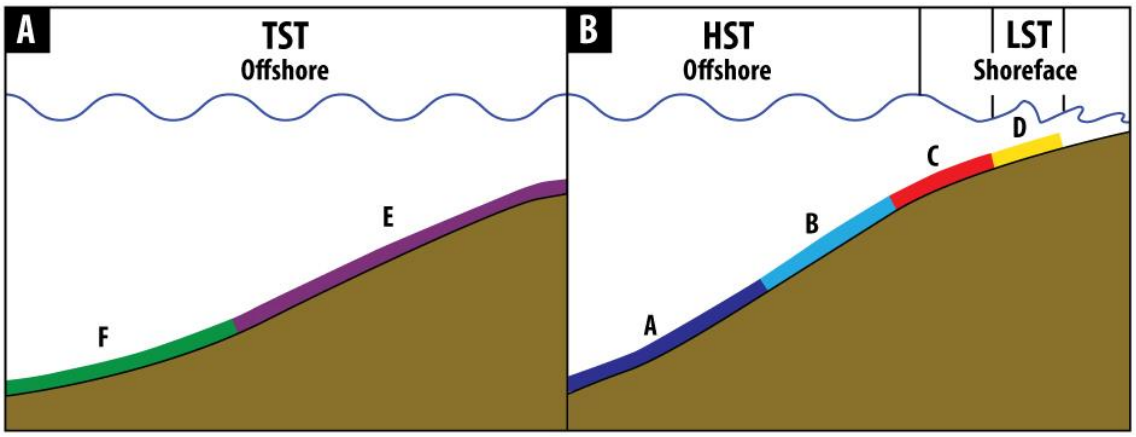

Figure 3.3 - Schematic section of the environment of deposition of individual facies. a) Transgressive systems tract (TST) b) Highstand systems tract (HST) and low stand systems tract (LST). After Simmenson (2010).

Lithology

Structure

Transmitted light slide scanning of the thin-sections showed different sedimentary structures within the middle Bakken. Almost all of the samples in the study are bioturbated, but to varying extents. The most bioturbated samples are found in facies B and E (Figure 3.4a & b). Many of the samples are laminated; which is particularly evident in the upper section of facies B (Figure 3.4d). Laminations vary in thickness from 1-5 mm. In facies E, there is no evidence of lamination, though it is here where bioturbation intensity is greatest. In some samples bioturbation has completely removed the fabric of the rock (Figure 3.4). Less pervasive burrowing is found in facies D2 and at the top of facies D1. Burrow intensity is greatest near the boundary with the lower Bakken/middle Bakken and middle Bakken/upper Bakken boundaries and sparse throughout the rest of the middle Bakken. The burrows have a branched nature with 30-40° branch inter-sections which suggests they may be Chondrites (Bromley & Ekdale, 1984).

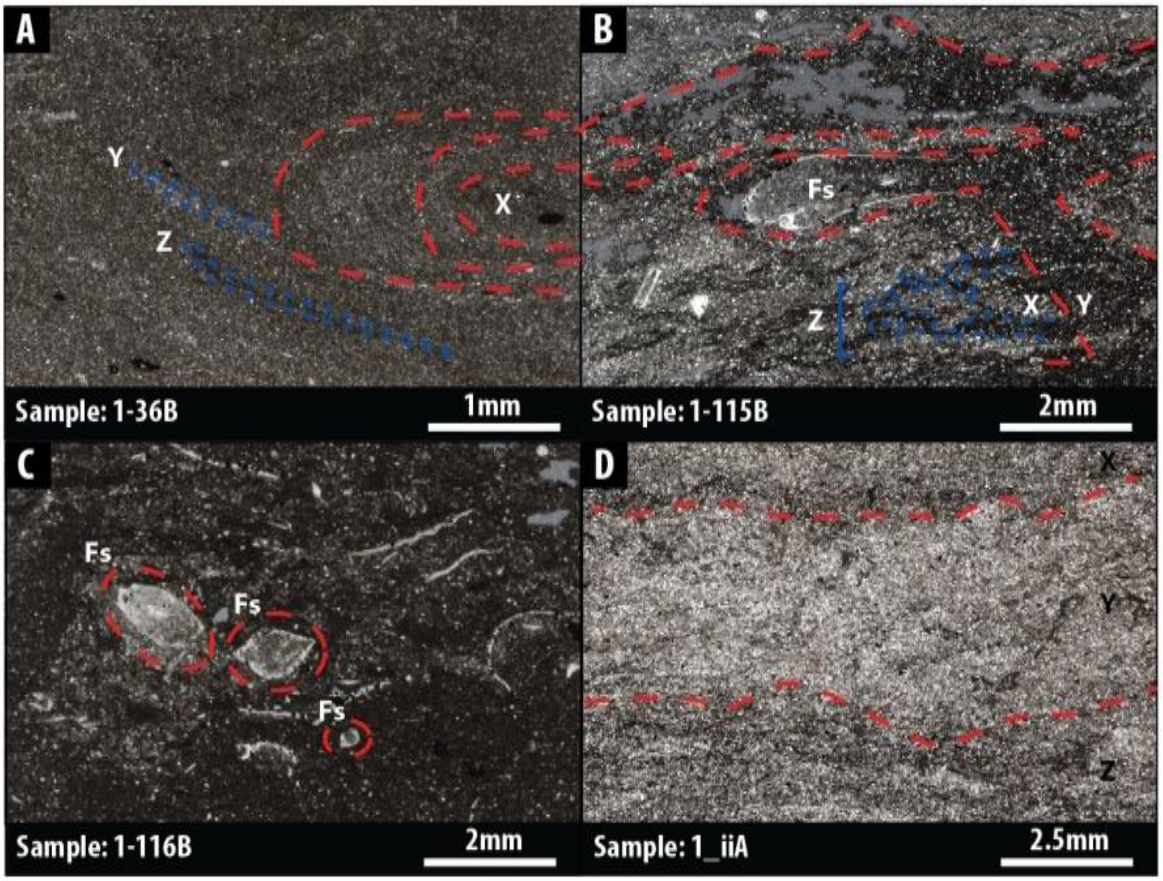

Figure 3.4 - Thin-section scans from the middle Bakken A) Burrow cross-section (X), variations in clay content highlight sediment variations. B) Vertical section of a burrow

made in a carbonate siltstone (X) which has been infilled with clays (Y). Sub-millimetre thick discontinuous sediment bands (Z). An articulated, complete brachiopod (Fs) is present in the burrow. Note: the sub-millimetre lenses of carbonate-rich sediment. C) Complete, articulate bivalves, showing no obvious effects of compaction. Note: colour variations from darker, clay-rich sediment to lighter, regions with lower clay content. D) Scan showing quartz-rich, carbonate-cemented band (Y) between clay-rich bands (X & Z).

Soft sediment deformation structures including slump structures and convolute bedding are exclusively found in the gradational facies of the middle Bakken. Small scale, load structures are observed only in silty layers which have depressed and enclosed within clay rich bands beneath; these structures are 5-10 mm across and ~5 mm in height. Slump folds are common in these samples, forming structures which are tight to almost isoclinal in shape. The folds have an amplitude of 5-10 mm and a wavelength of 1-5 mm. In some locations clay rich laminations have been folded around large, harder quartz grains.

Facies	Sample	Depth (m)	Laminated	Cross bedded	Load Structures	Soft Sediment Deformation	Ripples	No structure	Burrowing	Bioclasts
Facies E	1-36B	3182.17						■	■	■
	1-37B	3182.48			■		■		■	■
	1-38B	3182.75						■	■	■
	1-39B	3183.09						■	■	■
	1_iiA	3183.48						■	■	■
Facies D2	2_iiA	3185.62	■						■	■
	3_iiA	3185.65						■		■
	4_i	3185.71	■							■
	5_i	3185.74							■	■
	1-55B	3187.99						■		■
Facies D1	1-58B	3188.88	■						■	■
	9_iiA	3190.40	■							
	14_iiA	3194.21						■		
	15_iiA	3194.55						■		
	13_iiA	3194.67	■						■	■
	16_iiA	3194.88	■					■	■	■
	8_iiA	3195.25	■						■	■
	17_iiA	3195.37	■						■	■
Facies – Gradational	7_iiA	3197.11	■			■	■		■	■
	1-87B	3197.72								■
	18_iiA	3198.75	■						■	■
	12_iiA	3199.55	■			■			■	
	19_iiA	3199.73	■			■			■	■
	10_iiA	3200.16	■	■		■			■	
	20_iiA	3200.55	■						■	■
	11_iiA	3201.95	■						■	
	21_iiA	3202.14	■			■			■	■
Facies B	1-112B	3205.34	■						■	■
	1-113B	3205.76								■
	1-114B	3205.95								■
	1-115B	3206.25	■						■	■
	1-116B	3206.56	■						■	■

Table 3.2 - Sedimentary structures observed in middle Bakken samples using transmitted

light scanning. Samples are grouped by facies. Black fill = present.

Bulk Mineralogy

Mineralogy was determined by both XRD and transmitted point counting. Results from XRD show that the middle Bakken is a heterogeneous unit with large variations in mineral abundance down the vertical section. This trend is particularly distinct with respect to carbonate minerals, with samples varying from calcite-rich to dolomite-rich within close proximity (Figure 3.5). The abundance of clay minerals is relatively constant throughout the samples, showing only minor variations in the middle member. The maximum variation for matrix clays, chlorite and illite & mica is 0.4wt% and 2.6wt% respectively, Table 3.3.

	Sample												
	1-36B	1-37B	1-38B	1-39B	2_iiA	4_iiA	9_iiA	17_iiA	11_iiA	1-113B	1-114B	1-115B	1-116B
Quartz	42	33	19	28	46	46	38	45	31	18	29	23	30
Illite & Mica	13	16	4	10	3	4	5	8	6	11	12	10	13
K-Feldspar	4	4	2	4	4	3	6	8	5	4	4	3	4
Plagioclase	5	5	2	3	2	1	3	5	4	3	3	3	3
Calcite	3	3	56	7	31	30	36	14	11	21	37	53	36
Dolomite	29	37	16	47	14	15	12	21	42	41	12	5	9
Pyrite	2	2	1	1	1	1	0	1	1	1	2	3	3
Chlorite	0	0	0	0	0	0	0	0	0	1	1.2	1	1
Matrix	2	1	0	0	0	0	0	0	0	1	0	0	0

Table 3.3 - Mineralogy of middle Bakken Formation samples obtained by XRD (wt %). Dolomite includes dolomite and ferroan dolomite. Matrix minerals are those which individually constitute <1 wt% and includes: hematite, anhydrite, celestine, halite, and kaolinite.

Using a polarising microscope, a total of 8,100 grains were identified by point counting, on 27 samples covering all depositional facies to quantify the relationships between different mineral phases. Point counting showed, on average the most abundance phase is dolomite (on average 36%) and the least abundant phases are biotite and muscovite which were observed in 1% of the grains identified. Quartz varies in abundance from 15 to 65%, dolomite from 0-30%, calcite 2.5 to 45%, with the largest variations seen in clay and matrix minerals (5-65%, Table 3.4).

Sample	Depth (m)	Quartz	Feldspar	Calcite	Dolomite	Matrix - Clays & Organics	Pyrite	Mica	Pores
1-36B	3182.17	34	2	6	49	4	2	2	2
1-37B	3182.48	20	1	14	42	5	7	4	7
1-38B	3182.75	22	7	10	48	6	0	4	3
1-39B	3183.09	30	2	4	41	20	1	0	2
1_iia	3183.48	39	0	5	47	3	0	5	1
2_iia	3185.62	37	3	27	29	2	0	0	2
5_iia	3185.74	49	1	23	15	4	1	1	6
1-55B	3187.99	36	16	4	38	6	0	0	0
14_iia	3194.21	42	4	6	36	7	1	2	1
15_iia	3194.55	34	4	5	44	12	1	0	0
13_iia	3194.67	33	0	8	48	3	9	0	0
16_iia	3194.88	52	0	4	35	6	1	1	3
8_iia	3195.25	39	2	3	48	5	1	2	0
17_iia	3195.37	30	3	6	52	5	2	3	0
7_iia	3197.11	30	2	12	42	5	0	4	2
1-87B	3197.72	42	2	9	33	12	0	1	2
18_iia	3198.75	35	4	14	28	12	3	2	2
12_iia	3199.55	26	3	9	48	5	0	7	2
19_iia	3199.73	38	0	10	42	5	4	0	0
10_iia	3200.16	54	4	5	23	6	0	3	5
11_iia	3201.95	38	3	0	50	4	2	0	2
21_iia	3202.14	44	4	6	30	11	2	2	1
1-112B	3205.34	34	3	4	36	10	2	7	3
1-115B	3206.25	32	3	8	40	6	0	8	3
1-116B	3206.56	46	3	16	25	4	2	4	0

Table 3.4 - Mineralogy data obtained from thin-section point counting using transmitted light microscopy.

XRD vs Optical Microscopy

Comparing XRD data with mineralogy data obtained with transmitted light microscope, point counting we see an apparent shift; with notably higher clay content is measured in the transmitted light data set than the XRD results, Figure 3.5. The rocks of the middle Bakken have close to equal proportions of carbonates and silicates with only a small quantity of clays, Figure 3.5 & Appendix 3.

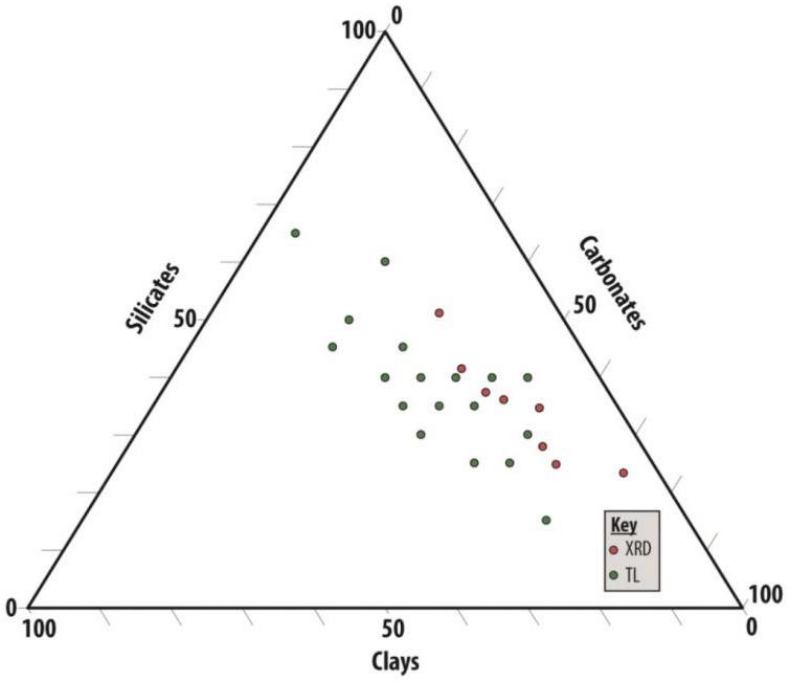

Figure 3.5 - Ternary plot showing the mineralogy of the middle Bakken samples. Data were obtained by XRD and transmitted light microscope. Carbonates - calcite, dolomite, ankerite; Clays - clays (illite, smectite, kaolinite), mica, oxide minerals & organic matter; Silicates - quartz and feldspar. Note: illite and mica were grouped together during XRD analysis so are assigned as clays here.

Detrital Mineralogy

Calcite

Detrital calcite was observed by optical microscope in the middle Bakken Formation as fossils and bioclastic fragments. Fossils varied in size between 0.2-1 mm. Bioclasts were observed in thin-section throughout the middle Bakken and include brachiopods, bivalves, crinoids, bryozoans, algal mats, ooids, and shell fragments. Whilst no clear, presence or absence of any individual class was noted in any of the facies groups, Facies D1 is less bioclastic than other facies in the middle Bakken, Appendix 1.

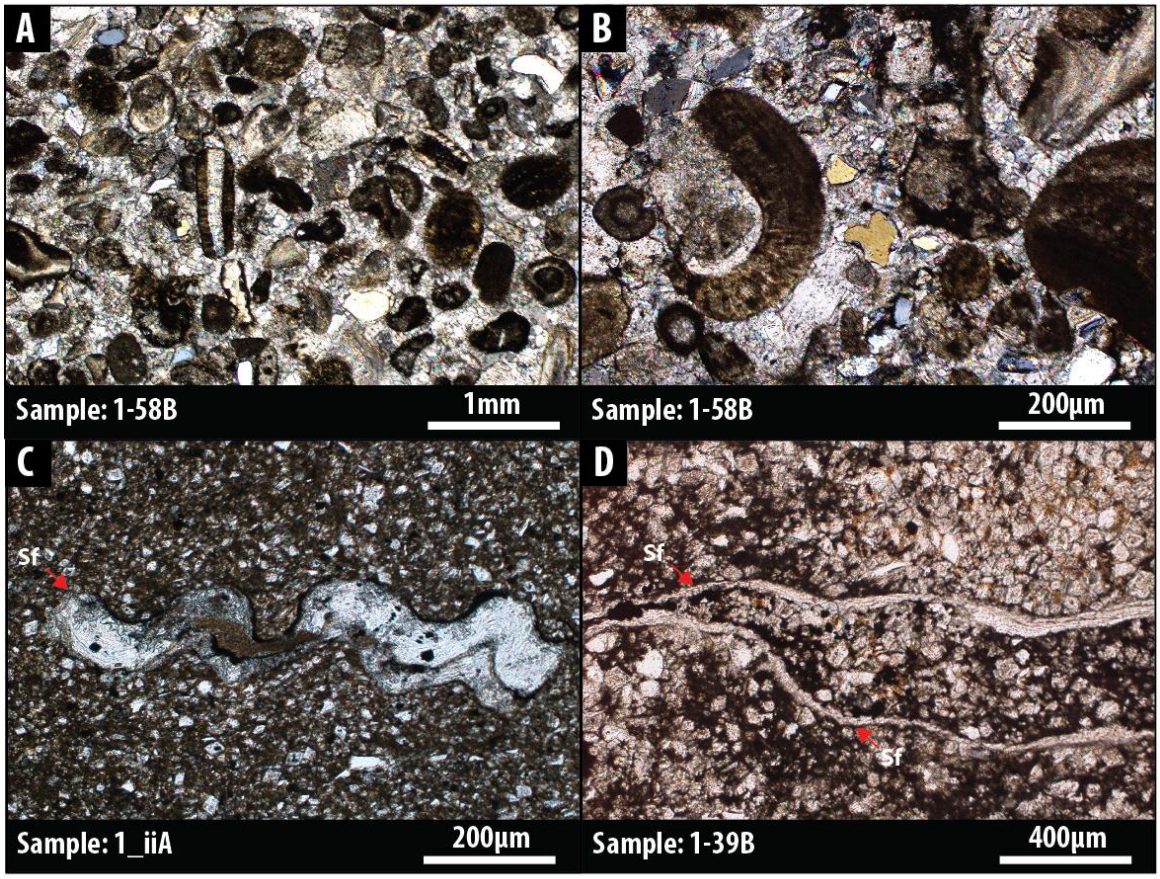

Figure 3.6 - Thin-section micrograph of bioclasts composed of calcite. A) Bioclasts in sample 1-58B, showing a range of taxa including brachiopods, crinoids and algal mats, viewed in XPL. B) Higher magnification micrograph of sample sample 1-58B showing bioclasts composed of calcite and and the occasional quartz grains, viewed in XPL. C) Shell fragment (Sf) cross-section in sample 1_iia, viewed in XPL. D) Articulated, complete and uncompacted shell fragments (Sf), infilled with quartz silt in cross-section, viewed in PPL in sample 1-39B.

Quartz

Quartz grains vary from well-rounded to angular in shape and range in size from ~2-50 µm across. Quartz is abundant (>30%) across all facies and shows only minor variations in abundance between facies, Figure 3.7. A significant proportion of quartz grains contain small, intragranular pores. These are 1-5 µm in diameter. Visual estimates suggest they are present in ~60% of quartz crystals of which they make up ~5% of the crystal volume.

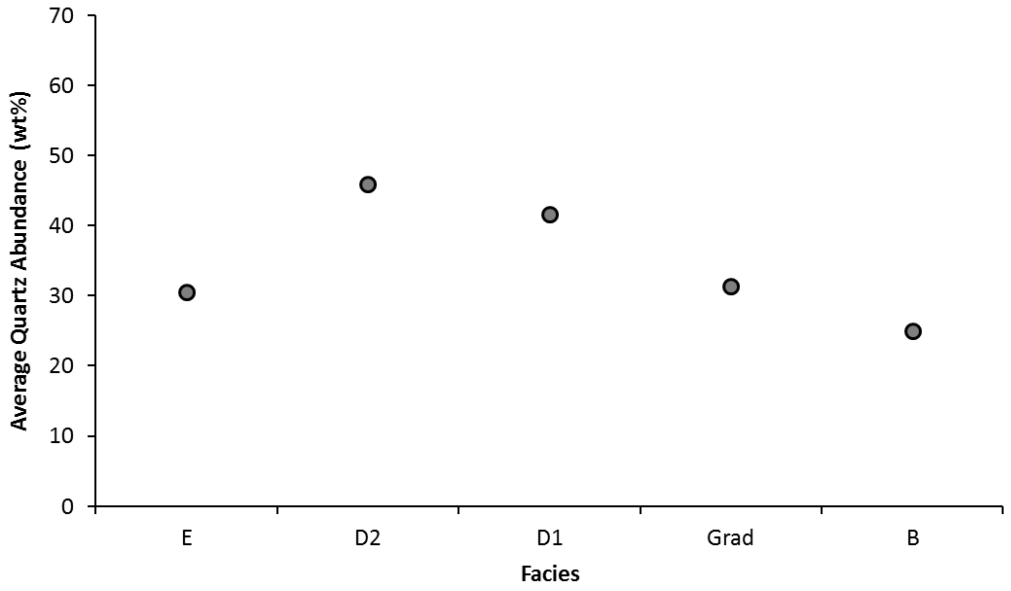

Figure 3.7 - Variation in quartz abundance from XRD in different middle Bakken member facies.

Qualitative observations were made using SEM-CL to investigate the provenance of detrital quartz in the middle Bakken. By combining SEM-CL images with SEM-EDX data, we found quartz grains which showed different CL emission characteristics, Figure 3.8.

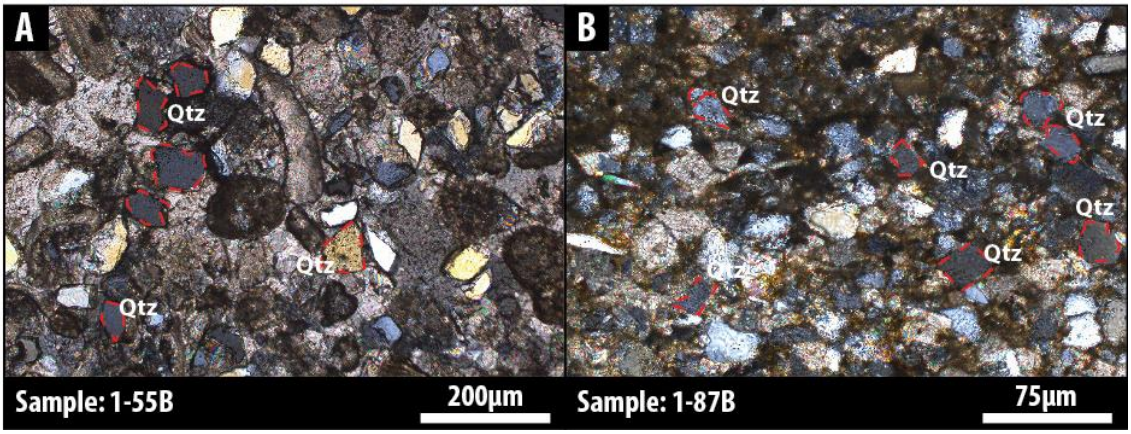

Figure 3.7 - Transmitted light images viewed in XPL, showing the range of quartz morphologies in A) calcite cemented sample [1-55B] B) clay-rich sample with an organic rich matrix [1-87B].

Previous workers have sought to use these as an indicator of the provenance of detrital grains (Zinkernagel, 1978; Matter and Ramseyer, 1985; Owen, 1991; Gotze et al., 2001). In the example of sample 11_iiA, (Figure 3.8), there was strong luminescence of grains 3 & 4

in the blue spectrum however the majority of quartz grains imaged in this study showed luminescence emissions in the red spectrum.

The variations in SEM-CL emission colour in Figure 3.8 are representative of those observed in 10 samples analysed in this study. However, the uncertainty introduced due to changes in CL colour identified with increased beam exposure (Richter et al., 2003) (see Discussion) has led to some workers using distinct caution in the application of SEM-CL in provenance interpretation (Boggs & Krinsley, 2006).

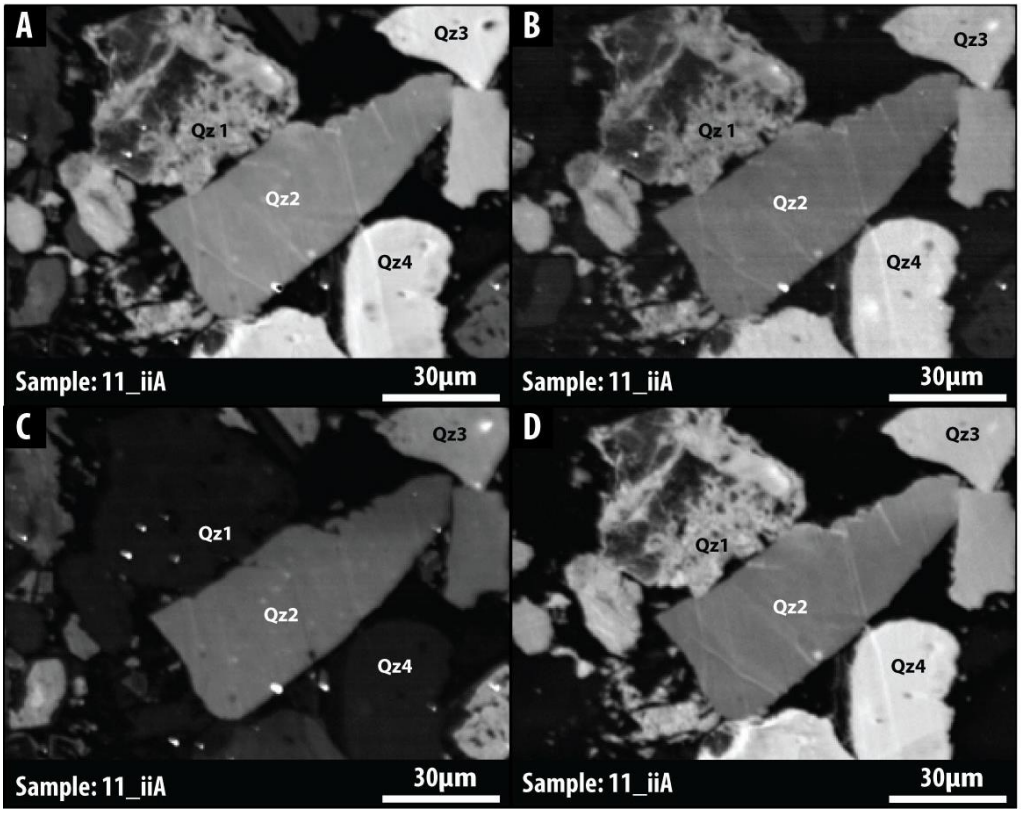

Figure 3.8 - Detrital quartz grains showing different CL character to each to other in sample 11_iia, 800x A) Panchromatic B) Red C) Green D) Blue.

Illite & Mica

Illite was identified from both SEM-EDX spectra and imaging of chip samples (Figure 3.9). Detrital illite is difficult to differentiate from diagenetic illite (Worden & Morad, 2009). Based on the morphology of the illite we suggest both detrital and authigenic forms exist.

Muscovite is a matrix mineral, constituting around 1% of the samples as characteristic fine tabular crystals aligned with bedding. The crystals have rounded and abraded edges forming subhedral forms. A similar challenge exists to illite in differentiating authigenic

and detrital forms. Based on the subhedral, rounded edges and very fine grained nature, we tentatively interpret these as detrital crystals.

XRD results group mica and illite together making it difficult to estimate the relative abundance. Combing observations from electron microscopy and transmitted light analysis we estimate muscovite mica makes up ~1-2% of the middle Bakken samples, from this we estimate that illite constitutes 1-15% of the middle Bakken.

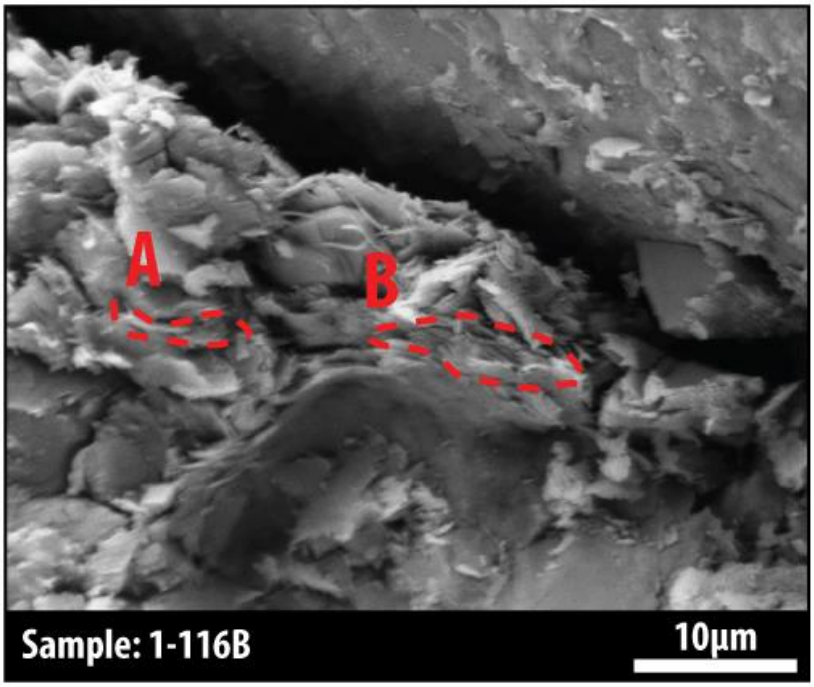

Figure 3.9 – Secondary electron micrographs of illite on a broken section, showing individual bedding aligned illite plates in sample 1-116B.

Combining the low estimate of illite abundance and the challenges associated with differentiating detrital and authigenic illite we make no attempt to quantify the relative abundance of detrital and authigenic illite.

Organic Matter

Organic matter is not commonly observed in the middle Bakken. It is unevenly distributed, occurring as fine elongate packages, some of which are thought to be faecal pellets, Figure 3.10a and 3.10b and others are sections of burrows where organisms have concentrated organic matter along the walls, Figure 3.4b. In some of the faecal pellets, pores are visible, Figure 3.4b. Pores vary in size from 0.2-5 µm in size. In clayey laminae

(notably in facies A and B) organic matter is largely constrained by burrows.

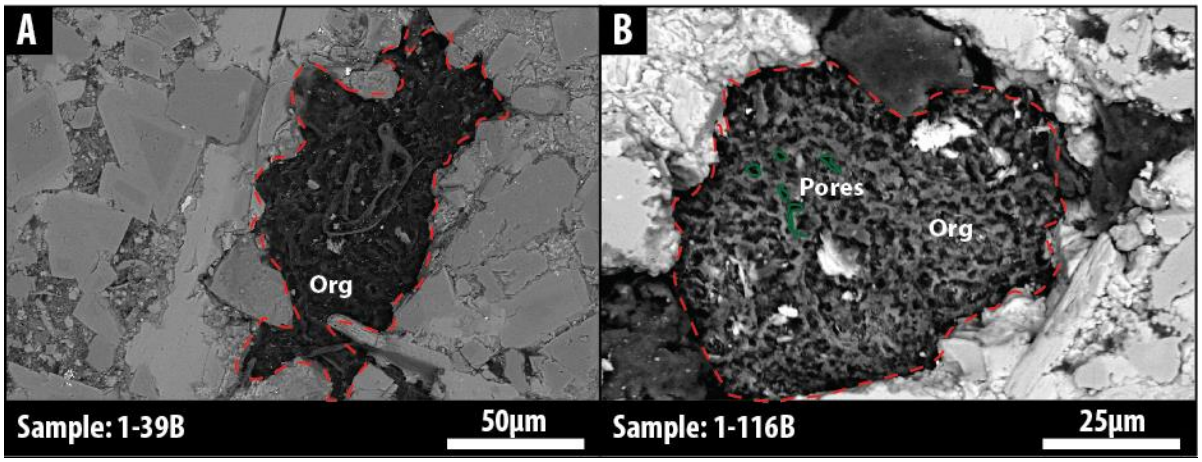

Figure 3.10 - Backscatter electron images of organic matter in the middle Bakken. a) Irregular elongate zone of organic matter in sample 1-39B, imaged at 15 kV, x500 b) Irregular, rounded zone of organic matter in sample 1-116B with examples of intragranular pores labelled (green), imaged at 15 kV, x900.

Diagenetic Composition

Principle Controls on Reservoir Quality

Diagenetic processes are many and complex but two of the main groups of processes are cementation and compaction (Lundegard, 1992). In order to determine whether cementation or compaction was the chief control on porosity, we used data obtained by thin-section point-counting, to estimate the relative proportion of porosity loss by compaction and cementation. This was done with the method proposed by Lundegard (1992) (see Chapter 4 for a full explanation). We assumed an initial porosity of 45%, by comparing the mineralogy and texture of the middle Bakken samples (above) with the mineralogy and texture of those analysed by Chuhan (2003).

Figure 3.11 shows that a high proportion (average of 39%) of the assumed initial porosity is lost by cementation and only a small proportion (average of 3%) is lost by compaction. The principle cause of porosity loss is thus due to cementation (Figure 3.11), see Chapter 4.

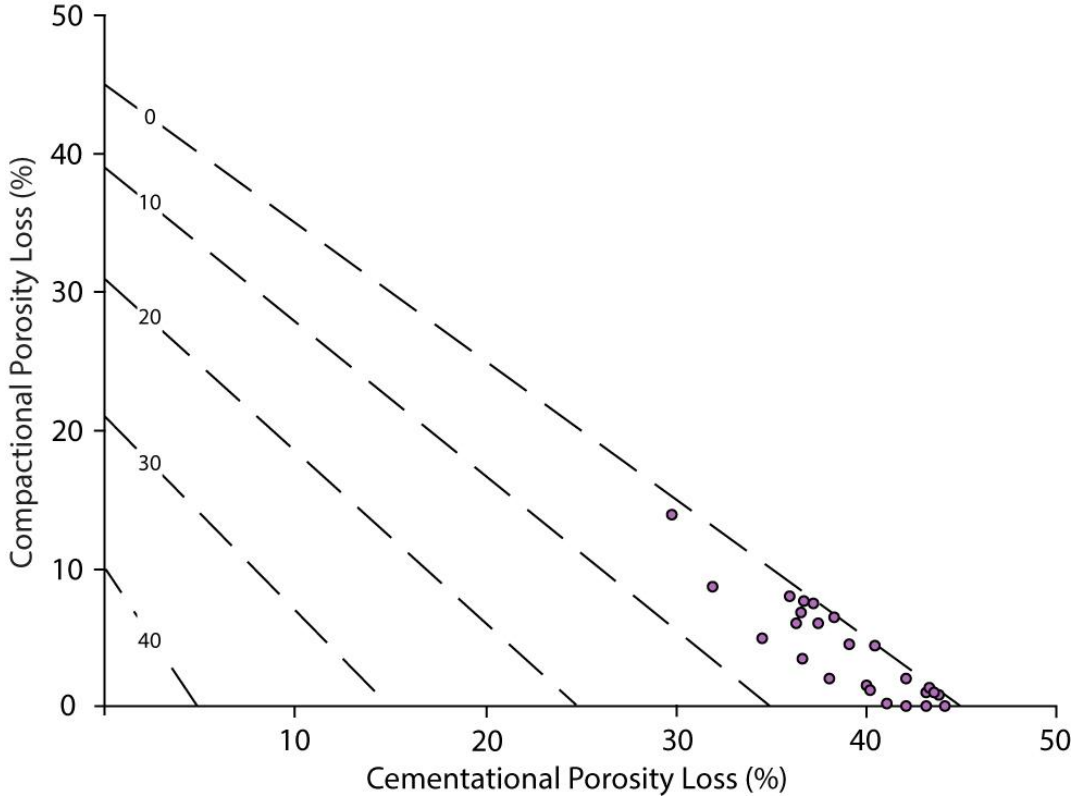

Figure 3.11 - Plot of cementational porosity loss (CEPL) versus compactional porosity loss (COPL), after Lundegard (1992). This method assumes an initial porosity of 45% (Chuhan, 2003). Lines of equal point count porosity are shown [NW-SE diagonals].

Compaction

Under-transmitted light, the contacts between framework grains are highly variable, showing a range of inter-granular interactions including no contact between detrital grains to concavo-convex contacts. By using the grain contact classification of Taylor (1950), the samples examined show evidence of ductile deformation in the form of long grain contacts and concavo-convex contacts, (Figure 3.12). No sutured or stylolite grain contacts were observed.

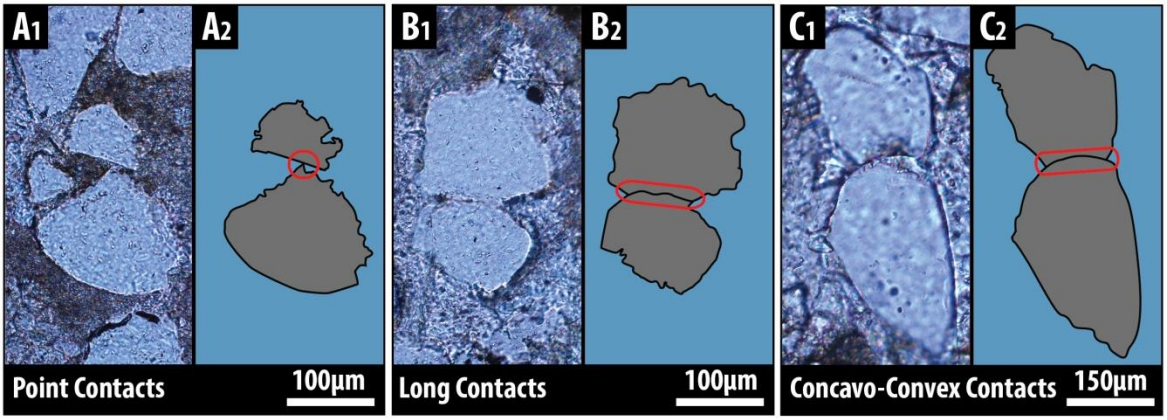

Figure 3.12 - Photomicrographs from transmitted light microscopy (1's) and sketch schematic (2's) of individual grain contacts. Red ellipses highlight the contact. a) Point contact in quartz, PPL from sample 5_iia. b) Long contact in quartz, PPL from sample 5_iia. c) Concavo-convex contact in quartz, PPL from sample 1-58B.

Grain contact, compaction features were most obvious in coarser grained samples, however imaging using high magnification electron microscopy, we also found they are present in finer grained quartz crystals. Fossil and shell fragments observed by optical microscope were also intact and show little evidence of deformation due to the effects of compaction (Figure 3.4 & 3.6).

Cementation: Calcite

Calcite is one of the most dominant minerals in the middle Bakken formation. Across all facies of the middle Bakken, measurement by point counting suggests calcite makes up ~20-40% of the samples. Bulk abundance measured using XRD found calcite (detrital and diagenetic) constitutes a maximum of 56% in sample 1-38B and a minimum abundance of 3% in samples 1-36B & 1-37B. Detrital calcite is dealt with separately and is referred to as 'type 1'.

Authigenic calcite occurs in two forms, pervasive cement and individual crystals. The principle morphology of diagenetic calcite is pervasive, poikilotopic cement (Figure 3.14a). Detrital grains are commonly observed 'floating' within the calcite cement, Figure 3.16e & Figure 3.16f. The pervasive nature of authigenic calcite cement is particularly evident in mineral phase maps obtained from SEM-EDX (Figure 3.14f). This phase is 'type 2' calcite.

Type 3 calcite grains are discrete individual precipitates which appear to locally cement small numbers of grains and grain edges; these grains vary from 5-30 µm in size, Figure 3.14c. This phase forms a sub-angular to rounded morphology and also as individual discreet grains of similar size and shape which do not connect other grains; though visual estimates from SEM imaging find both of these phase to be very rare. These 2 sub-phases are grouped and termed 'type 3 calcite'. We suggest it may be possible that these are undeveloped forms of 'type 2' calcite. For clarity we keep these separate.

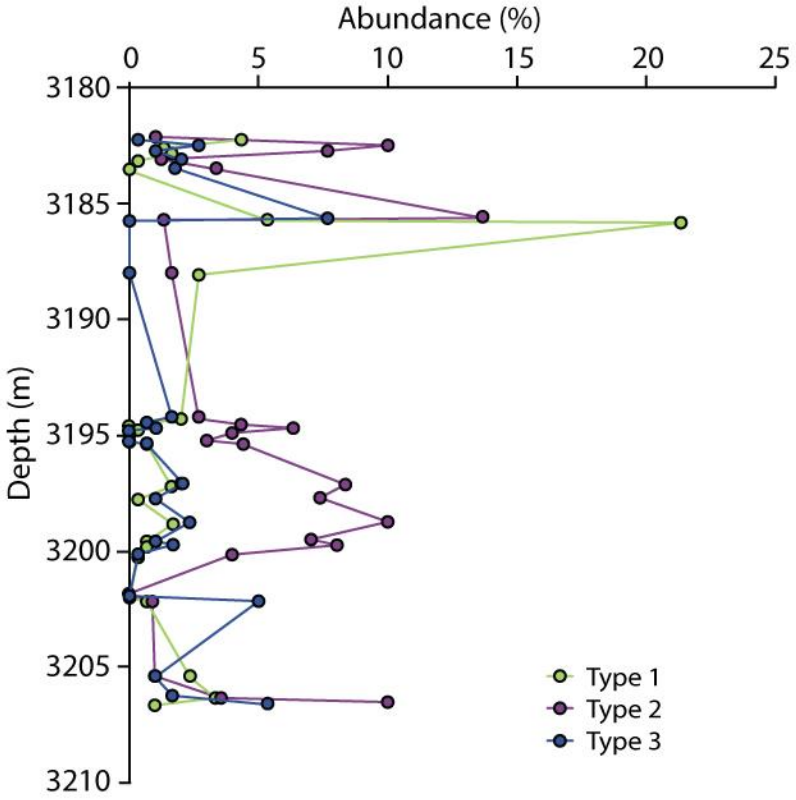

Figure 3.13 – Plot of abundance of individual calcite phase/types with depth, obtained from thin-section point counting. Type 1 - is detrital, bioclastic calcite, shown for comparison. Type 2 and type 3 calcite is authigenic.

We found type 2 calcite to be significantly more abundant in all samples of the middle Bakken. Type 2 calcite is most abundant in sample 2_iia (52.5% total calcite) and least abundant in sample 1-87B, where it is absent, Figure 3.13. There appears to be no depth or facies control on the presence of type 2 calcite. Type 3 is very rare.

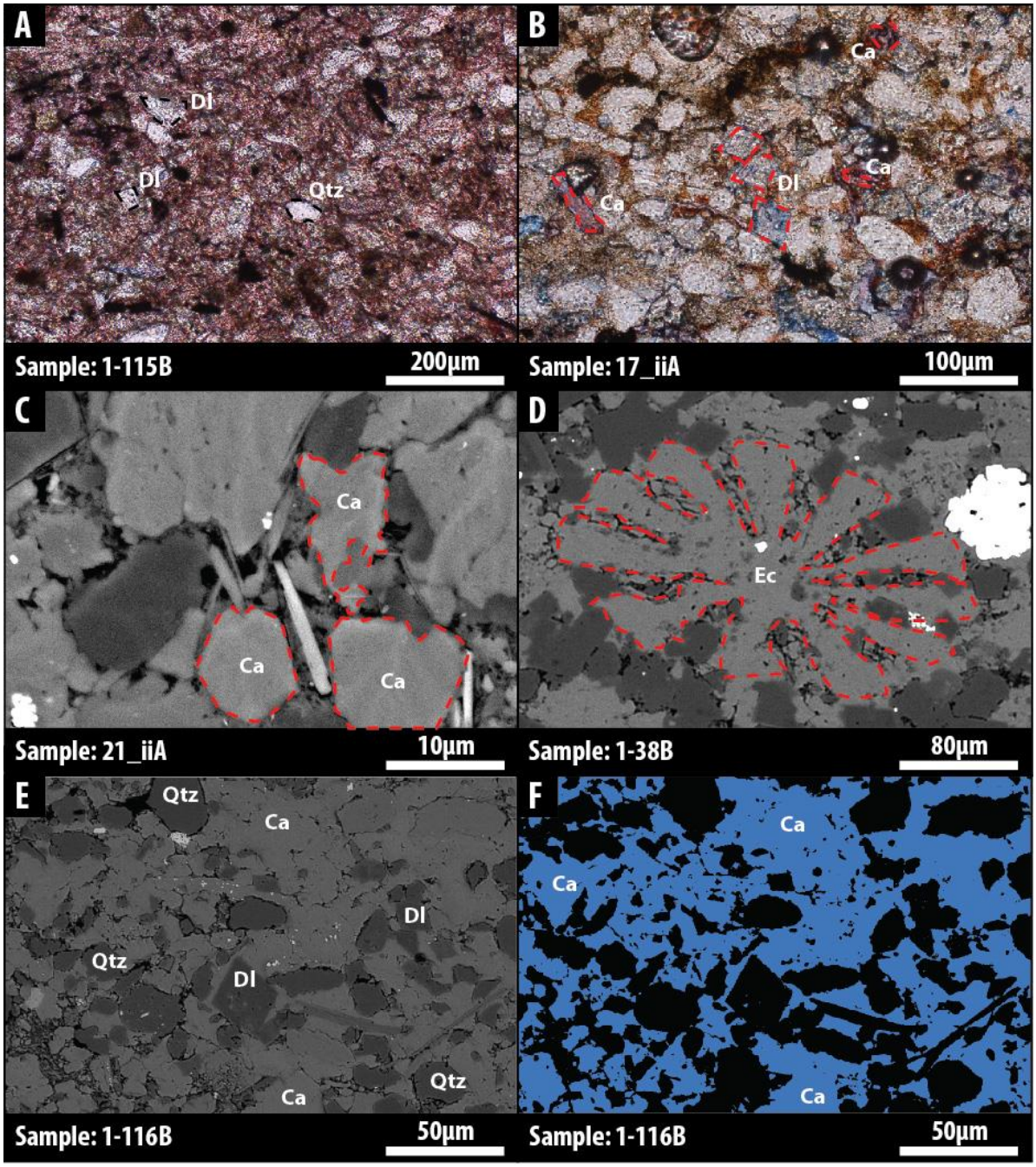

Figure 3.14 - Images of calcite cement from transmitted light microscopy (TL) and scanning electron microscopy (SEM).

A) TL photo-micrograph of sample 1-115B stained with Alizarin red dye, to highlight calcite and differentiate it from dolomite (calcite stains red, dolomite does not). The distinctly pink colour of this image indicates the abundance of calcite which is pervasive throughout the sample, cementing dolomite (Dl) and quartz (Qtz).

B) TL photo micrograph of sample 17_iiA stained with Alizarin red dye and blue dye (to highlight porosity). In contrast to image A, the only calcite (red stained areas) is found in bioclasts (Ca), where the cement is composed of clay minerals and organic matter. Pores

are found associated with rhombohedral, dolomite crystals (Dl).

C) Mixed BSE-SE image taken at 15 kV, showing rounded calcite crystals which are cementing earlier minerals.

D) BSE image of an echinoderm (Ec) in cross-section, the approximate outline is shown in red, it has been replaced by calcite cement which extends beyond the ambulacum (arms).

E) BSE micrograph of sample 1-116B imaged at 15 kV, 15 mm WD, showing the pervasive calcite cement (Ca), around grains of quartz (Qtz) and dolomite (Dl)

F) Calcite segmented and isolated from a mineral phase map to show the extensive and pervasive nature of cementation on the same area as image E.

Cementation: Dolomite

Diagenetic dolomite is present across all facies, as subhedral to euhedral rhombs, with a large grain size variation, from very fine, silt-sized matrix crystals up to larger, fine sand-sized framework crystals, over a range of 2-100 µm. Using the classification of Sibley & Gregg (1987) different phases of dolomite were described as: non-planar, planar-e, planar-e, planar-s, and planar-e (fine). Using this scheme, we found dolomite occurs in 6 different textural forms, Figure 3.15.

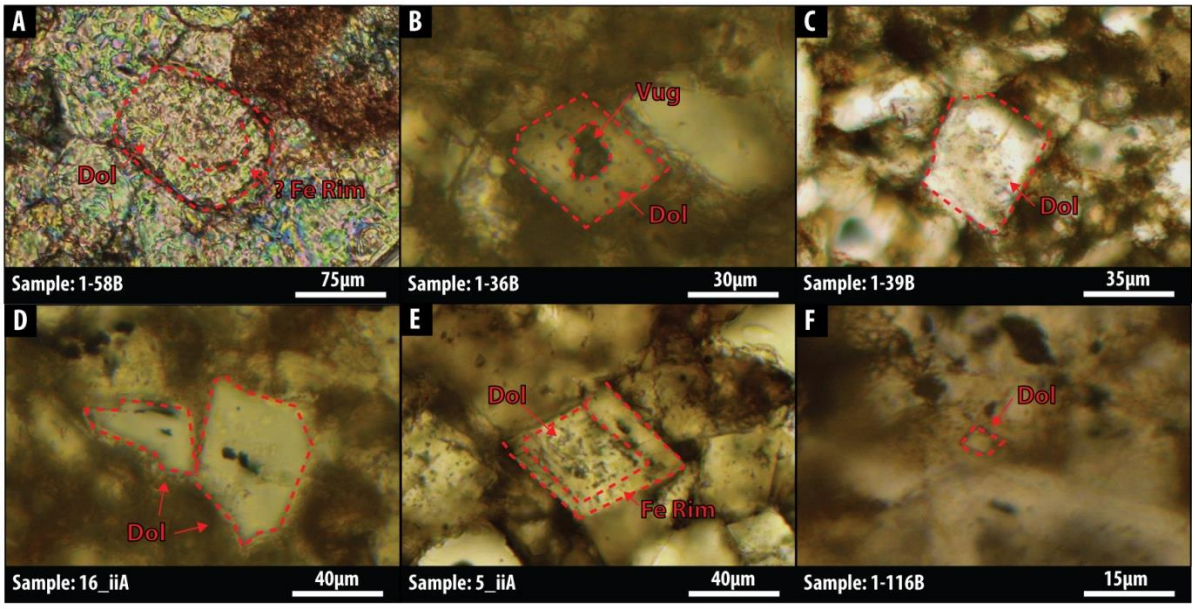

Figure 3.15 - Transmitted light microscopy photo-micrographs of individual morphologies of different dolomite phases. a) Type 1, in sample 1-58B [XPL] b) Type 2, in sample 1-36B [PPL] c) Type 3, in sample 1-39B [PPL] d) Type 4 in sample16_iia [PPL] e) Type 5, in sample 5_iia [PPL] f) Type 6, in sample 1-116B [PPL].

Type 1: Non-Planar

Type 1, non-planar dolomites occur as anhedral forms, which are 15-30 µm across. Some show iron-rich rims, which vary from anhedral (Figure 3.16a) to euhedral in shape. Almost all examples have intraparticle vuggy porosity. Type 1 dolomites are found in all of the samples of this study.

Type 2: Planar-E (coarse, vuggy)

Type 2 dolomites are large, euhedral, rhombohedral crystals, which vary in size from 10-50 µm across. The dolomite crystals are planar-e which have been variably and partially dissolved creating vuggy porosity. Some of these dolomites show simple concentric zoning (1-2 zones).

Type 3: Planar-E (coarse)

Type 3 dolomite crystals are texturally very similar to type 2 dolomites, however type 3 dolomites do not have vuggy intragranular pores, like type 2 crystals. They vary in size from around 10-50 µm across.

Type 4: Planar-S

Planar-S, dolomites are subhedral crystals showing distinct geometric grain boundaries. They show a grain size distribution from 15-50 µm across. The crystal boundaries do not form the characteristic rhomb shape; instead they form irregularly shaped, angular crystals.

Type 5: Ankerite rims

Ankerite rims are observed primarily as a distinct alteration zone of the primary mineral (Figure 3.16e). Composite mineral phase maps show that ankerite occurs around both the vuggy planar-e (type 2) dolomite rhombs, as well as the type 3 dolomites. In very rare instances, Fe-dolomite is also found as complete individual crystals. This morphology is challenging to identify by transmitted light and difficult to segment from SEM-EDX maps.

Type 6: Planar-E (fine)

This type of dolomite is common throughout the matrix of many of the samples. The

crystals are 1-5 µm across. They are euhedral crystals, showing rhombohedral forms with very sharp, pronounced straight edges. Some crystals show minor alteration to Fe-dolomite along the crystal edge (<1 µm). They are loosely packed and show no interaction with other dolomite phases.

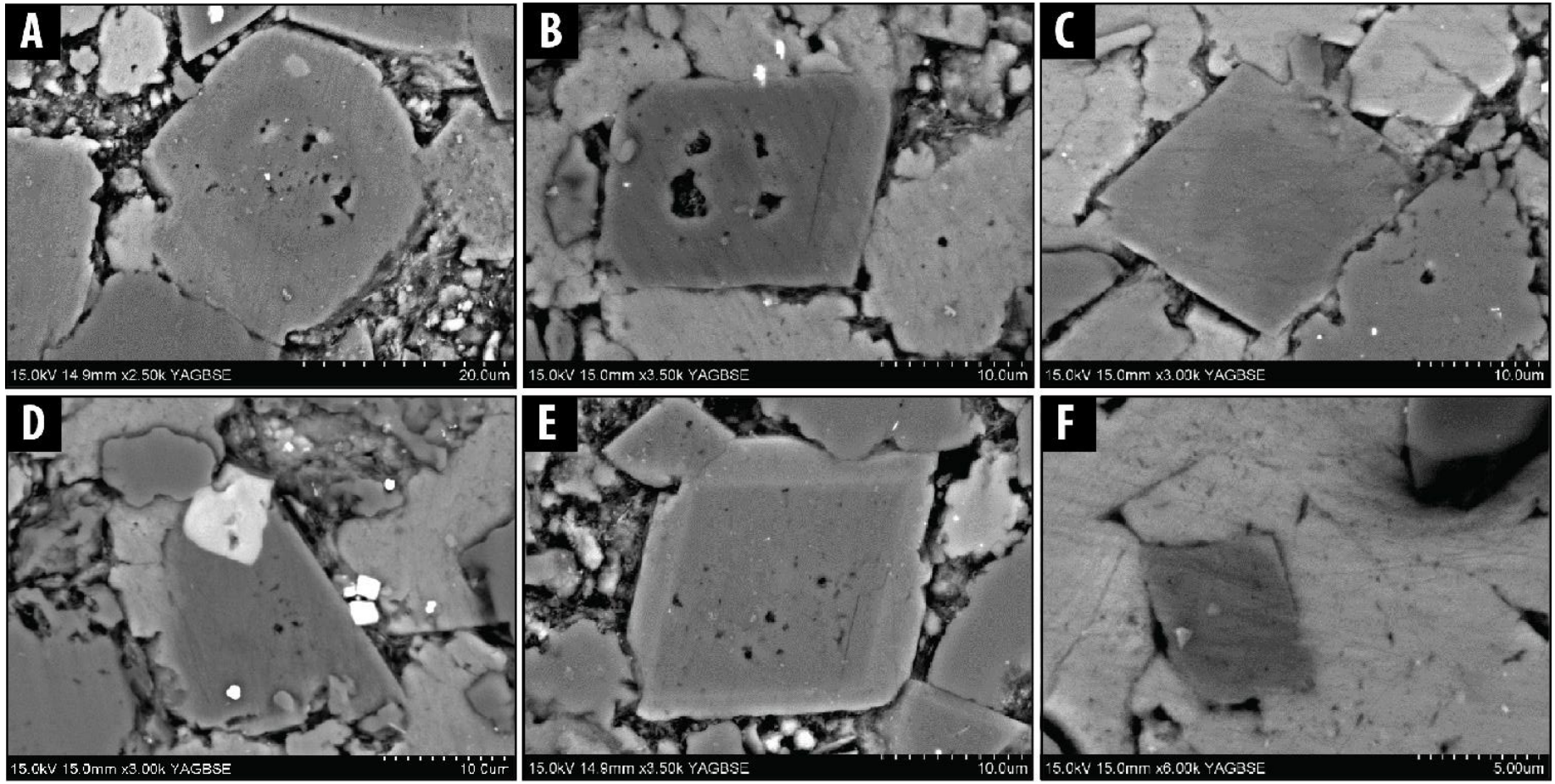

Figure 3.16 - Overview of different textural types of dolomite identified in the middle Bakken (backscattered electron micrographs). a) Type 1 - non-planar dolomite: Anhedral crystals that are 15-30µm long, occurring rarely. b) Type 2 - planar-e: euhedral rhombohedra, with intra-crystalline, vuggy porosity, occurring as crystals, 10-50µm long, abundant. c) Type 3 - planar-e: euhedral rhombohedra, 10-50µm, occurring occasionally. d) Type 4 - planar-s: sub hedral, angular crystals, 5-35µm long, occurring commonly. e) Type 5 - ankerite rim around a coarse, vuggy dolomite. f) Type 6 - planar-e: euhedral to subhedral rhombohedra, 1-5µm thick rim, occurring commonly.

Dolomite Abundance

The abundance of individual morphologies of dolomite was measured during point counting, Figure 3.17. There is no correlation between the abundance of individual phases with depth, Figure 3.17.

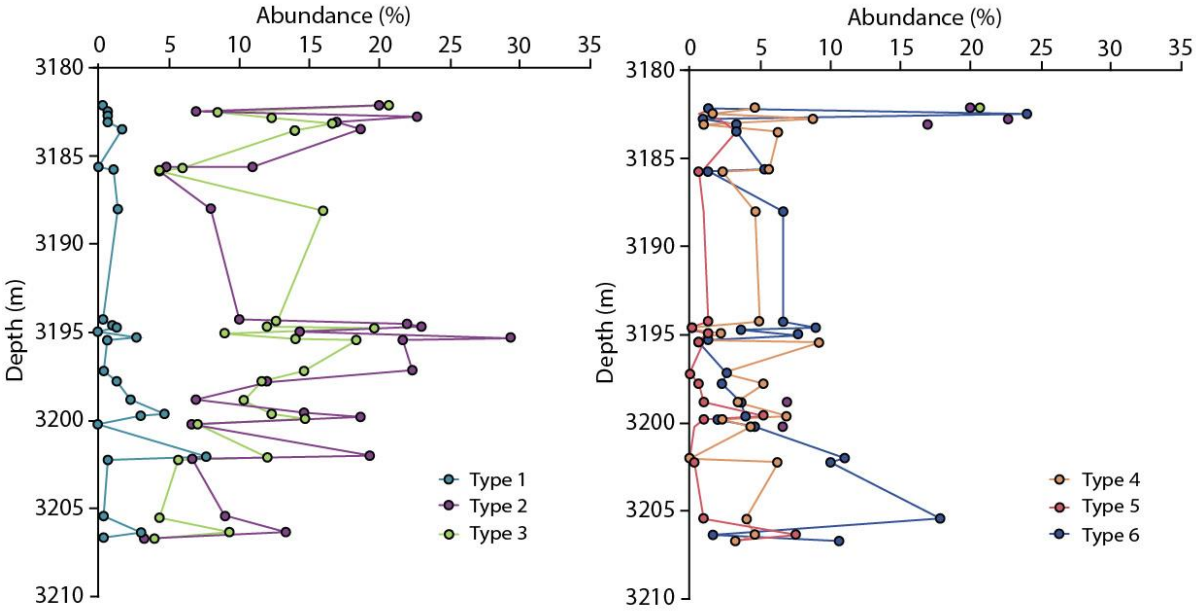

Figure 3.17 - Abundance of different dolomite phases obtained by point counting of thin-sections. Data is split into two plots for clarity.

Phases 5 and 6 were too fine to reliably differentiate by transmitted light microscope. In order to attempt to resolve this problem, phase abundances were determined using segmented SEM-EDX maps, Figure 3.18. It was still challenging to segment type 5 dolomite. In some crystals this is due to the variable distribution of iron but in others it is due to the thin nature of this phase; as a result, they were omitted from segmentation.

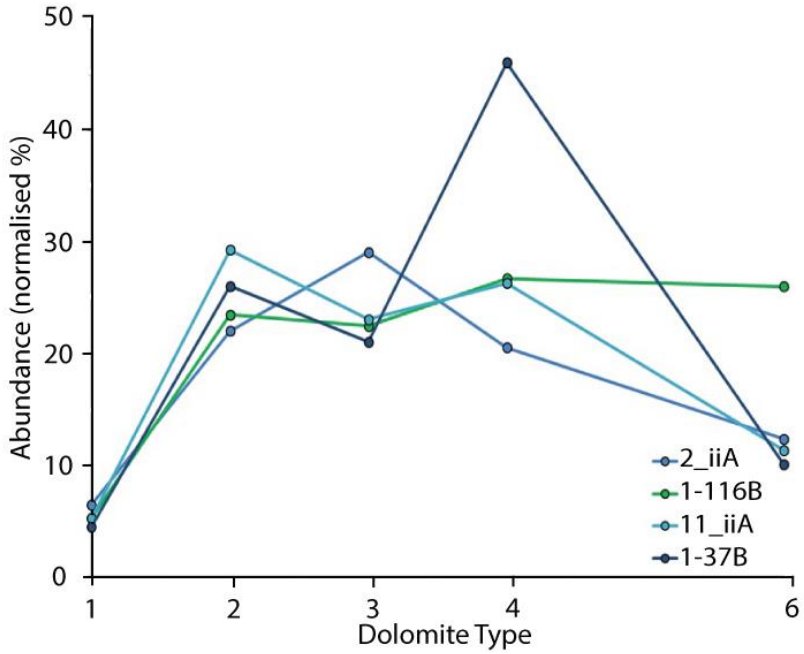

Figure 3.18 – Plot of variations in the relative abundance of different textural forms of dolomite, obtained from SEM-EDX maps. Data is normalised to omit 'type 5 dolomite'.

The least abundant phase is type 1 dolomites (mean 7%). The most abundant phases segmented from SEM-EDX maps are phases 2, 3 and 4 with an average normalised abundance of 25%, 24% and 30%; respectively. Type 6 dolomites make up on average 15% of the total dolomite. In sample 1-37B there is a dominance of type 4 dolomite crystals in sample 1-37B, Figure 3.18. Type 5 dolomite abundance was visually estimated from SEM imaging and it is thought Fe-dolomite constitutes ~5% of the total dolomite.

Quartz

Authigenic quartz was imaged using SEM-CL. Quartz overgrowths form uneven bands around some detrital grains. The bands are not always continuous or complete. They form as anhedral, rough edges which vary in thickness from 0.5-5 µm, Figure 3.19. Quartz overgrowths are found on ~10% of detrital quartz grains.

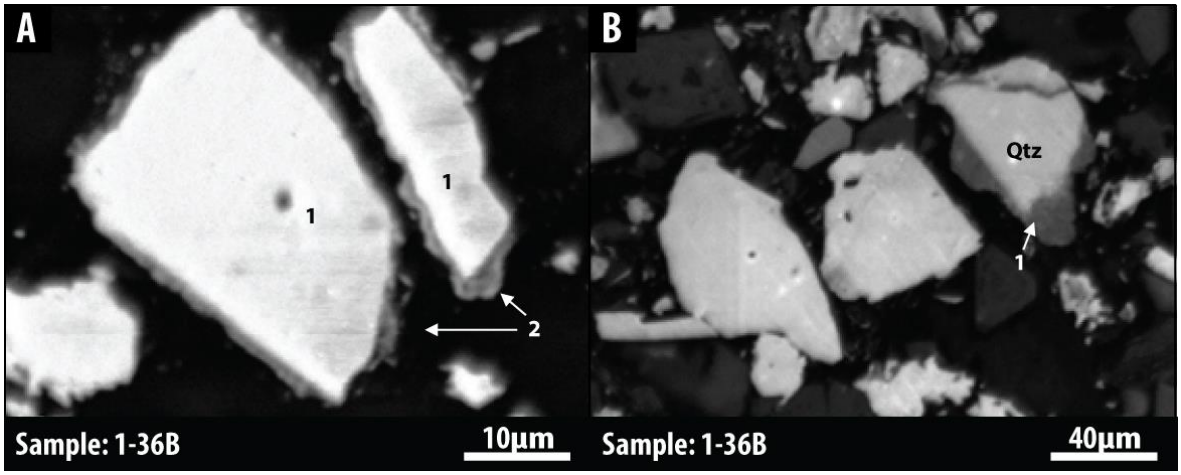

Figure 3.19 - Diagenetic features observed in SEM-CL images of quartz grains a) CL image of a quartz grains (1) showing secondary overgrowth (2) filtered using a 380 nm-500 nm (blue) filter in sample 1-36B, b) CL image of a quartz grain (Qz) showing a healed fracture (not visible in BSE) and a secondary overgrowth (1) filtered using a 380 nm-500 nm (blue) filter in sample 11_iia.

Pyrite

Pyrite is observed closely associated with clay rich bands close to the contacts with the upper and lower Bakken. It is common in several morphologies, the most abundant of which is as finely disseminated euhedral crystals, which varying in size from 0.5-4 µm, Figure 3.20. Fine, disseminated pyrite is interspersed by platy kaolinite and chlorite clay minerals, Figure 3.20. They are commonly found as aggregates forming framboids. They are most commonly found in facies B and the gradational zone.

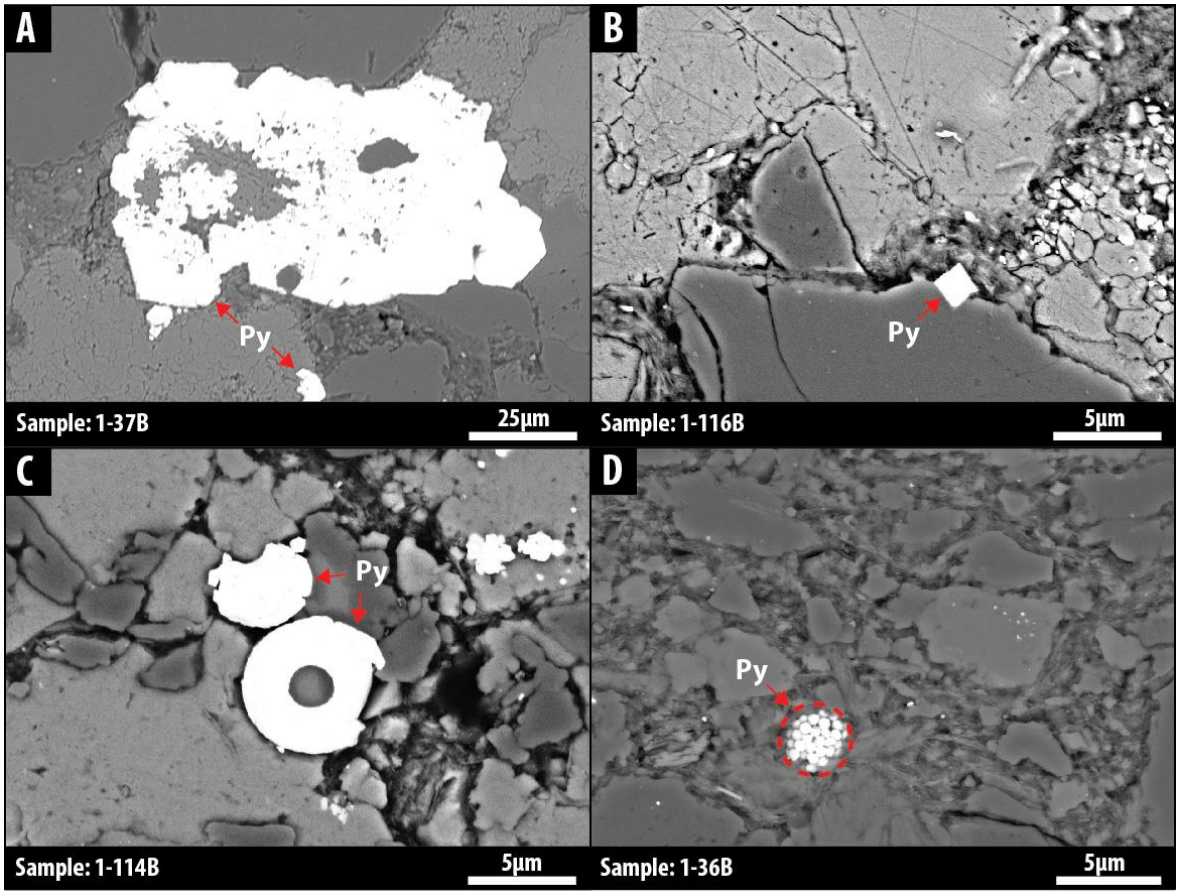

Figure 3.20 - Backscatter electron images of different morphologies of pyrite observed in the middle Bakken. a) Replacive pyrite cement (Py), replacing dolomite in sample 1-37B. b) Fine, individual pyrite crystal (Py), precipitated on the edge of a quartz crystal, observed in sample 1-116B. c) Pyrite (Py), replacing an echinoderm stem section in sample 1-114B d) Pyrite framboid (Py) in sample 1-36B.

Replacement of other crystals by pyrite is common. In some samples pyrite formed rhombs which we suggest were previously dolomites, Figure 3.20b. In other samples, fossil taxa have been pyritised which include; echinoderms, crinoids and shell fragments. These clasts vary significantly in size from 5 – 200 µm, which is a function of the size of the original bioclast. Anhedral blebs of pyrite are also seen in the middle Bakken. These show limited constraint on size or orientation, though in strongly laminated regions, elongate blebs are orientated sub-parallel to parallel to bedding. They are found both in the matrix and infilling secondary pores in crystals of dolomite, potassium feldspar and calcite.

Pyrite was readily identifiable under electron microscope on thin-sections, occurring in a range of morphologies, as individual anhedral blebs, euhedral pyrite framboids and replacing calcite in bioclasts. The pyrite is irregularly distributed across the sample and is most apparent as large unevenly formed masses, making up between~1-5% of the samples.

Feldspar

Feldspar is predominantly found in potassium-rich forms. There are two different phases of potassium feldspar. One phase varies in size from 20-80 µm; they have a subhedral to anhedral habit, with sub-rounded, abraded faces. This phase has been partially dissolved and show minor secondary porosity, Figure 3.21a. These crystals are commonly partially replaced by sodium-rich feldspar, Figure 3.21a.

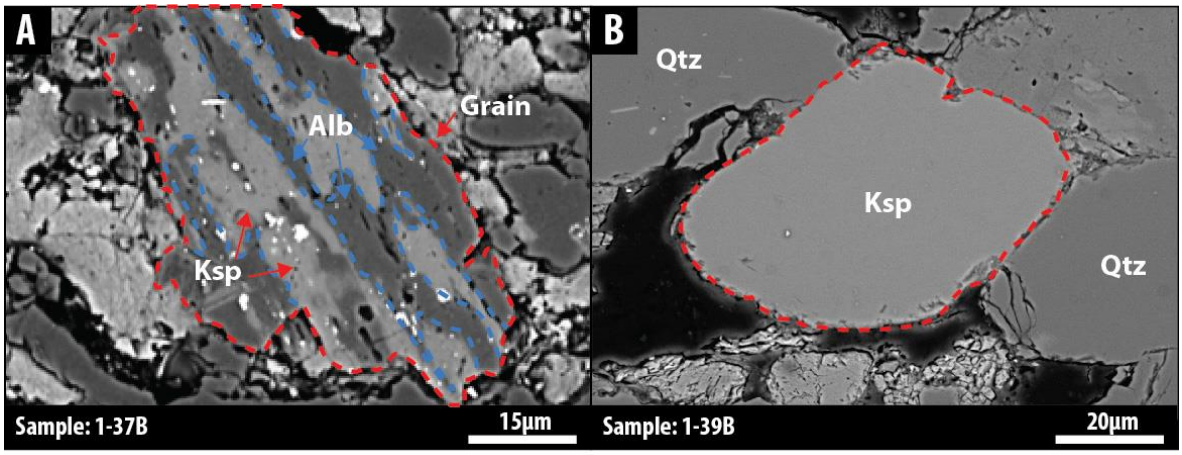

Figure 3.21 - SEM backscattered electron micro-graphs of potassium feldspar. A) Altered potassium feldspar crystal, showing replacement by albite. B) Unaltered potassium feldspar crystal showing only minor dissolution and abrasion near the crystal edges in sample 1-37B.

Potassium feldspar also occurs as a second, unaltered form. These crystals vary in size from 5-20 µm across, and are anhedral to subhedral in shape. They show no evidence of dissolution (Figure 3.21b). Potassium feldspar constitutes ~4%. Both morphological forms of feldspar occur throughout the middle Bakken.

Titania

Titanium oxide minerals are found in trace quantities in the middle Bakken. Most of the crystals observed are pure titanium and oxygen though some crystals were found to contain small quantities of iron. The exact mineral could not be determined by SEM examination so has been referred to as titania, as described in Pe-Piper et al., (2011). Titanium oxide occurs as both a mineral infill of quartz dissolution pores and as streaks on the surface of quartz grains (Figure 3.22).

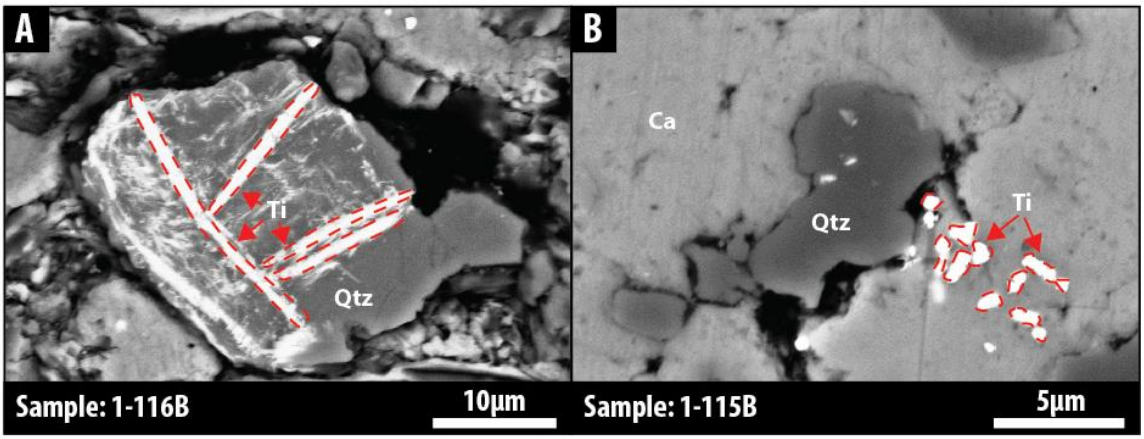

Figure 3.22 - Backscattered electron micrographs showing the different morphologies of rutile. A) Elongate titanium oxide structures (Ti) on a quartz (Qtz) substrate in sample 1-116B imaged at 15 kV, x5,000. B) Titania infilling pores in a quartz grain in sample 1-115B, taken at 20 kV, x3000.

Halite

Halite was only found in samples 1-36B and 1-37B of the middle Bakken, of facies E. It is precipitated predominantly along fractures as euhedral, cubic crystals. The crystals vary from 0.5µm to 3µm across, Figure 3.23.

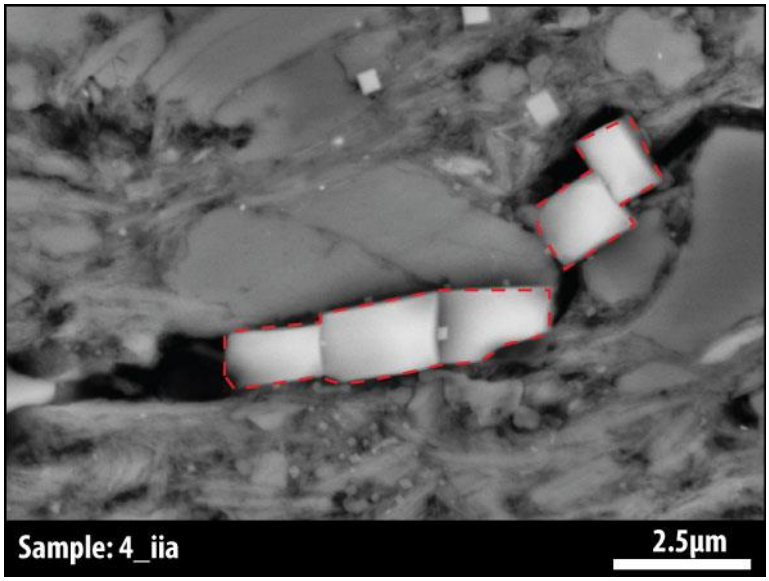

Figure 3.23 - SEM backscattered electron micrograph of cubic halite crystals, identified in middle Bakken sample. Halite crystals are circled in red.

Clays

The clay minerals illite and chlorite are found in the middle Bakken. Chlorite was not observed but was identified by XRD analysis. Diagenetic illite is found as both clay plates and hairy strands, Figure 3.24. Hairy illite is the most common morphology in the middle Bakken. The strands vary in length from 0.3-2 µm. The clay mineral plates vary from 0.5 - 1.5 µm in thickness and from 2-10 µm in length. The abundance of illite is estimated to be ~5% of the samples [reported in XRD analysis as a mixed phase of 'illite & mica']. XRD analysis suggests, illite is most abundant in facies B of the middle Bakken (though XRD does not differentiate detrital and diagenetic forms).

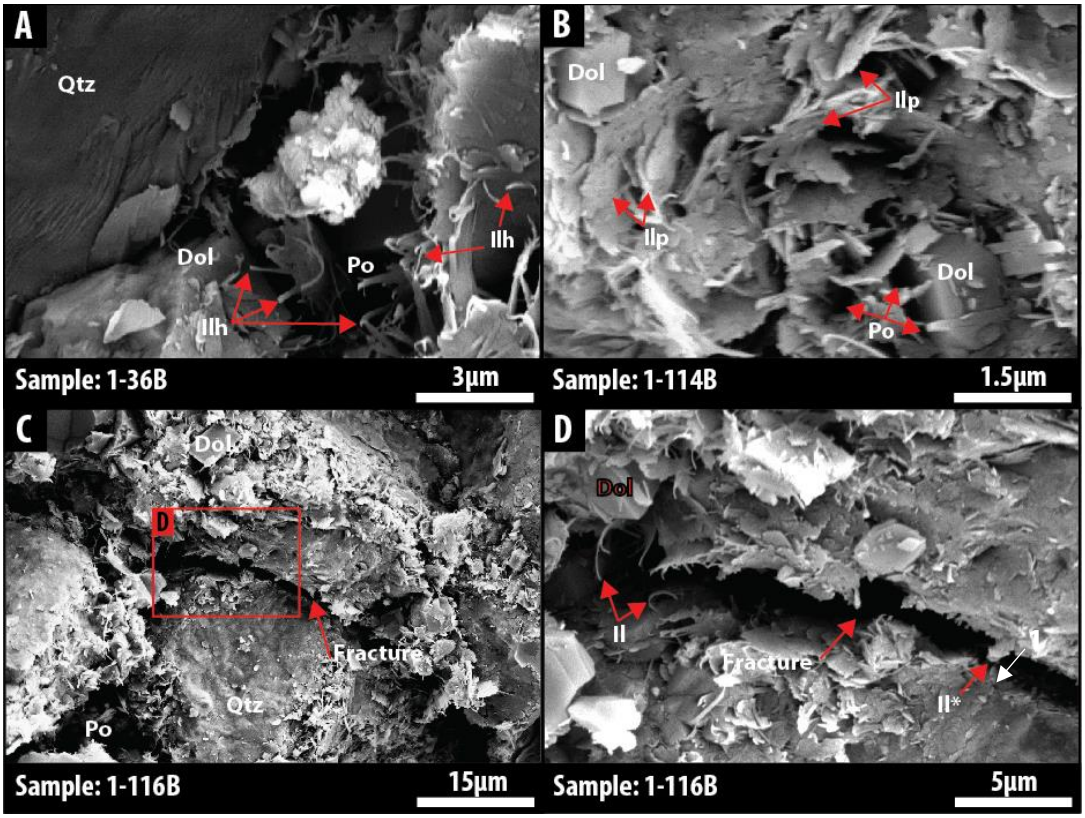

Figure 3.24 - Illite imaged on chip samples by scanning electron microscope at 8kV. A) Fine <<1 µm illite hair (Ilh) growing into intergranular pores (Po) in spaces between quartz (Qtz) and dolomite (Dol). B) Plates of illite (Ilp) and intergranular porosity (Po) is observed precipitated on and and around type 6 dolomites (Dol). C) Intergranular pore space and fracture/grain boundary porosity with illite growing into the space. The region of image D is delineated in red. D) Higher magnification image of fracture/grain boundary pore along edge of a quartz grain into which illite appears to growing to (il*). Fine, type 6 dolomite rhombs are also observed (Dol). Both plates and hairs of illite can be seen (Il).

Discussion

Detrital Mineralogy

Dolomite - Type 1

In this chapter we interpret dolomite genesis almost solely on texture alone. It has been acknowledged by several workers that to gain an understanding of dolomite genesis one must understand both texture and chemistry of the dolomite phase (Mazullo, 1992). We recognise that analysis of the morphology of the crystal alone does not provide definitive evidence to its genesis (Braithwaite, 1991). In Chapter 5 we will deal with the geochemical

evidence of dolomite genesis. We will bring together the findings of both analyses in the conclusions.

Type 1 dolomite is non-planar. This morphology has previously been documented as a product of late stage, high temperature diagenesis (Gregg & Sibley, 1984; Warren, 2000). One early study attempting to understand the origin of anhedral dolomite found it precipitated at a temperature of 300°C (Land, 1967). Later work suggested that the recrystallization of dolomite from euhedral to anhedral forms could occur at temperatures as low as 50°C (Gregg & Sibley, 1984 and Sibley & Gregg, 1987). The maximum temperatures reached in the Bakken were ~130°C, during the Eocene (Kuhn et al., 2012). In the model of Land (1967) much higher temperatures are required than exist in the middle Bakken; alternatively, in the model of Sibley & Gregg, recrystallization may have occurred where the crystals had a long residence time at shallow depths, at depths where temperatures are ~50°C.

Whilst in principle a long residence time at temperatures ~50°C and the neomorphism of earlier formed planar dolomites is not difficult to envisage during middle Bakken deposition. It is difficult to understand why such occurrences are so rare and do not cement or interact with other grains.

An alternative model is that these dolomites are detrital, given their distinctly different morphology and not interacting or cementing other grains. Many of the rock formations underlying the Bakken are dolomitic (Meissner, 1991).

It is possible the dolomite is a product of reworking of sediment either from early diagenetic dolomite in the lower Bakken or from the underlying Three Forks Formation. Simenson (2010), reports that reworking is common in the middle Bakken. We find a range of evidence of the reworking of sediment including bioturbation (Figure 3.4) and a suite of sedimentary structures which provide a good indication of sediment reworking; these include ripples and cross lamination, Figure 3.4 & Appendix 1.

Alternatively this phase may have been eroded from the Bakken hinterland, transported and deposited in the middle Bakken, during which, they were abraded during transport, forming the rounded, anhedral morphology which has made them so distinctive. Clastic inputs into the middle Bakken were considered in a study by Mohamed (2015), in which

they found clastic inputs into the Bakken were from four distinct age groups from middle Palaeozoic (middle Devonian) to Archean in age. The oldest ages suggest a detrital input would be from the hinterland of the Williston basin, whereas the youngest ages would support the theory of reworking of basin sediment.

From this discussion of textural evidence, we tentatively suggest, this phase of dolomite is detrital. This is principally, based on the rounded, anhedral shape of these crystals; quite different to other phases. The exact detrital source is unclear however the large range of clastic age dates proposed by Mohammed (2015), suggests there may have been several sources of detrital dolomite. See also Chapter 5 for further discussion.

Illite

Detrital Illite can be difficult to differentiate from authigenic forms (Meunier et al., 2004). From textural observations, the less delicate, more ordered, bedding aligned and folded nature of some the illite plates seen in Figure 3.24, suggest a detrital source pre-compaction. The detrital illite was principally identified by its SEM-EDX signature due to the undiagnostic crystal morphology of detrital illite, Figure 3.24b. Qualitative observations suggest detrital illite is less common than authigenic illite.

Diagenesis

The process of diagenesis was sub-divided into three different regimes by Chouquette & Pray (1970) which are: eogenesis, mesogenesis and telogenesis. These terms are commonly referred to in the literature and are referred to here. Eogenesis is the period of early diagenesis where authigenic reactions are principally controlled by the interaction of detrital assemblages with meteoric pore waters, still under the influence of the depositional system. Mesogenesis is often thought of as mid-diagenesis and refers to processes occurring during burial diagenesis where pore fluid chemistry is influenced by the products of diagenetic reactions. Telogenesis is often thought of as late-diagenesis which is associated with uplift but is concerned with reactions of meteoric water at shallow burial depths. Authigenic mineral formation is discussed in order with which they are proposed to have precipitated.

Mechanical & Chemical Compaction

Cementation is the principle control on porosity loss in the middle Bakken. Point count data suggests the effect of mechanical compaction on porosity loss is small. Cementation of the middle Bakken occurred prior to significant compaction, in all facies. In doing so evidence of mechanical compaction such as grain suturing is rare. Where compaction features are present, carbonate cement (dolomite and calcite) is lower in abundance. This is supported by the relative lack of anticipated mechanical compaction features such as long grain contacts, fused grain contacts and complete absence of stylolites, which would be indicative of very high overburden pressure (Nichols, 2009). Other Bakken studies report stylolites were relatively common (Ferdous, 2001 & Pitman et al., 2010), we observed very few examples of such textures. Our observations are supported by the observation in transmitted light of the presence of intact articulated shell fragments, which show little evidence of deformation (Figure 3.6c). The reason for the apparent difference in abundance of stylolites in our study compared to Ferdous (2001) and Pitman et al., (2010) is not clear, though we suggest this may be attributable to the variable spatial distribution or large abundance of calcite cement.

Pyrite

We suggest the earliest authigenic mineral growth is phase 1 pyrite. These are small individual crystals and framboids of smaller crystals which are found completely enclosed by early cements calcite and dolomite. We postulate that this phase of pyrite formed at shallow burial depths and low temperatures within a few meters of the sediment-water interface, typical of this morphology of pyrite (Berner, 1970). It was reported by Berner (1970 &1980) that most early authigenic pyrite formed in the sulphate reducing zone of the sediment column. For sulphate reduction to occur, the environment must itself be a reducing one (Berner, 1970 and Macquaker et al., 2007). It is thought that in the middle Bakken, the spatial proximity of pyrite to organic matter indicates the reducing environment was achieved by oxidation of organic matter. In order to precipitate pyrite a source of hydrogen sulphide is required. Hydrogen sulphide is formed by the reduction of sulphate dissolved in reservoir fluids by bacteria which use deposited organic matter as a reducing agent and energy source (Berner, 1984). This process forms iron monsulphides which are transformed to pyrite during burial diagenesis (Berner, 1984).

Anhedral blebs of pyrite such as those found in the middle Bakken, have previously been attributed to early diagenesis (Kortenski & Kostova, 1996), however textural relationships suggest they must be one of the last phases of growth as they infill secondary porosity in earlier diagenetic products. Karasinski (2006) speculates that the iron was sourced from diagenetic fluids in the middle Bakken reservoir and hydrogen sulphide may have been derived from the overlying and underlying shales.

The formation mechanism and timing of pyrite formation has been discussed in several previous studies though there is some disagreement to the exact formation conditions each morphology formed in. Last & Edwards (1991) suggest fine pyrite grains formed syndepositionally or during early diagenesis. Pitman et al. (2001) draw similar conclusions suggesting pyrite formed in anoxic environments, early in the diagenetic history of the middle Bakken. Karasinski (2006) shares this interpretation but only under circumstances where it is clear the pyrite is filling pore space and not replacing other minerals. However, Ferdous (2001) disagrees, he suggests that pore filling pyrite is an early diagenetic precipitate and replacement pyritisation is a late stage event. Alexandre et al., (2012) take a different stance suggesting pyritisation continued almost unabated throughout diagenesis.

Calcite

Calcite constitutes a large proportion of the cement of samples from the middle Bakken. The minus-cement porosity was on average 44%, which is very similar to the postulated depositional porosity of 45%. Of the total cement, calcite makes up an average 14%. The contribution of calcite to the minus-cement porosity and the 'floating-grain' texture when observed in highly cemented zones (Figure 3.16f), suggest calcite cementation commenced very early in the diagenetic history of the rock, filling much of the primary porosity.

We suggest the early calcite cement has impeded mechanical compaction of the sediment by adding structure and resisting the effects of overburden, lithostatic stress. Similar observations have been made by several other workers (e.g. Purser, 1978; Houseknecht, 1987; Xiong et al., 2016). In Purser's study of the Jurassic Paris basin, he found that sand

and gravel sized clasts were uncompacted due to the presence of an early carbonate cement, whereas in samples with low or no carbonate cement, the gravel sized clast exhibited much closer packing and compactional features, including stylolites along grain contacts. They argue the porosity has been preserved due to the presence of the early calcite cement. Whilst Houseknecht (1987) reports similar findings, he suggests that porosity is not always preserved however intergranular volume is preserved by early calcite cementation, Figure 3.25.

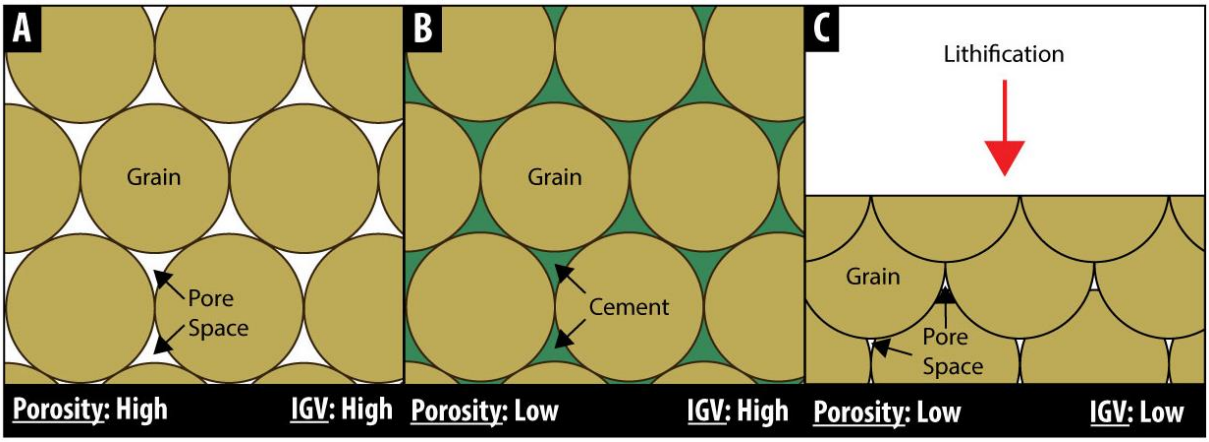

Figure 3.25 - Schematic showing the effect of cementation on intergranular volume (IGV). a) uncemented, uncompacted grains b) Cemented and Compacted, with the cement preserving the IGV. c) Uncemented, but compacted grains, showing the significant reduction in IGV. Porosities and IGV's are given as relative values.

We postulate that this is what has occurred in the middle Bakken. It is this process which we attribute to the preservation of detrital grain point contacts (Figure 3.12) and the apparent lack of fused and stylotised contacts in detrital grains, Figure 3.12. This mechanism also explains the presence of complete, uncompacted bioclasts, Figure 3.6.

Whilst several studies exist on the diagenesis of the middle Bakken few have considered in detail the origin of calcite cement. Of those that have, they agree that calcite occurred early in the diagenetic history, formed in a shallow marine environment (Ferdous, 2001; Pitman et al., 2001). The exact formation mechanism appears unknown and we offer no additional evidence in this chapter to answer this question, though previous workers have speculated on the process. Ferdous (2001) postulates, with little evidence, that the pervasive calcite cement formed by a complex series of compaction, cementation and

dissolution events. He suggests the calcite cement may be the product of extensive recrystallization of an early high magnesium calcite or aragonite. Whilst this seems plausible within the geological context of a shallow marine environment; in this study we find no clear evidence to support this, e.g. different individual grains of high magnesium calcite in EDX analyses or aragonite in XRD results (see Chapter 5 & Table 3.3, respectively). Calcite with between 2-30 mol% magnesium are regarded as high magnesium calcite (HMC), (Scholle & Ulmer-Scholle, 2003). Instead, EDX analysis of dolomite found some crystals of calcium rich dolomite, however the rhombohedral shape of these seems to suggest this is the result of a dolomitisation mechanism (see below). Pitman et al., (2001) are more conservative in their discussion, suggesting calcite cement it formed at temperatures <80°C and in neutral to weakly alkaline fluids but offer little more with respect to a formation mechanism.

We suggest the poikilotopic calcite cementation occurred very early in the diagenetic history of the middle Bakken due to: 1) High cement volume of the rock (>30%) of which calcite makes up 14% of the cement and up to 49% in calcite cemented samples, 2) Floating and point contacts of detrital grains in which other detrital grains appear to float within it (Figure 3.16f). 3) Well preserved bioclasts in fossiliferous beds (Figure 3.6). When considering the morphology of 'type 3' calcite, the sub-types seem to suggest this is a developing cement phase; precipitating from isolated grains to cementing small numbers of grains, to a poikilotopic 'type 2' calcite cement. We conclude this is an under-developed, early form of 'type 2' calcite

Dolomite: types 2, 3 & 4

Dolomite is a more abundant reservoir quality degrading cement than calcite in the middle Bakken. Previous studies on the middle Bakken have identified multiple textures of dolomite (Ferdous, 2001; Karasinkski, 2006; Staruiala et al., 2013).

We have both planar and non-planar dolomite, something also identified by Ferdous (2001). In addition, we also differentiated as well as a very fine phase of planar microdolomite. We identified phases as discrete, individual phases, which is in contrast to the observations of Staruiala (2013) who suggested that different dolomite phases grew concentrically, forming zones around each other.

Euhedral dolomite crystal fabrics such as those observed in type 2 and 3 morphologies have previously been attributed to formation during low temperature shallow burial at temperatures of 30-35°C and burial depths <100m (Chouquette & Hiatt, 2007). In many studies type 4 (planar-s) dolomite have been treated as planar-e dolomite and its formation conditions treated similarly (Gregg & Sibley, 1984; Sibley & Gregg, 1987; Mazullo, 1992). Mazullo (1992) state that all planar geometries of dolomite such as type 2 and 3 dolomites (including planar-S dolomite) formed at temperatures below 50-60°C.

Grain size has been used by some as evidence of formation mechanism. Medium to coarsely crystalline (10-100 μm), euhedral to subhedral mosaics of planar crystals were found to be typical of replacement dolomite whereas finer grained (<10 μm) dolomites are typically thought to be formed by syn-depositional mechanisms (Amthor et al., 1993; Warren, 2000).

The 'cloudy core-clear rim' texture observed in many of the middle Bakken dolomites is thought to be a characteristic dolomite replacement texture (Sibley, 1982; Budd, 1997; Kyser et al., 2002). The core represents the unreplaced, original phase found in the rock (calcite). The pure, clear exterior is the final, resultant phase (dolomite) (Sibley, 1982; Budd, 1997; Kyser et al., 2002; Scholle & Ulmer-Scholle, 2003). The presence of this texture and association with calcite replacement explains the large range of values observed in geochemical data in Chapter 5.

Vuggy porosity at the core of type 2 dolomites separates this phase from type 3 dolomites. Not only do the vugs appear isolated from pore system of the rock; type 2 dolomites also appear in close spatial proximity to type 3 dolomites (perfect crystals without vuggy porosity). Vuggy porosity in dolomites is common in burial dolomitisation models (Mattes & Mountjoy, 1980; Gregg & Sibley, 1984). Several models have been proposed including 1) mole-for-mole replacement (Weyl, 1960), 2) dissolution of calcite from a partially dolomitized rock after dolomitization and 3) excess solution over dolomite growth during the late stage of the dolomitizing process (Sun, 1995).

The mole-for-mole replacement theory was proposed by Weyl (1960), in which he suggested that because the abundance of carbonate in natural waters is small relative to the amount of calcium and magnesium then the carbonate used to precipitate secondary

dolomite must be locally sourced e.g. from the calcite or aragonite in the sediment. As a result, he proposed that dolomitisation would occur as mole-for-mole replacement. This conversion from calcite to dolomite would lead to an increase in porosity of 12–13% (Sun, 1995). This model is not widely accepted, principally because, if it were then dolomites would be consistently more porous than limestones, something which is not routinely observed (Sun, 1995).

The current held view is that replacement dolomitization took place along with calcite or aragonite dissolution (Landes, 1946; Lucia, 1962; Choquette et al., 1992; Sun, 1992). The evolution of porosity during the replacement of calcite by dolomite is controlled by the balance between rates of the dissolution of calcite and dolomite growth rates (Landes, 1946). If the rate of dissolution exceeds dolomite replacement, the porosity will be increased, Sun (1992). Whilst this would explain the presence of the vugs, it remains unclear to us why vuggy porosity does not exist in all dolomite crystals.

We suggest dolomite phases 2, 3 and 4 replaced the earlier formed calcite cement. Our principle evidence to suggest this is: 1) Presence of cloudy core, and clear rim dolomites textures, 2) Euhedral, medium to coarsely crystalline (10-100 µm, euhedral to subhedral mosaics of planar crystals 3) Presence of vuggy porosity in some textures.

Feldspar Dissolution

Potassium feldspars crystals have been observed both with dissolution voids and with replacement textures in the middle Bakken reservoir, Figure 3.21. Previous workers have made similar observations (Ferdous, 2001; Karasinski, 2006). Karasinski (2006) postulates that these are a product of late-stage diagenesis, from acidic reservoir fluid which were derived from carbon dioxide released into the formation during hydrocarbon generation.

We suggest feldspar dissolution commenced earlier, due to the introduction of acidic reservoir fluid. Other workers have previously suggested organic acids are present in hydrocarbon systems, derived from the source rocks during the maturation of organic matter prior to the generation of hydrocarbons (Surdam & Crossey, 1985). Yet this model has been questioned by some as it is unclear whether sufficient quantities can be expelled in the required timescale (Giles & Marshall, 1994). In the middle Bakken, where the thickness of the confining organic rich upper and lower Bakken (~35 m) is almost as thick

as the middle Bakken itself (~30 m) it seems plausible. The presence of organic acids is supported by many previous workers on the middle Bakken (Ferdous, 2001; Pitman et al., 2001; Karasinski, 2006, Alexandre et al., 2012; Jarvie, 2012).

An important consideration of acidic dissolution mechanisms is the effect of the dissolving on carbonate minerals such as calcite and dolomite, with the obvious potential to dissolve these minerals. It has been found that the dissolution associated with feldspar does not affect adjacent calcite cements (Siebert et al., 1984 In Mackenzie 2005). It is thought the dissolution of potassium feldspar buffers the acid, preventing dissolution of the calcite. Mackenzie (2005) calculated that the dissolution of 0.25 mol of potassium feldspar buffers the acid sufficiently to allow the precipitation of up to 1 mol of calcite. This is a significant finding, and may explain the apparent preservation of calcite cement and dolomite rhombs in the middle Bakken.

Albitisation

The albitization of potassium feldspar is thought to occur at temperatures of between 65-150°C; (Saigal et al. 1988). The simplest model of albite precipitation is a direct one-to-one replacement reaction. This mechanism requires the contemporaneous dissolution of potassium feldspar and albite precipitation, Equation 3.1, Saigal et al. (1988). In this model there is a requirement for a sodium supply. Dissolution of the underlying Three Forks Formation has been thought to result in very saline middle Bakken reservoir fluids (Kurtoglu, 2014).

$$Na^+ + KAlSi_3O_8 \longrightarrow NaAlSi_3O_8 + K^+$$

Equation 3.1 - Dissolution reaction for potassium feldspar. Saigal et al (1988) and Walker (1984).

It has been suggested by Aagaard et al. (1990) that albitization is more dependent on the removal of potassium than on the supply of sodium, and the reaction will cease if the liberated potassium is not removed from the system. This would be particularly prevalent in the middle Bakken where as we suggest, it is thought that reservoir fluids were saline (Kurtoglu, 2014). If the albitisation of potassium feldspar is related to the illitisation of

kaolinite then the reaction would follow that of Equation 3.2 (Morad et al. 1990).

$$2KAlSi_3O_8 + 2.5Al_2(Si_2O_5)(OH)_4 + Na^+ \rightarrow Na(AlSi_3O_8) + 2\ Al_2Si_2O_5(OH)_4 + 2SiO_2 + 2.5H_20 + H^+$$

Equation 3.2 - Albitisation of kaolinite and potassium feldspar (Morad et al., 1990).

Differentiating which reaction requires knowledge of the exact sodium and potassium composition of the reservoir fluid, from which the relative stability of individual mineral phases can be determined in those reservoir fluids. Combining evidence of illite formation and authigenic quartz precipitation, we suggest the model of Morad et al., (1990), Equation 3.2 effectively explains the albitisation of potassium feldspar in the middle Bakken.

The timing of dissolution of potassium feldspar and albitisation is thought to have occurred during the middle of the diagenetic history of the middle Bakken when basin temperatures were high enough (75-110°C) for the feldspar replacement reaction to have occurred. It is appropriate that, this temperature range is lower than the potassium feldspar 'disappearance' temperatures reported by Land & Miliken (1981) [130-150°C] as detrital potassium feldspar is still present in the middle Bakken in appreciable quantities, Table 3.3. The products of this process (Equation 3.2) supply reactants required for later diagenetic reactions (authigenic quartz formation and illite precipitation) so logically it follows albitisation occurred before these diagenetic events.

Illite

Whilst not a volumetrically significant phase in the middle Bakken, authigenic forms of illite are commonly found as a product of diagenesis in other hydrocarbon systems (Hower & Mowatt, 1966; Lázaro, 2007). Small volumes of illite have been shown to reduce the permeability of a system by several orders of magnitude, due to its high surface area, pore bridging morphology (Stalder, 1973; Pallatt et al., 1984; Leveille et al., 1997, Wilkinson et al., 2014). It has also been suggested that authigenic illite may also preserve the reservoir quality by preventing the precipitation of quartz cement (Ajdukiewicz & Larese, 2012).

In this study we have principally used textural observations made under electron microscope to differentiate authigenic from detrital illite. Described by one worker as the

'delicacy' of the clay plate (Wilson & Pittman, 1977); the habit of the plates is a robust way of differentiating detrital illite from authigenic illite. They suggest complex plates and delicate fibres could not have survived transport or compaction so must have been formed in-situ, so be of authigenic origin. Other workers look for the location of the precipitate and how continuous it is around a feature e.g. pore lining or grain coating may also be used to separate authigenic from detrital forms (Wilson & Pittman, 1977). Where illite forms thin coats around other coarser grains, then a strong argument exists for authigenic formation. Composition in SEM-EDX has also been used to differentiate authigenic and allogenic illite as authigenic forms can reach very pure compositions (Keller, 1970).

It has been shown that almost all of the clay present in the middle Bakken is illite (Kurtoglu et al., 2014; Li et al., 2015; Saidian & Prasad, 2015). Previous work on the origin of illite in the Bakken by Last & Edwards (1991) concluded that illite in the middle Bakken was of authigenic origin, formed by regeneration; precipitating from the dissolution products of potassium feldspar. Ferdous (2001) agrees, reporting that almost all of the illite is authigenic with only a small detrital component. They suggest that the dissolution of detrital potassium feldspar may have released the K^+ required for authigenic illite precipitation. Pitman et al., (2001) disagree; they suggest that most of the illite in the middle Bakken is detrital as well ordered illite is found in both mature and immature sample, though they postulate an authigenic source can't be ruled out. We maintain that such delicate structures formed in and across earlier diagenetic features are of diagenetic origin and could not have survived transport into the Bakken or have precipitated on newly formed diagenetic minerals. Saidian & Prasad (2015) show illite is a pore filling diagenetic phase; filling pores between dolomite and quartz.

Illite cements such as those we have observed in the middle Bakken have been found to form at temperatures of between 75°C and 140°C (Jeans, 1994). The maximum temperature modelled in the middle Bakken (120°C) (Kuhn, 2013) falls both within this range and towards up the upper limits of it. Diagenetic illite has been shown to precipitate either entirely from formation waters (neoformation) or through reactions of between precursor minerals (regeneration) (Wilson & Pittman, 1977).

Several mechanisms have been proposed for the formation of diagenetic illite. In shales, the transformation of smectite to illite via an intermediate mixed-layer smectite-illite is common and is widely accepted (Boles & Franks, 1979). Saidian & Prasad (2015) found some mixed layer illite-smectite, though they also report that much of this was illite.

$(Ca_{0.17}(Al,Fe,Mg)_2\ (Si,Al)_4O_{10}(OH)_2.nH_2O) + KAlSi_3O_8 \longrightarrow KAl_3Si_3O_{10}(OH)_2 + 2SiO_2 + (Ca^{2+}, Mg^{2+}, Na^{+})$

Equation 3.3 - Smectite-illite transformation reaction, (Bjorlykke & Egeberg, 1993).

In this study we find no evidence of smectite. If this model stands then we would expect there to be a mixed clay fraction and therefore we would be more likely to find smectite in SEM-EDX analyses. Without evidence of smectite either in bulk analyses or by SEM-EDX, it is difficult to support this interpretation.

Instead we propose that illite formed from Kaolinite-K-feldspar dissolution, Equation 3.2. This is supported by XRD analysis which showed evidence of small quantities of kaolinite remains present in the samples. Petrographic observations under electron microscope also support this interpretation as dissolved and replaced potassium feldspars are present in the middle Bakken, Figure 3.21 (above). The platy morphologies of illite crystals such as some of those observed under SEM have previously been attributed to the replacement of kaolinite by transformation, pseudomorphing the previous kaolinite crystal (Ehrenberg and Nadeau, 1982). Therefore we suggest, illite formed by both neoformation precipitating as hairy illite and also by transformation, pseudomorphing pre-existing kaolinite crystals.

$KAlSi_3O_8 + Al_2Si_2O_5(OH)_4 \longrightarrow KAl_3Si_3O_{10}(OH)_2 + 2SiO_2 + H_2O$

Equation 3.4 - Kaolinite - Potassium feldspar to illite conversion reaction.

To further prove this mechanism has occurred, previous workers on burial illite in sandstones have attempted to relate the percentage of illite in the clay fraction to the percentage of potassium feldspar in the sample. In this case study we deem this would be

inappropriate due to the low clay fraction of the middle Bakken samples (Ehrenberg and P. H. Nadeau, 1989).

This reaction is often, perhaps misleadingly referred to as 'deep burial' illite; as it has been reported in many studies of deeply buried sandstones (Bjørlykke et al., 1986; Lanson et al., 1996; Berger et al., 1997). It has however been found in several studies of much more shallowly buried sandstones where temperatures are between 90-95°C (Ehrenberg, 1993; Beaufort, et al., 1998). Whilst the commonly held view is that the reaction of kaolinite occurs at deep burial temperature >120°C, which is close to the maximum middle Bakken burial temperature. Lanson et al., (2002) surmise there is no systematic relationship between temperature and intensity of kaolin illitization. It has been suggested by Berger et al., (1997) that a high K^+ /H^+ activity ratio exists in low temperature systems, which allows the kinetic barrier to illite formation to be overcome. In this geochemical model potassium feldspar cannot be the source of K^+. Either an external source of K^+ and/or a pH increase is needed to reach the K^+/H^+ ratio. This model may offer a solution to the high burial temperatures required.

$3Al_2Si_2O_5(OH)_4 + 2K^+ \rightarrow 2KAl_3Si_3O_{10}(OH)_2 + 2H^+ + 3H_2O$ (3) Illite

Equation 3.5 – Berger model of kaolinite conversion to illite, Reaction of Kaolinite and potassium forming illite, hydrogen ions and water. Berger et al., (1995), In Lanson et al., 2002.

Neomorphic, hairy morphologies of illite have been attributed to shallower burial and more platy forms associated with deeper illitisation (Lanson et al., 2002), however we are cautious not to over interpret what is unquestionably a volumetrically small phase of the middle Bakken and a controversial subject in the literature.

In the context of the carbonate rich middle Bakken, it is noteworthy, that the distribution of early carbonate cements are thought to influence the distribution of clay minerals such as illite (Jeans, 1994). We have shown throughout this thesis that carbonate cements are a significant component of the middle Bakken (see also, Chapter 5). It is however not clear to what extent carbonate cements influence illite precipitation. Whilst logically we would assume, early carbonate would precipitate on potential illite nucleation sites and inhibit

illite growth; Huggett (1995) studied marine Eocene London Clay and showed that the clay fraction of calcite-cemented septarian nodules in contain considerably more illite and less smectite and quartz than the mudstone matrix. This difference was attributed to the selective replacement of smectite and quartz by the calcite cement (Huggett, 1996).

Textural petrographic evidence suggests that illite is a late stage diagenetic event in the middle Bakken as the illite is found in pores, uncompacted and with no preferred orientation, growing on and between earlier diagenetic products, Figure 3.24. As discussed above; typical formation temperatures are thought to be of the order of 75°C to 140°C (Jeans, 1994), from which we attribute illite genesis to a mid to late stage of diagenesis.

Quartz

The distribution of authigenic quartz cement has a major effect on the porosity and permeability and therefore reservoir quality in many sandstone hydrocarbon reservoirs around the world (e.g. Smith 1985; Pittman and Larese, 1987; Bjørlykke & Egeberg, 1993; Worden et al., 1998).

In the middle Bakken we have identified dull and non-luminescent quartz by SEM-CL which we interpret to be authigenic quartz (Boggs & Krinsley, 2006). Based on the thin nature of these overgrowths (0.5-3 µm) we have described them as micro-quartz overgrowth. Microquartz has previously been defined as overgrowths that are between 0.5-10 µm thick (Vagle et al., 1994).

Previous workers on middle Bakken diagenesis have identified secondary quartz in the middle Bakken (Ferdous, 2001; Pitman et al., 2001; Karasinski, 2006; Alexandre et al., 2012). Ferdous (2001) reports only trace quantities of authigenic quartz are present and are found only in the deepest samples. They suggest this was internally sourced by pressure-solution from deeper parts of the basin from the products of the dissolution of potassium feldspar. Pitman et al. (2001) also observed small volumes of secondary quartz, which they assert is the product of the chemical compaction of detrital grains. In Karasinski's (2006) study, they found diagenetic quartz, which they describe as varying from incipient to fully enclosing cements. These cements were thought to be of late diagenetic origin, also

forming from the products of feldspar dissolution. Alexandre et al. (2012) also observed quartz cementation; the growth of which they suggest had been inhibited by sphalerite. The genesis of authigenic quartz is the source of much controversy (Worden & Morad, 2000). The main factors which are thought to control quartz cementation in sandstones are detrital rock composition (a silica source and nucleation site), temperature, fluid flow and chemistry (McBride, 1989). Large quantities of fluid are thought to be required for diagenetic quartz precipitation (Land & Dutton, 1978), even though it is thought that silica concentrations are generally greater than saturation in reservoir fluids (Lynch et al., 1997). Several studies have shown that quartz cementation is correlated with temperature (e.g. Land et al., 1987; Bjorlykke and Egeberg, 1993; Walderhaug, 1994). It is thought that where sandstones are heated above 70°C during diagenesis that quartz cementation will occur (Bjorlykke & Egeberg, 1993). At this temperature the activation energy for quartz precipitation is breached and quartz precipitation occurs (Maast et al 2011). Other work has also shown the surface area of precipitation sites and therefore detrital quartz abundance is also an important factor (Lander & Walderhaug, 1999). It follows that samples with finer grained detrital quartz will be cemented faster as they have a larger surface area on which the authigenic quartz can form (Walderhaug, 1996). Middle Bakken samples do contain appreciable quantities of fine grained detrital quartz, which would as Walderhaug suggests form ideal nucleation sites for authigenic quartz.

Our analyses showed authigenic quartz makes up only a very small percentage of both the total quartz and the total rock. A similar technique to quantify quartz overgrowth was employed by Evans et al., (1994); in their work they studied 48 samples from 4 basins around the world; they found authigenic quartz varied from 3-26.3% of the total. Other studies found values ranging from <1% to 17.6% (Waulderhaug, 1990; Hogg et al., 1992; Schmid et al., 2004).

Determining the exact source of silica from which authigenic quartz precipitated is somewhat problematic. The very small abundance of authigenic quartz in this study means the potential mechanism does not need to mobilise significant quantities of silica; this in itself points towards an internal quartz source. Silica mobilising processes which may be accountable include: 1) Pressure-solution of detrital quartz along grain boundaries; whilst no stylolites were observed, quartz can still be mobilised along

concave-convex grain contacts which are common in the middle Bakken (Walderhaug et al., 2006; Worden and Morad, 2000). 2) Dissolution of feldspar; whilst it has been suggested that feldspar dissolution typically occurs after diagenetic quartz precipitation (Land et al., 1987), we do not have any petrographic evidence which would support or reject this, yet other workers considering middle Bakken diagenesis have suggested this a possibility (Ferdous, 2001). 3) Whilst we have observed no evidence of smectite, previous workers have suggested authigenic illite in the middle Bakken is a product of transformation from smectite, a reaction in which silica is mobilised.

The timing of quartz cementation has been considered by some workers as a continuous process which once started, continues until all the pore space has been filled with cement (Walderhaug, 1996). Other workers consider quartz cementation as an episodic process, which is started and stopped by other factors (Robinson and Gluyas, 1992). We suggest that the limited abundance of quartz cement would point toward a single precipitation event. Whilst we found quartz as one single phase with no cement stratigraphy observed in SEM-CL, we recognise this piece of evidence is very limited and more evidence would be required to robustly support this assertion.

Comparing the findings of the earlier studies and the results of this study, it is evident that both the nature and extent of authigenic quartz cementation is highly variable. All of the previous studies attribute at least in part to feldspar dissolution to the mobilisation of silica. We suggest some quartz may have been mobilised by chemical compaction, along convex-concave quartz contacts. In the Sorenson well, we attribute the relative apparent lack of authigenic quartz to the very early precipitation of calcite and dolomite cement (discussed above), something shown by other studies (Houseknecht, 1987; Xiong et al., 2016). Early carbonate cementation has engulfed many of the detrital quartz grains, forming a physical barrier between individual quartz grains and inhibiting chemical compaction.

Titania

Titanium oxide minerals were found in trace quantities in the middle Bakken, in two textural phases. Whilst historically titanium oxide minerals have been associated with high temperature metamorphism and were generally regarded as immobile under diagenetic conditions, there has been growing suggestion this may not always be the case (Pe-Piper

et al., 2001). Earlier work suggested it may form as a diagenetic alteration product of other titanium bearing minerals (Morad & Aldahan, 1982; Morad, 1988). Within the mesogenetic zone two mechanisms could have resulted in titania precipitation. The first of which, is thought to occur during late - eogenesis to early mesogenesis, at near surface depths and relatively low temperatures, in the presence of phosphate and with meteoric water flows, alteration of ilmenite, biotite and muscovite has been found to form small amounts of neoformed titanium oxide minerals (Morad, 1988 and Pe Piper et al., 2001).

$$FeTiO_3 + 2H_2S \rightarrow TiO_2 + FeS_2 + H_20 + H_2$$

Equation 3.6 – Reaction of the alteration of ilmenite by dissolved sulphides forming titanium oxide and pyrite, Reynolds and Goldhaber (1978).

The formation of the acicular structures found by Pe Piper et al., (and similar to those observed in this study) were attributed to exsolution of ilmenite. We have found some although, limited evidence of both unaltered ilmenite laths and phosphate that is present in EDX spectra. Phosphate is precipitated as both calcium phosphate crystals and also in association with faecal pellets. Titania could also be mobilised by albitisation of potassium feldspar (Morad & Aldahan, 1982). This process releases phosphorous from potassium feldspar which is thought to facilitate titanium mobility (Pe-piper et al., 2001). We suggest that authigenic precipitation of titania cannot be discounted. Whilst titania minerals are present in only trace quantities, understanding the origin of titanium oxides could be important as previous studies have used these minerals to determine the timing of oil emplacement, as shown by Prozorovich (1970) and Yurkova (1970).

<u>Dolomite - Type 5</u>

Iron rich rims on dolomites are easily identified in BSE images, Figure 3.16e. Pitman et al., (2001) and Ferdous (2001) both postulate that ferroan dolomite rims precipitated late in the diagenetic sequence after the dissolution of earlier formed dolomite cement. Staruiala et al., (2013) is less confident however and questions whether this phase formed in a near surface environment or a deeper burial environment.

Several different potential sources of iron have been postulated, Pitman et al., (2001) suggest the most likely source of iron is from sulphide minerals in the underlying and

overlying shales, whereas Ferdous (2001) suggests that iron may have been liberated from clay coatings. In contrast to this Karasinski (2006) and Staruiala et al., (2013) suggest that iron was obtained from the dissolution of the overlying and underlying evaporitic units.

We have limited evidence to support or reject these ideas. The sharp contact and euhedral grain form between the Fe-dolomite and planar dolomite seems unlikely to have formed on a dissolved crystal; and of which there is petrographic evidence, which would seem to discount the suggestion made by previous workers that this was a product of dissolution and precipitation. It follows, if a period of dolomite dissolution did not occur then we suggest, there is unlikely to be sufficient intergranular volume to allow the precipitation of an overgrowth.

We propose an alternative mechanism; that the ferroan-dolomite is a replacive phase on the pre-existing dolomite. It is understood that iron is present at very low levels in seawater yet is often present in significant quantities in diagenetic pore fluids (Warren, 2000). For iron to directly substitute into the dolomite lattice without dissolution, solid state diffusion must have occurred. Yet solid state diffusion is thought to be too slow to have occurred during late diagenesis or even early metamorphism (Freer, 1981). The exact mechanism of formation remains unclear, though if possible, this mechanism would explain the sharp euhedral crystal edges and contacts with the ferroan rims observed.

Dolomite - Type 6

Euhedral dolomites which are <5 µm across were classified as 'type 6' dolomites. Such fine grained dolomites have previously been attributed to syn-depositional precipitation environments (Amthor et al., 1993), however the apparent pore-filling and pore-clinging nature of these dolomites suggests they were much later in the diagenetic history of the middle Bakken.

Ferdous (2001) suggested that micro-dolomites similar to this phase formed during the post-Mississippian exposure of the middle Bakken at which time meteoric water could have percolated down into the reservoir and mixed with reservoir fluids creating favourable conditions for dolomite precipitation. Other workers have suggested fine-

grained micro-dolomites such as these are formed in syn-depositional environments such as normal marine or peritidal environments (Warren, 2000).

The angular euhedral character of these dolomites is akin to type 2 and type 3 dolomites which have concluded were formed in a shallow burial environment. The 'floating' and 'pore-clinging' nature and relationship of these dolomites suggests they formed late in the diagenetic history of the middle Bakken after the formation of other diagenetic precipitates. During much of the Bakken's history, burial was shallow and estimated reservoir temperatures were correspondingly low (Kuhn, 2013). From this we suggest they could have formed as late as the Cretaceous when estimated reservoir temperatures could have been as low as ~70°C. We can offer limited additional evidence to this problem. We also recognise that we have no control on the reservoir fluid chemistry and whether it was conducive to dolomite precipitation.

Halite

In the samples of this study we observed halite as euhedral cubic crystals precipitated along fractures. Evaporite minerals previously reported in the middle Bakken member include gypsum, anhydrite and halite (Ferdous, 2001; Pitman et al., 2001). These minerals are thought to have derived from dissolution and reprecipitation of the underlying Prairie formation, which resulted in structural deformation of the overlying units (Anderson & Hunt, 1964; Christiansen, 1967; Bachu & Hitchon, 1996). Another potential source of halite is saline pore fluid trapped in the rock prior to burial and fluid expulsion.

The presence of the halite crystals along fractures, cross-cutting all other earlier cements suggest they precipitated during the latest stages of diagenesis. There is also a second textural form of halite; dendrites, and rosette structures. Kurtoglu et al., (2014) report that the current reservoir fluid is very saline. We propose that halite precipitated from connate water as the core equilibrated with atmospheric conditions when it was brought to the surface (after Radjef pers com). Our conclusion acknowledges the caution expressed by previous workers who have suggested the presence of some evaporate minerals in the Bakken are contamination from drilling mud (Pitman et al., 2001).

Oil Charge

Oil emplacement within the middle Bakken has previously been thought to have occurred during diagenesis at depths of ~3000 m and temperatures of ~120°C (Pitman et al., 2001). It is generally regarded that the onset of oil emplacement within the middle Bakken halted diagenetic change (Last & Edwards, 1991; Pitman et al., 2001; Alcoser et al., 2012). Previous workers have concluded that the most likely form of oil migration was as one phase of movement by continuous-phase migration (Webster, 1984).

If the oil charge occurred as one single event then it is possible to make an estimate of the timing of oil migration. For oil generation to occur a minimum temperature and pressure conditions need to be reached (1000-4000 m and 40-150°C) (Nichols, 2009). Using the burial model of Kuhn (2013), the lower limits of this range would have been reached around middle Cretaceous to late Cretaceous. This corresponds with the suggestion by Webster (1984) that by the end of the Cretaceous enough oil would have been generated to fill the pores of the upper and lower Bakken and generate an anomalous overpressure, fracturing the shale and forcing the oil into the middle Bakken, halting or at least slowing diagenesis.

There are two main perspectives on this. Some workers have shown that oil emplacement halts diagenesis (Purser, 1978; Feazel & Schatzinger, 1983; Gluyas et al., 1993) whilst others suggest that diagenesis can continue largely unaffected by the presence of oil in the reservoir (Walderhaug, 1990; Bjorkum et al., 1993; Taylor et al., 2010).

Evidence which would suggest that oil emplacement did not effectively stop (or significantly slow the rate of diagenesis include: abundant oil inclusions in quartz cement, and no significant difference in cement between oil and water wet zones. Extensive, focussed, petrographic analysis on middle Bakken samples in this study, has found no oil inclusions in quartz cement. Whilst it is possible they simply are not present, it may be the product of such small quantities of authigenic quartz observed in the middle Bakken member and any inclusions are likewise, small or alternatively it may be that the reduction in porosity due to the precipitation of early calcite cement has prevent the migration and preservation of fluid inclusions. Analysis of cement distributions suggests there is no variation with depth and therefore hydrocarbon saturation zones.

Diagenetic Sequence

From the discussion of petrographic observations, a post-depositional sequence can be proposed, Figure 3.26. The paragenetic sequence is as synthesis of observations of grain and crystal growth relationships in this petrographic study. The sequence details how the diagenetic events changed the original sediments into the sedimentary rock we now observe.

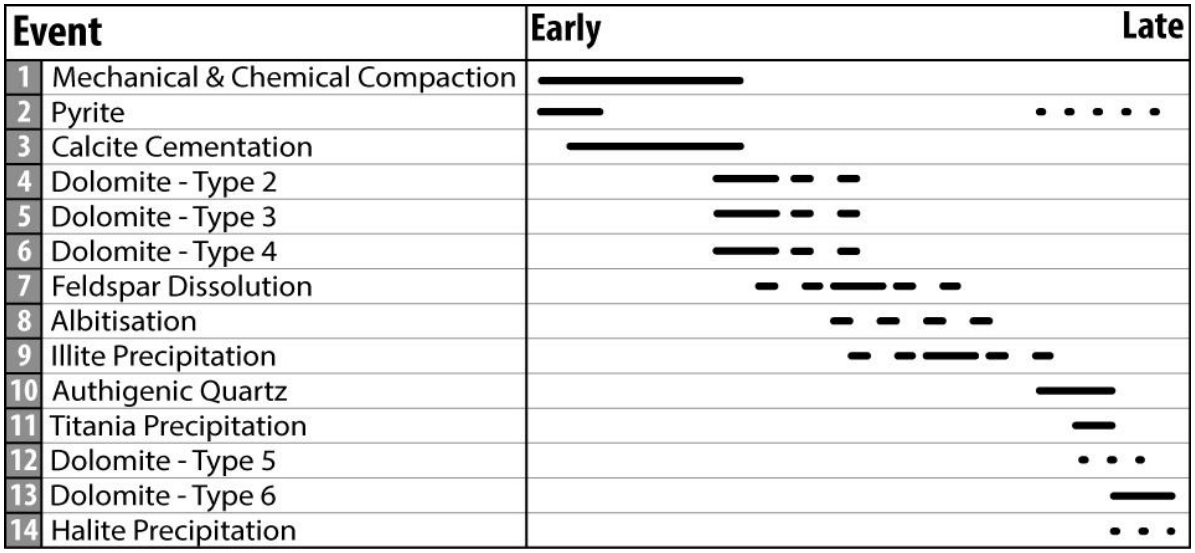

Figure 3.26 - Post-depositional events observed in samples of the middle Bakken Formation as inferred from petrographic observations.

We have assumed diagenetic alteration in the middle Bakken ceased at the onset of hydrocarbon generation in the Late Cretaceous when the sediment was close to the greatest burial depth and highest temperature. Whilst our study found no direct evidence to support this, equally we found no evidence to discount this. Citing previous studies of middle Bakken diagenesis, we have used this to mark the cessation of diagenesis.

Conclusion

The results of combining transmitted light, SEM and XRD analyses has shown that diagenesis has significantly affected the reservoir quality of the Bakken at a scale smaller than that of a facies. During diagenesis these rocks units have undergone mechanical compaction, chemical compaction, mineral dissolution, and authigenic mineral precipitation.

Textural analysis shows that pyrite was the earliest authigenic mineral to form. Pyrite formed within a few meters of the sediment-water interface forming both framboids and individual crystals. Carbonate minerals make up on average 49% of the middle Bakken. Calcite is observed as 3 different textures. The precipitation of calcite cement occurred early in the diagenetic history, inhibiting compaction. Evidence for mechanical compaction is limited. Dolomite is present in 6 different textural forms of which one is interpreted to be of detrital origin. There is no relationship between dolomite abundance or the abundance of individual dolomite textures and facies. Diagenetic dolomite formed by the replacement of calcite.

Potassium feldspars have been dissolved forming intragranular pores. In some cases, the potassium feldspar has been replaced by albite. Illite is a late diagenetic product which is found growing within pores. Authigenic quartz cement is present in the middle Bakken but occurs in small quantities overgrowing detrital quartz grains. Ferroan dolomite formed euhedral iron rich rims of earlier replacive dolomites.

Authigenic mineral growth during diagenesis has reduced the porosity of the middle Bakken by infilling pore space. Our investigation of the effects of diagenesis on mineralogy has shown there has been significant alteration of the detrital mineralogy by diagenetic processes. These changes have significantly changed the reservoir quality. This investigation of diagenesis forms the basis for more detailed pore systems analysis.

References

Aagaard, P., Egeberg, P., Saigal, G., Morad, S. & Bjorlykke, K. (1990). Diagenetic Albitization of Detrital K-Keldspars in Jurassic, Lower Cretaceous and Tertiary Clastic Reservoir Rocks from Offshore Norway, II. Formation Water Chemistry and Kinetic Considerations. Journal of Sedimentary Research 60, p. 575 - 581.

Aguilera, R. (2014). Flow units: From conventional to tight-gas to shale-gas to tight-oil to shale-oil reservoirs. SPE Reservoir Evaluation & Engineering 17, p. 190-208.

Ajdukiewicz, J. M. & Lander, R. H. (2010). Sandstone reservoir quality prediction: The state of the art. AAPG Bulletin 94, p. 1083-1091.

Ajdukiewicz, J. M. & Larese, R. E. (2012). How clay grain coats inhibit quartz cement and preserve porosity in deeply buried sandstones: Observations and experiments. AAPG Bulletin 96, p. 2091-2119.

Alcoser, L., Ovalle, A. & Parsons, M. (2012). The Bakken: Utilizing a Petroleum System Based Analysis to Optimally Exploit One of the World's Largest Oil Deposits. Paper SPE 58918 presented at the SPE Hydrocarbon, Economics, and Evaluation Symposium held in Calgary, Alberta, Canada, p. 24-25.

Alexandre, C. S., Sonnenberg, S. & Sarg, J. (2012). Diagenesis of the Bakken Formation, Elm Coulee Field, Richland County, Montana. AAPG Annual Convention and Exhibition.

Amthor, J. E., Mountjoy, E. W. & Machel, H. G. (1993). Subsurface dolomites in Upper Devonian Leduc formation buildups, central part of Rimbey-Meadowbrook reef trend, Alberta, Canada. Bulletin of canadian petroleum geology 41, p. 164-185.

Anderson, S. B. & Hunt, J. B. (1964). Devonian salt solution in north central North Dakota. 3rd Williston Basin Symposium, p. 93 - 104.

Angulo, S. & Buatois, L. (2010). Sedimentary facies distribution of the Upper Devonian–Lower Mississippian Bakken Formation. Williston Basin, southeastern Saskatchewan: Implications for understanding reservoir geometry, paleogeography, and depositional history: Summary of Investigations, 2010-2014.

Bachu, S. & Hitchon, B. (1996). Regional-scale flow of formation waters in the Williston Basin. AAPG Bulletin 80, p. 248-264.

Berger, G., Lacharpagne, J.-C., Velde, B., Beaufort, D. & Lanson, B. (1995). Mécanisme et contraintes cinétiques des réactions d'illitisation d'argiles sédimentaires, déduits de modélisations d'interaction eauroche. Bulletin de Centre de Recherches. Exploration et Production 19, p. 225-234.

Berger, G., Lacharpagne, J.-C., Velde, B., Beaufort, D. & Lanson, B. (1997). Kinetic constraints on illitization reactions and the effects of organic diagenesis in sandstone/shale sequences. Applied Geochemistry 12, p. 23-35.

Berner, R. A. (1970). Sedimentary pyrite formation. American Journal of Science 268, p. 1-23.

Berner, R. A. (1980). Early diagenesis: A theoretical approach. Princeton University Press, p. 241.

Berner, R. A. (1984). Sedimentary pyrite formation: an update. Geochimica et Cosmochimica Acta 48, p. 605-615.

Bjorkum, P. A., Walderhaug, O. & Aase, N. E. (1993). A model for the effect of illitization on porosity and quartz cementation of sandstones. Journal of Sedimentary Research 63, p. 1089-1091.

Bjørlykke, K., Aagaard, P., Dypvik, H., Hastings, D. & Harper, A. (1986). Diagenesis and reservoir properties of Jurassic sandstones from the Haltenbanken area, offshore mid-Norway. Habitat of hydrocarbons on the Norwegian continental shelf, p. 275-286.

Bjorlykke, K. & Egeberg, P. (1993). Quartz cementation in sedimentary basins. AAPG Bulletin 77, p. 1538-1548.

Boggs, S. and Krinsley, D., 2006. Application of cathodoluminescence imaging to the study of sedimentary rocks. Cambridge University Press.

Boles, J. R. & Franks, S. G. (1979). Clay diagenesis in Wilcox sandstones of southwest Texas: implications of smectite diagenesis on sandstone cementation. Journal of Sedimentary Research 49, p. 55 - 70.

Bouch, J. (2006). Development of capability in the SEM-CL of carbonates. Technical Report. British Geological Survey, p. 17.

Braithwaite, C. J. R. (1991). Dolomites, a review of origins, geometry and textures. Earth and Environmental Science Transactions of the Royal Society of Edinburgh 82, p. 99-112.

Bromley, R. G. & Ekdale, A. (1984). Chondrites: a trace fossil indicator of anoxia in sediments. Science 224, p. 872-874.

Budd, D. (1997). Cenozoic dolomites of carbonate islands: their attributes and origin. Earth-Science Reviews 42, p. 1-47.

Choquette, P. W., Cox, A. & Meyers, W. J. (1992). Characteristics, distribution and origin of porosity in shelf dolostones: Burlington-Keokuk Formation (Mississippian), US mid-continent. Journal of Sedimentary Research 62, p. 167-189.

Choquette, P. W. & Hiatt, E. E. (2008). Shallow-burial dolomite cement: a major component of many ancient sucrosic dolomites. Sedimentology 55, p. 423-460.

Choquette, P. W. & Pray, L. C. (1970). Geologic nomenclature and classification of porosity in sedimentary carbonates. AAPG Bulletin 54, p. 207-250.

Christiansen, E. (1967). Collapse structures near Saskatoon, Saskatchewan, Canada. Canadian Journal of Earth Sciences 4, p. 757-767.

Chuhan, F. A., Kjeldstad, A., Bjørlykke, K. & Høeg, K. (2003). Experimental compression of loose sands: relevance to porosity reduction during burial in sedimentary basins. Canadian Geotechnical Journal 40, p. 995-1011.

Curtis, M. E., Ambrose, R. J. & Sondergeld, C. H. (2010). Structural characterization of gas shales on the micro-and nano-scales. Canadian Unconventional Resources and International Petroleum Conference: Society of Petroleum Engineers. SPE Paper 137693, p.15.

Davies, D. K. & Almon, W. R. (1981). The Role of Diagenesis in Successful Formation Interpretation, Well Production, Stimulation, And Enhanced Recovery. Society of Petroleum Engineers, p. 175 - 176.

Doyen, P. M. (1988). Porosity from seismic data: A geostatistical approach. Geophysics 53, p. 1263-1275.

Ducharme, D. & Murray, D. L. (1980). Heavy oil occurrences of the Cactus Lake area Saskatchewan. Saskatchewan Geological Society Special Publication Number 5, p. 64 – 95.

Ehrenberg, S. (1990). Relationship Between Diagenesis and Reservoir Quality in Sandstones of the Garn Formation, Haltenbanken, Mid-Norwegian Continental Shelf (1). AAPG Bulletin 74, p. 1538-1558.

Ehrenberg, S. (1993). Preservation of anomalously high porosity in deeply buried sandstones by grain-coating chlorite: examples from the Norwegian continental shelf. AAPG Bulletin 77, p. 1260-1286.

Ehrenberg S.N. & Nadeau P.H. (1989) Formation of diagenetic illite in sandstones of the Garn formation, Haltenbanken area, mid-Norwegian continental shelf. Clay Minerals, 24, p. 233–253.

Ehrenberg, S. & Nadeau, P. (2005). Sandstone vs. carbonate petroleum reservoirs: A global perspective on porosity-depth and porosity-permeability relationships. AAPG Bulletin 89, p. 435-445.

Evans, J., Hogg, A. J., Hopkins, M. S. & Howarth, R. J. (1994). Quantification of quartz cements using combined SEM, CL, and image analysis. Journal of Sedimentary Research 64, p. 334-338.

Feazel, C. & Schatzinger, R. (1983). Prevention of carbonate cementation in petroleum reservoirs. Society of Economic Paleontologists and Mineralogists 67, p. 97 - 106.

Ferdous, H., (2001). Regional sedimentology and diagenesis of the Middle Bakken Member: implications for reservoir rock distribution in southern Saskatchewan. Unpublished thesis, Department of Geological Sciences: University of Saskatchewan, p. 467.

Folk, R. L. (1980). Petrology of sedimentary rocks. Hemphill Publishing Company.

Freer, R. (1981). Diffusion in silicate minerals and glasses: a data digest and guide to the literature. Contributions to Mineralogy and Petrology 76, p. 440-454.

Friedman, G. M. (1965). Terminology of crystallization textures and fabrics in sedimentary rocks. Journal of Sedimentary Research 35, p. 643-655.

Galloway, W. E. (1979). Diagenetic Control of Reservoir Quality in Arc-Derived Sandstones Implications for Petroleum Exploration: SEPM Special Publication 26, p. 251-262.

Giles, M. R. & Marshall, J. D. (1986). Constraints on the development of secondary porosity in the subsurface: re-evaluation of processes. Marine and Petroleum Geology 3, p. 243-255.

Gluyas, J., Robinson, A., Emery, D., Grant, S. & Oxtoby, N. (1993). The link between petroleum emplacement and sandstone cementation. Geological Society, London, Petroleum Geology Conference series: Geological Society of London, p. 1395-1402.

Götze, J., Plötze, M. & Habermann, D. (2001). Origin, spectral characteristics and practical applications of the cathodoluminescence (CL) of quartz–a review. Mineralogy and Petrology 71, p. 225-250.

Gregg, J. M. & Sibley, D. F. (1984). Epigenetic dolomitization and the origin of xenotopic dolomite texture. Journal of Sedimentary Research 54, p. 908-931.

Hogg, A., Sellier, E. & Jourdan, A. (1992). Cathodoluminescence of quartz cements in Brent group sandstones, Alwyn South, UK North Sea. Geological Society, London, Special Publications 61, p. 421-440.

Holland Jr, F., Hayes, M., Thrasher, L. & Huber, T. (1987). Summary of the biostratigraphy of the Bakken Formation (Devonian and Mississippian) in the Williston basin, North Dakota. 5th Williston Basin Symposium, p. 68 - 76.

Houseknecht, D. W. (1987). Assessing the relative importance of compaction processes and cementation to reduction of porosity in sandstones. AAPG Bulletin 71, p. 633-642.

Hower, J. & Mowatt, T. C. (1966). The mineralogy of illites and mixed-layer illite/montmorillonites. American Mineralogist 51, p. 825-854.

Huggett, J. (1996). Aluminosilicate diagenesis in a Tertiary sandstone-mudrock sequence from the central North Sea, UK. Clay minerals 31, p. 523-536.

Jarvie, D. M. (2012). Shale resource systems for oil and gas. Part 2—Shale-oil resource systems. AAPG Memoir 97, p. 89 - 119.

Jeans, C., Mitchell, J., Scherer, M. & Fishers, M. (1994). Origin of the Permo-Triassic clay mica. Clay minerals 29, p. 575-589.

Karasinski, D. R. (2006). Sedimentology and Hydrocarbon Potential of the Devonian Three Forks and Mississippian Bakken Formations, Sinclair Area, Southeast Saskatchewan-southwest Manitoba: University of Manitoba (Canada).

Keller, W. (1970). Environmental aspects of clay minerals. Journal of Sedimentary Research 40, p. 788-813.

Kortenski, J. & Kostova, I. (1996). Occurrence and morphology of pyrite in Bulgarian coals. International Journal of Coal Geology 29, p. 273-290.

Kuhn, P. P. (2013). Integrated geochemistry and basin modeling study of the Bakken Formation, Williston Basin. PhD Thesis. Technical University of Berlin, p. 241.

Kuhn, P. P., di Primio, R., Hill, R., Lawrence, J. R. & Horsfield, B. (2012). Three-dimensional modeling study of the low-permeability petroleum system of the Bakken Formation. AAPG Bulletin 96, p. 1867-1897.

Kupecz, J. & Land, L. (1994). Progressive recrystallization and stabilization of early-stage dolomite: Lower Ordovician Ellenburger Group, west Texas. Dolomites: A volume in Honour of Dolomieu. B. Purser, M., Tucker, D. Zenger (eds.). International Association of Sedimentology Special Publication, p. 255-279.

Kurtoglu, B., Kazemi, H., Rosen, R., Mickelson, W. & Kosanke, T. (2014). A Rock and Fluid Study of Middle Bakken Formation: Key to Enhanced Oil Recovery. SPE/CSUR Unconventional Resources Conference - Canada: Society of Petroleum Engineers.

Kyser, T. K., James, N. P. & Bone, Y. (2002). Shallow burial dolomitization and dedolomitization of Cenozoic cool-water limestones, southern Australia: geochemistry and origin. Journal of Sedimentary Research 72, p. 146-157.

Land, L.S., 1967. Diagenesis of skeletal carbonates. Journal of Sedimentary Research, 37(3), p. 914-930.

Land, L. & Dutton, S. (1978). Cementation of a Pennsylvanian deltaic sandstone: isotopic data. Journal of Sedimentary Research 48, p. 1167-1176.

Land, L. S. & Milliken, K. L. (1981). Feldspar diagenesis in the Frio Formation, Brazoria County, Texas Gulf Coast. Geology 9, p. 314-318.

Landes, K. K. (1946). Porosity through dolomitization. AAPG Bulletin 30, p. 305-318.

Lanson, B., Beaufort, D., Berger, G., Baradat, J. & Lacharpagne, J.-C. (1996). Illitization of diagenetic kaolinite-to-dickite conversion series: Late-stage diagenesis of the Lower Permian Rotliegend sandstone reservoir, offshore of the Netherlands. Journal of Sedimentary Research 66, p. 501-518.

Lanson, B., Beaufort, D., Berger, G., Bauer, A., Cassagnabere, A. & Meunier, A. (2002). Authigenic kaolin and illitic minerals during burial diagenesis of sandstones: a review. Clay minerals 37, p. 1-22.

Last, W. & Edwards, W. (1991). Petrology of the Middle Bakken Member in the Daly Field, southwestern Manitoba. Williston Basin Symposium, p. 64-69.

Lázaro, B. B. (2007). Illitization processes: Series of dioctahedral clays and mechanisms of formation. Diagenesis and Low-Temperature Metamorphism. Theory, Methods and Regional Aspects. Seminarios SEM 3, p. 31-39.

Lee, M. R. (2000). Imaging of calcite by optical and SEM cathodoluminescence. Microscopy and Analysis 70, p. 15-16.

Leveille, G. P., Primmer, T. J., Dudley, G., Ellis, D. & Allinson, G. J. (1997). Diagenetic controls on reservoir quality in Permian Rotliegendes sandstones, Jupiter Fields area, southern North Sea. Geological Society, London, Special Publications 123, p. 105-122.

Li, H., Dawson, M., Hart, B. & Radjef, E. (2015). Characterizing the Middle Bakken: Laboratory Measurement of Middle Bakken Properties. Unconventional Resources Technology Conference (URTEC).

Loucks, R. G., Dodge, M. M. & Galloway, W. E. (1984). Regional controls on diagenesis and reservoir quality in lower Tertiary sandstones along the Texas Gulf Coast: Part 1. Concepts and principles. Clastic Diagenesis. AAPG Memoir, p. 15 - 45.

Lucia, F. J. (1962). Diagenesis of a crinoidal sediment. Journal of Sedimentary Research 32, p. 848-865.

Lundegard, P. D. (1992). Sandstone Porosity Loss-A "Big Picture" View of the Importance of Compaction. Journal of Sedimentary Research 62, p. 250 - 260.

Lynch, F. L., Mack, L. E. & Land, L. S. (1997). Burial diagenesis of illite/smectite in shales and the origins of authigenic quartz and secondary porosity in sandstones. Geochimica et Cosmochimica Acta 61, p. 1995-2006.

Maast, T. E., Jahren, J. & Bjorlykke, K. (2011). Diagenetic controls on reservoir quality in Middle to Upper Jurassic sandstones in the South Viking Graben, North Sea. AAPG Bulletin 95, p. 1937-1958.

Mackenzie, F. T. (2005). Sediments, diagenesis, and sedimentary rocks. Treatise on Geochemistry. Elsevier, p. 446.

Macquaker, J. H., Taylor, K. G. & Gawthorpe, R. L. (2007). High-resolution facies analyses of mudstones: implications for paleoenvironmental and sequence stratigraphic interpretations of offshore ancient mud-dominated successions. Journal of Sedimentary Research 77, p. 324-339.

Marshall, D. J. & Mariano, A. N. (1988). Cathodoluminescence of geological materials, Taylor & Francis, p. 146.

Matter, A. & Ramseyer, K. (1985). Cathodoluminescence microscopy as a tool for provenance studies of sandstones. Provenance of arenites: Springer, p. 191-211.

Mattes, B. W., and E. W. Mountjoy, (1980). Burial dolomitization of the Upper Devonian Miette Buildup, Jasper National Park, Alberta, in Concepts and models of dolomitization: SEPM Special Publication 28, p. 259-297.

Mazzullo, S. (1992). Geochemical and neomorphic alteration of dolomite: a review. Carbonates and evaporites 7, p. 21-37.

McBride, E. F. (1989). Quartz cement in sandstones: a review. Earth-Science Reviews 26, p. 69-112.

McCabe, H. R. (1959). Mississippian stratigraphy of Manitoba: Manitoba: Department of Mines and Natural Resources. Mines Branch, p. 1 - 58.

Meissner, F. (1978). Petroleum geology of the Bakken Formation Williston basin, North Dakota and Montana. The economic geology of the Williston basin: Montana Geological Society 24th Annual Conference. Williston Basin Symposium, p. 207 - 227.

Meissner, F. F. (1991). Petroleum Geology of the Bakken Formation Williston Basin, North Dakota and Montana. Montana Geological Society. Guidebook to Geology and Horizontal Drilling of the Bakken Formation, p. 19 – 42.

Meunier, A., Velde, B. & Velde, B. (2004). Illite: Origins, evolution and metamorphism: Springer, p. 288.

Mohamed, T.I., 2015. Sequence Stratigraphy and Provenance of the Bakken Formation in Southeast Alberta and Southwest Saskatchewan (Doctoral dissertation, University of Calgary).

Moore, C. H. (2001). Carbonate Reservoirs: Porosity, Evolution & Diagenesis in a sequence stratigraphic framework: Elsevier, p. 460.

Moore, C. H. & Druckman, Y. (1981). Burial diagenesis and porosity evolution, upper Jurassic Smackover, Arkansas and Louisiana. AAPG Bulletin 65, p. 597-628.

Morad, S. (1988). Diagenesis of titaniferous minerals in Jurassic sandstones from the Norwegian Sea. Sedimentary Geology 57, p. 17-40.

Morad, S. & Aldahan, A. A. (1982). Authigenesis of titanium minerals in two Proterozoic sedimentary rocks from southern and central Sweden. Journal of Sedimentary Research 52, p. 1295-1305.

Morad, S., Bergan, M., Knarud, R. & Nystuen, J. P. (1990). Albitization of detrital plagioclase in Triassic reservoir sandstones from the Snorre Field, Norwegian North Sea. Journal of Sedimentary Research 60, p. 411-425.

Murray, R. C. (1960). Origin of porosity in carbonate rocks. Journal of Sedimentary Research 30, p. 59 – 84.

Nelson, P. H. (2009). Pore-throat sizes in sandstones, tight sandstones, and shales. AAPG Bulletin 93, p. 329-340.

Nichols, G. (2009). Sedimentology and stratigraphy: John Wiley & Sons.

Nordquist, J. W. (1953). Mississippian stratigraphy of northern Montana. Billings Geological Society: Guidebook: Montana Geological Society, p. 68-82.

Owen, M. R. (1991). Application of cathodoluminescence to sandstone provenance. Society for Sedimentary Geology, p. 67 - 75.

Pallatt, N., Wilson, J. & McHardy, B. (1984). The relationship between permeability and the morphology of diagenetic illite in reservoir rocks. Journal of petroleum technology 36, p. 2,225-2,227.

Pe-Piper, G., Karim, A. & Piper, D. J. (2011). Authigenesis of titania minerals and the mobility of Ti: new evidence from pro-deltaic sandstones, cretaceous scotian basin, Canada. Journal of Sedimentary Research 81, p. 762-773.

Pitman, J. K., Price, L. C. & LeFever, J. A. (2001). Diagenesis and fracture development in the Bakken Formation, Williston Basin: Implications for reservoir quality in the middle member: US Department of the Interior, US Geological Survey Professional Paper 1653.

Pittman, E.D. and Larese, R.E., 1987. Experimental compaction of lithic sands. In SEPM Annual Midyear Meeting 4, p. 66.

Prozorovich, G. (1970). Determination of the time of oil and gas accumulation by epigenesis studies. Sedimentology 15, p. 41-52.

Purser, B. H. (1978). Early diagenesis and the preservation of porosity in Jurassic limestones. Journal of Petroleum Geology 1, p. 83-94.

Randazzo, A. F. & Zachos, L. G. (1984). Classification and description of dolomitic fabrics of rocks from the Floridan aquifer, USA. Sedimentary Geology 37, p. 151-162.

Reed, R. M. & Milliken, K. L. (2003). How to overcome imaging problems associated with carbonate minerals on SEM-based cathodoluminescence systems. Journal of Sedimentary Research 73, p. 328-332.

Reynolds, R. L. & Goldhaber, M. B. (1978). Origin of a South Texas roll-type uranium deposit; I, Alteration of iron-titanium oxide minerals. Economic Geology 73, p. 1677-1689.

Richter, D., Götte, T., Götze, J. & Neuser, R. (2003). Progress in application of cathodoluminescence (CL) in sedimentary petrology. Mineralogy and Petrology 79, p. 127-166.

Robinson, A. & Gluyas, J. (1992). Duration of quartz cementation in sandstones, North Sea and Haltenbanken Basins. Marine and Petroleum Geology 9, p. 324-327.

Saidian, M. & Prasad, M. (2015). Effect of mineralogy on nuclear magnetic resonance surface relaxivity: A case study of Middle Bakken and Three Forks formations. Fuel 161, p. 197-206.

Saigal, G. C., Morad, S., Bjorlykke, K., Egeberg, P. K. & Aagaard, P. (1988). Diagenetic albitization of detrital K-feldspar in Jurassic, Lower Cretaceous, and Tertiary clastic reservoir rocks from offshore Norway, I. Textures and origin. Journal of Sedimentary Research 58, p. 1003-1013.

Schmid, S., Worden, R. & Fisher, Q. (2004). Diagenesis and reservoir quality of the Sherwood Sandstone (Triassic), Corrib Field, Slyne Basin, west of Ireland. Marine and Petroleum Geology 21, p. 299-315.

Scholle, P. A. & Ulmer-Scholle, D. S. (2003). A Color Guide to the Petrography of Carbonate Rocks: Grains, Textures, Porosity, Diagenesis, AAPG Memoir 77: AAPG.

Sibley, D. F. (1982). The origin of common dolomite fabrics: clues from the Pliocene. Journal of Sedimentary Research 52, p. 1087-1100.

Sibley, D. F. & Gregg, J. M. (1987). Classification of dolomite rock textures. Journal of Sedimentary Research 57, p. 967-975.

Siebert, R., Moncure, G. & Lahann, R. (1984). A theory of framework grain dissolution in sandstones: Part 2. Aspects of porosity modification. p. 163 - 175.

Simenson, A. (2010). Depositional facies and petrophysical analysis of the Bakken Formation. Parshall Field, Mountrail County, North Dakota: Master's Thesis, Colorado School of Mines, Golden, Colorado.

Sippel, R. F. (1968). Sandstone petrology, evidence from luminescence petrography. Journal of Sedimentary Research 38, p. 530-554

Smith, G. (1985). Geology of the deep Tuscaloosa (Upper Cretaceous) gas trend in Louisiana. Habitat of Oil and Gas in the Gulf Coast: Proc. of the Fourth Annual Research Conf., Gulf Coast Section Society of Economic Paleontologists and Mineralogists Foundation, p. 153-190.

Smith, M. G. & Bustin, R. M. (1996). Lithofacies and paleoenvironments of the Upper Devonian and Lower Mississippian Bakken Formation, Williston Basin. Bulletin of canadian petroleum geology 44, p. 495-507.

Stalder, P. (1973). Influence of crystallographic habit and aggregate structure of authigenic clay minerals on sandstone permeability. Geologie en Mijnbouw 52, p. 217-220.

Staruiala, A. (2013). Diagenesis of the Bakken Formation, Southeastern Saskatchewan. Williston Basin Symposium. Twenty-first Williston Basin Petroleum Conference: Core Workshop Volume, p. 25-44.

Stone, W. N. S., R. (1996). Quantifying compaction, pressure solution and quartz cementation in moderately-and deeply-buried quartzose sandstones from the Greater Green River Basin, Wyoming. Siliciclastic diagenesis and fluid flow: concepts and applications: SEPM Special Publication 55, p. 129‑150.

Summa, L. L. (1995). Diagenesis and reservoir quality prediction. Reviews of Geophysics 33, p. 87-94.

Sun, S. Q. (1995). Dolomite reservoirs: porosity evolution and reservoir characteristics. AAPG Bulletin 79, p. 186-204.

Surdam, R., Crossey, L. J., Eglinton, G., Durand, B., Pigott, J., Raiswell, R. & Berner, R. (1985). Organic-inorganic reactions during progressive burial: Key to porosity and permeability enhancement and preservation [and discussion]. Philosophical Transactions of the Royal Society of London A: Mathematical, Physical and Engineering Sciences 315, p. 135-156.

Taylor, J. M. (1950). Pore-space reduction in sandstones. AAPG Bulletin 34, p. 701-716.

Taylor, T. R., Giles, M. R., Hathon, L. A., Diggs, T. N., Braunsdorf, N. R., Birbiglia, G. V., Kittridge, M. G., Macaulay, C. I. & Espejo, I. S. (2010). Sandstone diagenesis and reservoir quality prediction: Models, myths, and reality. AAPG Bulletin 94, p. 1093-1132.

Vagle, G. B., Hurst, A. & Dypvik, H. (1994). Origin of quartz cements in some sandstones from the Jurassic of the Inner Moray Firth (UK). Sedimentology 41, p. 363-377.

Walderhaug, O. (1990). A fluid inclusion study of quartz-cemented sandstones from offshore mid-Norway--possible evidence for continued quartz cementation during oil emplacement. Journal of Sedimentary Research 60, p. 203-210.

Walderhaug, O. (1994). Precipitation rates for quartz cement in sandstones determined by fluid-inclusion micro-thermometry and temperature-history modelling. Journal of Sedimentary Research 64, p. 324 - 333.

Walderhaug, O. (1996). Kinetic modeling of quartz cementation and porosity loss in deeply buried sandstone reservoirs. AAPG Bulletin 80, p. 731-745.

Walker, T. R. (1984). 1984 SEPM presidential address: diagenetic albitization of potassium feldspar in arkosic sandstones. Journal of Sedimentary Research 54.

Warren, J. (2000). Dolomite: occurrence, evolution and economically important associations. Earth-Science Reviews 52, p. 1-81.

Webster, R. L. (1984). Petroleum source rocks and stratigraphy of the Bakken Formation in North Dakota. Rocky Mountain Association of Geologists, p. 490-507.

Weyl, P. K. (1960). Porosity through dolomitization: conservation-of-mass requirements. Journal of Sedimentary Research 30 (1), p. 85-90.

Wilkinson, M., Haszeldine, R. & Fallick, A. (2014). Authigenic illite within northern and central North Sea oilfield sandstones: evidence for post-growth alteration. Clay minerals 49, p. 229-246.

Wilson, M. D. & Pittman, E. D. (1977). Authigenic clays in sandstones: recognition and influence on reservoir properties and paleoenvironmental analysis. Journal of Sedimentary Research 47, p. 3-31.

Worden, R. & Burley, S. (2003). Sandstone diagenesis: the evolution of sand to stone. Sandstone Diagenesis: Recent and Ancient 4, p. 3-44.

Worden, R. & Morad, S. (2000). Quartz cementation in oil field sandstones: a review of the key controversies. Quartz cementation in sandstones, Special publications of international association of sedimentologists 29, p. 1-20.

Worden, R. & Morad, S. (2003). Clay minerals in sandstones: controls on formation, distribution and evolution. Clay cements in sandstones: International Association of Sedimentologists Special Publication 34, p. 3‑41.

Worden, R. H., Oxtoby, N. H. & Smalley, P. C. (1998). Can oil emplacement prevent quartz cementation in sandstones? Petroleum Geoscience 4, p. 129-137.

Xiong, D., Azmy, K. & Blamey, N. J. (2016). Diagenesis and origin of calcite cement in the Flemish Pass Basin sandstone reservoir (Upper Jurassic): Implications for porosity development. Marine and Petroleum Geology 70, p. 93-118.

Yao, J., Deng, X., Zhao, Y., Han, T., Chu, M. & Pang, J. (2013). Characteristics of tight oil in Triassic Yanchang Formation, Ordos Basin. Petroleum Exploration and Development 40, p. 161-169.

Yurkova, R. M. (1970). Comparison of post-sedimentary alterations of oil, gas and water-bearing rocks. Sedimentology 15, p. 53-68.

Zinkernagel, U. (1978). Cathodoluminescence of quartz and its application to sandstone petrology. Contributions to Sedimentology 8, p. 1-69.

Chapter 4

Pore Systems

Introduction

The Bakken has previously been described as one of the most prolific low-permeability hydrocarbon reservoirs in North America, with a recovery factor of 8-12% of the oil in place (Kurtoglu et al., 2014), which is in contrast to typical hydrocarbon recovery factors of between 35-45% (Tzimas et al., 2005). The Bakken petroleum system has an estimated total oil in place of between 100-900 billion barrels, worth an estimated 4,000-36,000 billion dollars. Clearly small percentage increases in the recovery of hydrocarbons, will have a significant value. Hydrocarbon plays with low permeability such as the Bakken are referred to as 'tight'.

Tight formations are routinely split into 'tight gas' and 'tight oil' formations. The Bakken is predominantly treated as the latter. Tight formations require stimulation using techniques such as hydraulic fracturing, fluid injection or directional drilling to reach economic production rates (Medeiros et al., 2007). Production strategies can be improved with better understanding of the petrophysical and fluid transport properties of the lithology (Amann-Hildenbrand et al., 2015). Since the early 2000's, research into tight-oil has gathered pace, driven largely due to high oil prices (e.g. Shanley et al., 2004; Rushing et al., 2008; Tobin et al., 2010; Clarkson et al., 2013).

In order to do this several studies have characterised the pore system in order to understand the barriers to flow in these formations. Pore system studies can be divided into two broad groups. Some researchers have focussed on the estimation of porosity using mercury intrusion and gas sorption analyses (e.g. Chalmers and Bustin, 2007; Bustin et al., 2008; Ross and Bustin, 2009; Chalmers et al., 2012; Kuila and Prasad, 2013; Robinet et al., 2015), whereas others have utilised predominantly microscopic techniques to resolve the microstructure of tight rock formations (Fishman et al., 2013; Loucks et al., 2009; Milner et al., 2010; Schieber, 2011; Slatt and O'Brien, 2011; Loucks et al., 2012; Curtis et al., 2013; Milliken et al., 2013).

More recently workers have suggested that, in order to gain a better understanding of the microstructure of complex tight rocks, the combined application of these techniques is required (Bustin et al., 2008; Chalmers and Bustin, 2012; Chalmers et al., 2012; Clarkson et al., 2013; Klaver et al., 2015). In doing so workers have recognised these different techniques often lead to differences in the results of measurements of the same property;

however, such variations can, in themselves provide valuable information (Athy, 1930; Cepuritis et al., 2014). Using porosity data, many studies have linked porosity to the abundance of specific minerals (e.g. Dahlberg & Fitz, 1988; Ramm & Bjørlykke, 1994; Ehrenberg and Nadeau, 2005; Taylor et al., 2010). It is hoped by doing so; future workers will be able to identify zones of good reservoir quality at the reservoir scale.

Previous work to specifically characterise the microstructure of the Bakken has been limited. Porosity measurements have however been made on samples at both the macro-scale (decimetres) from drill stem testing (DST) and the micro-scale (millimetres) by laboratory measurement (Meissner, 1978; Ducharme & Murray, 1980; Webster, 1984; Kent, 1987, Pitman et al., 2001). The most recent work on the middle Bakken was conducted by Li et al., (2015). In their study they attempted to link pore system characteristics to mineralogy and facies, as a mechanism to upscale their findings at the pore-scale. They showed with increasing calcite content there was a reduction in porosity and permeability.

From our assessment of diagenetic processes in the middle Bakken (Chapter 3), it is evident that authigenic minerals have changed the pore system; the aim of this chapter is to better understand how it has changed and what was the principle control on that change. In this study we have characterised the pore system by the size, distribution, pore-mineral relationships and connectivity, in order to relate this to the permeability and therefore the producibility of the Bakken Formation.

Background

Pore Morphology: Definitions

A traditional definition of a pore might describe it as a void space with a pore throat being the narrow region which forms the connection between two joined pores (Baldwin et al., 1996; Nelson, 2009). In a study of pore systems affected by diagenesis, we differentiate primary porosity as that which has formed pre or syn-deposition and secondary porosity as that which has formed post-deposition. At a smaller scale, pores can be classified by their connectivity and shape (Figure 4.1) (Rouquerol et al., 1994). In this scheme, closed pores are those which are completely isolated from the surrounding environment, these

pores make up the intra-granular porosity (Figure 4.1g). Pores which are connected by one throat include ink-bottle and blind pores.

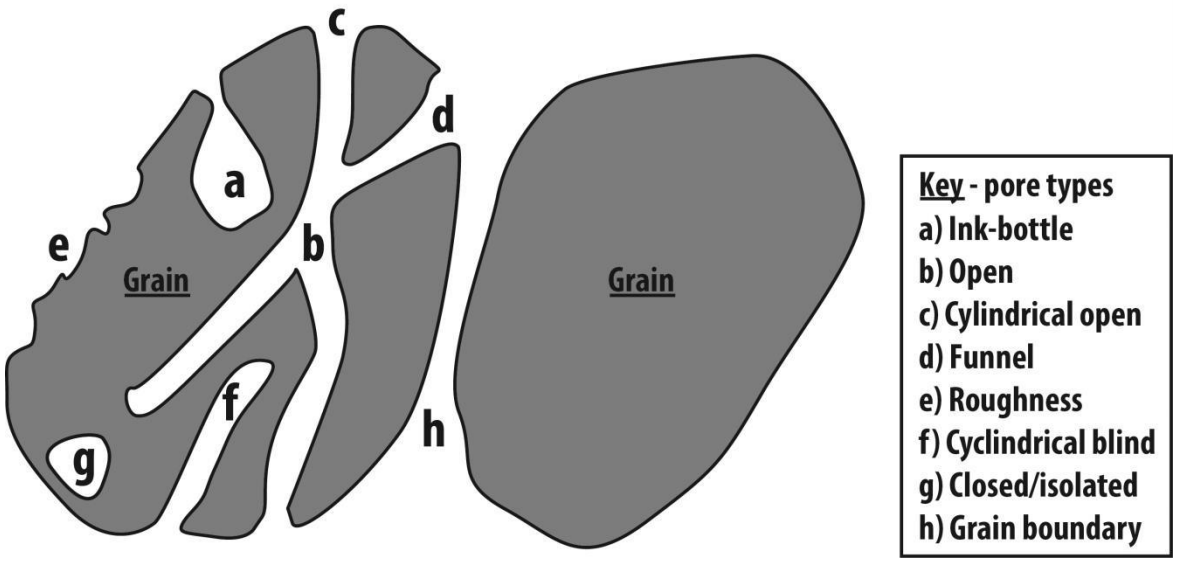

Figure 4.1 - Schematic of pore system components for qualitative descriptions. After Rouquerol et al., 1994.

Pores can be classified based on both the spatial relationships with respect to rock grains and their formation mechanism (Choquette and Pray, 1970). In this scheme we can consider pores as intragranular (within a grain), intergranular (between grains), dissolution (within a grain but formed by dissolution of the grain), moldic, fenestral, fracture, and vuggy.

Pore Width (nm)	Classification	Sub-classification
<0.7	Micropores	Ultramicropores
0.7 - 1.4		Micropores
1.4 - 2.0		Supermicropores
2 - 50	Mesopores	-
> 50	Macropores	-

Table 4.1 - IUPAC pore classification. After Sing et al., 1982 and Rouquerol et al., 1994.

Pores can also be categorised based on their size. A standard method for this is that proposed by the International Union of Pure and Applied Chemistry (IUPAC), Table 4.1 (Sing et al., 1982 and Rouquerol et al., 1994). Solely using pure carbonate or sandstone pore system descriptors is inappropriate in a mixed, carbonate siltstone sample such as

this. As a result, in this study we use a combination of these descriptors to most effectively categorise the different pores observed in the middle Bakken.

In sedimentary rocks pores commonly occur across the full range of sizes outlined in the IUPAC classification scheme. This makes measuring the pore size distribution particularly challenging. To do this, a range of different techniques are implemented. The limits of resolution for each technique are compared in Figure 4.2.

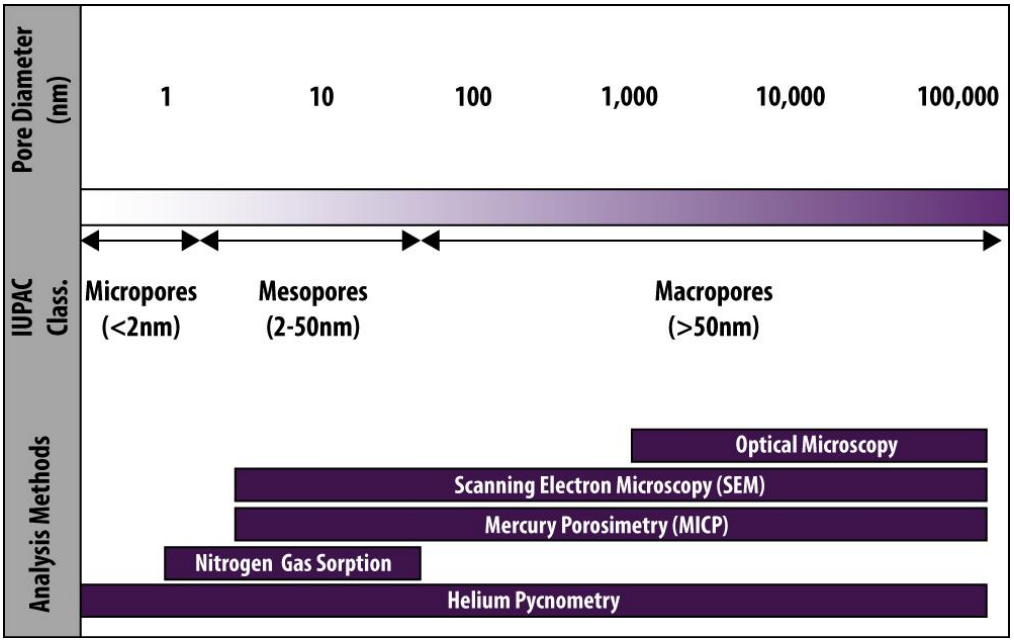

Figure 4.2 – Comparison of pore analysis techniques and their respective resolution. After Anovitz & Cole (2015).

Methods

Samples

The samples of this study were obtained from the Bakken-Sorrenson core drilled in August, 2013 by Brigham Oil and Gas. The samples were initially plugged at specific intervals and double wrapped in plastic film and aluminium foil.

For this study, 32 samples were obtained from the middle Bakken section representing the full range of different facies identified and discussed in Chapter 3. For each sample both a thin-section and a ~1 cm cube was cut. The thin-section was taken from the edge of the cube, perpendicular to bedding. Five of these samples were blue dye impregnated in order to highlight porosity.

Facies	Depth of Facies in Middle Bakken (m)	Description	Representative sample and (depth m)
B	3198.88 - 3206.74	Bioturbated, argillaceous, calcareous, very fine-grained, siltstone/sandstone.	**1-116B** (3206.56)
$D_{(2)}$	3184.55 - 3188.21	Fine-grained sandstone with thin discontinuous shale laminations. Low angle bedding, planar to slightly undulose, cross-laminated.	**2_iiA** (3185.62)
E	3182.11 - 3184.55	Finely Inter-Laminated, bioturbated, dolomitic-mudstone and dolomitic siltstone/sandstone.	**1-37B** (3182.48)
Grad	3197.05 - 3198.88	Grading of material from upper facies into lower.	**11_iiA** (3201.95)

Table 4.2 – Middle Bakken depositional facies descriptions with corresponding selected representative samples. Depths are given in cored measurements. Facies names & description after Karasinski (2006).

From petrographic analysis, a smaller subset of 5 samples was then identified to represent the 5 main facies observed in the middle Bakken unit (Table 4.2). A 1 mm slice was cut from the corresponding sample cubes. This was used for used BIB-SEM analyses.

Wireline Logs: Porosity

In order to obtain a reservoir scale perspective of porosity variations with depth through the middle Bakken, porosity was determined from density and neutron porosity wireline logs. Density log signal is a function of the density of the rock, pore space and pore fluid. To determine porosity from a standard density log we used an average grain density from measurements of 21 samples from the full vertical section of the middle Bakken, which gave a grain density value of 2.74 g / cm^3 and pore fluid was assumed to have an average density of 1 g cm^3 (Ellis & Singer, 2007).

Petrography

In order characterise the lithology of the samples, extensive petrographic analysis was conducted using a combination of transmitted light microscopy, scanning electron microscopy (SEM) and x-ray diffraction (XRD). These techniques and the results of the petrographic analysis are discussed in detail in Chapter 3.

In order to quantify the effect of cementation and compaction on the middle Bakken, we used the point counting method devised by Lundegard (1992). Minerals and pores were differentiated and counted on 15 polished thin-sections. Carbonate minerals were discriminated into bioclasts and different textural cement phases (see Chapter 3).

Lundegard (1992) showed that porosity loss due to compaction and cementation can be calculated from the initial (unconsolidated) porosity (P_i), total optical porosity (P_O) and volume-percent pore-filling cement (C). We assumed the depositional porosity to be 45% by comparing the mineralogical and textural characteristics of the middle Bakken samples with samples analysed by Chuhan (2003). The porosity loss due to compaction (COPL) was determined using Equation 4.1 and the porosity loss due to cementation (CEPL) was determined using Equation 4.2.

$$COPL = P_i - \left(\frac{(100 - P_i)\ x\ P_{mc}}{100 - P_{mc}}\right)$$

Equation 4.1 - Method for determining the porosity loss due to compaction (COPL) where P_i is initial porosity, P_{mc} is the minus cement porosity [sum of the optical porosity (P_o) and pore-filling cement (P_c)], Lundegard (1992).

$$CEPL = (P_i - COPL)\left(\frac{C}{P_{mc}}\right)$$

Equation 4.2 - Method for determining the porosity loss due to cementation (CEPL) where P_i is initial porosity, P_{mc} is the minus cement porosity [sum of the optical porosity (P_o) and pore-filling cement (P_c)], Lundegard (1992).

This method has several potential sources of error, the first of which is the estimation of the initial porosity of the sand. If the estimate of initial porosity is too high, it will result in an over-estimation of the effect of compaction. In an effort to avoid this problem we chose an experimentally derived value of initial porosity for sandstone which is texturally and compositionally similar to that of the middle Bakken (Lundegard, 1992). However other workers have identified that irrespective of what value chosen, using only one value is a compromise as depositional porosity is a variable, and would be particularly variable in a

heterogeneous unit such as the middle Bakken. It has also been shown there is notable operator variability in point counting (Solomon, 1963; Demirmen, 1971; Lundegard, 1990).

Helium Porosity

Helium gas expansion porosimetry is a method used to accurately measure the skeletal volume of a sample which can be used to calculate the total effective porosity of the sample if the bulk volume of the sample is known. Both the sample cell and a reference cell are filled with a known volume of helium; the difference in pressure is due to the difference in the volume between the two cells created by the presence of sample. The pressure difference is used to determine the skeletal volume of the sample. Prior to analysis the sample was dried in an oven for 12 hours at 105°C to remove excess water. The samples were then weighed and placed in a Micromeritics AccuPyc II 1340 gas displacement pycnometer for the grain volume to be determined. The envelope volume was then measured using a vernier caliper. The connected pore volume/connected porosity is the difference between the skeletal volume and the envelope volume. The precision was calculated from 10 repeat measurements of bulk density of the same sample. The average precision was determined to be 0.11% over the whole sample set.

MICP

Mercury Injection Capillary Pressure (MICP) analysis is the standard method of determining the pore throat size distribution in a rock from the micron scale to the nanometer scale (Josh et al., 2012). It was first introduced by Ritter and Drake (1945) to measure macro-pore size distributions. Mercury intrusion data was collected in a Micromeritics Corporation, Autopore II 9220 Porosimeter, at Newcastle University. Each sample was loaded with mercury at 56 standard pressure steps of between 3-39,000 psi. The mercury density porosity was also obtained from the mass of the sample and the volume of the sample, as determined by the difference between the total volume of the mercury penetrometer and that filled by mercury at 1 atm. This is thought to be more accurate than the sample volume measured by Vernier calliper.

In this study, the minimum pore throat size that was intruded by mercury was 5.6 nm. This means that all smaller pores; pores which are only accessible through throats <5.6 nm and

blind pores were not analysed by this technique (Bustin et al., 2008). Whilst the minimum pore throat size is defined, the upper limit was also determined. Using these pressure steps no pore throats > 200 µm were analysed. At 200 µm (and above), it is thought the pores will fill very quickly under low pressures, within very few pressure steps and may lead to erroneous results. This point is described as the cut off radius (Gueven & Hicsasmaz, 2013).

To determine the true pore throat size distribution, from the onset of mercury intruding into the pore network, a cut-off radius was determined. By applying a cut-off radius, artefacts such as surface asperities on the chip surface are not included in the calculation of porosity, which it is thought gives a more accurate result.

Gas Sorption

Low pressure gas sorption was used to characterise the type and size of pore bodies. In total 14 samples were crushed using a percussion mortar & pestle and sieved to obtain a 0.5-1 mm size fraction. This size fraction is ~5-100 times larger than the grain size and ~50-100 times larger than the pore throats. The crushed sample was then air dried at 110°C (383K) for 12 hours. The samples were degassed to a constant weight (3-4 hours) at $<10^{-4}$ Pa and 110°C (383K). Low pressure gas sorption analysis was conducted on a Micromeritics ASAP 2020 to obtain information about micropores, mesopores and macropores. Nitrogen isotherms were obtained at 196°C (77 K), up to a pressure of 99 kPa. Liquid nitrogen was used to control the temperature during nitrogen isotherm acquisition. The Micromeritics Kaolinite standard was chosen to confirm the accuracy of the measurements. The standard has a single point specific surface area of 15.8 ± 0.9 m^2/g and a multipoint specific surface area of 16.1± 0.8m^2/g which was thought to be similar to anticipated values in the middle Bakken siltstones. The standard was run prior to commencing sample analysis.

Nitrogen adsorption isotherms were interpreted using the characterisation proposed by Sing, (1985). The Brunauer-Emmett-Teller (BET) model was used for surface area determination (Brunauer et al., 1938). In response to interpretation of pore size distributions from the isotherm, mesopore volume and pore size distributions between 1.7-300 nm were determined using the Barret, Joyner and Halenda (BJH) model (Barret et al., 1951).

BIB-SEM

To determine the morphology of individual pores and spatial pore-mineral relationships we used high resolution scanning electron microscopy. The resolution is limited here not by the instrument but by the quality of the sample surface, more precisely the variation in topography on the surface. Using white-light interferometry we found our samples typically had a surface roughness of 2-5 microns. This can be reduced and the image resolution increased to ~30 nm (depending on the magnification) through the use of broad ion beam Argon polishing (BIB-SEM). Another key advantage of BIB-SEM analysis is that the mineralogy and texture of the sample can also be determined enabling associations between pore morphology and mineralogy to be investigated. The BIB-SEM technique allows large enough areas (mm^2) of the sample to be analysed that the results are statistically representative.

A thin ~1.5 mm slice of the rock sample was taken from core sample plugs and cut into 5 mm^2 squares. The rock slices were then polished using 15 µm & 9.5 µm aluminium oxide powder. The square sample slice was then inserted into the sample chamber of a Gatan 691 Precision Ion Polishing System (PIPS). The sample was then polished with an argon broad ion beam for 12 hours using a rotation speed of 2.5 rpm, a voltage of 3.5 kV and a beam angle of 2. In total 4 samples were polished representing the main facies identified in the Bakken Formation. The samples were then coated with 30 nm of carbon to prevent charging during electron imaging.

BIB polished sections were imaged using a Hitachi SU-70 FEG SEM, primarily with a backscatter electron (BSE) detector for phase contrast imaging and also a secondary electron detector (SE) for investigation of surface topography. Ultra-high resolution images of the samples were obtained by working at distance of 12 mm and using a beam current of 46 µA with a low accelerating voltage of 10 kV. Information on the elemental composition of the areas imaged was obtained using an energy-dispersive x-ray spectroscopy detector (EDX) at 15 kV. Thin-section and palladium and platinum coated 'chip' samples were also imaged at 15 kV with a 15 mm working distance.

Using the EDX system, elemental mapping was conducted on the 4 BIB polished samples. The system was used to generate 0.6 mm^2 chemical composition maps of the samples. The maps were then segmented into individual mineral phases using aZtec micro-analysis software with the 'analyse phases' function. This feature groups individual pixels into phases based on the chemical composition. This software requires the use of limits for segmentation. We used a boundary tolerance of 3 and a grouping level of 2 which were determined iteratively. The boundary tolerance controls how a phase is defined at a boundary; a high boundary tolerance places pixels in the phase which most closely fits whereas a low tolerance will return pixels which do not fit the chemical composition as unknowns (black). The grouping level combines the phases which are chemically similar resulting in a more manageable data set which can then be further grouped into individual minerals by hand. The resulting phases were then interpreted, labelled and where appropriate, merged.

The representative elementary area of each sample EDX mineral phase map was determined using a modified box counting method (Houben et al., 2013). With this method, the region of interest was increased by 5 µm on each axis of the box (Figure 4.3). Continuous variations of any given property (in this case mineral abundance) can be established. The box counting method was implemented for the following minerals: quartz, alkali feldspar, potassium feldspar, calcite, dolomite and matrix (all other minerals including clays). In this study an area was deemed representative if the change in abundance of an individual mineral phase did not exceed +/-10% relative to the previous area (Vanden Bygaart and Protz, 1999), when incrementally increasing the size of the region of investigation.

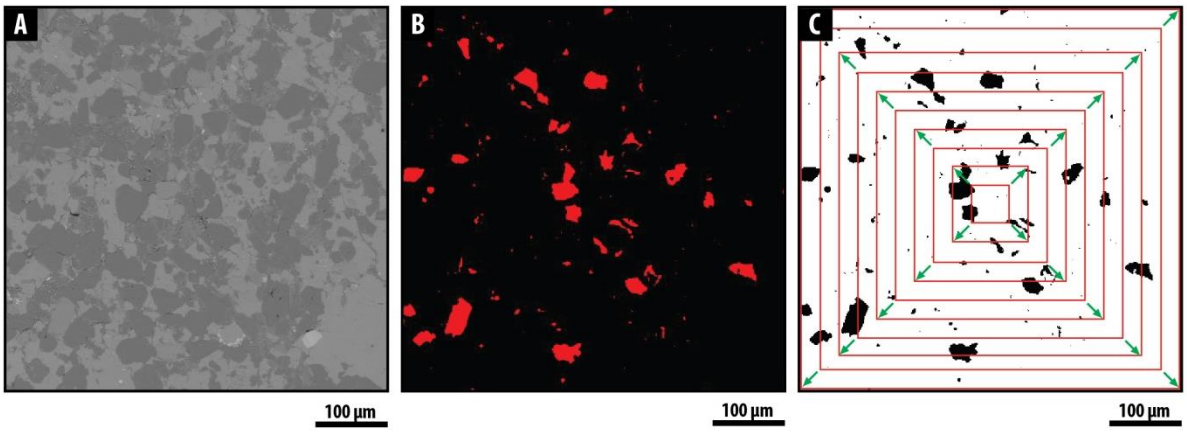

Figure 4.3 - Modified box counting method, shown on sample 2ii_A. a) Backscattered electron micrograph of area the elemental map was obtained. b) Minerals are segmented individually (Potassium Feldspar in this example). c) Image is binarised, and the area of the mineral is measured for regions of interest (red squares), which are increased in size incrementally (green arrows).

The companion higher magnification (1000x), high resolution (1280 x 720), backscattered electron images were then montaged to cover the area mapped by EDX. The image was cropped to the size of the largest representative area obtained from analysis of the minerals phases. The pores within this area were then identified and hand-segmented to obtain the total image porosity for each representative area.

The total area of pores was measured using ImageJ to determine the total 2D image porosity for the site. This process was repeated for one 600µm^2 site from each sample. A result of the limited image resolution at any magnification is the possibility that not all pores could be fully visualized in the BIB image mosaics. This technique is still limited by its spatial resolution (1 pixel = 57 nm). Therefore, it is not possible to see pores less than ~150 nm across (~3 pixels). At 3 pixels x 3 pixels a shape is defined. Features smaller than this may be surface asperities in the sample or shadows from the edges of other grains.

Permeability

Pore throat size obtained by mercury intrusion porosimetry has been shown to be related to permeability by several workers (Swanson, 1981; Katz & Thompson, 1986; Pittman, 1992; Yang & Aplin, 1998). The Yang & Aplin (1998) model assumes pores are composed of two cones which are connected at their base. In this model the shape of the pores

changes in response to compaction. Whilst compaction is not thought to be the key control on porosity in the middle Bakken, the presence of high and low aspect ratio pore morphologies is. This model was developed for shales, which are generally low porosity rocks. Whilst the middle Bakken is not a shale it has been found to be a low porosity rock.

$$k = \frac{9\,x\,10^{-18}\phi(sin\alpha)^2}{16}\ \frac{J_1^3}{J_2(1+J_1+J_1^2)^2}$$

Equation 4.3 - Yang & Aplin permeability equation. Where K is permeability, ϕ is porosity, α is the average pore alignment angle relative to the bedding direction (degrees), J_1 is the ratio of the largest radius of a pore and its pore throat radius, J_2 is the ratio of half the length of the pore and its pore throat radius (J_1 and J_2 are assumed to be identical for all pores in a given sample). From Yang & Aplin (1998).

Air permeability measurements were obtained during routine core analysis by Weatherford Laboratories. They used a Frank Jones steady-state air Permeameter to obtain the air permeability. Previous workers using this technique have reported accuracies of ±5% (Keelan, 1972). The Klinkenberg correction was used to correct anomalously high permeabilities. Anomalous permeability values such as these are thought to be a product of pores which are a similar size to the gas molecules which are flowing through them (Klinkenberg, 1941). Both raw and Klinkenberg corrected data are reported.

Results

Porosity from Wireline Logs

The responses from the neutron porosity and standard resolution density porosity wireline log tools in the middle Bakken are shown in Figure 4.4. Also plotted is the porosity calculated from the standard resolution density log. All three log responses show porosity in the middle Bakken is consistently low, with an average log porosity of 7.0% (density log porosity/RHOZ) and 5.7% (standard resolution density porosity/DPHZ). The highest porosity values are found at the top of the middle Bakken, with values of 31.4% for RHOZ and 31.6% DPHZ in gradational zone with the more porous Bakken shale (a discussion of which is beyond the scope of this study). The neutron porosity log response deviates from

the trend of the density log porosity values between depths of ~3191m to 3193m. In this zone the neutron porosity log is ~5% higher than the density log trend.

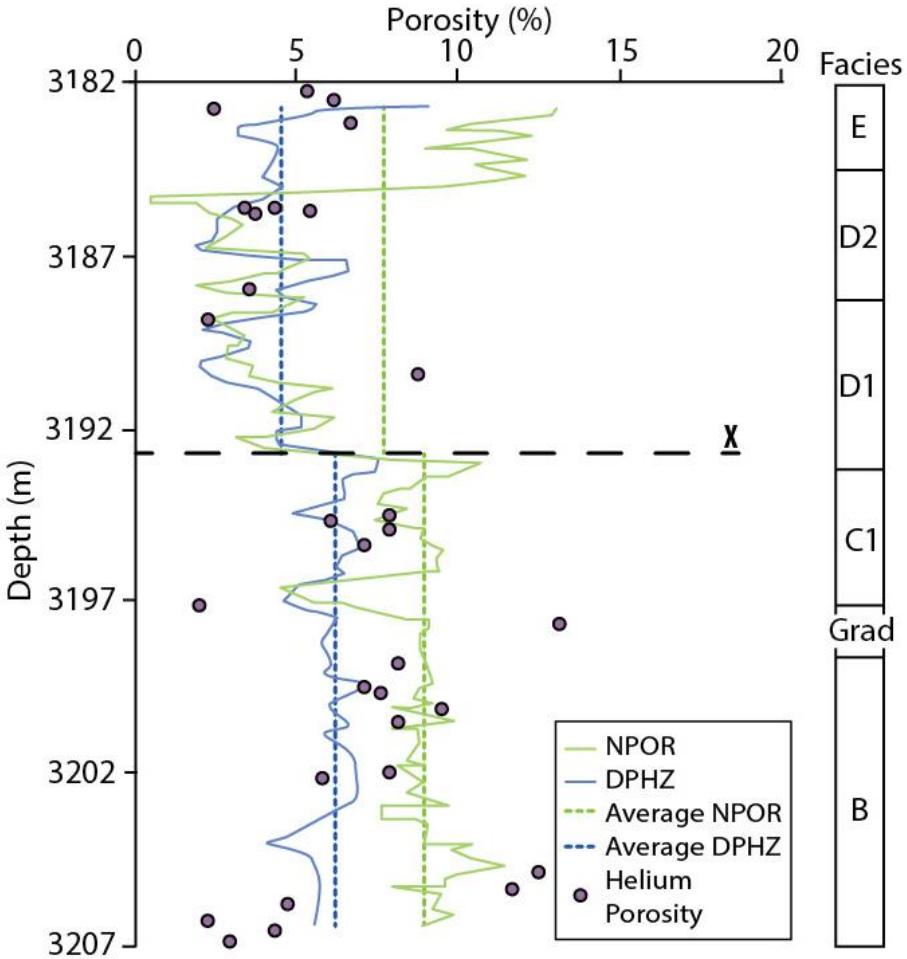

Figure 4.4 - Porosity from wireline logs. Standard Resolution Density Porosity (DPHZ) is plotted as raw data. Density Log Porosity (RHOZ) was obtained from Porosity = (average experimental rock density - logged density (RHOZ)) / (average rock density - assumed formation fluid density), using an average rock density of 2.74 g / cm^3 and an average formation fluid density of 1 g / cm^3 (Ellis & Singer, 2007). Data plotted is for the middle Bakken (3189.43 m - 3214.10 m) in logged depths. Helium porosity measurements are also plotted. The corresponding facies are shown.

The maximum variation in density log porosity is found in facies E where density log porosity varies by 6.81% and the lowest is found in the gradational facies where there is a maximum variation of 1.85% in density log porosity. There is a sharp increase in log porosity at ~3193 m (Figure 4.4 - point X). The average porosity above and below this point was calculated and plotted in Figure 4.4. There is a shift of ~2.5% in both logs. This

point is close to the boundary of facies C1 and D1. There is no clear relationship between log porosity and helium porosity.

Transmitted Light - Point Counting

Pores were identified in thin-sections under optical microscope however very few pore system features were visible at this scale. In the largest dolomite rhombohedra, vugs were observed in several samples. In some dolomites these were in the form of central vugs (something commonly observed under electron microscope). In such cases the vugs resolved were 1-10 µm in diameter (Figure 4.5b). Central vugs are common with dolomite of the middle Bakken, see Chapter 3.

In several samples fractures were observed. The fractures have apertures of 5-10 µm and penetrated the complete sample (~1 cm across). The fractures appear to follow bedding planes and were attributed to the combined effects of core/sample unloading, drying and handling. No other pore features were observed using transmitted light microscopy.

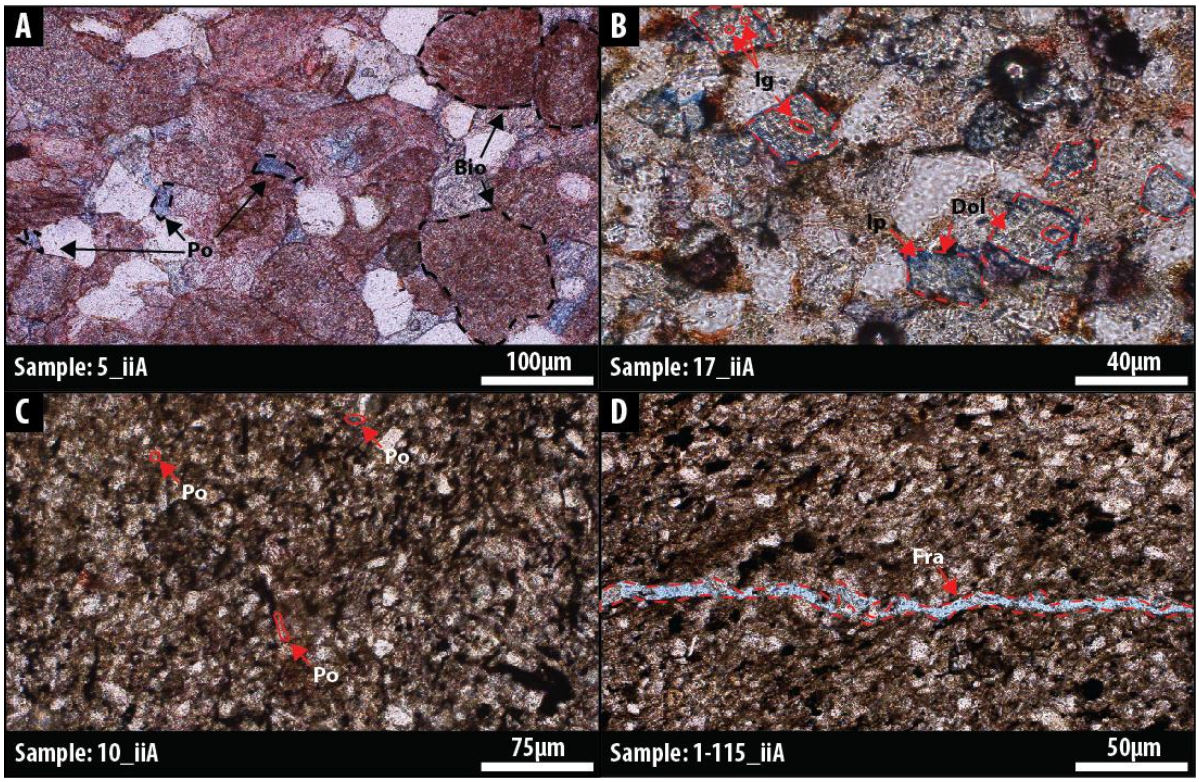

Figure 4.5 - Photomicrographs of stained thin-sections viewed under transmitted light. a) Calcite rich sample (5_iia) showing intergranular porosity (Po) between grains and

bioclasts (Bio). b) Porosity (Ip) associated with the dolomite, close to the grain edge and vuggy porosity (Ig) near the core of the dolomites. c) A blue dyed sample, showing only minor porosity d) Fracture porosity (Fra) in sample 1-115B highlighted by blue stain; note there is no other visible porosity (blue stain) in the sample.

Porosity values from point counting averaged 3% with a range of 0-10%. Applying the method of Lundegard (1992), Figure 4.6, porosity loss is principally due to cementation (CEPL: average 39.0%, range 29.9-47.5) with compaction contributing only a minor loss in porosity (COPL: average 4.0%, range 0-13.9%) therefore cementation is the primary control on porosity loss. The nearly consistent range (difference of 0.3%) between CEPL and COPL values suggests similar cementation processes have occurred at similar times, resulting in very little compaction. The porosity loss due to cementation is almost equal the assumed depositional/initial porosity (Pi). This suggests that cementation occurred very early in the diagenetic history of the Bakken Formation.

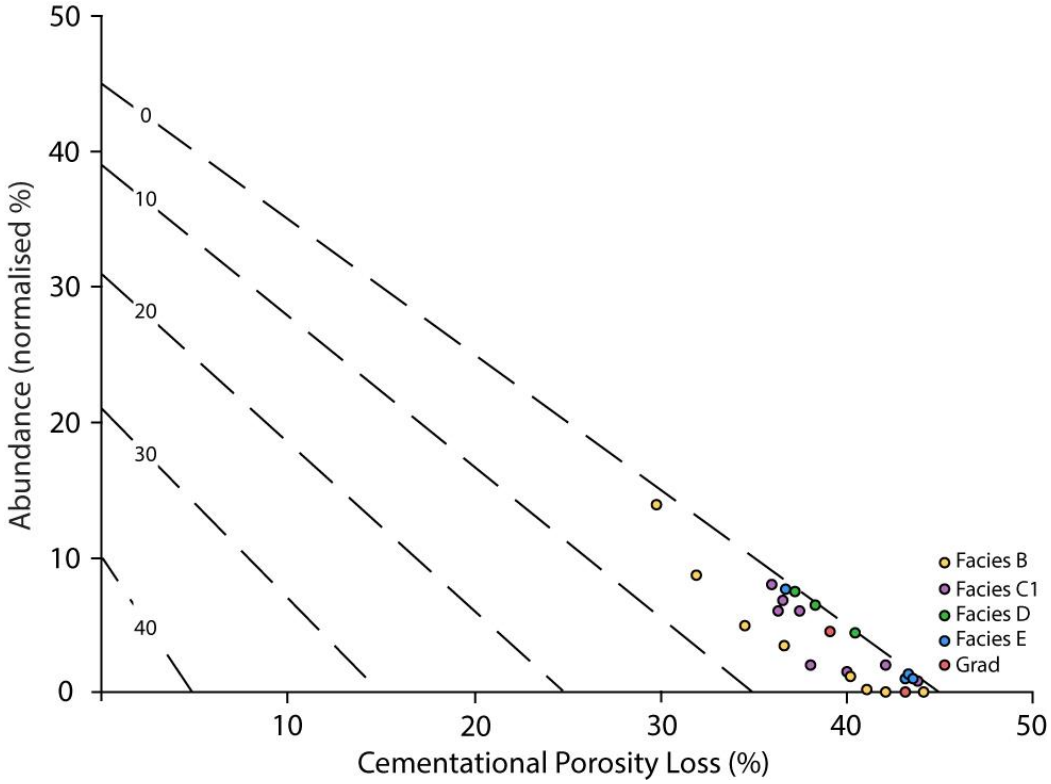

Figure 4.6 - Plot showing compactional porosity loss (COPL) against cementational porosity loss (CEPL). This plot assumes an initial porosity 45%. The diagonals are lines of equal porosity (%).

The difference in porosity of individual samples within a facies are similar (line up along the NW-SE diagonals), which suggests there is a relationship between depositional facies and therefore mineralogy with porosity after diagenetic alteration (Figure 4.6). Within individual facies, the effect of cementation and compaction on porosity is variable. This is most significant in facies E where the difference in average porosity loss between cementation and compaction is 39% and least significant in facies D2 where the difference is 31%.

XRD

From XRD analysis the bulk properties of the middle Bakken samples show large variations in major mineral abundance, Chapter 3. At the top and base of the middle Bakken the mineralogy is notably more variable, Chapter 3.

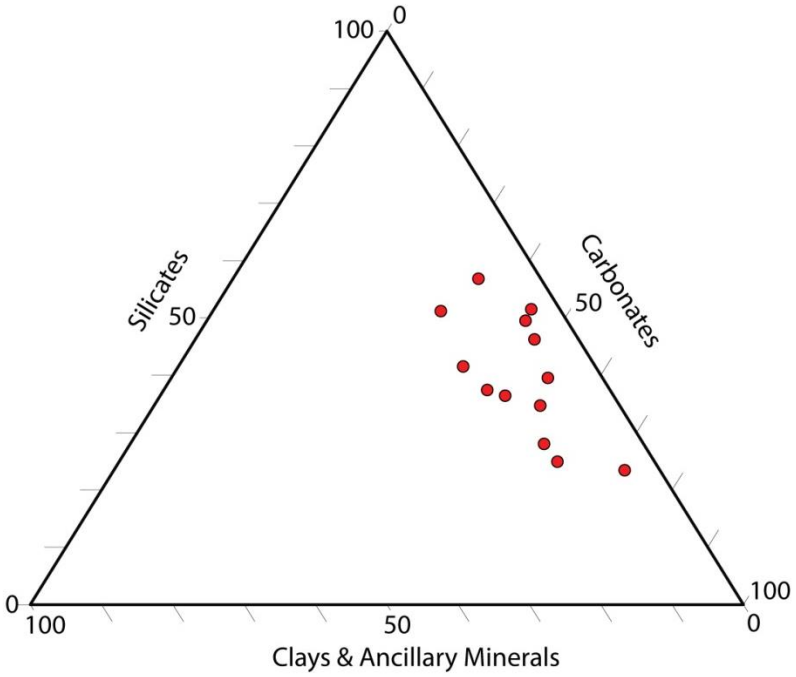

Figure 4.7 - Ternary plot of minerals grouped into carbonate, silicate and clay minerals as determined from XRD analysis. Carbonates - calcite, dolomite, ferroan dolomite. Silicates - Quartz, Plagioclase Feldspar and Potassium Feldspar. Clays + Ancillary Minerals - Pyrite, Marcasite, Hematite, Anhydrite, Celestine, Halite, Kaolinite, Chlorite, Illite and Mica.

Grouping the minerals into clays, silicates and carbonates, clearly shows the low abundance of clays and near equal abundance of carbonate and silicate minerals in the middle Bakken (Figure 4.7).

Whilst a full discussion of the relative abundance of detrital vs authigenic minerals is given in Chapter 3 minerals, which are predominantly detrital are: quartz, potassium feldspar, bioclastic calcite, whereas the minerals which are predominantly authigenic are dolomite, calcite, illite, and plagioclase feldspar.

SEM-EDX Mineral Maps

The samples selected for EDX mapping exhibit a range of compositions which summarise the facies which they represent (Figure 4.14). Sample 1-37B (facies E) is a dolomitised siltstone, sample 2_iiA (facies D2) is a heterogeneous mix of carbonates, quartz and matrix clays, sample 11_iiA (facies gradational) is a bioturbated unit of carbonates, quartz and lesser matrix clays and sample 1-116B (facies B) is a calcareous rock with quartz and minor matrix minerals.

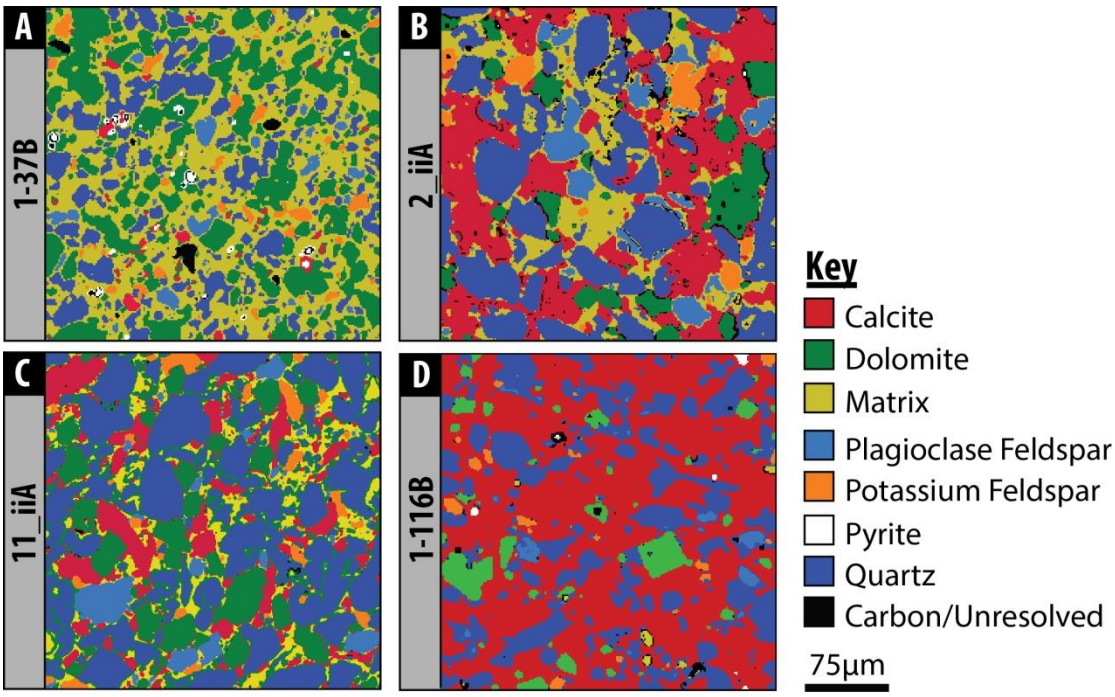

Figure 4.8 - EDX element maps processed into mineral phase maps. The four selected samples are shown, a) 1-37B, b) 2_iiA, c) 11_iiA, d) 1-116B. Matrix includes clay minerals and minerals which are too fine to be resolved at this magnification and EDX map

resolution. Carbon/Unresolved includes carbon coating and spectra which could not be confidently identified as individual minerals.

From Figure 4.8 it is clear there is significant variability in mineral abundances in the middle Bakken. In Figure 4.8a, there are abundant clay minerals, and dolomite is common, with only relatively small quantities of calcite. In Figure 4.18b calcite is far more abundant and clays minerals and dolomite is much less common. In Figure 4.8c, detrital quartz is significantly more abundant, yet calcite, dolomite and clays are in near equal abundance. In Figure 4.8d pervasive calcite cement is the most abundant mineral, cementing detrital quartz grains. It is clear from mineral maps that calcite forms a pervasive cement, with dolomite being far more patchy. These observations from SEM images and SEM-EDX maps correspond with the results of XRD mineralogy. In samples where calcite abundance is measured by XRD to be high, it is present as a cement. There is however a scaling issue, as whilst a pervasive cement it is very variable, with cement forming bands between tens of microns up to a tens of centimeters - which is in contrast to an XRD sample which was initially taken as a $1cm^3$.

In order to determine representative porosity values from BIB polished SEM images, the representative elementary area was determined for the bulk mineral phases from EDX maps of the imaged area. Individual phases were segmented into separate images for dolomite, calcite, quartz, plagioclase feldspar, potassium feldspar, pyrite and the matrix (unresolved minerals at that magnification).

A box counting method was performed for each sample. The box was positioned at the centre of the montage, from a random location. The axes of the region of interest box were increased in size by increments of 25 µm until the box reached a size of 500 µm x 500 µm.

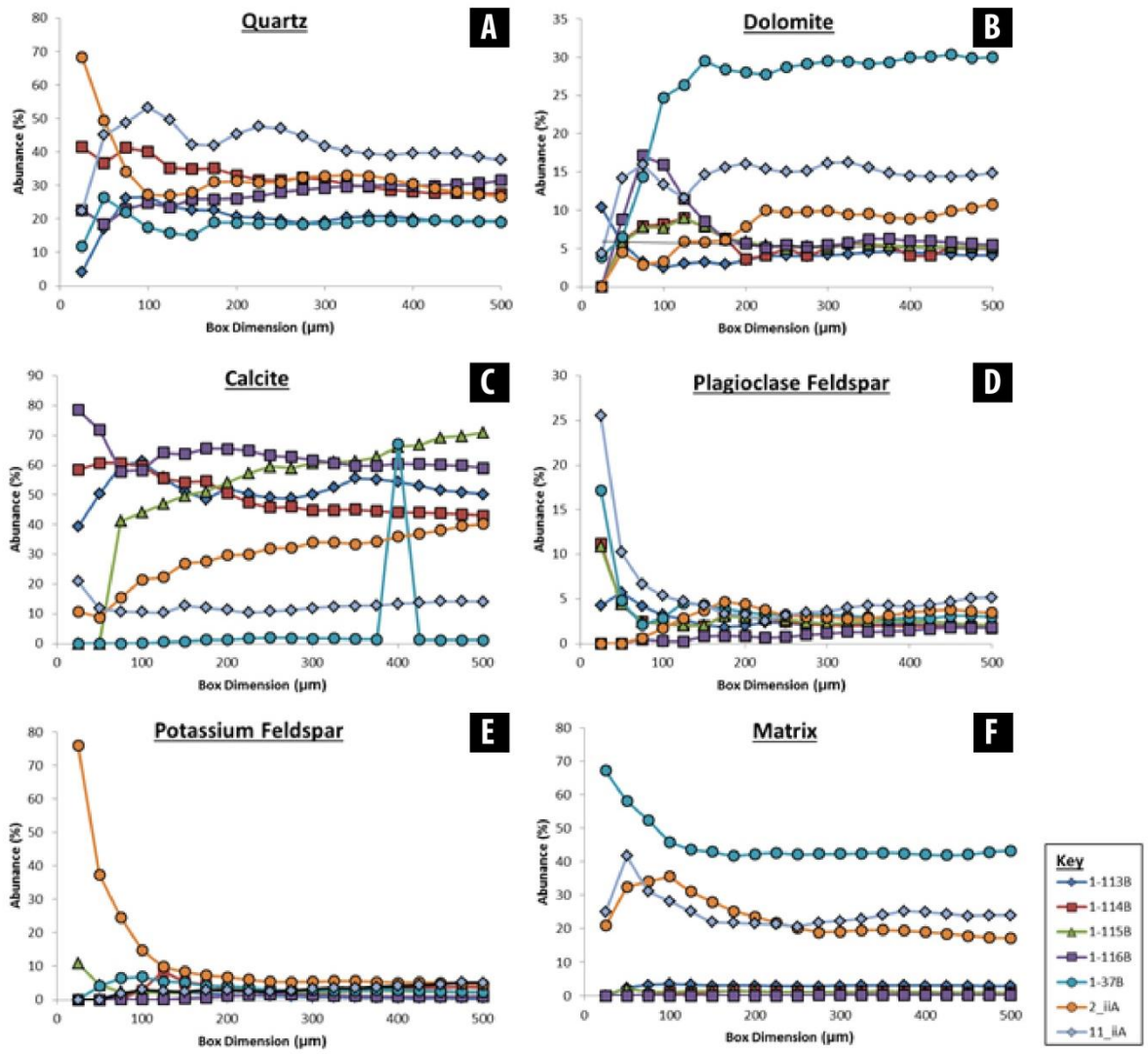

Figure 4.9 - Plots showing the change in abundance of each phase with increasing box size. a) Quartz, b) Dolomite, c) Calcite, d) Plagioclase Feldspar, e) Potassium Feldspar, f) Matrix. Matrix is defined as the minerals which are too fine to be segmented. Note the different y-axis value range.

From Figure 4.9 we can see that all the analysed minerals in the sample sub-set have reached a representative size, at or before a region of interest of 300 x 300 µm is obtained. In many instances the REA is reached much sooner; and the change in percentage abundance of that phase is small (<10%). Several different trends are apparent in this data. For dolomite there is an initial increase in abundance which rapidly reaches a plateau, showing only limited increase in abundance with increasing box size. Quartz and matrix mineral abundance remains relatively constant irrespective of the size of the region of interest.

The abundance of calcite in sample 1-37B is significantly lower throughout the analysis, with a significant spike at a box size of 400 x 400 µm. Analysis of the backscattered electron image shows that this sample is cemented by calcite in the same way that many of the other samples are. The anomalous spike was found to be due to the mapping of a bioclast.

To determine the REA from the modified box counting method, the variance between box sizes was calculated and the representative elementary area was marked as the point at which there was less than a 10% relative change in the area of a mineral phase (Table 4.3) (Vanden Bygaart and Protz, 1999).

REA (um)	Sample						
Mineral	**1-113B**	**1-114B**	**1-115B**	**1-116B**	**1-37B**	**2ii_A**	**11_iiA**
Dolomite	150	100	75	100	125	150	175
Calcite	100	50	100	100	200	125	75
Quartz	100	100	75	100	75	125	75
Plagioclase Feldspar	250	100	75	175	75	200	75
Potassium Feldspar	100	50	75	275	75	200	75
Matrix	125	200	100	75	50	150	100
Pores [Thresholded]*	-	-	-	125	75	100	75

Table 4.3 - Minimum areas required to obtain a relative change in the mineralogical composition which does not exceed 10%. Largest REA box dimension shaded red.

Using this method, we found the largest representative area to be 62,500 µm^2 (box dimensions of 250 µm x 250 µm), which resulted in a change of phase abundance of <10% with increasing box size. To reduce this variability further it was decided to use a region of interest with dimensions of 300 µm x 300 µm.

Composition

The mineral composition of individual REAs (300 µm^2), determined by SEM-EDX was compared with bulk values obtained by XRD for the minerals quartz, dolomite, calcite and pyrite.

Phase	Quartz (vol%)		Dolomite (vol %)		Calcite (vol %)		Pyrite (vol %)	
Method	**EDX**	**XRD**	**EDX**	**XRD**	**EDX**	**XRD**	**EDX**	**XRD**
2_iia	27.0	46	5.8	14	22.3	31	0.0	1
11_iia	49.0	31	15.6	0	10.7	11	0.1	1
1-37B	17.0	33	29.5	37	1.2	3	0.0	2
1-113B	26.0	18	6.0	41	61.0	21	0.2	1
1-114B	42.0	29	8.0	0	44.0	37	0.5	2
1-115B	29.4	23	5.2	0	71.0	53	0.9	3

Table 4.4 - Comparison of sample composition from EDX representative areas with bulk mineralogy from XRD analysis.

From Table 4.4 it is clear that there are significant variations in mineralogy between that measured by XRD and EDX.

Helium Porosimetry

The grain density of each sample was determined by both helium pycnometry and MICP. From the 29 middle Bakken samples analysed, the grain density was found to vary with facies. The average grain density for the middle Bakken was 2.74 g cm^{-3}. Grain density varies by less than 3% between different samples of the middle Bakken samples. Facies D1 has a lower grain density than the other facies of 2.71 cm^{-3}. For comparison the average grain density of the upper and lower Bakken members was measured to be 2.29 g cm^{-3} and 2.42 g cm^{-3} respectively.

The values of grain density obtained by helium pycnometry were then used to determine the connected porosity of the samples. The average helium porosity in the middle Bakken is 8%. Porosity values range from 2-17%. The highest porosity values and the greatest range of values are found in the gradational facies where porosity varies over a range of 10%. The lowest porosity sample is found in facies B. Facies D1 and D2 have similar ranges and similar average porosities (Figure 4.10).

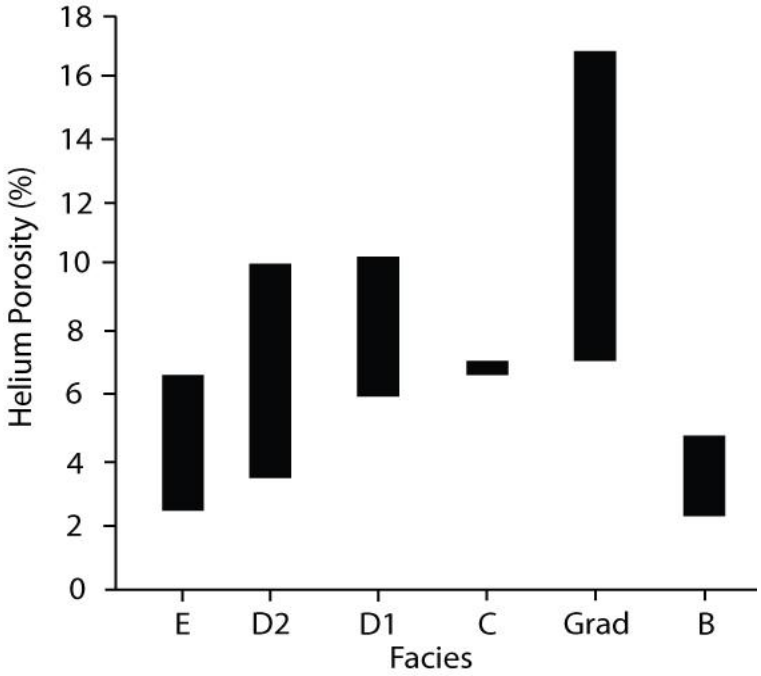

Figure 4.10 - Range of helium porosity values measured for each facies. Only one value is available for facies C.

The relationship between individual minerals and porosity is shown in Figure 4.9. Plots were made for all samples where both helium porosity and XRD mineralogy data was obtained. From these plots we see no relationship between porosity with quartz or clay abundance. As feldspar abundance increases so does the porosity. For calcite, there is an initial increase in porosity as the abundance of calcite increases. At around 11% calcite, the relationship changes and increases in calcite leads to a decrease in porosity. In dolomite, there is a general increase in porosity as the abundance of dolomite increases. The plot of total carbonate (Figure 4.11f) shows the overall effect; an increase in carbonate minerals results in a fall in porosity. Large changes in the relative abundance of carbonate minerals leads to relatively small changes in porosity.

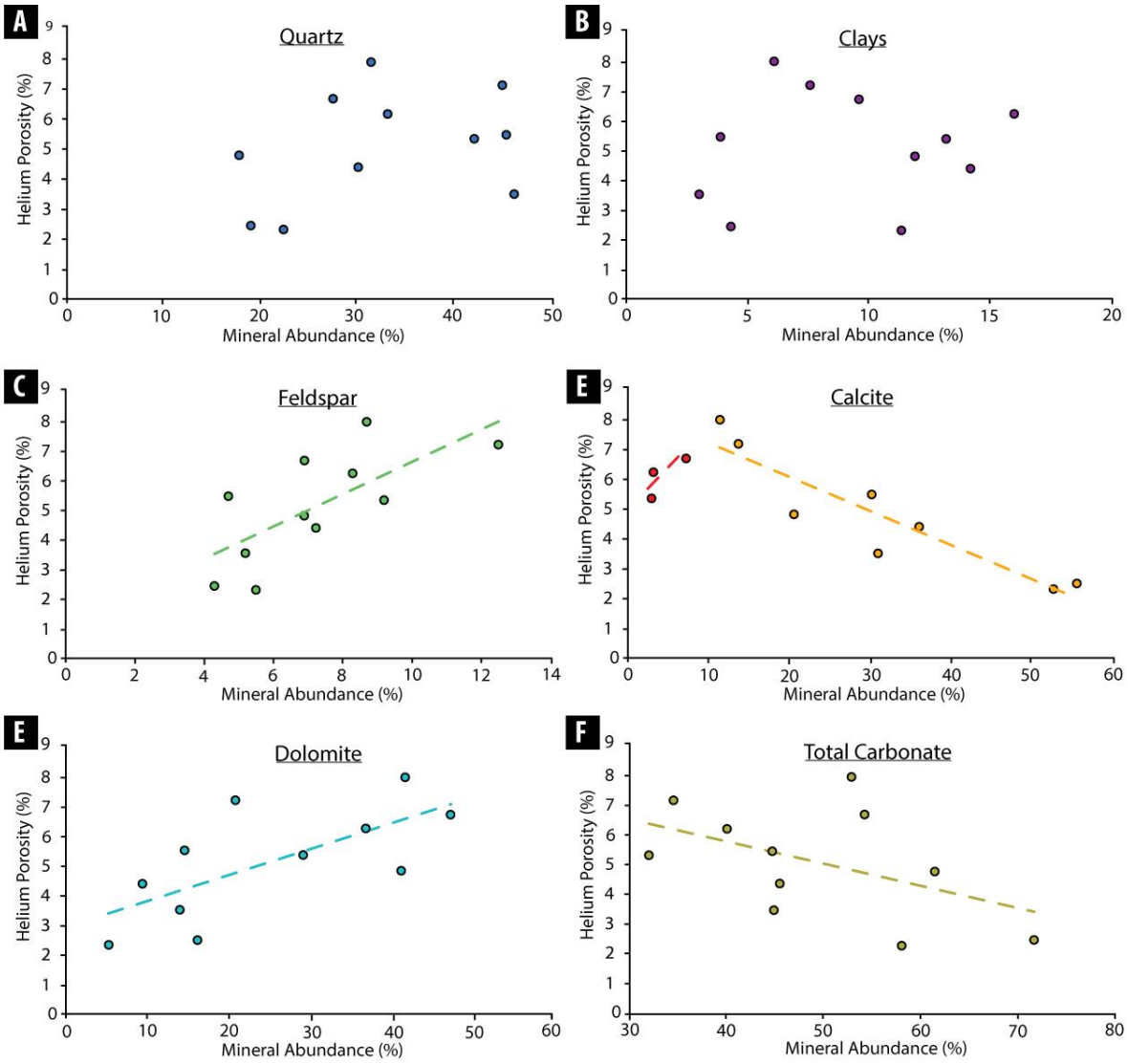

Figure 4.11 - Porosity variations (He porosity) relative to changes in mineral abundance (XRD) a) Quartz b) Clays [Kaolinite, Chlorite, Illite & Mica] c) Feldspar [Potassium Feldspar & Plagioclase Feldspar] <$R^2 = 0.82$>d) Calcite <R^2_{red}=0.93 & R^2_{orange}=0.82 > e) Dolomite [Dolomite & Ankerite] <$R^2 = 0.54$> f) Total Carbonate [Calcite, Dolomite & Ankerite] <R^2 =0.36 >. Linear trendlines are plotted where a recognisable relationship exists. For calcite, 2 trend lines are plotted, for calcite abundance <11% and ≥11%.

Gas Sorption

Nitrogen gas adsorption isotherms for the middle Bakken are 'type IV' according to the BDDT classification scheme (Figure 4.10a) (Brunauer et al., 1940). All isotherms show similar characteristics however, 3 samples adsorb significantly lower quantities of N_2, forming two discrete populations which have been labelled 'group X' and 'group Y', Figure

4.10a. Group X samples are from Facies D. The differences in the nature of the isotherm groups X and Y suggests samples of these groups have a different pore system structure. The isotherms in group Y do not go to the baseline, whereas isotherms in group X go much closer to it. This characteristic indicates the presence of micropores (Gregg & Sing, 1982). The difference in total gas adsorption between the two groups is 8.6 cm^3 / g (3.3 cm^3 / g and 12.0 cm^3 / g). Sample 2_iiA adsorbs the largest volume of gas whereas sample 1-58B adsorbs the smallest volume of gas.

Hysteresis loops which are found in type IV isotherms are caused by capillary condensation in mesopores (Gregg & Sing, 1982). The shape of the hysteresis loop can be used to determine the pore shape of the sample (Gregg & Sing, 1982). Using the classification of International Union of Pure and Applied Chemistry (IUPAC), both groups of isotherms appear to show type H3 hysteresis loops (Gregg & Sing, 1982).

The BJH (Barrett Joyner Halenda) pore body size distributions are plotted from 4 nm to remove the products of the tensile strength effect, (Figure 4.10d) (Groen et al., 2003). All samples exhibit very similar unimodal pore size distributions. The peak in pore volume occurs at pore bodies of ~12 nm in diameter. Within the measurement range of the technique, very little porosity is present in pores greater than 50 nm. The mean and median BJH pore size was determined to be 13.1 nm and 13.3 nm (range of 1.8-15.0 nm). BJH porosity values obtained from gas sorption data are all <2%. The average porosity value was 1.2%, varying between 0.3 - 1.9%, Table 4.3.

Adsorption experiments showed BET surface area values of 0.8 - 5.4 m^2/g. Rocks in conventional hydrocarbon reservoirs typically have BET surface areas of <1 m^2/g (Clarkson et al., 2013). The lowest surface area values are found in Facies D.

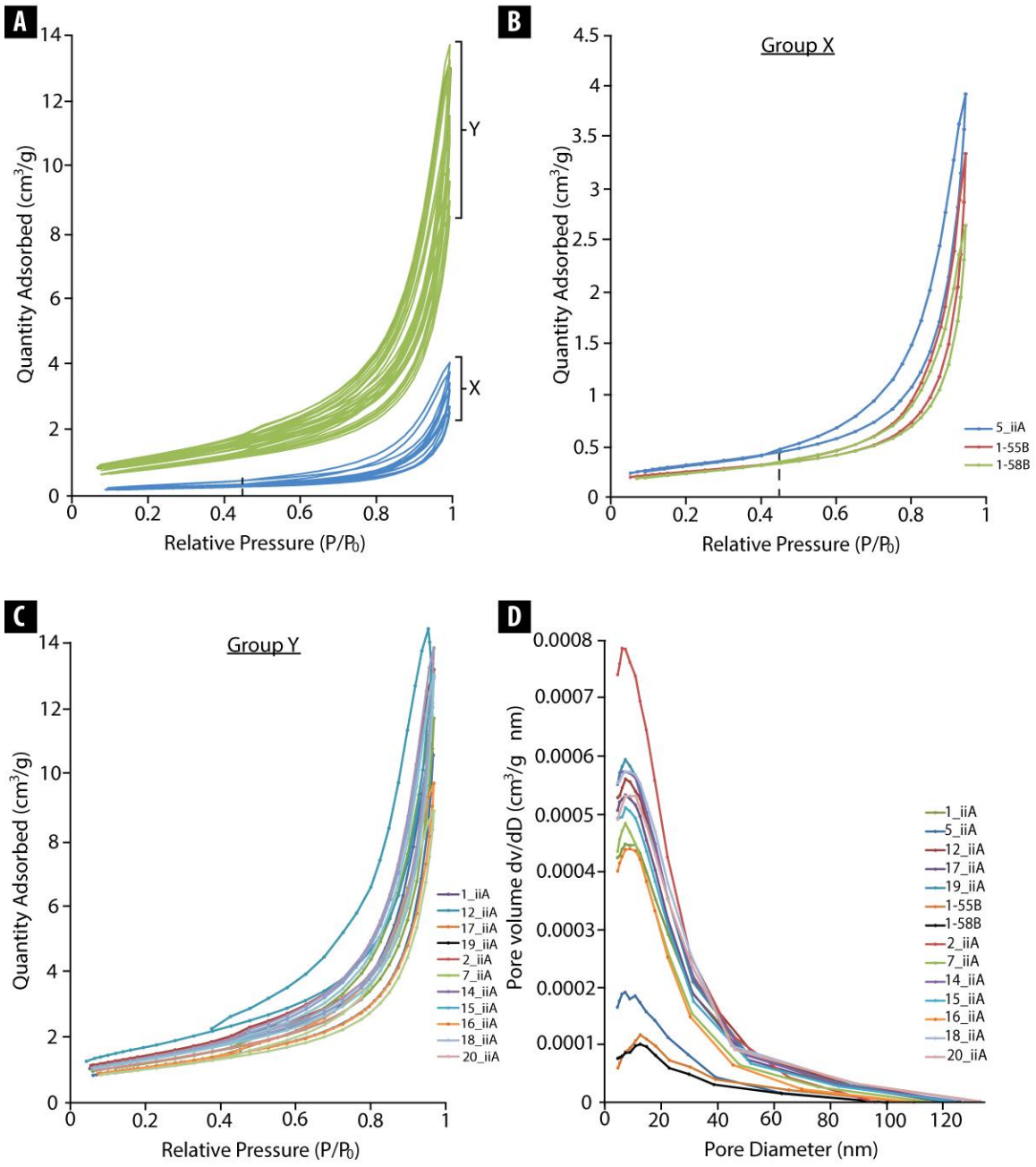

Figure 4.12 - Low-pressure Nitrogen adsorption isotherms at 77K for 12 samples of middle Bakken sandstones. a) Nitrogen isotherms of middle Bakken samples (average of 2 repeats). The volume of gas adsorbed falls into two discrete groups, labelled as X and Y respectively. b) Group X isotherms c) Group Y isotherms d) Pore size distribution between (4-130 nm) obtained using BJH method (Barret et al., 1951). Pore diameters are plotted up to 130 nm for clarity. Between 130-300 nm no porosity is identified by this technique.

MICP

Porosity values obtained from the volume of injected mercury during MICP vary from 0.01 to 6%, Table 4.5. The largest MICP porosity value is found in facies E and the smallest value is found in facies D2. Mercury density porosity was also calculated and are very similar to helium porosity, Table 4.5.

It would be expected that Hg density porosity > He Porosity > BJH porosity > Hg_{inj}. In many of the samples helium porosity is larger than the mercury density porosity. Where this is small, ~2%, it may be attributable to measurement error. Kazimierz et al. (2004) reported errors of upto 1% for helium porosimetry measurements. Sample volume measurements were repeated and found to vary by a maximum of 1%. Where the values are the same or very similar, this would suggest that all of the porosity in the sample is accessed by helium and therefore all the porosity in the rock is connected. In samples 15_iia, 18_iia, 10_iia and 11_iia the difference in porosity values was >2% (max. 2.73%).

Sample	Depth (m)	Hg Injection Porosity (%)	Hg Density Porosity (%)	He porosity (%)	BJH Porosity [1.7-300nm] (%)	Image Porosity (%)
1-36B	3182.17	4.33	5.39	5.32	-	
1-37B	3182.48	5.67	6.52	6.19	-	1.10
1-38B	3182.74	0.86	1.32	2.47	-	
1-39B	3183.09	5.82	7.11	6.66	-	
2_ii	3185.62	0.93	3.19	3.50	1.89	1.32
3_ii	3185.65	3.38	4.21	4.44	-	
4_ii	3185.70	4.13	4.63	5.45	-	
5_ii	3185.74	0.04	2.60	3.66	0.50	
1-55B	3187.99	0.01	1.55	3.50	0.42	
1-58B	3188.86	0.02	1.45	2.28	0.34	
15_ii	3194.55	0.05	5.45	7.88	1.45	
16_ii	3194.87	0.10	6.09	7.97	1.09	
17_ii	3195.37	0.13	6.26	7.13	1.37	
7_ii	3197.11	0.04	2.96	2.03	1.23	
18_ii	3198.76	0.12	6.12	8.15	1.75	
12_ii	3199.55	0.19	5.95	7.08	1.70	
19_ii	3199.71	0.19	5.78	7.65	1.67	
10_ii	3200.14	0.11	6.78	9.51	-	
20_ii	3200.55	0.15	6.35	8.18	1.63	
11_ii	3201.95	0.12	5.66	7.92	1.40	1.52
21_ii	3202.12	0.23	4.45	5.79	-	
1-113B	3205.76	1.82	5.05	4.78	-	
1-115B	3206.25	1.56	2.30	2.31	-	
1-116B	3206.56	3.53	4.64	4.36	-	1.60

Table 4.5 - Porosity values determined from mercury injection compared to those obtained by helium pycnometry, low pressure gas adsorption (BJH equation for 1.7-300 nm pores) and segmented image maps.

Comparing mercury porosity with helium porosity; at injected mercury porosities (Hg_{Inj}) >0.5%, there is a positive correlation with helium porosity, (Figure 4.11). Below 0.5% Hg_{Inj} the helium porosity values are very variable, (Figure 4.11). Samples with Hg_{Inj} porosity of <0.5% are all found between a depth 3185.74 - 3202.12m. They are present in facies D2 (lower section), D1, C, and the gradational facies. There are no samples between these depths which have a Hg_{inj} porosity >0.5%.

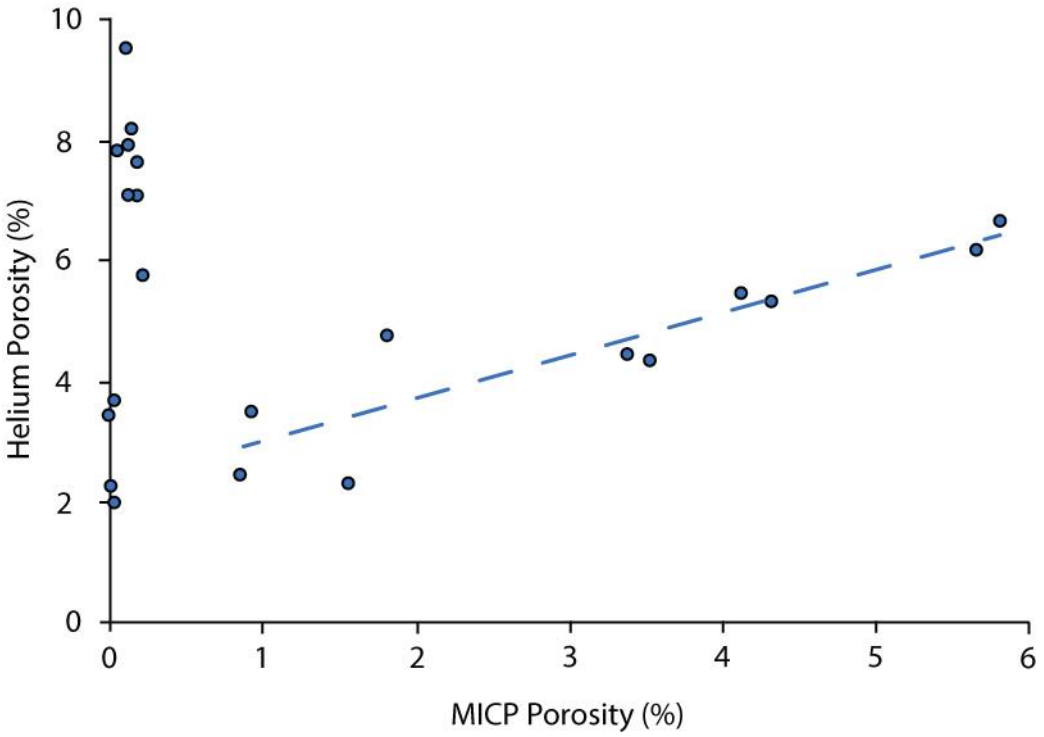

Figure 4.13 - Cross-plot of injected mercury (MICP) porosity with helium porosity. Trend line is plotted for MICP porosities >0.5%. Trendline: $R^2 = 0.82$.

The volume of mercury intruded into the sample at different pressures was also used to determine the size distribution of the pore throat radii using the Washburn equation (Equation 4.4) (Washburn, 1921).

$$Pc = -\frac{2\sigma \mathrm{Cos}\theta}{\mathrm{rc}}$$

Equation 4.4 - Washburn equation, where: Pc = capillary pressure (psi), σ = surface tension of Hg, θ = contact angle of mercury/air, rc = radius of pore-throat aperture (μm) assuming a cylindrical pore (Washburn, 1921). The surface tension of mercury was assumed to be 0.48 Nm^{-1} and the contact angle between mercury and the particle surface was assumed to be 141° (Yang & Aplin, 2007).

Results of MICP tests are presented as plots of the cumulative volume of intruded mercury (non-wetting phase) against pore-throat size. A range of characteristic pressures are associated with MICP curves, and a variety of often conflicting names have been used to describe these features of intrusion curves (Dullien, 2012).

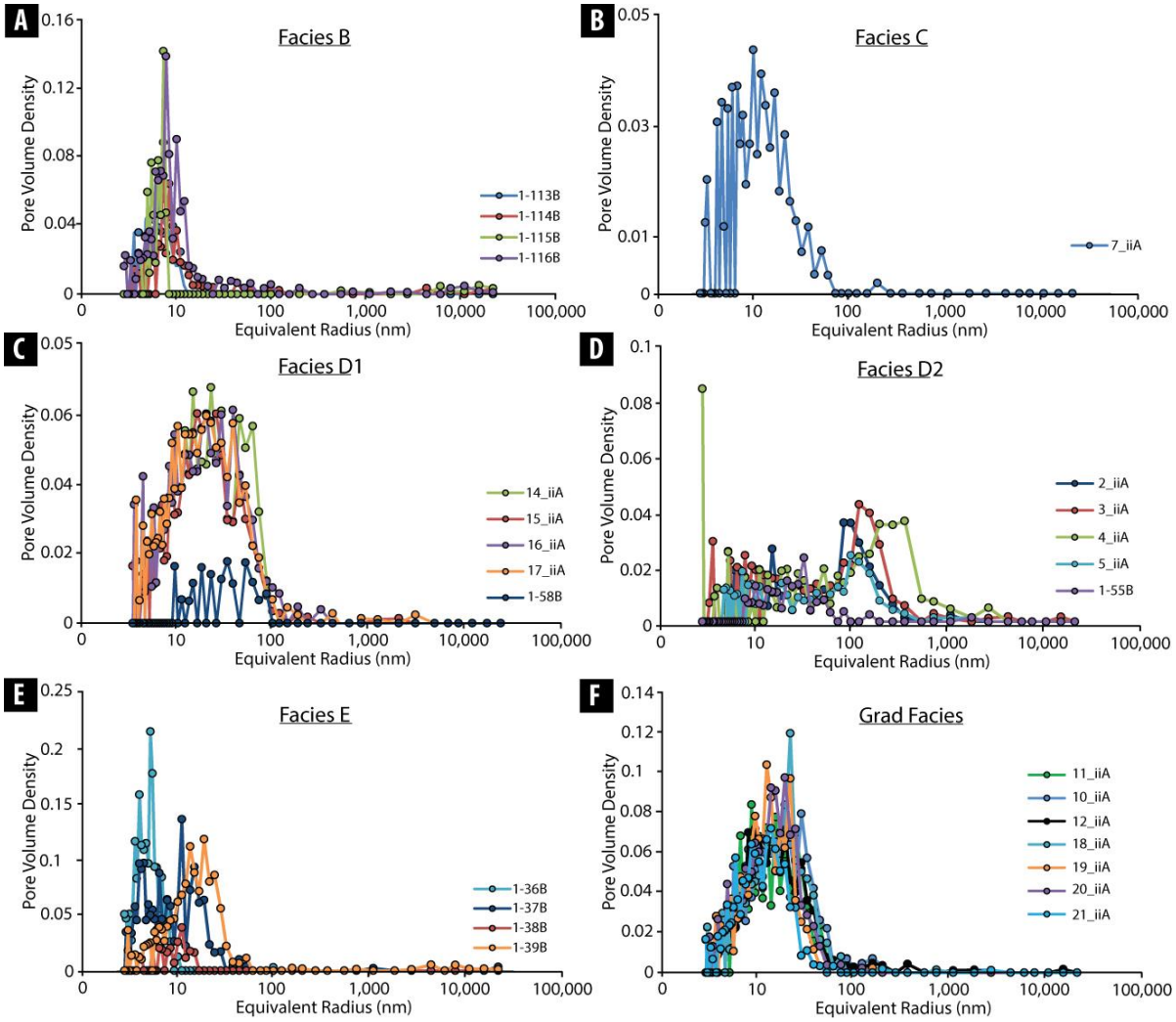

Figure 4.14 - Plots showing the relationship between pore size and cumulative volume of mercury injected (RAW with no cut-off radius applied). a) Facies B b) Facies C c) Facies D1 d) Facies D2 e) Facies f) Gradational Facies.

Individual facies show quite different pore throat size distributions (PTSD). Facies B has a very narrow size distribution, with a peak in pore throats at ~10 nm. Different samples within the facies have a very consistent pore throat size distribution, made of pore throats which are small. Only one sample was tested for facies C has a broader PTSD than facies B

but similarly has a peak at ~10 nm. Facies B and C have similar pore throat characteristics. Facies D1 and D2 have very different distributions but both have pore throats which are in both the mesopore and macropore size range. D1 has a unimodal throat size distribution whereas D2 exhibits a weak bimodal PTSD, present over a large range of pore throat sizes. Facies D1 has a peak ~18 nm, whereas Facies D2 has peaks at ~8 nm and 195 nm. Samples in Facies D2 are the only ones with pore throats greater than ~100 nm. Facies E has a similar distribution to Facies B; narrow PTSD, with predominantly small pore throats, which are in the mesopore range. Sample 1-39B within this facies shows characteristics similar to the gradational facies with a peak in PTSD at ~19 nm. The PTSD's for the gradational facies are consistent across all of the samples in this facies with a peak in PTSD ~19 nm.

Permeability

Permeability values estimated from mercury intrusion porosimetry (Yang and Aplin, 1998) are is shown in Table 4.6. The MICP permeability vary from 3.08×10^{-7} to 4.37×10^{-4} md and are around one order of magnitude lower than Klinkenberg corrected air permeabilities. Both the highest and lowest mercury permeability are found in facies D2.

Sample	Depth (m)	Yang Aplin Permeability (mD)	RCA Permeability (mD)	
			Air	Klinkenberg
1-36B	3181.41	8.00E-6		
1-37B	3182.17	2.57E-5	2.36E-3	7.30E-4
1-38B	3182.48	2.60E-6		
1-39B	3182.74	4.04E-5	9.50E-4	2.20E-4
1-113B	3183.09	5.02E-6		
2_iiA	3185.62	3.34E-6		
3_iiA	3185.65	3.08E-7		
4_iiA	3185.70	4.37E-4		
5_iiA	3185.74	4.58E-5		
14_iiA	3194.21	3.86E-5	7.60E-4	1.60E-4
15_iiA	3194.55	3.28E-5		
16_iiA	3194.87	4.40E-5		
17_iiA	3195.37	3.74E-5		
7_iiA	3197.11	1.11E-5		
18_iiA	3198.76	3.07E-5		
12_iiA	3199.55	3.44E-5		
19_iiA	3199.71	2.23E-5		
10_iiA	3200.14	4.40E-5		
20_iiA	3200.55	2.77E-5		
21_iiA	3202.12	1.61E-05		
1-114B	3205.76	5.57E-06		
1-115B	3205.95	3.76E-04		
1-116B	3206.25	9.37E-05	1.00E-3	2.30E-4

Table 4.6 - Permeability values calculated from MICP data using the Yang & Aplin (1998) model. RCA Permeability's were obtained by Weatherford Core Laboratories (Hart, 2016, pers. comm., 4th January).

SEM Imaging

From both BIB polished rock sections and coated broken surface samples, secondary electron images were taken, from which pores were identified and categorised. A range of pore types were identified including intra-granular pores (Figure 4.15a), inter-granular pores (Figure 4.15b), and grain-boundary pores (Figure 4.15c)

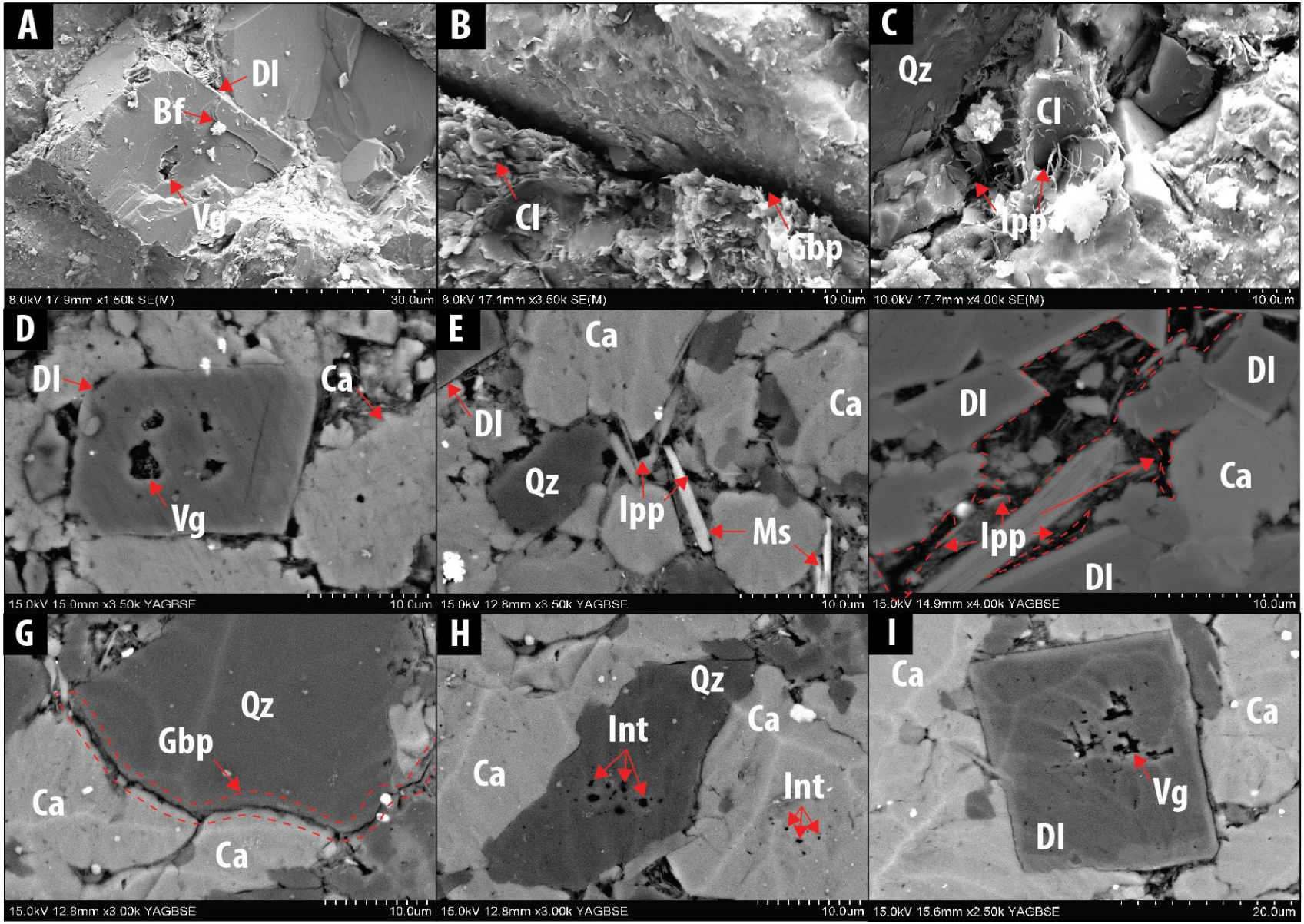
A
Dl
Bf
Vg
8.0kV 17.9mm x1.50k SE(M)
30.0um
B
Cl
Gbp
8.0kV 17.1mm x3.50k SE(M)
10.0um
C
Qz
Cl
Ipp
10.0kV 17.7mm x4.00k SE(M)
10.0um
D
Dl
Ca
Vg
15.0kV 15.0mm x3.50k YAGBSE
10.0um
E
Ca
Dl
Ca
Qz
Ipp
Ms
15.0kV 12.8mm x3.50k YAGBSE
10.0um
Dl
Dl
Ca
Ipp
Dl
15.0kV 14.9mm x4.00k YAGBSE
10.0um
G
Qz
Gbp
Ca
Ca
15.0kV 12.8mm x3.00k YAGBSE
10.0um
H
Qz
Ca
Int
Ca
Int
15.0kV 12.8mm x3.00k YAGBSE
10.0um
I
Ca
Ca
Vg
Dl
15.0kV 15.6mm x2.50k YAGBSE
20.0um

Figure 4.15 - SEM images of pore morphologies observed in the middle Bakken a) Central vug (Vg) on a dolomite rhomb (Dl) visible as the crystal has been cracked (Bf) (chip of sample 1-116B in facies B. b) Grain boundary pore in sample 1-116B, with clay minerals growing on the host grain. c) Inter-granular pores (IPP) between quartz (Qz) and dolomite (Dl) partially infilled with platy and hairy illite (Cl). d) Intra-partical vuggy porosity in a dolomite (Dl), adjacent to calcite (Ca). e) Inter-particle pores between quartz (Qz), dolomite (Dol) and calcite (Cal) partially infilled by platy minerals, ?muscovite (Ms). f) Zones of inter-particle pores between dolomite (Dl) and calcite (Ca) infilled with matrix minerals including clays. g) Grain boundary pore (Gbp) between calcite (Ca) grains and quartz (Qz) grains h) Intragranular porosity in quartz (Qz) and calcite (Ca) i) Vuggy (Vg) porosity in a type 2 dolomite rhomb cemented by calcite (Ca).

Intra-granular pores are most commonly found in dolomite but also occur in calcite cement and quartz grains. In dolomites, the pores vary in size from <1 µm – 10 µm. They are rounded to sub-rounded in shape with rounded forms being most abundant. They are often observed at the core of the rhomb as either a single large vug or multiple smaller vugs (Figure 4.15d). Vuggy porosity in dolomite crystals does not contain any other minerals e.g. lining or infilling the pore space. SEM observations of pores at the core of dolomite crystals appear to be closed and unconnected, unlike intergranular pores which are found to form a connected network.

Intra-granular pores in calcite are predominantly small, 1-3 µm, equant, and rounded in shape. They are present in groups showing a dispersed, sieve like texture, (Figure 4.15f). In quartz they form similar textures and morphologies to those observed in calcite but also commonly occur as small (<5 µm), single, isolated voids (Figure 4.15h).

Intergranular pores are most commonly found along grain boundaries. These pores are <1 µm wide and vary in length from ~20-150 µm in length, grain boundary pores do not appear to be associated with clays but in some, small clay bridges have formed connecting opposite sides of the pore (Figure 4.15b). These pores have a very high aspect ratio.

Intergranular pores associated with clay rich regions are highly variable in shape from rounded, equant forms through to elongate, stubby morphologies. SEM images on broken

surfaces show intergranular pores between illite hairs and also around aggregates of kaolinite plates (Figure 4.15). In clay rich zones, intergranular pores are also found between crystals of pyrite in framboids. These pores are connected both within the clay-rich region and into other more quartz rich domains (Figure 4.15). Intergranular pores are also found between other grains including quartz, dolomite and calcite but many of these voids are at least partially infilled with clay minerals including authigenic illite and kaolinite [see Chapter 3].

Image Porosity

From image analysis of the representative areas (300 μm^2) of 4 samples the 2D image porosity was measured. This technique allows us to associate pores with specific minerals. Using this technique intergranular porosity is included in the 'matrix'. Porosity measured from image segmentation was lower than bulk porosity measurement techniques on the same sample. The difference in the two measurements was on average 5.1%.

This is most likely due to the limitation of image resolution, meaning we have not resolved the smallest pores in the SEM images. To limit this, the highest possible image resolution was used with the compromise of magnification. With these settings, 1pixel size = 57 nm. This means that any pores less than ~150 nm are either unresolved or significantly underestimated, therefore generating a value of total porosity which would be lower than 'absolute' total porosity. A similar relationship was reported in other pore-scale studies (Klaver et al., 2012; Houben et al., 2013; Mathia, 2015).

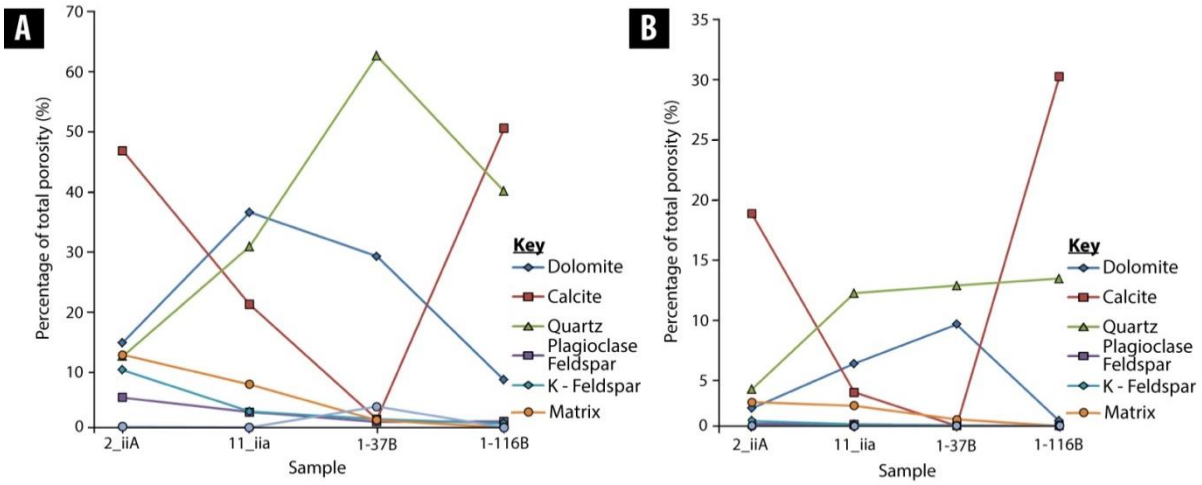

Figure 4.16 - a) Plot of the percentage of total porosity present in each mineral phase in images segmented for the four BIB polished samples b) Plot showing the percentage of porosity for each mineral phase weighted to the relative abundance of each phase in individual samples. Matrix - is the intergranular porosity; all other phases represent intra-granular porosity present within that mineral.

In the four samples of this analysis, porosity is predominantly found in carbonate minerals (calcite and dolomite), except in sample 1-37B (Figure 4.16a). In sample 1-37B, quartz is the dominant host of most intra-granular porosity (Figure 4.16a). No porosity is measured in calcite in sample 1-37B, which is in contrast to samples 2_iiA and 1-116B where calcite holds the greatest porosity; in which >45% of the porosity is hosted. When the abundance of porosity in calcite is high, the abundance of porosity in dolomite is low (the opposite is also true).

The difference in total porosity per phase is influenced by the relative abundance of individual phases. The aim is to understand the relative proportion of porosity in each phase e.g. what is the percentage of total porosity is there in each mineral when the abundance of all of the minerals are equal. To do this the porosity was weighted to the abundance of each mineral phase. The total porosity (%) in each mineral phase was divided by the normalised abundance of that mineral phase.

In porosity data weighted for mineral abundance, there is a consistently high percentage of porosity in quartz (11_iiA, 1-37B, 1-116B), which is consistent, varying by 1.25% between these three samples. Where porosity is dominant in calcite it is low in dolomite (samples 2_iiA and 1-116B). Intergranular porosity ('Matrix') porosity values are consistently low.

From observations of SEM images it is evident that the intergranular matrix pores are the smallest pores (Figure 4.15c & 4.15e), whereas the intragranular pores are much larger (Figure 4.15d & 4.15i). Therefore, we suggest this data set best assesses the contribution of intragranular porosity >150 nm.

Quantitative Shape Analysis

Aspect ratio is a measure of how equant or elongate a structure or body is, in this instance, pores. The aspect ratio of all of the pores was determined from the best fit ellipse (major axis/minor axis). The best fit ellipses are used to address the issue of the irregular nature of pore shapes in measuring size. The closer the aspect ratio is to 1, the more equant the pore.

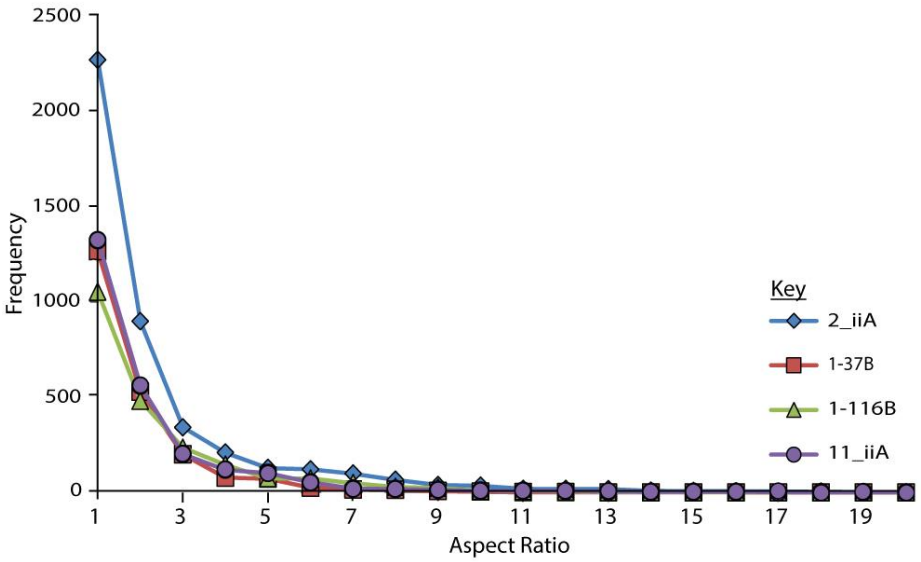

Figure 4.17 - Aspect ratio of pores obtained from BIB polished SEM images from 4 middle Bakken samples. Two anomalous values of 212 and 494 for sample 2_iiA are not shown.

Two anomalies with values of 212 and 494 were identified in sample 2_iiA. It is unclear what they are. Clay bridges breaking up pores have been identified in other elongate pores. It is possible that such clay bridges were polished out during sample preparation or were unresolved at this magnification. It is also possible they are fractures in the sample, either naturally occurring as observed by several workers (e.g. Meissner, 1991; Pitman et al., 2001; Webster, 2011) or by introduced during sample handling.

From Figure 4.17 it is evident that pores in these sample are not circular (AR=1) but are ellipses with AR values of ~ 3 (mean 2.94 including outliers) (Figure 4.18). The highest frequency aspect ratio was found to be 1. This was the same for all four samples analysed. There are 2 significant outliers present in sample 2_iiA; these have aspect ratios of 212 and 494 (not shown in Figure 4.17).

Discussion

Rock Typing

The aim of rock typing is to classify reservoir rocks into distinct units which were deposited under similar geological conditions and experienced similar diagenetic histories (Gunter et al., 1997; Rushing et al., 2008). If implemented correctly each rock type has a unique porosity-permeability relationship, capillary pressure profile and set of relative permeability curves (Gunter et al., 1997). Whilst a full rock typing scheme is beyond the scope of this work, we have tried to relate porosity and pore morphology features to facies based on mineralogy, and therefore diagenesis. This forms the basis for a full rock typing scheme.

A generalised rock typing scheme associated directly with facies has been suggested for the middle Bakken by Sonnenberg & Pramudito (2009). In this scheme the reservoir quality is assessed for each facies, however this scheme makes only limited recognition of the heterogeneity in both the detrital and diagenetic mineralogy that both we (see Chapter 3) and other studies have identified (Kurtoglu, 2007; Long et al., 2011; Li et al., 2015).

Porosity

Transmitted light point count data indicates porosity in the middle Bakken is low. CEPL and COPL plots of point count data indicate cementation is the main driver of porosity loss. This interpretation is supported by compaction-cementation plots (Figure 4.6). These plots showed the low porosity is principally due to cementation with compaction responsible for only a small reduction in porosity. This relationship is true for all facies. In Chapter 3 we concluded that early calcite cementation largely inhibited compaction of the middle Bakken. This is an effect which has been reported in previous studies of diagenesis in other formations (Hesse and Abid, 2009; Xiong et al., 2015).

In cemented facies (B, C, D_2, E) the porosity loss due to cementation (CEPL) was highest, however the relationship between facies and CEPL is not absolute. For such significant porosity loss to have occurred (~40% in some samples, assuming an initial porosity of 45% [Chuhan et al., 2003]), the pore filling phase must also therefore be of similar abundance. The most common single phase in the middle Bakken is quartz, however the percentage of pore filling authigenic quartz cement was found to be ~0.5% of total rock and ~5% of

total quartz [Chapter 3]; whilst a contributor to porosity reduction, it is clearly not present in sufficient abundance to be the principle porosity occluding cement. Carbonate minerals are the second most abundant phases. Textural analysis suggests these phases are predominantly authigenic [Chapter 3]. Semi-quantitative analysis by point counting suggests ~75% of carbonate minerals are authigenic. Many previous studies have highlighted the pore filling, porosity reducing effects of precipitating authigenic carbonate minerals in Devonian and Mississippian sediments (Hurley & Lohman, 1987; Lima & Ros, 2002; Al-Ramadan et al., 2004). This suggests carbonate cements may be the porosity occluding phase.

Comparing XRD values of carbonate abundance and with helium porosity values (~1 cm^3 samples), we found porosity decreased when carbonate content increases (Figure 4.9). This relationship was also observed at the millimetre scale, on point-counted thin-sections. Regions of samples with higher carbonate content had lower porosity values, Chapter 3, Table 3.4.

It has been suggested that differences in depositional facies exert a strong control over the porosity of the middle Bakken (Sonnennberg & Pramudito, 2009). Similarly, generalised rock-typing schemes have been made by Ferdous, (2001) and Ramakrishna et al., (2010).

At the reservoir scale, porosity logs of the middle Bakken show consistently low values throughout the middle unit. Typical porosity values for reservoir sandstones and siltstones are between 20-30% (Gluyas & Swarbrick, 2013); whereas in the middle Bakken, the average log porosity is 7.0% and 5.7%. In this core, log porosity values show no distinct variation with respect to facies (Figure 4.4). There is only one small change at ~3192.5m, where there is an increase in porosity of ~2.5% in both porosity logs. This point is close to the boundary of facies D1 (shallower) and C1 (deeper); facies D1 is richer in clay and more highly calcite-cemented than facies C1 is a clean, laminated fine silt and sandstone.

In facies-porosity plots (Figure 4.8) there is a weak relationship between porosity and facies. Petrographic observations showed that when calcite cement is present in a facies, it does not pervade the whole facies, Appendix 1. Zones of uncemented or less cemented rock are common within a 'cemented facies'. A similar relationship was noted by Li et al.,

(2015) who found that the abundance of calcite can vary significantly at several analysis scales within the middle Bakken.

From this, we suggest the current facies designations cannot be used in isolation for rock typing of the middle Bakken. Recent work on the Bakken by Li et al., (2015) agrees. In their study they also attempted to form a rock typing scheme for the middle Bakken. They suggest that large variations in mineral abundance and associated pore type can be found within a core plug; a scale much smaller than the current facies models.

From this discussion we deduce that cementation is the principle process occluding porosity in the middle Bakken. Carbonate cementation is most likely the principle occluding cement in part due to its large abundance. Variations in porosity are controlled by variations in the abundance of carbonate cements which occur at a scale smaller than the size of a facies. The log-facies relationship identified suggests that clay minerals may also have contributed to the reduction in porosity; however, clay minerals are far less abundant than carbonate minerals calcite and dolomite.

Porosity Measurement

Variations in porosity values measured using different techniques have been recognised and discussed by many previous workers (e.g. Manger, 1963, Sahimi, 2011; Anovitz & Cole, 2015). One of the principle causes of porosity measurement differences is the scale of the region of investigation of different techniques.

Differences between values of porosity measured by logs and helium pycnometry are thought be a product of both the scale of heterogeneity of the formation and the sampling resolution of the different porosity sonde. We suggest that the low values recorded by helium pycnometry represent low porosity bands and laminae which separate regions of higher porosity. These bands are ~0.1 cm - 1 cm thick, which is much smaller than the sampling resolution of a porosity log (15 cm) (Figure 4.18). The result of a lower resolution log is the averaging of data through the region of investigation.

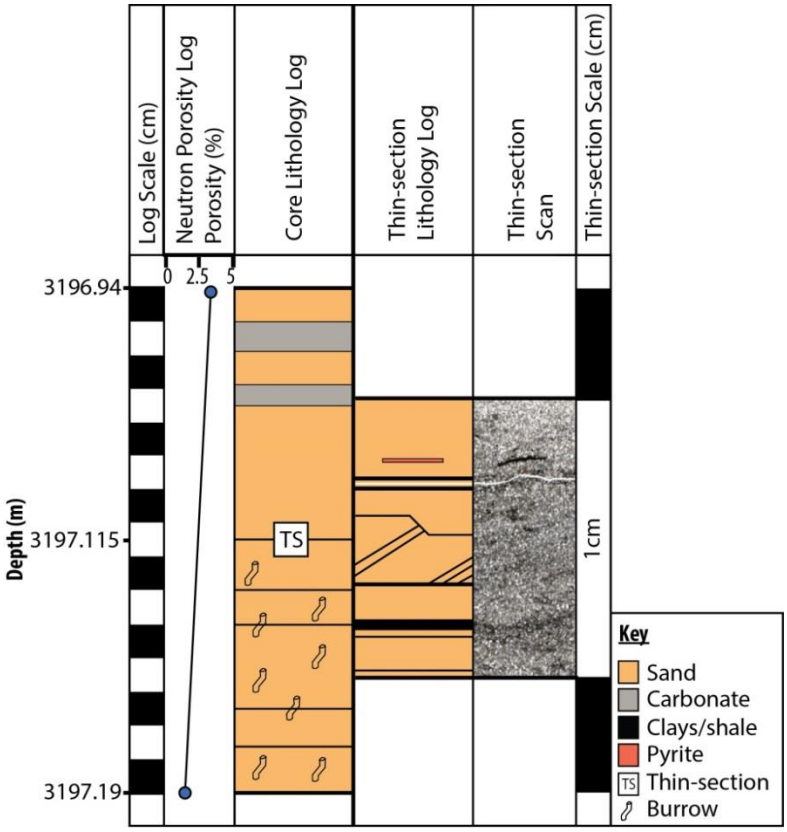

Figure 4.18 - Schematic showing a 15 cm section of the Sorenson well, to demonstrate the heterogeneities on multiple scales and the effect of such variations on the log porosity (neutron porosity) response. Thin-section is of sample 7_iiA, showing the heterogeneity in a 1 cm section.

The porosity values obtained from the calculation of grain density were compared to mercury injection porosity (Hg_{inj}) measurements. Hg_{inj} is the porosity obtained by forcing mercury into the sample as opposed to mercury density porosity/total porosity where mercury does not enter the pores of the sample. It would be expected that: density porosity > helium porosity > Hg_{inj} porosity. The largest values would be expected to be obtained by density porosity as this method captures the contribution of void spaces in both connected and unconnected realms. Helium is able to enter connected pores to 0.1 nm (Nawaby et al., 2009) and MICP (at a maximum analysis pressure of 39,000 psi) is able to interrogate connected pore throats to 5.6 nm.

This relationship is largely found in the middle Bakken, however in the regions near to the contact with the upper and lower Bakken, we see helium porosity values which are greater

than the total porosity (density porosity). We attribute this anomaly to small heterogeneities in individual samples. Whilst the samples analysed were cut from directly adjacent pieces of the same sample for the two different techniques, we found that that there are variations in mineralogy at the sub-millimetre to millimetre scale caused by small changes in detrital mineralogy or the products of diagenesis, see Chapter 3. Where calcite abundance is highest the porosity is lowest (Figure 4.11). It is suggested that the presence of a higher abundance of calcite in a sample or section of a sample, may have reduced the porosity in that analysis.

Pore Structure

The pore structure of unconventional, tight reservoirs such as the Bakken are challenging to characterise due to their nano-pore structure (Clarkson et al., 2012). Detailed work on the pore structure of the middle Bakken is significantly limited and restricted to pore system characterisation studies by Ramakrishna et al., (2010), Li et al., (2015) and Anyanwu (2015).

Pores can be thought of as having two main morphological features; throats and bodies. In this study we have obtained detailed size distributions for throats and bodies of connected pores.

Pore Throats

The pore throats of the middle Bakken have size distributions that are smaller than are those that are typically reported in sandstones (Nelson, 2009). In the middle Bakken, Anyanwu (2015), similarly showed the average pore throat size distribution is similar to that of the overlying and underlying Bakken shales.

In plots of PTSD's grouped by facies (Figure 4.20a) we noted that there are distinct differences between the PTSD's of different facies, yet within individual facies the PTSD's are largely similar. Where several facies have similar PTSD's we have grouped the facies into 'forms' (Figure 4.20b), where each showing different PSD characteristics. The smallest pore throats are observed in cemented facies (B, C, E) whereas the largest pore throats are observed in the uncemented facies (D1). We suggest the bimodal pore throat size distribution observed in facies D2 reflects variable calcite cementation; where the smallest

pore throats are common in the most cemented zones and larger pore throats represent larger pores in uncemented zones.

From this we have grouped the facies and averaged the intrusion volume at each pressure step/equivalent radius and fitted a moving average trend line to simplify the plot and allow direct comparison of the groupings. Form 1 is facies B, C, E & D1 and has an equivalent ~3-100 nm. Form 2 is composed of facies D2, which shows a characteristic non-symmetric biomodal pore throat size distribution with peaks at ~4 nm and 250 nm. A similar pore throat size distribution was recorded by Ramakrishna et al., (2010), in their study of the petrophysics of the middle Bakken. They suggested this trace-morphology was representative of the pore PTSD in the middle Bakken; from our data we suggest this is an over-simplification and several pore throat size distributions exist within the rocks of the middle Bakken.

A bi-modal pore size distribution such as 'form 3' has previously linked to lithology changes within a sample (Luo and Machel, 1995). In the work by Lou and Machel, they considered a very heterogeneous, dolomitised unit of Devonian age which is not significantly different to the samples of this study. In the middle Bakken this is likely to be due to millimetre scale lithological heterogeneity. We suggest this is a product of variable calcite cementation; here the peak at ~4 nm is due to calcite cementation whereas the peak at ~250 nm is attributed to inter-granular porosity in cleaner sandstone laminae, which is uncemented or less cemented region.

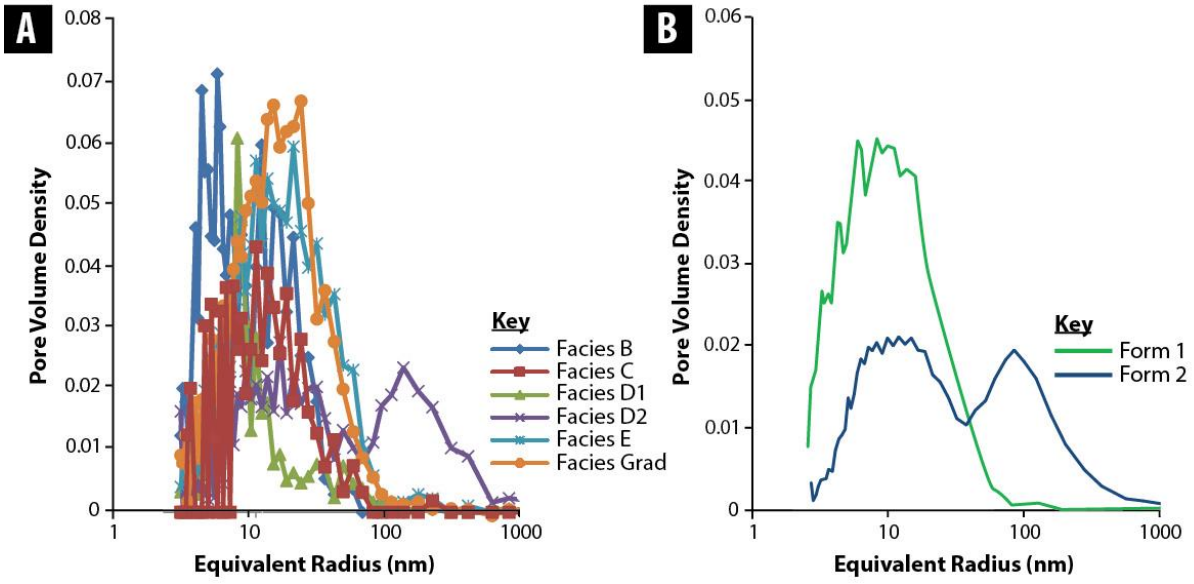

Figure 4.19 – Pore throat size distributions from mercury intrusion a) Plot of average pore throat size distribution of each middle Bakken facies. This was calculated by taking the mean intrusion volume of mercury for all the samples of each facies at each pressure step. b) The pore throat size distributions have been grouped into different forms of similar morphology and the pore volume density averaged for each pressure step/equivalent radius. For easy comparison, a trendline of the moving average (period 5) was fitted to the data. Form 1 includes samples from facies B, C, D1, & E and gradational. Form 2 includes facies D_2.

A similar approach was used by Li et al., 2015, in which they were unable to link pore type to mineralogy but instead identified three pore (PTSD)-mineral types; calcite- related pores (intragranular), clay-related pores and inter-granular pores. Comparing our PTSD-Facies relationship with the work of Li et al., 2015, we suggest that we can extend the association to a pore (PTSD)-mineral-facies relationship. In this Form 1 represents more calcite related pores, Form 2 – the bi-modal distribution of this form represents both calcite related pores and inter-granular pores.

Pore Bodies

The characteristics of the pore bodies were investigated by gas sorption. Low-pressure nitrogen gas isotherms were interpreted to be 'of type IV'; due to the persistence of convexity of the isotherm and the presence of the hysteresis loop (Figure 4.12) (Gregg and Sing, 1982). Type IV isotherms are thought to indicate weak gas-solid interactions and have been associated with mesoporous samples. Three samples, in group X, (Figure 4.12a) adsorbed significantly lower volumes of nitrogen than the rest of the samples. These samples were from both facies D1 and D2. There appears to be no obvious mineral control on these samples. Whilst these samples do have low porosities; they do not as a group have the lowest porosities by any of the techniques implemented. It is unclear why as a group these exhibit these pore system characteristics.

Pore body size distributions were measured using the BJH equations for pore bodies between 5- and 300 nm. Within this analysis range pore bodies are predominantly between 5-20 nm across and range up to ~134 nm across. Between 134 nm and the maximum resolvable pore body size (300 nm), no pores were identified.

Two pores were identified with apparently anomalous aspect ratios of 212 and 494. We suggest these 'pores' may not be pores and could be fractures or a product of unloading. As discussed previously their morphology suggests they are unlikely to be fractures, even though micro-cracks and fractures are thought to be an important featrure of the middle Bakken with respect to permeability (Li et al., 2015). An unloading mechanism was considered by Shanley et al., (2004) in tight, low permeability sandstones in the Greater Green River Basin; they found increases in over-burden stress on low permeability sandstones was small. Similar conclusions were drawn by Byrnes (1997) when comparing downhole in-situ measurements with helium porosimetry measurements.

Alternatively, pores such as these with extreme aspect ratios are interpreted to be sheet pores. Sheet pores have previously been identified and associated with dolomite crystals in both replacement dolomites (types 2, 3, 4 of this study) and void filling, microspar (type 6 dolomites in this study) (Wardlaw, 1976; Lindsay & Roth, 1982; Woody et al., 1996). It has been suggested that pores associated with dolomites are initially formed in polyhedral forms, which with further dolomite growth are reduced to tetrahedral forms and ultimately are destroyed leaving inter-boundary sheet-like pores (Wardlaw, 1976). Looking at the segmented images of pores, there are other similar pores, which have been broken by bridges, so are recorded as shorter pores. These pores are 'grain boundary' pores, many of which run parallel to sub-parallel to bedding and are a component of inter-granular porosity.

Inter-granular Porosity

The H3 hysteresis loop form observed in the low pressure gas sorption isotherms of all middle Bakken samples have previously been reported in samples with slit-like pores or plate-like particles (Gregg and Sing, 1982). This pore morphology has previously been observed in other tight gas reservoirs plays (e.g. Shanley et al., 2004; Silin et al., 2011). In the study of quartz and calcite cemented sandstones by Shanley et al., they found the majority of the pores were of slit morphologies (referred to as slot pores). These pores were found to connect grain dissolution pores. They suggest the flow paths within these rocks are provided by the slot pores. Several workers go further suggesting that this morphology of thin intergranular pore, <3 µm across are common within sandstones, e.g. Figure 4.13g (Keighin & Sampath, 1982; Brower & Morrow, 1985).

We acknowledge that interpreting pore shape from the form of an isotherm hysteresis loop is not on its own conclusive as there may be a mixture of pore morphologies in the samples. Direct observation of individual pores and image analysis of large area electron image maps we are able to largely mitigate this uncertainty. Image analysis showed there are both elongate and rounded pores present within the samples (Figure 4.18). Inspection of the elongate shaped apparently slit-pores on chip samples at high-magnification suggests there are clay minerals within these pores, which in some instances appear to 'bridge' these pores. What remains unclear from both our observations is whether these elongate pores are 'real' and not a product of unloading of the sample as observed in the work on the microstructure of shales by Heath et al., (2011). We also, question whether the observations of clay filling and clay bridges formed from drying of clay minerals after coring; forming the curled-up morphology; a form observed in laboratory experiments by Nahlawi & Kodikara (2002). This uncertainty aside, what is clear is that a seemingly slit-pore or grain boundary pores does have clay minerals in it; which are only observed at higher magnification. Therefore, we suggest our estimates of inter-granular porosity are most likely over estimated.

Conversely pore-body sizes distributions have resolved inter-granular porosity at sizes below the resolution of BIB-SEM image segmentation, so in this respect, pores are underestimated. To capture these pores on representative elementary areas would be impractical and potentially computationally difficult if married with SEM-EDX maps.

We have identified intergranular pores <90 nm (smallest resolved pore in thresholded images) by electron microscopy. This appears particularly prevalent in clay rich zones, where small <50 nm inter-granular pores are not uncommon, particularly between delicate authigenic clay structures.

The results of low pressure gas sorption, suggest intergranular pores present between 4-300 nm are predominantly between 5-20 nm in size. Comparing the results of BIB-SEM observations and low pressure gas sorption measurements, it seems likely that grain boundary/slit pores exist, though to what extent and the exact cause of which is less clear.

Intra-granular Porosity: Pore 'Hosts'

Intra-granular pores are voids within individual mineral grains. By overlaying segmented pores onto mineral maps, the intergranular porosity (pores >90 nm) of individual mineral phases was estimated. By doing so we have assumed that there is no connectivity in the plane of the image. Intra-granular porosity was observed in detrital grains of quartz, feldspar and dolomite. Intra-granular porosity was predominantly found in calcite, dolomite, and quartz.

Quartz

Intra-granular pores in quartz have contributed significantly to the intra-granular porosity of the middle Bakken. Intra-granular porosity in quartz has been reported by several studies (Burley and Kantorowicz, 1986). Previous workers have suggested these pores are the product of dissolution. The formation of quartz dissolution pores is thought to occur in alkaline conditions; similar to those required for calcite precipitation (e.g., Epstein and Freidman, 1983; Normore, 2006; Zaid and Gahtani, 2015). It has been suggested that the change in pH was a product of biological activity (Friedman et al., 1976; Bennett and Siegel, 1987; Gorbushina and Palinska, 1999). Photosynthesis of algae results in more alkaline conditions. Highly alkaline environments are however not common in nature. This apparent dissolution texture has also been observed in quartz which has been deposited in shallow marine sediments and is similar in nature to textures formed by biofilm growth in laboratory experiments (Brehm et al., 2005).

Calcite

Detrital calcite has preserved some intragranular porosity due to the shape of the bioclast in which it is present. For the calculation of intragranular porosity in diagenetic cements bioclasts are easily identified and omitted. Intragranular porosity is common in diagenetic calcite cements in the middle Bakken.

Primary porosity in calcite cement in sandstones and siltstones has previously been attributed to incomplete cementation of the framework (Murray, 1960). The framework can be of organic or inorganic composition. This framework is thought to act like a scaffold, creating the intergranular lattice. The voids of which are termed constructional vugs when the cement does not infill them (Murray, 1960). It is also thought such vugs can

form where cements encapsulate organic matter which later matures to hydrocarbon products and migrates away, leaving a pore space behind (Murray, 1960). Chouquette and Pray (1970) support this perspective, arguing that much of the intragranular porosity present in carbonate minerals such as calcite is a primary, constructional fabric. In their study they refer to this type of porosity as 'growth-framework porosity'.

In an earlier study of porosity in middle Bakken diagenesis, Ferdous (2001) suggests porosity in the early calcite cement was a result of dissolution. The patchy corroded remnants which Ferdous (2001) describes as evidence for dissolution could, possibly be equivalent to 'type 3' calcite (Chapter 3) described in this study. We suggest whilst this is possible, the very rare nature of this phase, variable spatial abundance and rounded, and often lobate morphology of these cements makes this suggestion unlikely.

Dolomite

If we assume that remaining intragranular porosity is preserved primary porosity, this appears to support our earlier assertion that carbonate minerals are a chief control on porosity loss. Whilst this seems likely in the case of calcite; the central location of the largest vugs in dolomite indicates this is unlikely to be the case for dolomite. Lucia (1995) suggests that individual vugs are connected only by inter-granular porosity; therefore, individual vugs contribute little to the overall permeability of the rock; that is dolomite vugs are unlikely to be important for connected porosity.

Some previous workers have postulated there has been a period of dolomite dissolution in the middle Bakken (Last & Edwards, 1991; Ferdous, 2001; Pitman et al., 2001; Alexandre, 2011). In chapter 3 we suggested that the presence of sharp, euhedral edges discounts a dissolution mechanism in these samples. Furthermore, in this chapter we identified that much of the intragranular porosity is at the core of the dolomite rhombs which coupled with the absence of connectivity to the edge of the cement or a connection to the inter-granular main pore network, leads us to suggest they are unlikely to be formed by dissolution.

The assertion that much of the middle Bakken dolomite is a replacement of earlier formed calcite, made in Chapters 3 & 5 has implications for the origin of the intra-granular porosity in dolomite. Early workers on the replacement of calcite by dolomite suggested there was

a volume reduction during the process (Weyl, 1960; Morrow, 1982; Machel & Mountjoy, 1986). Weyl (1960) suggests there can be up to a 13% decrease in rock volume during the transformation of calcite to dolomite and therefore a 13% increase in porosity by ion-for-ion replacement reactions as calcium is replaced by magnesium. This model assumes a local source of magnesium and carbonate ions, mechanisms for both of which are proposed in Chapter 3. Murray (1960) suggests this is only a viable mechanism if there is a mechanism to remove the calcium ions replaced by magnesium ions. We can only make reasoned suggestions to the fluid paths ways during the Devonian. In Chapter 3 we suggested that dolomite formation was very early and likely occurred at very shallow depths before significant compaction had occurred so it possible there was fluid communication into underlying formations, driven in part due to the addition of percolating pore fluids from above.

Assuming magnesium ions were at excess, we cautiously suggest small differences in local fluid flow may explain how vuggy (type 2) dolomites can occur in close spatial proximity to non-porous (type 3) dolomites. Where calcium ions were not efficiently removed, dolomitisation continues and the porosity is filled; yet where local fluids are able to remove calcium ions, the porosity is enhanced.

The mechanism proposed by Weyl (1960) for mole-for-mole replacement and supported by Murray (1960) has however been much disputed (Halley & Schmoker, 1983; Lucia, 2004). Several workers have suggested porosity in dolomites is inherited porosity from the precursor rock (Halley & Schmoker, 1983; Sun, 1995; Lucia, 2004). In the Lucia (2004) study, they suggest that in a precursor limestone (of their study) the porosity was likely to have been in the range of 30-40%, which would be inherited by the dolostone during the replacement phase. They suggest any change in molar volume will be offset by the precipitation of pore-filling dolomite using carbonate transported in the dolomitizing fluid. Once replacement is completed, dolomitisation is thought to be able to continue by the process of over-dolomitisation. A process which Lucia (2004) suggests could reduce the porosity to as low as 5%. Equations for replacement and over-dolomitisation were proposed by Morrow (1990), in Equations 4.5 and 4.6 respectively.

$$(2 - x)CaCO_3 + Mg^{2+} + xCO_3^{2-} \rightarrow CaMg(CO_3)_2 + (1 - x)Ca^{2+}$$

Equation 4.5 - Replacement of calcite by dolomite (Morrow, 1982). Where x is the moles of carbonate added from the dolomitising fluid.

$$Ca^{2+} + Mg^{2+} + 2CO_3 \rightarrow CaMg(CO_3)_2$$

Equation 4.6 - Pore filling, over-dolomitisation reaction (Lucia, 2004).

The process of over-dolomitisation is based on the idea that dolomitisation continues after calcite is replaced. In this model the assumption is that carbonate will continue to be available for the precipitation of dolomite after the replacement of calcite; until such time the water reaches equilibrium with dolomite and calcite/aragonite (Lucia, 2004).

A key commonality and limitation with all of the studies that oppose this theory is that they refer to the dolomitisation of a limestone (as with the Lucia study discussed above), however in this study we are dealing with a variably calcite cemented sandstone. This introduces uncertainty; can this and does this mechanism apply in a different geological regime i.e. that of a carbonate cemented sandstone?

The presence of more intragranular porosity in dolomite than calcite supports the suggestion the assertion that porosity in dolomite was created and not inherited from the calcite precursor. We cannot say for certain whether the vuggy intragranular porosity in dolomite formed by mole-for-mole replacement of calcium by magnesium though this seems to be only possible mechanism. We do suggest that the process of over-dolomitisation did not occur in the middle Bakken as significant quantities of the early calcite cement remains in the samples and was observed in this study.

As part of our assessment of dolomite morphologies, we identified planar-s textures within the middle Bakken (Chapter 3). Woody et al., (1996) showed that permeability increases in planar-e morphologies a greater rate than in planar-s morphologies. They also found less vug porosity and less inter-crystalline porosity associated with subhedral dolomites (planar-s) than euhedral (planar-e) morphologies of dolomite; however they were unsure to why they this difference occurs.

Application to Fluid Transport

The description of porosity measured at different scales and the detailed characterisation of the pore morphology with respect to the effect of mineralogy allows a better understanding of the fluid transport capacity of a rock (Dullien, 2012; Bear, 2013). By identifying the principle pore occluding minerals; calcite and dolomite; higher porosity and permeability areas can be more quickly identified from readily identifiable carbonate-poor regions (Bloch, 1991; Pöppelreiter et al., 2005; Tobin et al., 2010).

Permeability models often use assumptions and/or simplifications of the pore and assume the pore morphology is constant. Permeability obtained from MICP with the Yang & Aplin (1998) equation is consistently around one order of magnitude lower than Klinkenberg corrected air permeability. Large variations between MICP permeability calculations and direct permeability measurements have been reported by previous workers (Olsen & Grigg, 2008). Similarly, Kurtoglu et al. (2014) noted that RCA air permeability values, were around 1 order of magnitude smaller again than permeability values obtained from downhole well tests. They attribute this discrepancy to the contribution of micro-fracturing to the reservoir permeability of the middle Bakken.

Irrespective of the technique used, the permeabilities we report both from MICP and RCA calculations are very low. These values are comparable to other studies of middle Bakken permeability (Murray, 1968; Webster et al., 1984; Pitman et al., 2001; Hawthorne et al., 2013; Kurtoglu et al., 2014; He & Ling, 2015; Karimi et al., 2015; Li et al., 2015).
Le Fever et al., found the middle Bakken measured permeability values of between <0.01 mD to 5.8 mD. Kurtoglu et al., (2014) found the average middle Bakken RCA air permeability to be 0.00144 mD, which is 2 orders of magnitude higher than the average value of 6.02×10^{-5} mD calculated from MICP in this study. Sonnenberg & Pramudito, (2009), report slightly higher values with an average middle Bakken permeability of 0.5 mD.

In the most recent study of permeability in the middle Bakken, Li et al., (2015) calculated permeability from mercury intrusion data using the method developed by Swanson (1981). They found permeability values range from 1.00×10^{-3} to 1.00×10^{-5} mD which is similar to values obtained in this study of between 3.76×10^{-4} and 8×10^{-6}mD. We attribute

the slightly increased permeability in their study to micro-fractures identified in their work but not observed in samples of this study.

We have identified permeability variations over three orders of magnitude from permeability calculations on mercury intrusion data. The lack of fractures observed in samples of this well, means from the data presented here we cannot suggest a viable explanation to the apparent variation in permeability in the Sorenson core. Edwards (1993) suggests the reduction in water flood injection rates due to fines migration indicates that zones of decreased permeability may be due to illite and fine grained dolomite may be blocking pore throats; preventing communication between pores. SEM observations suggest both fine grained dolomite (Type 6, see Chapter 3) and authigenic illite, Figure 3.24, does form in and across pore spaces, which would in principle support Edwards (1993) assertions, though this sole observation is not sufficient to support this conclusion. A similar idea has been proposed in studies by Soeder and Randolph (1987) and Dutton et al. (1993). They suggest that this mechanism of 'pore throat plugging by clay minerals' is common in reservoirs with permeability values of 0.01 - 0.1 mD. Middle Bakken permeability's are generally a little lower; however, recognising the variations in permeability measurement (discussed above), it should not be discounted, and perhaps considered with caution and the basis for further investigation.

Conclusions

The middle Bakken is a low porosity, and very low permeability formation. Early calcite cementation has largely inhibited compaction in the middle Bakken. The highest porosity is found in facies D_1 and the lowest in facies B.

Controls on the porosity are predominantly below the scale of a facies. Within a facies the best reservoir quality is found in areas of low carbonate mineral abundance. The principle pore occluding minerals are calcite and dolomite.

Interpretation of low pressure nitrogen isotherms indicates the middle Bakken is a mesoporous unit. Intergranular pores are associated with clay rich zones. Intragranular pore space makes up a significant component of the pore system of the middle Bakken. Intragranular porosity is predominantly found in quartz, calcite and dolomite. Porosity in quartz grain is thought to be a product of dissolution, whereas the intragranular porosity

in calcite is thought to be due to incomplete cementation, creating framework-pores. Porosity in dolomite is postulated to be a product of the process of calcite replacement.

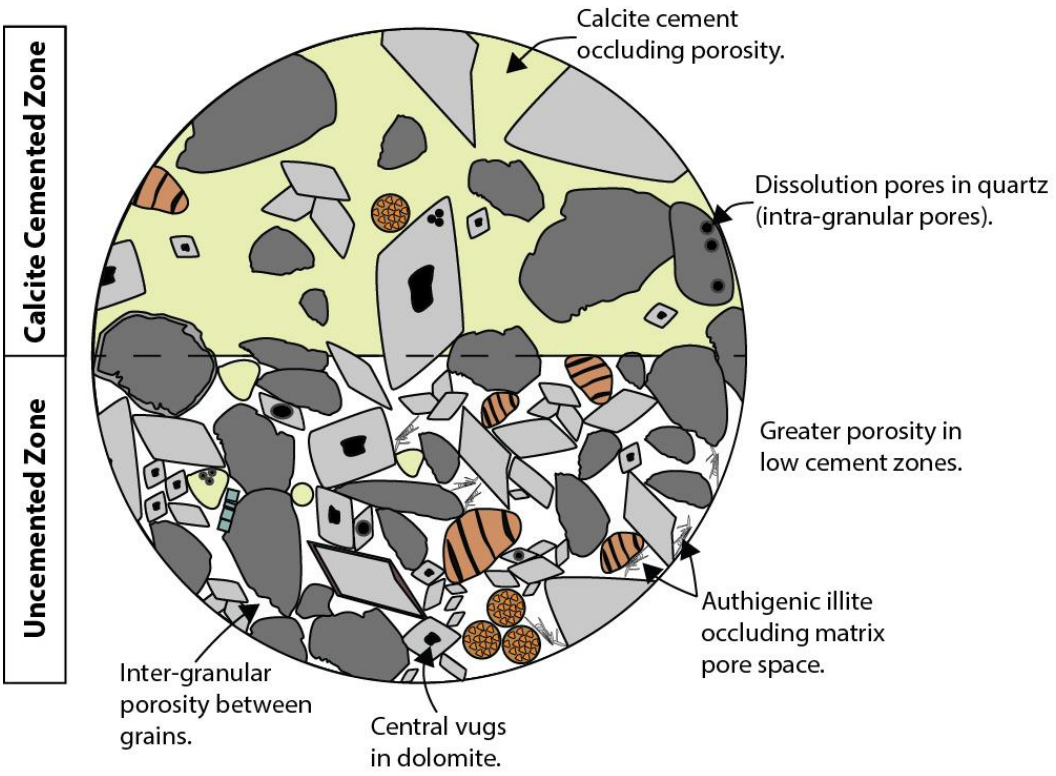

Figure 4.20– Summary schematic showing the different types of porosity present in the middle Bakken member. The contrast in pore types is shown between a zone of calcite cementation and a region lacking cement.

Pores of the middle Bakken have pore throats with radii which are < 100 nm; they are small. Only in facies D2 are pore throats with a radii >100 nm found. Pore bodies are all < 135 nm but predominantly between 5 – 20 nm in size. Porosity and permeability measurements indicate that these are very tight rocks composed of small pores.

References

Alexandre, C.S., Sonnenberg, S. and Sarg, J.F., 2012. Diagenesis of the Bakken Formation, Elm Coulee Field, Richland County, Montana. In AAPG Annual Convention and Exhibition.

Al-Ramadan, K. A., Hussain, M., Imam, B. & Saner, S. (2004). Lithologic characteristics and diagenesis of the Devonian Jauf sandstone at Ghawar Field, eastern Saudi Arabia. Marine and Petroleum Geology 21, p. 1221-1234.

Amann-Hildenbrand, A., Dietrichs, J. P. & Krooss, B. M. (2015). Effective gas permeability of Tight Gas Sandstones as a function of capillary pressure – a non-steady-state approach. Geofluids.

Anovitz, L. M. & Cole, D. R. (2015). Characterization and analysis of porosity and pore structures. Rev Mineral Geochem 80, p. 61-164.

Anyanwu, J.I., (2015). Nanopetrophysics Characterization of The Bakken Formation, Williston Basin, North Dakota, USA. Masters Thesis. University of Texas Arlington.

Athy, L. F. (1930). Density, porosity, and compaction of sedimentary rocks. AAPG Bulletin 14, p. 1-24.

Baldwin, C. A., Sederman, A. J., Mantle, M. D., Alexander, P. & Gladden, L. F. (1996). Determination and characterization of the structure of a pore space from 3D volume images. Journal of Colloid and Interface Science 181, p. 79-92.

Barrett, E. P., Joyner, L. G. & Halenda, P. P. (1951). The determination of pore volume and area distributions in porous substances. I. Computations from nitrogen isotherms. Journal of the American chemical society 73, p. 373-380.

Bear, J. (2013). Dynamics of fluids in porous media. Courier Corporation.

Bennett, P. & Siegel, D. (1987). Increased solubility of quartz in water due to complexing by organic compounds. Nature 326, p. 684 – 686.

Bloch, S. (1991). Empirical Prediction of Porosity and Permeability in Sandstones (1). AAPG Bulletin 75, p. 1145-1160.

Brehm, U., Gorbushina, A. & Mottershead, D. (2005). The role of microorganisms and biofilms in the breakdown and dissolution of quartz and glass. Palaeogeography, Palaeoclimatology, Palaeoecology 219, p. 117-129.

Brower, K. & Morrow, N. (1985). Fluid flow in cracks as related to low-permeability gas sands. Society of Petroleum Engineers Journal 25, p. 191-201.

Brunauer, S., Deming, L. S., Deming, W. E. & Teller, E. (1940). On a theory of the van der Waals adsorption of gases. Journal of the American chemical society 62, p. 1723-1732.

Brunauer, S., Emmett, P. H. & Teller, E. (1938). Adsorption of gases in multimolecular layers. Journal of the American chemical society 60, p. 309-319.

Burley, S.D. and Kantorowicz, J.D., (1986). Thin section and SEM textural criteria for the recognition of cement-dissolution porosity in sandstones. Sedimentology, 33(4), pp.587-604.

Bustin, R. M., Bustin, A. M., Cui, A., Ross, D. & Pathi, V. M. (2008). Impact of shale properties on pore structure and storage characteristics. SPE shale gas production conference: Society of Petroleum Engineers.

Byrnes, A. P. (1997). Reservoir characteristics of low-permeability sandstones in the Rocky Mountains. Mountain Geologist 34, p. 39-48.

Cepuritis, R., Wigum, B., Garboczi, E., Mørtsell, E. & Jacobsen, S. (2014). Filler from crushed aggregate for concrete: Pore structure, specific surface, particle shape and size distribution. Cement and Concrete Composites 54, p. 2-16.

Chalmers, G. R. & Bustin, R. M. (2007). The organic matter distribution and methane capacity of the Lower Cretaceous strata of Northeastern British Columbia, Canada. International Journal of Coal Geology 70, p. 223-239.

Chalmers, G. R., Bustin, R. M. & Power, I. M. (2012). Characterization of gas shale pore systems by porosimetry, pycnometry, surface area, and field emission scanning electron microscopy/transmission electron microscopy image analyses: Examples from the Barnett, Woodford, Haynesville, Marcellus, and Doig units. AAPG Bulletin 96, p. 1099-1119.

Chalmers, G. R., Ross, D. J. & Bustin, R. M. (2012). Geological controls on matrix permeability of Devonian Gas Shales in the Horn River and Liard basins, northeastern British Columbia, Canada. International Journal of Coal Geology 103, p. 120-131.

Choquette, P. W. & Pray, L. C. (1970). Geologic nomenclature and classification of porosity in sedimentary carbonates. AAPG Bulletin 54, p. 207-250.

Chuhan, F. A., Kjeldstad, A., Bjørlykke, K. & Høeg, K. (2003). Experimental compression of loose sands: relevance to porosity reduction during burial in sedimentary basins. Canadian Geotechnical Journal 40, p. 995-1011.

Clarkson, C. R., Solano, N., Bustin, R., Bustin, A., Chalmers, G., He, L., Melnichenko, Y. B., Radliński, A. & Blach, T. P. (2013). Pore structure characterization of North American shale gas reservoirs using USANS/SANS, gas adsorption, and mercury intrusion. Fuel 103, p. 606-616.

Curtis, M., Sondergeld, C. & Rai, C. (2013). Relationship between organic shale microstructure and hydrocarbon generation. Paper SPE 164540 presented at SPE Unconventional Resources Conference, Woodland, Houston, USA.

Dahlberg, K. E. & Fitz, D. (1988).: An Integrated Approach. SPWLA 29th Annual Logging Symposium: Society of Petrophysicists and Well-Log Analysts, p. 1 – 18.

Demirmen, F. (1971). Counting error in petrographic point-count analysis: a theoretical and experimental study. Journal of the International Association for Mathematical Geology 3, p. 15-41.

Ducharme, D. & Murray, D. L. (1980). Heavy oil occurrences of the Cactus Lake area Saskatchewan. Saskatchewan Geological Society Special Publication Number 5, p. 64 – 95.

Dullien, F. A. (2012). Porous media: fluid transport and pore structure. Academic press, p.574.

Dutton, S. P. (1993). Major low-permeability sandstone gas reservoirs in the Continental United States. Bureau of Economic Geology, University of Texas at Austin.

Edwards, W. W. (1993). Sedimentology and diagenesis of the Bakken Formation in Daly Field, southwest Manitoba. Master's Thesis. University of Manitoba.

Ehrenberg, S. & Nadeau, P. (2005). Sandstone vs. carbonate petroleum reservoirs: A global perspective on porosity-depth and porosity-permeability relationships. AAPG Bulletin 89, p. 435-445.

Ellis, D. V. & Singer, J. M. (2007). Well logging for earth scientists. Springer Science & Business Media, p. 708.

Epstein, S. A. & Friedman, G. M. (1983). Depositional and diagenetic relationships between Gulf of Elat (Aqaba) and Mesozoic of United States east coast offshore. AAPG Bulletin 67, p. 953-962.

Ferdous, H., (2001). Regional sedimentology and diagenesis of the Middle Bakken Member: implications for reservoir rock distribution in southern Saskatchewan. Unpublished thesis, Department of Geological Sciences: University of Saskatchewan, p. 467.

Fishman, N. S. E., Sven O. (2013). Traces In the Dark—Sedimentary Processes and Facies Gradients In the Upper Shale Member of the Upper Devonian–Lower Mississippian Bakken Formation, Williston Basin, North Dakota, U.S.A. Journal of Sedimentary Research 83, p. 803-824.

Friedman, M. (1976). Porosity, permeability, and rock mechanics-a review. The 17th US Symposium on Rock Mechanics (USRMS). American Rock Mechanics Association.

Gluyas, J. & Swarbrick, R. (2013). Petroleum Geoscience. John Wiley & Sons, p. 376.

Gorbushina, A. A. & Palinska, K. A. (1999). Biodeteriorative processes on glass: experimental proof of the role of fungi and cyanobacteria. Aerobiologia 15, p. 183-192.

Gregg, S. & Sing, K. (1982). Adsorption, surface area and porosity academic. New York, p. 242-245.

Groen, J. C., Peffer, L. A. & Pérez-Ramírez, J. (2003). Pore size determination in modified micro-and mesoporous materials. Pitfalls and limitations in gas adsorption data analysis. Microporous and Mesoporous Materials 60, p. 1-17.

Gueven, A. & Hicsasmaz, Z. (2013). Pore Structure in Food: Simulation, Measurement and Applications. Springer, p. 50.

Gunter, G., Pinch, J., Finneran, J. & Bryant, W. (1997). Overview of an integrated process model to develop petro-physical based reservoir descriptions. SPE Annual Technical Conference and Exhibition: Society of Petroleum Engineers.

Halley, R. B. & Schmoker, J. W. (1983). High-porosity Cenozoic carbonate rocks of south Florida: progressive loss of porosity with depth. AAPG Bulletin 67, p. 191-200.

Hawthorne, S. B., Gorecki, C. D., Sorensen, J. A., Steadman, E. N., Harju, J. A. & Melzer, S. (2013). Hydrocarbon Mobilization Mechanisms from Upper, Middle, and Lower Bakken Reservoir Rocks Exposed to CO. SPE Unconventional Resources Conference Canada: Society of Petroleum Engineers.

He, J., Ling, K., Pei, P. & Ni, X. (2015). Experimental Investigation on the Effect of Pore Pressure on Rock Permeability-Bakken Formation Case. 49th US Rock Mechanics/Geomechanics Symposium: American Rock Mechanics Association.

Heath, J. E., Dewers, T. A., McPherson, B. J. O. L., Petrusak, R., Chidsey, T. C., Rinehart, A. J. & Mozley, P. S. (2011). Pore networks in continental and marine mudstones: Characteristics and controls on sealing behavior. Geosphere 7, p. 429-454.

Hesse, R. & Abid, L. (2009). Carbonate cementation-the key to reservoir properties of four sandstone levels (Cretaceous) in the Hibernia Oilfield, Jeanne d'Arc Basin, Newfoundland, Canada. Carbonate Cementation in Sandstones: Distribution Patterns and Geochemical Evolution (Special Publication 26 of the IAS) 72, 363.

Houben, M., Desbois, G. & Urai, J. (2013). Pore morphology and distribution in the Shaly facies of Opalinus Clay (Mont Terri, Switzerland): Insights from representative 2D BIB–SEM investigations on mm to nm scale. Applied Clay Science 71, p.82-97.

Hurley, N. F. & Lohmann, K. C. (1989). Diagenesis of Devonian reefal carbonates in the Oscar Range, Canning Basin, Western Australia. Journal of Sedimentary Research 59, p. 127-146.

Josh, M., Esteban, L., Delle Piane, C., Sarout, J., Dewhurst, D. N. & Clennell, M. B. (2012). Laboratory characterisation of shale properties. Journal of Petroleum Science and Engineering 88–89, p. 107-124.

Karasinski, D. R. (2006). Sedimentology and Hydrocarbon Potential of the Devonian Three Forks and Mississippian Bakken Formations, Sinclair Area, Southeast Saskatchewan-southwest Manitoba. Masters Thesis. University of Manitoba (Canada).

Karimi, S. & Kazemi, H. (2015). Capillary Pressure Measurement using Reservoir Fluids in a Middle Bakken Core. SPE Western Regional Meeting: Society of Petroleum Engineers.

Katz, A. & Thompson, A. (1986). Quantitative prediction of permeability in porous rock. Physical review B 34, p. 8179 - 8188.

Kazimierz, T., Jacek, T. and Stanisław, R., 2004. Evaluation of rock porosity measurement accuracy with a helium porosimeter. Acta Montanistica Slovaca, 9(3), pp.316-318.

Keelan, D. K. (1972). A critical review of core analysis techniques. Journal of Canadian Petroleum Technology 11, p. 42 - 55.

Keighin, C. W. & Sampath, K. (1982). Evaluation of pore geometry of some low-permeability sandstones-Uinta Basin. Journal of petroleum technology 34, p. 65-70.

Kent, D. M. (1987). Paleotectonic Controls on Sedimentation in the Northern Williston Basin, Saskatchewan. In: Longman, M. (ed.) Williston Basin: Anatomy of a Cratonic Oil Province. Denver: The Rocky Mountain Association of Geologists, p. 44 - 55.

Klaver, J., Desbois, G., Littke, R. & Urai, J. L. (2015). BIB-SEM characterization of pore space morphology and distribution in postmature to overmature samples from the Haynesville and Bossier Shales. Marine and Petroleum Geology 59, p. 451 - 466.

Klaver, J., Desbois, G., Urai, J. L. & Littke, R. (2012). BIB-SEM study of the pore space morphology in early mature Posidonia Shale from the Hils area, Germany. International Journal of Coal Geology 103, p. 12-25.

Klinkenberg, L. (1941). The permeability of porous media to liquids and gases.

American Petroleum Institute, p. 200 – 213.Kuila, U. & Prasad, M. (2013). Specific surface area and pore-size distribution in clays and shales. Geophysical Prospecting 61, p. 341-362.

Kurtoglu, B., Kazemi, H., Rosen, R., Mickelson, W. & Kosanke, T. (2014). A Rock and Fluid Study of Middle Bakken Formation: Key to Enhanced Oil Recovery. SPE/CSUR Unconventional Resources Conference–Canada: Society of Petroleum Engineers.

Li, H., Dawson, M., Hart, B. & Radjef, E. (2015). Characterizing the Middle Bakken: Laboratory Measurement of Middle Bakken Properties. Unconventional Resources Technology Conference (URTEC).

Lima, R. D. & De Ros, L. F. (2002). The role of depositional setting and diagenesis on the reservoir quality of Devonian sandstones from the Solimoes Basin, Brazilian Amazonia. Marine and Petroleum Geology 19, p. 1047-1071.

Lindsay, R. F. & Roth, M. S. (1982). Carbonate and evaporite facies, dolomitization and reservoir distribution of the Mission Canyon Formation, Little Knife Field, North Dakota. Williston Basin Symposium.

Long, R. & Yost, A. (2011). Bakken–The Biggest Oil Resource in the United States? Center for Natural Gas & Oil 281, p. 494-2520.

Loucks, R. G., Reed, R. M., Ruppel, S. C. & Hacmes, U. (2012). Spectrum of pore types and networks in mudrocks and a descriptive classification for matrix-related mudrock pores. AAPG Bulletin 96, p. 1071-1098.

Loucks, R. G., Reed, R. M., Ruppel, S. C. & Jarvie, D. M. (2009). Morphology, genesis, and distribution of nanometer-scale pores in siliceous mudstones of the Mississippian Barnett Shale. Journal of Sedimentary Research 79, p. 848-861.

Lucia, F. J. (1995). Rock-fabric/petrophysical classification of carbonate pore space for reservoir characterization. AAPG Bulletin-American Association of Petroleum Geologists 79, p. 1275-1300.

Lundegard, P. D. (1992). Sandstone Porosity Loss-A "Big Picture" View of the Importance of Compaction. Journal of Sedimentary Research 62, p. 250 - 260.

Luo, P. & Machel, H. G. (1995). Pore size and pore throat types in a heterogeneous dolostone reservoir, Devonian Grosmont Formation, Western Canada sedimentary basin. AAPG Bulletin 79, p. 1698-1719.

Machel, H.-G. & Mountjoy, E. W. (1986). Chemistry and environments of dolomitization—a reappraisal. Earth-Science Reviews 23, p. 175-222.

Manger, G. E. (1963). Porosity and bulk density of sedimentary rocks. USGS Bulletin 1144-E, p. 60.

Mathia, E. J. (2015). Geological evaluation of posidonia and wealden organic-rich shales: geochemical and diagenetic controls on pore system evolution. PhD Thesis. Newcastle University, p. 252.

Medeiros, F., Ozkan, E. & Kazemi, H. (2007). Productivity and drainage area of fractured horizontal wells in tight gas reservoirs. Rocky Mountain Oil & Gas Technology Symposium: Society of Petroleum Engineers.

Meissner, F. (1978). Petroleum geology of the Bakken Formation Williston basin, North Dakota and Montana. The economic geology of the Williston basin: Montana Geological Society 24th Annual Conference. Williston Basin Symposium, p. 207 - 227.

Meissner, F. F. (1991). Petroleum Geology of the Bakken Formation Williston Basin, North Dakota and Montana. Montana Geological Society. Guidebook to Geology and Horizontal Drilling of the Bakken Formation, p. 19 – 42.

Milliken, K. L., Rudnicki, M., Awwiller, D. N. & Zhang, T. (2013). Organic matter–hosted pore system, Marcellus formation (Devonian), Pennsylvania. AAPG Bulletin 97, p. 177-200.

Milner, M., McLin, R. & Petriello, J. (2010). Imaging texture and porosity in mudstones and shales: Comparison of secondary and ion-milled backscatter SEM methods. Canadian Unconventional Resources and International Petroleum Conference: Society of Petroleum Engineers.

Morrow, D. (1982). Diagenesis. 1. Dolomite. 1. the Chemistry of Dolomitization and Dolomite Precipitation. Geoscience Canada 9, p. 5-13.

Murray, R. C. (1960). Origin of porosity in carbonate rocks. Journal of Sedimentary Research 30, p. 59 – 84.

Nabawy, B. S., Géraud, Y., Rochette, P. & Bur, N. (2009). Pore-throat characterization in highly porous and permeable sandstones. AAPG Bulletin 93, p. 719-739.

Nahlawi, H. & Kodikara, J. (2002). Experimental observations on curling of desiccating clay. Proc., Third International Conference on Unsaturated Soils, p. 553-556.

Nelson, P. H. (2009). Pore-throat sizes in sandstones, tight sandstones, and shales. AAPG Bulletin 93, p. 329-340.

Normore, L. S. (2006). Origin, Distribution and Paragenetic Sequence of Carbonate Cements in the Ben Nevis Formation, White Rose Field, Jeanne D'Arc Basin, Offshore Newfoundland, Canada. Master's Thesis. Memorial University of Newfoundland.

Olson, R. K. & Grigg, M. W. (2008). Mercury Injection Capillary Pressure (MICP): A Useful Tool for Improved Understanding of Porosity and Matrix Permeability Distributions in Shale Reservoirs. Search and Discovery Article 40322.

Pitman, J. K., Price, L. C. & LeFever, J. A. (2001). Diagenesis and fracture development in the Bakken Formation, Williston Basin: Implications for reservoir quality in the middle member: US Department of the Interior, US Geological Survey Professional Paper 1653.

Pittman, E. D. (1992). Relationship of porosity and permeability to various parameters derived from mercury injection-capillary pressure curves for sandstone (1). AAPG Bulletin 76, p. 191-198.

Pöppelreiter, M., Borkhataria, R., Aigner, T. & Pipping, K. (2005). Production from Muschelkalk carbonates (Triassic, NE Netherlands): unique play or overlooked opportunity? Geological Society, London, Petroleum Geology Conference series: Geological Society of London, p. 299-315.

Ramakrishna, S., Balliet, R., Miller, D., Sarvotham, S. & Merkel, D. (2010). Formation evaluation in the Bakken complex using laboratory core data and advanced logging technologies. SPWLA 51st Annual Logging Symposium: Society of Petrophysicists and Well-Log Analysts.

Ramm, M. & Bjørlykke, K. (1994). Porosity/depth trends in reservoir sandstones: Assessing the quantitative effects of varying pore-pressure, temperature history and mineralogy, Norwegian Shelf data. Clay minerals 29, p. 475-490.

Ritter, H. & Drake, L. (1945). Pressure porosimeter and determination of complete macropore-size distributions. Pressure porosimeter and determination of complete macropore-size distributions. Industrial & Engineering Chemistry Analytical Edition 17, p. 782-786.

Robinet, J. C., Sardini, P., Siitari-Kauppi, M., Prêt, D. & Yven, B. (2015). Upscaling the porosity of the Callovo-Oxfordian mudstone from the pore scale to the formation scale; insights from the 3H-PMMA autoradiography technique and SEM BSE imaging. Sedimentary Geology 321, p. 1-10.

Ross, D. J. & Bustin, R. M. (2009). The importance of shale composition and pore structure upon gas storage potential of shale gas reservoirs. Marine and Petroleum Geology 26, p. 916-927.

Rouquerol, J., Avnir, D., Fairbridge, C., Everett, D., Haynes, J., Pernicone, N., Ramsay, J., Sing, K. & Unger, K. (1994). Recommendations for the characterization of porous solids (Technical Report). Pure and Applied Chemistry 66, p. 1739-1758.

Rushing, J. A., Newsham, K. E. & Blasingame, T. A. (2008). Rock typing: Keys to understanding productivity in tight gas sands. SPE Unconventional Reservoirs Conference: Society of Petroleum Engineers.

Sahimi, M. (2011). Flow and transport in porous media and fractured rock: from classical methods to modern approaches: John Wiley & Sons.

Schieber, J. (2011). Shale microfabrics and pore development–an overview with emphasis on the importance of depositional processes. Gas Shale of the Horn River basin: Canadian Society of Petroleum Geologists, Calgary, p. 115-119.

Shanley, K. W., Cluff, R. M. & Robinson, J. W. (2004). Factors controlling prolific gas production from low-permeability sandstone reservoirs: Implications for resource assessment, prospect development, and risk analysis. AAPG Bulletin 88, p.1083-1121.

Silin, D. B., Kneafsey, T. J., Ajo-Franklin, J. B. & Nico, P. S. (2011). A multimodal 3D imaging study of natural gas flow in tight sands. SPE annual technical conference and exhibition: Society of Petroleum Engineers.

Sing, K. (1982). Reporting physisorption data for gas/solid systems with special reference to the determination of surface area and porosity (Provisional). Pure and Applied Chemistry 54, p. 2201-2218.

Sing, K. S. (1985). Reporting physisorption data for gas/solid systems with special reference to the determination of surface area and porosity (Recommendations 1984). Pure and Applied Chemistry 57, p. 603-619.

Slatt, R. M. & O'Brien, N. R. (2011). Pore types in the Barnett and Woodford gas shales: Contribution to understanding gas storage and migration pathways in fine-grained rocks. AAPG Bulletin 95, p. 2017-2030.

Soeder, D. & Randolph, P. (1987). Porosity, permeability, and pore structure of the tight Mesaverde Sandstone, Piceance Basin, Colorado. SPE Formation Evaluation 2, p. 129-136.

Solomon, M. (1963). Counting and sampling errors in modal analysis by point counter. Journal of Petrology 4, p. 367-382.

Sonnenberg, S. A. & Pramudito, A. (2009). Petroleum geology of the giant Elm Coulee field, Williston Basin. AAPG Bulletin 93, p. 1127-1153.

Sun, S. Q. (1995). Dolomite reservoirs: porosity evolution and reservoir characteristics. AAPG Bulletin 79, p. 186-204.

Swanson, B. F. (1981). A Simple Correlation Between Permeabilities and Mercury Capillary Pressures. Journal of Petroleum Technology, 33, p. 2-498.

Taylor, T. R., Giles, M. R., Hathon, L. A., Diggs, T. N., Braunsdorf, N. R., Birbiglia, G. V., Kittridge, M. G., Macaulay, C. I. & Espejo, I. S. (2010). Sandstone diagenesis and reservoir quality prediction: Models, myths, and reality. AAPG Bulletin 94, p. 1093-1132.

Tobin, R. C., McClain, T., Lieber, R. B., Ozkan, A., Banfield, L. A., Marchand, A. M. & McRae, L. E. (2010). Reservoir quality modeling of tight-gas sands in Wamsutter field: Integration of diagenesis, petroleum systems, and production data. AAPG Bulletin 94, p. 1229-1266.

Tzimas, E., Georgakaki, A., Garcia-Cortes, C. & Peteves, S. (2005). Enhanced oil recovery using carbon dioxide in the European energy system: Publications Office.

VandenBygaart, A. & Protz, R. (1999). The representative elementary area (REA) in studies of quantitative soil micromorphology. Geoderma 89, p. 333-346.

Wardlaw, N. (1976). Pore geometry of carbonate rocks as revealed by pore casts and capillary pressure. AAPG Bulletin 60, p. 245-257.

Washburn, E. W. (1921). Note on a method of determining the distribution of pore sizes in a porous material. Proceedings of the National Academy of Sciences of the United States of America 7, p. 115.

Webster, R. L. (1984). Petroleum source rocks and stratigraphy of the Bakken Formation in North Dakota. Rocky Mountain Association of Geologists, p. 490-507.

Weyl, P. K. (1960). Porosity through dolomitization: conservation-of-mass requirements. Journal of Sedimentary Research 30, p. 85 – 90.

Woody, R. E., Gregg, J. M. & Koederitz, L. F. (1996). Effect of texture on petrophysical properties of dolomite: evidence from the Cambrian-Ordovician of southeastern Missouri. AAPG Bulletin 80, p. 119-131.

Xiong, D., Azmy, K. & Blamey, N. J. (2016). Diagenesis and origin of calcite cement in the Flemish Pass Basin sandstone reservoir (Upper Jurassic): Implications for porosity development. Marine and Petroleum Geology 70, p. 93-118.

Yang, Y. & Aplin, A. C. (1998). Influence of lithology and compaction on the pore size distribution and modelled permeability of some mudstones from the Norwegian margin. Marine and Petroleum Geology 15, p. 163-175.

Yang, Y. & Aplin, A. C. (2007). Permeability and petrophysical properties of 30 natural mudstones. Journal of Geophysical Research: Solid Earth 112, p. 1 – 14.

Zaid, S. M. & Al Gahtani, F. (2015). Provenance, diagenesis, tectonic setting, and geochemistry of Hawkesbury Sandstone (Middle Triassic), southern Sydney Basin, Australia. Turkish Journal of Earth Sciences 24, p. 72-98.

Chapter 5

Geochemistry of Authigenic Cements

Introduction

In Chapter 3 we showed that authigenic carbonate cements are a significant constituent of the middle Bakken (average ~40%). We identified two different diagenetic textures in calcite and six different diagenetic textures in dolomite. We also found evidence of small amounts of authigenic quartz cement. Detailed pore systems analysis (Chapter 4) showed that these cements have significantly changed the pore systems of the middle Bakken. Whilst the authigenic carbonate cements are thought to have preserved the inter-granular volume and inhibited compaction, they have infilled intergranular space and resulted in a significant net porosity reduction. Textural analysis did not however indicate the exact time, temperature, or nature of the formation fluids from which the different phases precipitated from.

Petrographic work in Chapter 3 showed, quartz exists in the middle Bakken both as authigenic cement and as detrital grains. Authigenic quartz cement is only a minor proportion of the total quartz. There is an abundance of studies which consider quartz cementation and its effect on reservoir quality (McBride,1989). Logically these studies have been conducted on samples where the abundance of quartz cement is high; unlike samples of the middle Bakken.

For the much more abundant carbonate phases, petrographic analysis alone is not sufficient to understand the complex genesis of these cements. Therefore, we look to geochemical tools to further unravel the complex carbonate history to help understand the mechanism by which these pore filling cements have formed.

The geochemistry of diagenetic calcite cement has been considered in many previous studies (e.g. Meyers & Lohmann, 1985; Carpenter et al., 1991; Walderhaug & Bjørkum, 1998); however work focussed specifically on the middle Bakken is limited (Last & Edwards, 1991; Ferdous, 2001; Pitman et al., 2001; Karasinski, 2006); (see also Chapter 3 for detailed analysis of the previous work).

The origin of dolomite is considered one of the most exciting topics in geology as the process of dolomitization is one of the least understood problems in the field of carbonates (Fritz & Smith, 1970; Michalowski & Asuero, 2012). Dolomite can form both as primary sedimentary dolomite and as secondary diagenetic dolomite. A significant

amount of dolomite in the geological record is secondary dolomite, which formed under burial diagenetic conditions in the subsurface (Hardie 1987; Warren 2000; Machel, 2004).

Since the process of dolomitization strongly influences reservoir characteristics and porosity evolution, the reconstruction of the dolomitization and diagenetic history of carbonate sequences is of great economic importance. This study considers the formation of secondary, burial dolomite in the mixed carbonate-clastic middle Bakken.

Previous studies of the middle Bakken have identified multiple carbonate phases and proposed several models for the timing and origin of dolomite formation (Last & Edwards, 1991; Ferdous, 2001; Pitman et al., 2001; Karasinski, 2006). From textural and geochemical evidence, Ferdous (2001) suggests that dolomite diagenesis occurred by multiple phases of dissolution of calcite and precipitation of dolomite throughout the burial history of the middle Bakken. This is in contrast to the study by Pitman et al. (2001), who suggested that carbonate evolution occurred mid-diagenesis and was a comparatively simple process which occurred in a more restricted period of time. With the addition of bulk carbon and oxygen data, Karasinski (2006) postulated that the middle Bakken carbonates were the product of complex diagenesis between early to mid-diagenetic time. Karasinski (2006) concluded that more detailed grain-scale isotopic analysis would be required to understand the carbonates of the middle Bakken further. An attempt was made to do this by Staruiala et al. (2013), who identified 3 different dolomite phases which are identified as differences in growth layers rather than discretely different crystal morphologies identified in our study. They found that the outer phase of dolomite is more enriched in ^{18}O relative to ^{16}O than the inner phase (closer to the core). In this chapter, we have combined both high resolution SEM analyses with in-situ SIMS in order to improve our understanding of the origin of the diverse cement phases in the middle Bakken at the grain-scale. Making measurements at the grain scale gives us better insights into complex formation processes and the timing of these processes which may otherwise be hidden in bulk analyses.

Methods

Samples

The samples used in this study were obtained from the Bakken-Sorrenson well by Brigham Oil and Gas in August 2013. The samples were plugged at specific intervals along the core and double wrapped in plastic film and aluminium foil. For this study, 32 samples were obtained from the middle Bakken section representing the full range of different facies identified in the core (see Chapter 3 for a full explanation of individual facies associations).

SIMS Sample No.	Sample No.	Depth (m)	Facies	Formation
1	2-55B	982.84	-	Three Forks Fm
2	11_iiA	975.96	Grad	Middle Bakken
3	17_iiA	973.95	C	Middle Bakken
4	9_iiA	972.43	D1	Middle Bakken
5	4_iiA	971.00	D2	Middle Bakken
6	2_iiA	970.98	D2	Middle Bakken
7	1-36B	969.93	E	Middle Bakken

Table 5.1 - Sample information for the 7 selected SIMS samples and the corresponding depths and facies.

A sub-set of 7 samples was taken for SIMS analysis; 6 from the middle Bakken and 1 from the underlying Three Forks Formation (Table 5.1). Petrography and XRD analysis showed these samples contain a significant component of calcite and dolomite of all the phases identified (see Chapter 3). The Three Forks sample was included in the sample sub-set to investigate the possibility that some of the dolomite identified in Chapter 3 was eroded from the underlying Three Forks Formation.

Petrography & Mineralogy

Detailed petrographic analysis was conducted using a combination of transmitted light microscopy, scanning electron microscopy (SEM) and x-ray diffraction (XRD). These techniques are discussed in detail in Chapter 3. This is an important part of the study which allows detailed and robust interpretation.

We are aware of very few studies which have combined SEM imaging with SIMS analysis on carbonate minerals (e.g. Rollion-Bard et al., 2008; Sayani et al., 2011; Kozdon et al., 2009). Studies of the middle Bakken, that have combined detailed petrographic work with stable isotope analysis are very limited (Geske et al., 2015). Of those studies, we are aware of only one study which has successfully measured the stable oxygen isotope composition of carbonate minerals in the middle Bakken at the grain scale (Staruiala et al., 2013). Previous attempts by earlier workers have been hampered due to the fine grained nature of these phases (Karasinski, 2001).

X-ray diffraction (XRD) was performed on 13 selected middle Bakken samples. The analysis was conducted by KT GeoServices, Inc. The XRD analysis was performed using a Siemens D500 automated powder diffractometer equipped with a copper X-ray source (40kV, 30mA) and a scintillation X-ray detector. A full description of the methods used and discussion of these results can be found in Chapter 3.

Wavelength Dispersive Spectroscopy (WDS)

Analysis of the composition of calcite and dolomite was conducted at grain-scale using Scanning Electron Microscopy-Wavelength Dispersive Spectroscopy (SEM-WDS). This was completed using an INCA Wave 700 spectrometer WDS detector attached to a Hitachi SU-70 FEG SEM. The operation was controlled by and the data processed using INCA microanalysis software. Three sets of standards were used. An elemental cobalt instrument standard was used at the start of every session. Additionally, at the start and end of the sample analysis session, calcite standard UWC-3 (see Kozdon et al., 2009) mounted to the centre of all of the analysed samples was measured 5 times. Finally, a series of carbonate standards (calcite, ankerite, dolomite and siderite) were analysed to measure accuracy and precision, see Appendix 4.

The 'spot-size' (beam diameter) was determined to be between 1.7-5 nm depending on the exact instrument setup with an interaction volume of up ~800 nm in depth into the sample (Bowen pers. comm, 2015). To limit any contamination between the beam and other coincident minerals, only crystals with the shortest visible length >2 µm were analysed.

SEM-CL

SEM-CL is a powerful tool in detecting emissions generated by differences in trace element concentrations in growth layers; as opposed to intrinsic luminescence which is the product of lattice imperfections. This technique can detect differences in elemental concentrations several orders of magnitude smaller than can be detected by x-ray microanalysis (EDX & WDS) (Edwards & Lee, 2014). The cathodoluminescence of individual calcite and dolomite phases was used to characterise the number of different dolomite generations found within the different textures of dolomite. We used a Gatan Mono-CL detector operated in panchromatic mode. Images were obtained using a SEM at an accelerating voltage of 10kV and a working distance of 17 mm. The samples were highly polished thin-sections and polished resin blocks, coated with 30-35 nm of carbon to prevent charge build-up.

Previous workers have found CL imaging of mixed silicate-carbonate samples such as those in this study of be challenging due to the significant difference in brightness between highly luminescent carbonate phases and less luminescent silicate phases (Reed & Milliken, 2003). In our initial experiments we encountered difficulties associated with streaking in the image. This artefact has been observed in other studies and is thought to be due to persistence of luminescence (phosphorescence) (Marshall, 1988 and Reed & Miliken, 2003). For analysis of the carbonate minerals we used the approach proposed by Lee (2000), who used long dwell times (~3,200 µs per pixel) during imaging. Other approaches such as those proposed Reed & Milliken (2003) do not capture longer wavelengths, such as red emissions which have been previously recorded in dolomites (Boggs and Krinsley, 2006). Spectral information was obtained over a wavelength search range of 505 - 800 nm and the intensity values were corrected using the system response curve. Using this method, we are able to obtain high quality images in order to determine the number of generations of dolomite growth whilst limiting damage to the sample surface due to over-exposure to the electron beam.

Bulk C & O Isotope Analysis

To determine the carbon and oxygen stable isotope composition of the calcite and dolomite samples were analysed at Scottish Universities Environmental Research Centre

(SUERC) on an Analytical Precision AP2003 mass spectrometer equipped with a separate acid injector system, after reaction with 105% H_3PO_4 under a Helium atmosphere at 70 °C, in order to selectively leach calcite and dolomite for analysis.

Isotope results are reported using the conventional δ‰-notation (Equation 5.1). This is the ratio of the most abundant (heavier isotopes) to the least abundant (light) stable isotopes. The results are reported as the deviation (in per mil [‰]) from an internationally accepted standard. The ratio can bear either a positive or negative sign. Positive ratios indicate that the sample has a higher $^{18}O/^{16}O$ ratio relative to the standard and negative are lower relative to the standard.

$$\delta^{18}O = \left(\left(\frac{R_{sample}}{R_{std.}}\right) - 1\right) \cdot 1000$$

Equation 5.1 - R_{sample} corresponds to the $^{18}O/^{16}O$ ratio of the sample and $R_{standard}$ is the $^{18}O/^{16}O$ ratio of the reference standard (i.e. mean ocean water or SMOW) (Sharp, 2007).

Mean analytical precision based on replicates of the SUERC laboratory standard MAB-2 (Carrara Marble) was ±0.2‰ for both carbon and oxygen. $\delta^{13}C$ is reported relative to PDB (Pee Dee Belemnite), whereas $\delta^{18}O$ is quoted relative to VSMOW (Vienna Standard Mean Ocean Water).

Grain Scale Oxygen Stable Isotope Analysis

Grain-scale oxygen stable isotope analysis of authigenic cements was achieved using Secondary Ion Mass Spectrometry (SIMS). SIMS offers a spatial resolution improvement, in comparison with conventional acid-digestion techniques allowing stable isotope analysis of multi-phase carbonates. Many previous studies have identified the limitations of extracting multiple phases using chemical and mechanical extraction techniques for bulk analysis due to potential of contamination by other phases (Karasinski, 2006; Geske et al., 2015). SIMS mitigates these difficulties.

In order to remove any organic material which may contaminate the samples, the 7 selected SIMS samples (Appendix 10) were treated using a standard soxhlet extraction procedure, during which they were placed in a mixture of dichloromethane and methanol for 96 hours. The samples were then mounted in epoxy resin in 1-inch blocks. A crystal of

calcite standard UWC-3 [$\delta^{18}O$(SMOW) of UWC-3 is 12.49‰ (±0.03‰ 1 SD, n= 9) and the $\delta^{13}C$(PDB) is −0.91‰ (±0.04‰ 1 SD, n= 9)] was mounted at the centre of the sample (Kozdon et al., 2009). The sample was then polished sequentially using 6 µm, 3 µm and 1 µm diamond paste on a low-nap pad. The final polish was obtained using 0.05 µm colloidal alumina solution on a vibrating pad. The samples were then rinsed and then dried in a vacuum oven for 5 hours at 40°C. To prevent charging during analysis the samples were coated with a 60 nm gold coat. The flatness across the samples was confirmed using a white-light profilometer. Flatness was measured both across the polished rock and across the mounted and polished calcite standard. The maximum topography recorded was 3 µm (sample) and 7 µm (sample and standard).

In-situ oxygen stable isotope data were acquired using a CAMECA ims-1280 large radius multi-collector ion microprobe at the WiscSIMS Laboratory at the University of Wisconsin-Madison (Kita et al., 2009; Valley and Kita, 2009). Calcite and dolomite were analysed over 4 consecutive sessions between the 6th and 9th October 2015. The $^{133}Cs^{+}$ primary ion beam with a current of 1.2 nA was aligned to a spot size of 13 µm. This ablated ellipsoidal pits which were approximately 10 x 13 µm in size. The typical secondary $^{16}O^{-}$ ion intensity was ~2.5x10^{9} cps for analyses using the 1.2 nA beam.

Instrument standards for the dolomite-ankerite series were run for this work. In addition, a quartz instrument standard was also run. Before and after every set of 8-17 sample analyses, a sample mounted calcite standard (UWC-3) was measured 4 consecutive times. Stable isotope values are reported using delta notation (δ), using the same method used for bulk stable oxygen isotope analysis (above).

The accuracy is reported as the magnitude of the calibration residual, which was <0.25‰. The precision (reproducibility) of a set of bracketing standard analyses is assigned as uncertainty of unknown samples; the average 2SD of bracketed analyses was 0.27‰. Detailed analytical protocols can be found in Kita et al., (2009).

Earlier petrographic and XRD analyses (see Chapter 3), indicated the presence of iron in the dolomite crystals. From the work of Śliwiński et al. (2015) an instrumental bias is generated by the presence of iron in the analysed samples. In order to correct for this each crystal analysed by SIMS was identified by SEM and the iron composition of the crystal was measured using SEM-WDS. Using the results of SEM-WDS analysis we used the mass bias

calibration method proposed by Śliwiński et al. (2015) to correct for the presence of iron in the dolomite crystals, Appendix 7.

Paleo Formation Temperature Calculation

Oxygen stable isotopes have been used in geothermometry since Urey (1947) first suggested that enrichment of ^{18}O in calcite relative to seawater was a temperature-dependent process. Since this early work, several different equations have been proposed to determine the temperature from the $\delta^{18}O$ of CO_2 obtained from the reaction of calcite and dolomite with H_3PO_4. Whilst most of this work has focussed on biogenic carbonate (Epstein et al., 1953; Tarutani et al., 1969; Bemis et al., 1998), some studies have proposed temperature equations for inorganic calcite precipitation (McCrea, 1950; O'Neil et al., 1969).

All of these models assume that the oxygen isotopic composition of the carbonate is primary and that the isotopic composition of the carbonate reached equilibrium and was fixed at formation. In diagenetic systems it is difficult to prove these assumptions so an assumption is made about the isotopic composition of the mineralising fluid (Emery & Robinson, 1993). It is thought the pore waters in equilibrium with the earliest cements are the same as marine water so these early cements will be in isotopic equilibrium with the ocean water (Sharp, 2007). It seems logical that pore fluids early in the diagenetic history of the middle Bakken member would be marine water trapped during deposition of the sediment and the chemistry of such fluids would not have changed significantly during early diagenesis.

Estimates of the $\delta^{18}O$ composition of Devonian seawater have been made by van Geldern et al., (2001) and Hudson & Anderson (1989) who proposes values of -1‰ $_{SMOW}$ and -2‰$_{SMOW}$ respectively. Late Devonian seawater for the Bakken Formation was estimated in calculations by Staruiala et al., (2013). Assuming a seawater temperature of 25°C they estimated the $\delta^{18}O$ of the seawater to be between -5.3 and -7.1‰ $_{SMOW.}$ Staruiala et al., (2013) recognise this calculated value is much lower than would be expected. For this reason, we have used the mean of those reported in the studies of van Geldern et al., (2006) and Hudson & Anderson (1989). This gave an assumed Devonian seawater value of -1.5‰$_{SMOW}$.

Calculation: Calcite

Mineral specific temperature equations were used to determine the paleo temperature of formation for calcite and dolomite. Assuming all the calcite is inorganic cement we used the equation proposed by O'Neil et al., (1969); Equation 5.2.

$$1000\ \ln\alpha_{(calcite-water)} = 2.78\ (10^6\ T^{-2})\ - 3.39$$

Equation 5.2 - Paleo temperature equation proposed for inorganic calcite precipitation, O'Neil et al., (1969) in Sharp (2007), where T is in Kelvin and α is the calcite-water fractionation factor.

Calculation: Dolomite

Paleo-thermometry equations for oxygen stable isotopes in dolomite have been proposed by several previous workers (Mathews & Katz, 1977; Friedman & O'Neil, 1977; Vasconcelos et al., 2005). We use the experimentally derived, dolomite specific equation proposed by Vasconcelos et al. (2005), Equation 5.3. We used this equation as it was derived for low temperatures as indicated for the middle Bakken member by the burial model of Kuhn et al. (2012).

$$1000\ \ln\alpha_{(dolomite-water)} = 2.73\ (10^6\ T^{-2}) + 0.26$$

Equation 5.3 - Paleo-temperature equation proposed for dolomite precipitation, Vasconcelos et al., (2005), where T is in Kelvin and α is the dolomite-water fractionation factor.

The mineral-mineral fractionation factor is calculated using equation 5.4 (Emery & Robinson, 1993).

$$\alpha_{A-B} = \frac{1 + \delta_A\ /\ 1000}{1 + \ \delta_B/\ 1000} = \frac{1000 + \ \delta_A}{1000 + \ \delta_B}$$

Equation 5.4 - Relationship between fractionation factor (α) and δ values (Emery & Robinson, 1993).

Results

Petrographic Characterisation

Petrographic analysis showed the middle Bakken member is a heterogeneous siltstone unit with variable authigenic cementation by carbonate minerals, dolomite and calcite (discussed in detail in Chapter 3). Calcite is observed in 3 textural forms, whereas dolomite is present in 6 different textural forms (Figure 5.2). In chapter 4 we showed that calcite and dolomite were the principle pore-occluding cements in the middle Bakken member; combined, they constitute between 32-72% of the samples (from XRD). Using plots of mineralogy and porosity from transmitted light point-count data (Chapter 3 & 4) we showed that early cementation by carbonate minerals has occluded porosity and inhibited compaction.

Calcite

Diagenetic calcite is principally observed as pervasive poikilotopic cement (Figure 5.1a), which occurs variably without any clear control on it is spatial distribution, Chapter 3. This phase is 'type 1 calcite'. Also present are discrete individual grains of calcite which appear to both cement small numbers of grains forming a globular type morphology, Figure 5.1b and also as individual, discrete grains which do not connect other grains; visual estimates from SEM imaging find both of these phases to be very rare. These 2 sub-phases are grouped and termed 'type 2 calcite'. Although it may be possible that these are undeveloped forms of 'type 1' calcite, for clarity we keep them separate. Bulk abundance as measured using XRD suggests calcite constitutes between 3-56% of the rock volume.

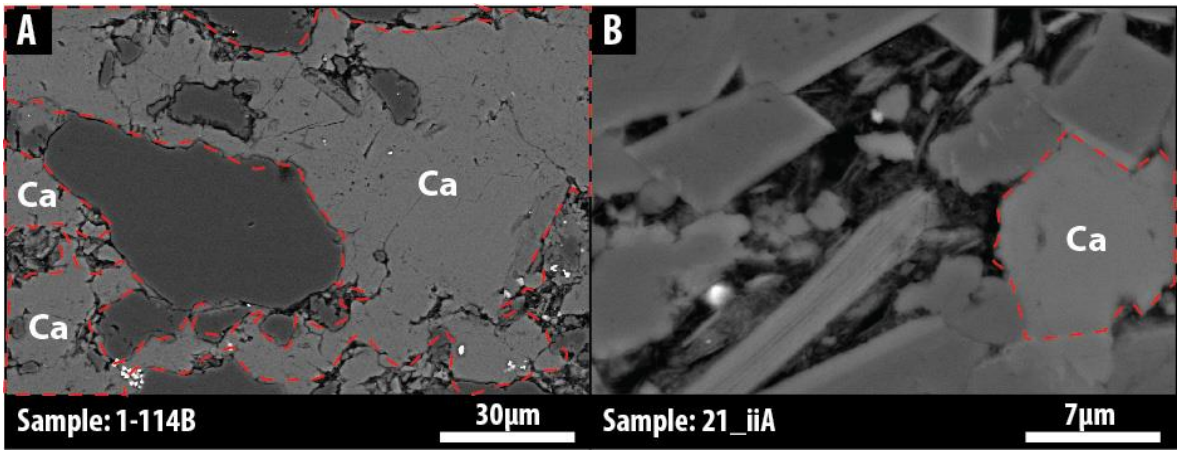

Figure 5.1 - Backscatter Electron Micrographs of the different textural phases of diagenetic calcite identified in the middle Bakken member. a) Type 1 calcite; forming a

pervasive cement b) Type 2 calcite; forming discrete grains, partially cementing other grains.

Dolomite

XRD analysis shows dolomite makes up 5-41% of the mineral volume of middle Bakken member samples. Petrographic analysis showed the dolomite crystals occur in different morphologies. In order to differentiate the different dolomite textures we have used the terminology proposed by Gregg and Sibley (1984). Whilst these classification schemes are descriptive, they carry implications for dolomite genesis as size distribution is controlled by both nucleation and growth kinetics and crystal-boundary shape is thought to be affected by growth kinetics (Sibley and Gregg, 1987). Results are discussed in detail in Chapter 3 but are summarised here for context.

Type 1 dolomites are non-planar, anhedral, forms with rounded edges, 15-30 µm in size (Figure 5.2a). Type 2 dolomites are euhedral rhombs, 10-50 µm in size with vuggy porosity at their core, Figure 5.2b. Type 3 dolomites are euhedral rhombs, 10-50 µm in size with perfect crystal faces, Figure 5.2c. Type 4 dolomites are subhedral, geometric, angular crystals which vary in size from 5-35 µm in size, Figure 5.2d. Type 5 dolomites are ferroan rims which are 2-10 µm thick rims around more stoichiometric, iron-poor dolomite. This phase has been observed around all other morphological phases of dolomite, Figure 5.2e. Type 6 dolomites, are very fine euhedral rhombs which are less than 5 µm in diameter, Figure 5.2f and Table 5.2. Under transmitted light microscope, some of the dolomite rhombs show compositional variations towards the core of the crystal. This texture has previously been referred to as ‘cloudy core’.

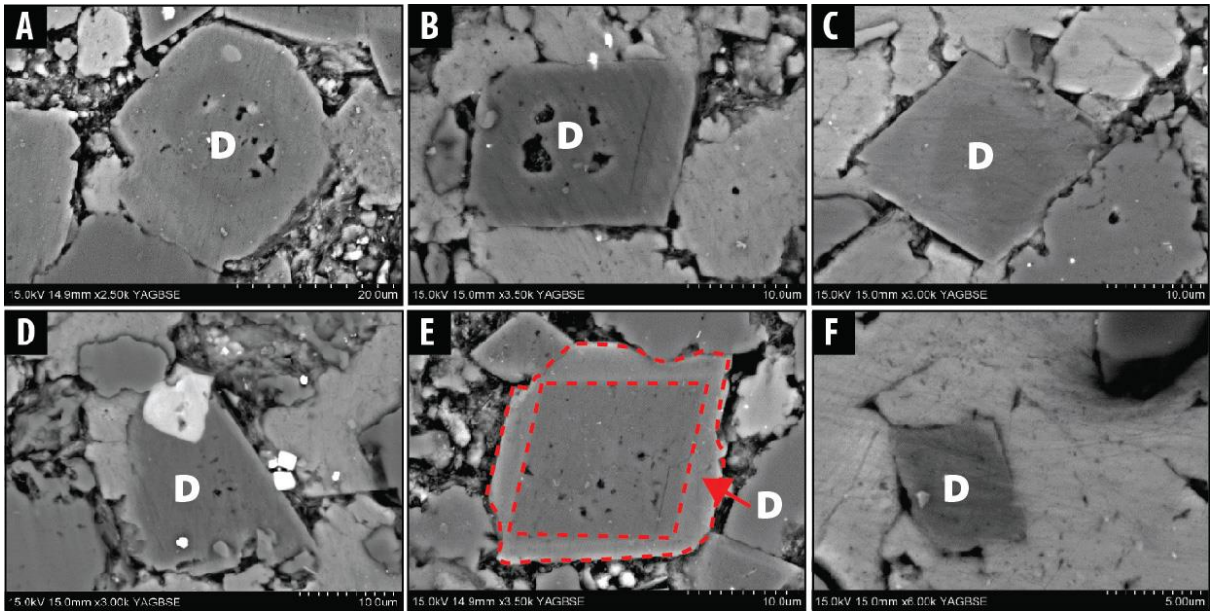

Figure 5.2 - Backscattered Electron Micrographs of the different textural phases of dolomite identified in the middle Bakken member. A) Type 1 - non-planar dolomite B) Type 2 - planar-e with vuggy porosity C) Type 3 - planar-e D) Type 4 - planar-s E) Type 5 - ferroan-dolomite rims around dolomite. F) Type 6 - planar-e (fine). D is the dolomite crystal of interest.

The relative abundance of the different dolomite phases is based on visual estimates by petrographic microscope and SEM imaging of thin-sections; quantitative dolomite phase abundance data on representative samples by SEM-EDX mapping is reported and discussed in Chapter 3. The most abundant dolomite phases are type 2, 3 and 5 dolomites. Coarse (>10 µm), euhedral dolomites are found throughout the middle Bakken member, with and without vuggy porosity (type 2 and 3). Iron rich rims and iron alteration is common in dolomites, though sharp, discrete rims are the by far the most abundant form. The rims form in bands that are 2-10 µm thick around the edge of all other dolomite phases; Table 5.2. Ferroan rims are not present in calcite.

Phase	Name	CL Colour	CL Features	Zone thickness
1	Non-planar	Red	Irregular zoning	1-4µm
2	Planar-e (coarse, corroded)	Red	Concentric zoning	Rim: 2-10µm
3	Planar-e (coarse, uncorroded)	Red	Concentric zoning	Rim: 1-5µm
4	Planar-s	Red	Concentric zoning	Rim: 5-10µm
5	Fe-Dolomite (rims)	Red	Unzoned	-
6	Planar-e (fine)	Red	Concentric zoning	1-3µm

Table 5.2 - Summary of the petrographic characteristics and relative abundance of the different middle Bakken member dolomite phases.

Phase abundances were more quantitatively determined by transmitted light point counting and SEM-EDX mapping. For point counting, the percentage of counts per phase is reported and for SEM-EDX maps, the relative abundance (area) of each textural phase (Figure 5.3) is shown (see Chapter 3 for method). Dolomite type 5 was omitted as the small variations in iron which define these overgrowths can be challenging to reliably detect and segment at the magnification and resolution at which these data were acquired.

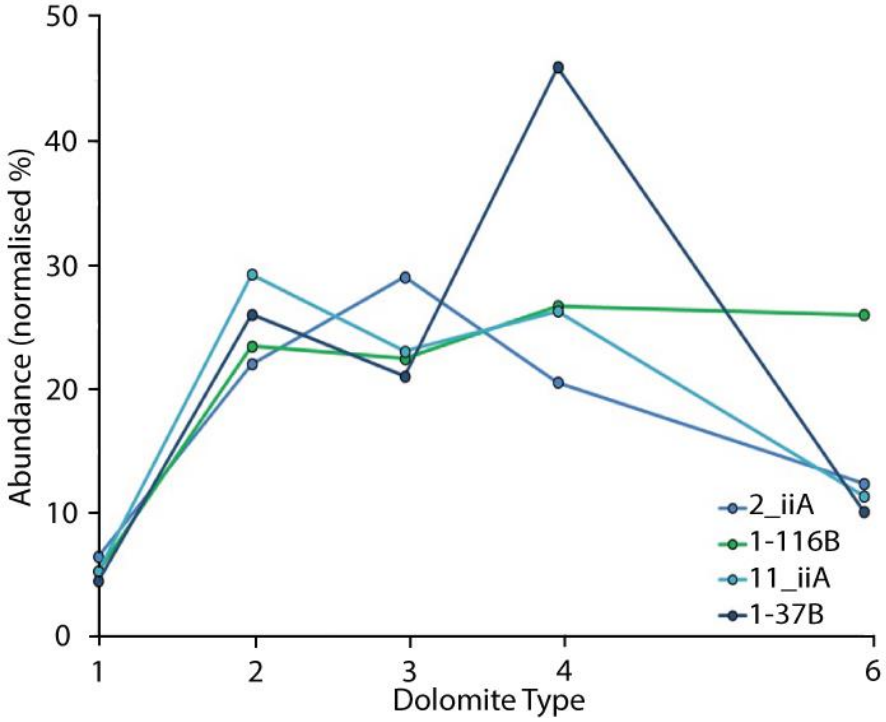

Figure 5.3 - Variations in relative abundance of different textural forms of dolomite, obtained from SEM-EDX maps. Data are normalised to omit 'type 5 dolomite'.

The most abundant phases segmented from SEM-EDX maps are phases 2, 3 and 4 with an

average normalised abundance of 25%, 24% and 30%; respectively. The least abundant phase is type 1 dolomite (mean 7%). Type 6 dolomite make up on average 15% of the total dolomite. There is a dominance of type 4 dolomite crystals in sample 1-37B.

Composition

Using SEM-WDS analysis, the elemental composition of the different cements was determined. In total, 126 calcite crystals and 494 dolomite crystals of different textures in 12 samples were determined, of which 402 were characterised by texture. The analyses were repeated three times per crystal and the results for each crystal are reported as the mean of the three analyses (Table 5.3 & Appendix 9).

Phase	Name	$CaCO_3$	$MgCO_3$	$FeCO_3$
Dolomite 1	Non-planar	50.4 (42.5 - 60.3)	48.2 (38.9 - 56.1)	1.4 (0.0 - 4.6)
Dolomite 2	Planar-e (coarse, corroded)	50.2 (36.2 - 76.9)	48.6 (22.2 - 63.6)	1.2 (0.0 -12.4)
Dolomite 3	Planar-e (coarse, uncorroded)	47.7 (28.7 - 63.6)	50.8 (38.5 - 71.3)	1.5 (0.0 -20.0)
Dolomite 4	Planar-s	49.8 (36.9 - 65.0)	49.1 (33.1 - 63.0)	1.1 (0.0 - 5.9)
Dolomite 5	Fe-Dolomite (rims)	54.4 (49.9 - 62.6)	44.4 (35.0 - 48.8)	1.3 (0.0 - 4.0)
Dolomite 6	Planar-e (fine)	50.3 (41.7-64.8)	47.8 (33.5 - 89.6)	1.9 (0.1 - 6.6)
Calcite	Cement	97.2 (92.5 - 99.1)	2.5 (0.7 - 7.5)	0.3 (0 -1.3)

Table 5.3 - Chemical composition (average normalised at%) of different carbonate phases; the range of values is given in parentheses.

Perfectly stoichiometric dolomite has a calcium to magnesium ratio 50:50 [$Ca_{0.5}Mg_{0.5}CO_3$] (Sperber et al., 1984). The most stoichiometric dolomite is type 4 dolomite whereas the least stoichiometric dolomite is type 5. Type's 1, 2 and 6 dolomites are broadly stoichiometric with a small average (~2 at%) depletion in calcium, which has been replaced by iron Table 5.3.

The average composition of Type 1, 2 & 6 dolomite phases are broadly similar; however, within these textural phases there are large variations in composition (Table 5.3 & Figure 5.4). Type 5 dolomite (ankerite rims) were not systematically measured and not included in the plots (Figure 5.4) due to the very fine nature of this phase. Type 5 dolomites form rims around all other textural forms of dolomite, to varying extents, and also form individual crystals with anhedral to euhedral habits. This makes classification difficult. From the backscattered electron micrographs, it is clear that there is some compositional variation between ferroan dolomite rims and the more stoichiometric dolomitic core, this varies from discrete rims to more diffuse, alteration zones. From the few analyses that were conducted on this morphology; the dolomite cores tend to be relatively enriched in calcium. The average iron content of the iron-rims is similar to that of some of the other dolomite phases. This is most likely due to a combination of 1) WDS regions of interest breaching the ferroan edge thereby measuring 'dolomite', and the opposite; measurements of dolomite, breaching rims (particularly on diffuse boundaries) and measuring iron-rich rims 2) occasional crystals of dolomite, which have anomalously high iron content biasing the average.

Calcium and magnesium average values are ~50 at%. Lowest average calcium content is found in type 3 dolomites (47.7 at%) and the highest in type 5 dolomites (54.4 at%). The highest average magnesium abundance is found in type 3 dolomites (50.8 at%) and lowest in type 6 dolomites (47.8 at%). Iron content varies significantly across all crystals there is an average of ~1.2 at%. There is no systematic variation in iron, magnesium or calcium with depth.

Calcite cement had a much less variable chemistry with high average abundance of calcium (97.23 at%) and corresponding low average values of magnesium and iron (2.52 at% and 0.26 at% respectively).

The average values (Table 5.3) are broadly consistent with those reported by Ferdous, (2001) for middle Bakken dolomites; ($CaCO_3$: 49.8 at%, $MgCO_3$: 43 at% and $FeCO_3$: 3.89 at%). Whilst the average values are consistent with previous studies, the range of compositions for different crystals when grouped by textural phase is huge (~40%), Table 5.3.

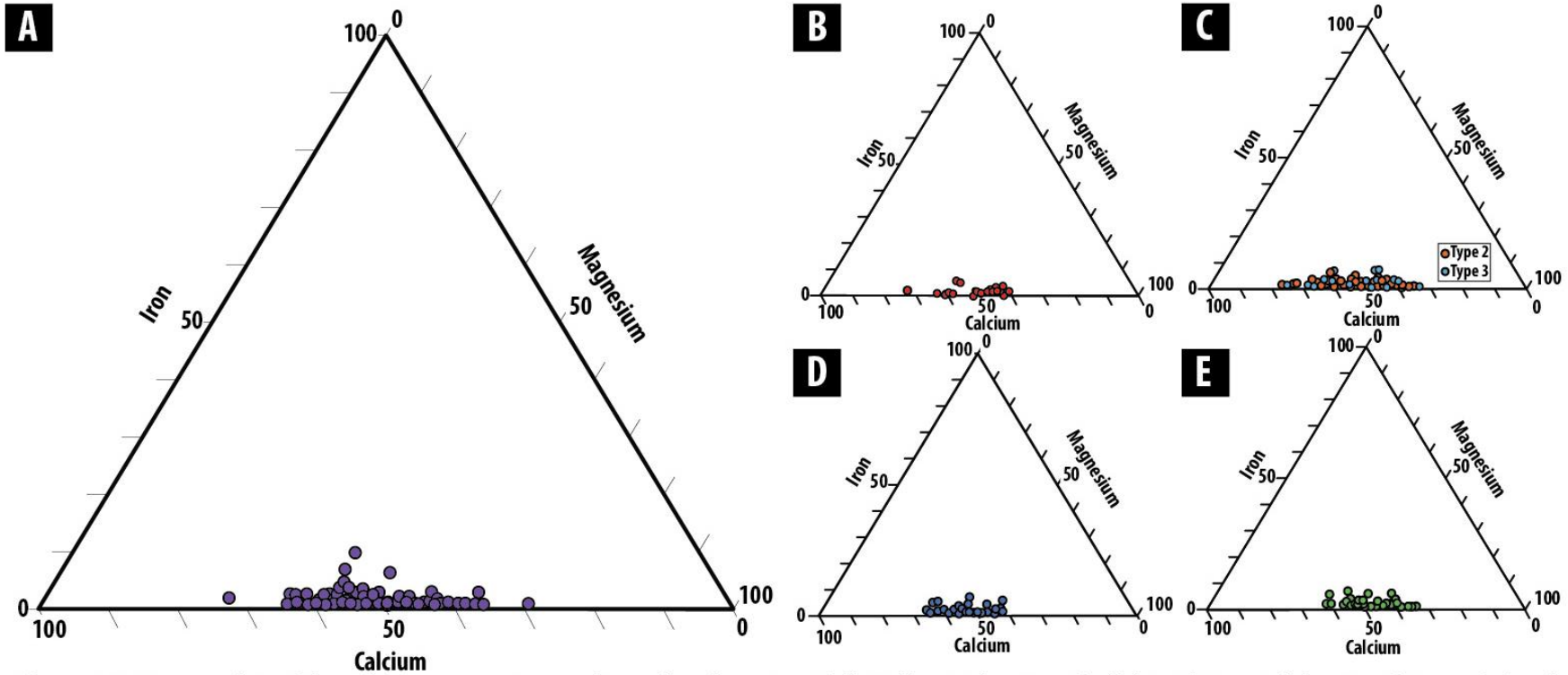

Figure 5.4 - Ternary plots of the calcium, magnesium and iron abundance in middle Bakken Dolomites. A) All data B) Type 1 dolomites C) Type 2 (●) and Type 3 (●) dolomites D) Type 4 dolomites E) Type 6 dolomites. Note type 5 dolomites were omitted due to their scarcity and fine nature.

From our data we identify two potential outliers, in samples 1-36B and 17_iiA, Figure 5.4a. The analysis in sample 1-36B has a high calcium value of 72% and in sample 17_iiA the calcium abundance is low at 29wt%. Comparing the abundance of iron, magnesium or calcium with textural type we found significant variations in calcium in 'type 6' dolomites.

SEM-CL

Scanning Electron Microscopy - Cathodoluminescence (SEM-CL) was used to identify zoning within individual dolomite crystals. Zones of differential luminescence in dolomite crystals represent either changing growth conditions or variations in growth mechanisms (Boggs & Krinsley, 2006). Crystal-scale heterogeneity has implications for both our analytical approach (e.g. composition) but also in our discussion of the mechanism of dolomite formation. In total 48 crystals were viewed in 10 samples. The CL character of individual dolomite types was consistent throughout the samples and is reported in Table 5.4.

Phase	Name	CL Colour	CL Features	No. of Zones	Zone thickness
1	Non-planar	Red	Irregular zoning	3-8	1-4µm
2	Planar-e (coarse, corroded)	Red	Concentric zoning	2	Rim: 2-10µm
3	Planar-e (coarse, uncorroded)	Red	Concentric zoning	2	Rim: 1-5µm
4	Planar-s	Red	Concentric zoning	2	Rim: 5-10µm
5	Fe-Dolomite (rims)	Red	Unzoned	-	-
6	Planar-e (fine)	Red	Concentric zoning	2	1-3µm

Table 5.4 - SEM-CL characteristics of different dolomite morphologies observed in the middle Bakken member.

All dolomite phases luminesce in the red spectrum, including the apparently 'dull' zones, which have a lower intensity luminescence (Figure 5.5). Anhedral, type 1 dolomites show incomplete concentric zones which have decreasing luminescence intensity towards the edge of the crystals. Textural phases 2-4 exhibit similar CL characteristics. These phases all have a single, concentric, low intensity luminescence zone around a much more intensely luminescing core. The rims are ~1-10 µm in thickness, (Table 5.4 & Figure 5.5). Type 5 dolomites, ankerite rims, form single homogenous layers which form around another dolomite crystal and is compositionally rich in iron. This layer has low emission intensity in the red spectrum. In all phases the core of the dolomite is always the 'thickest' zone.

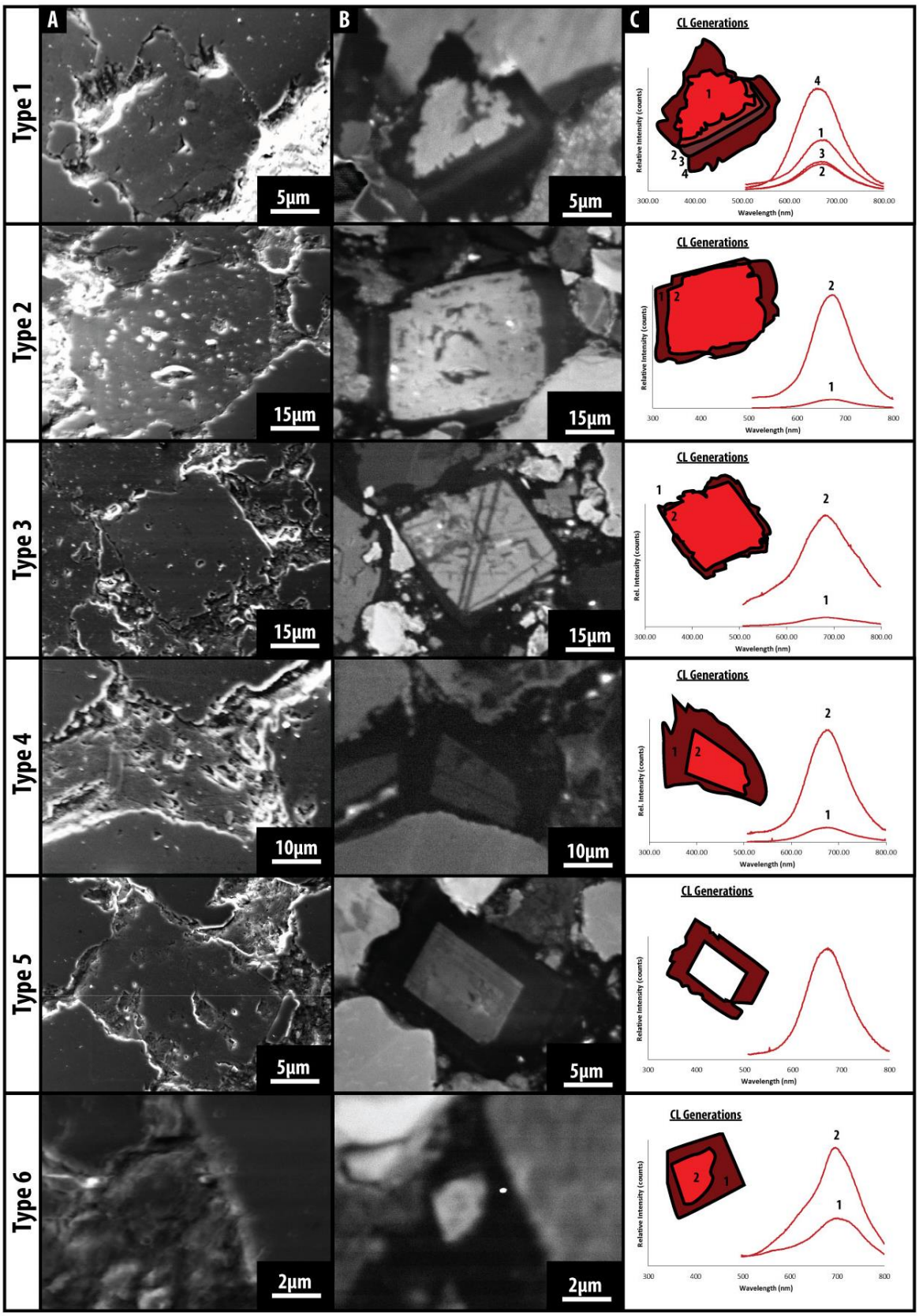

Figure 5.5 – SEM-CL spectra of the 6 different dolomite textures a) Mixed SE-inline BSE image b) SEM-CL image c) Averaged CL spectra (for each zone) with schematic sketch of the CL generations and their relative luminescence [inset].

Bulk Stable Carbon & Oxygen Isotopes

We determined the stable isotope composition of calcite and dolomite individually using sequential acid dissolution in an attempt to differentiate the isotopic compositions of carbon and oxygen values in calcite from those in dolomite.

We found middle Bakken member calcite had $\delta^{13}C_{PDB}$ values which varied between -3.2% and 3.3%, with $\delta^{18}O_{SMOW}$ values of between 23.7% and 27.1%. For dolomite, $\delta^{13}C_{PDB}$ values varied between -3.30% and 3.6%, $\delta^{18}O_{SMOW}$ values ranged from -19.8% to 30.9% (Figure 5.6 & Appendix 6).

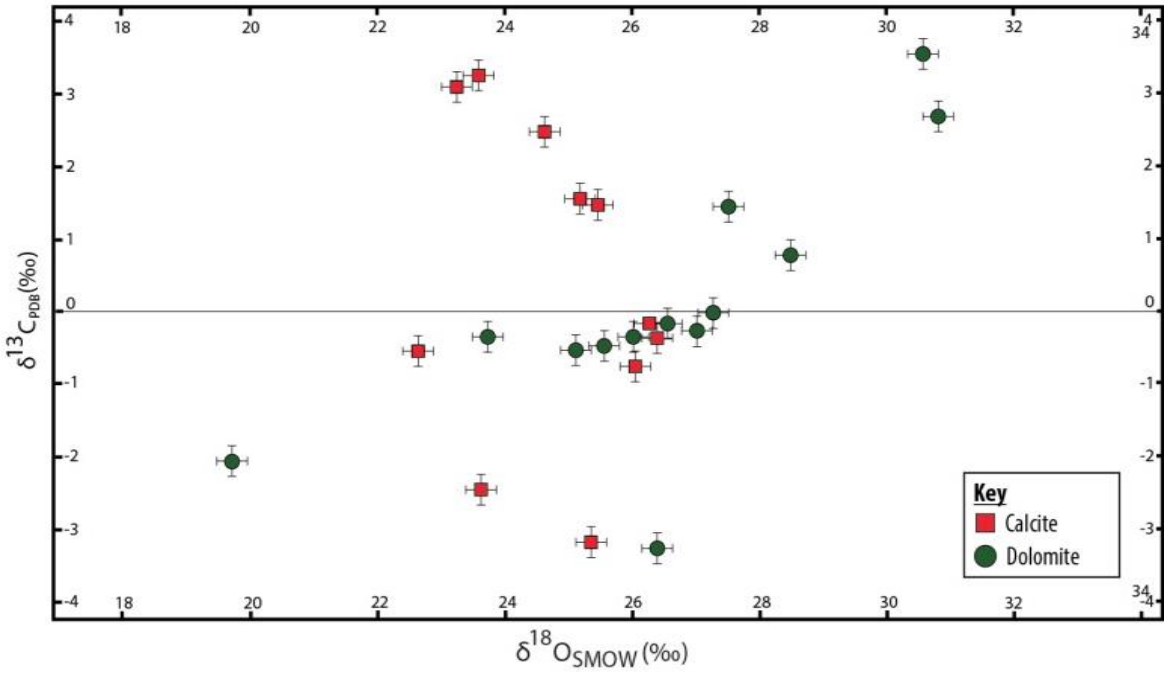

Figure 5.6 - Cross-plot showing the bulk stable isotope compositions obtained by sequential acid dissolution on samples from the middle Bakken member. Trendline for dolomite, highlighting the relationship between O and C isotope composition. Anomalous dolomite result shown (dashed black square).

Formation temperature

Using the calcite palaeo-thermometer proposed by O'Neil et al. (1969) and assuming a $\delta^{18}O$ of the seawater of -1.5‰, calcite was calculated to have formed at temperatures ranging from 42 - 59°C with a mean formation temperature of 48.5°C. A value of -21.7°C was calculated for a $\delta^{18}O_{SMOW}$ value of 42.5 in sample 4_iiA we regard this value as an analytical anomaly and it is excluded from further analysis. Dolomite formation

temperatures determined using the equation of Vasconcelos et al., (2007) were calculated to be between 17 - 85°C with a mean temperature of 37°C. Figure 5.7 shows there is no correlation between the depth of the sample or the morphological type for either dolomite or calcite.

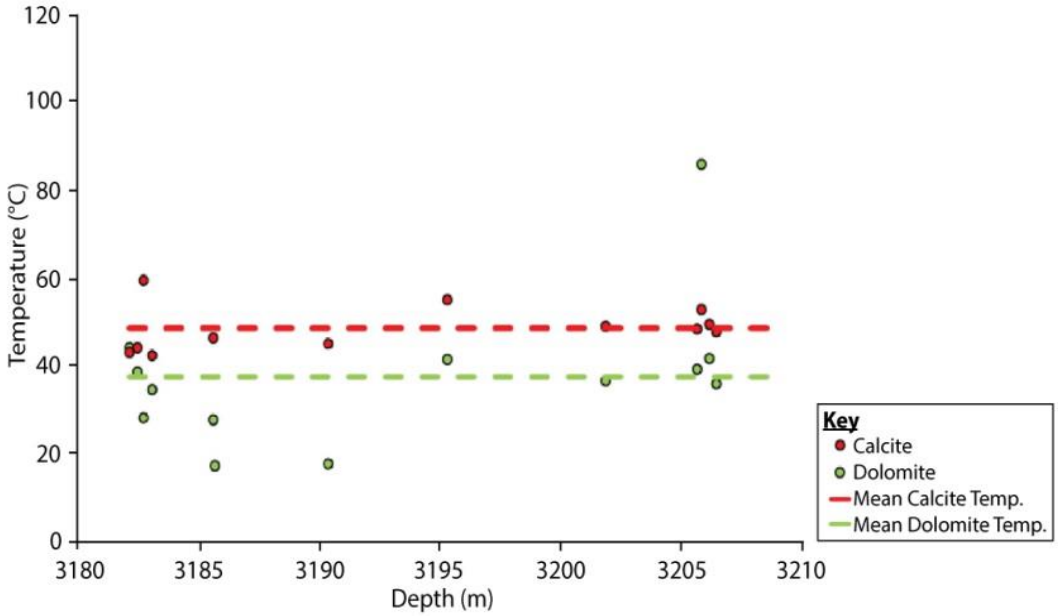

Figure 5.7 – Variations in the mean calculated paleo-formation temperatures for calcite and dolomite obtained from oxygen stable isotope measurements following sequential acid dissolution. Assuming the $\delta^{18}O_{water}$ = -1.5‰.

SIMS: Grain Scale Oxygen Isotopes

In total 351 grains were analysed. In previous ion microprobe studies of $\delta^{18}O$, workers found a correlation between micro-volumes affected by open-system exchange of $\delta^{18}O$ and morphologically irregular pits (Cavosie et al., 2005). Whilst every effort was made to ensure the highest quality data were obtained, SEM imaging of the ablated pits post-analysis found 23% of pits to be 'irregular'. In this study 'pit irregularity' is defined as and includes pits which are positioned on cracks, spots which break into crystals and/or inclusions other than the target mineral and spots which overlap pores and vugs (Figure 5.8). Comparison of the $\delta^{18}O$ value of the irregular pits with $\delta^{18}O$ values of the accepted data found 85% of data points in irregular pits are within the range of the values from regularly ablated pits. Whilst this suggests the data may be accurate, data from irregular pits was not used in this study to ensure absolute data reliability.

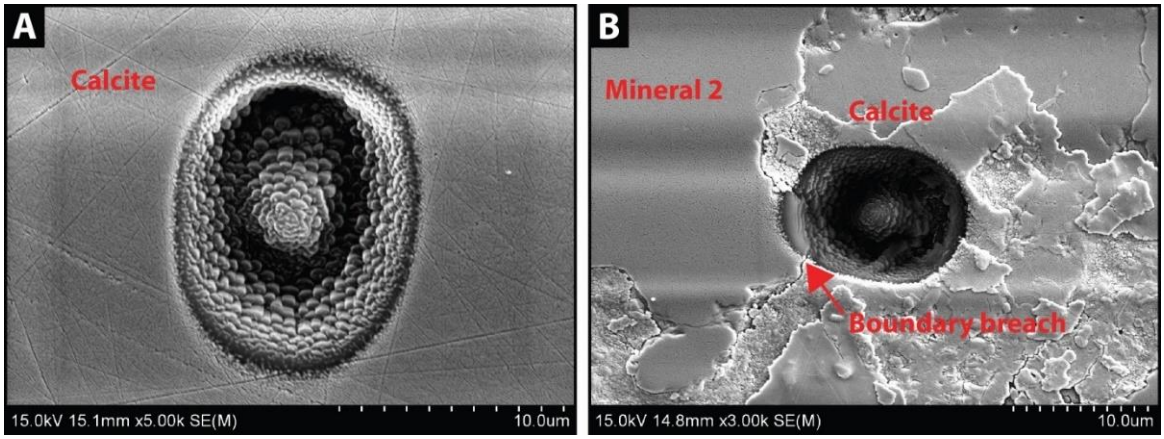

Figure 5.8 - Examples of SIMS pits a) Regular pit, positioned in the centre of a calcite crystal in sample 2-55B; note the ellipsoidal shape and size; b) Irregular pit positioned at the edge of calcite cement, breaking into a second mineral (mineral 2), contaminating the ablated sample, in sample 2-55B.

The total of accepted analyses was 270. Post-SIMS SEM-WDS analysis showed these were composed of 60 calcite grains, 175 dolomite grains and 35 quartz grains. Whilst we were principally targeting carbonate phases, SIMS optics make it challenging to resolve phase differences.

Results

The oxygen stable isotope composition obtained at the grain-scale is shown in Figure 5.9. There is a distinctly different signature for an individual mineral; calcite, dolomite and quartz. Calcite $\delta^{18}O_{VSMOW}$ values vary from 24.9 - 33.7 ‰, dolomite from 16.4 - 32.2‰ and quartz from 9.0 - 19.8‰, Appendix 8. The $\delta^{18}O_{VSMOW}$ is almost consistently higher in calcite than dolomite. The difference in average values is 4.6‰ (31.3‰ and 26.7‰ [respectively without outliers, see below]). Three clear outliers are identified in the dolomite measurements, which have $\delta^{18}O_{VSMOW}$ values of 16.4, 17.4 & 18.0‰. These are type 4 in sample 7, type 2 in sample 2 and type 3 in sample 7 respectively. For these analyses, the pits show good, regular pit morphologies, however pre-ablation SIMS screen captures show some surface asperities/compositional heterogeneities in the crystals which are not seen in other crystals, which may explain the apparently anomalous values.

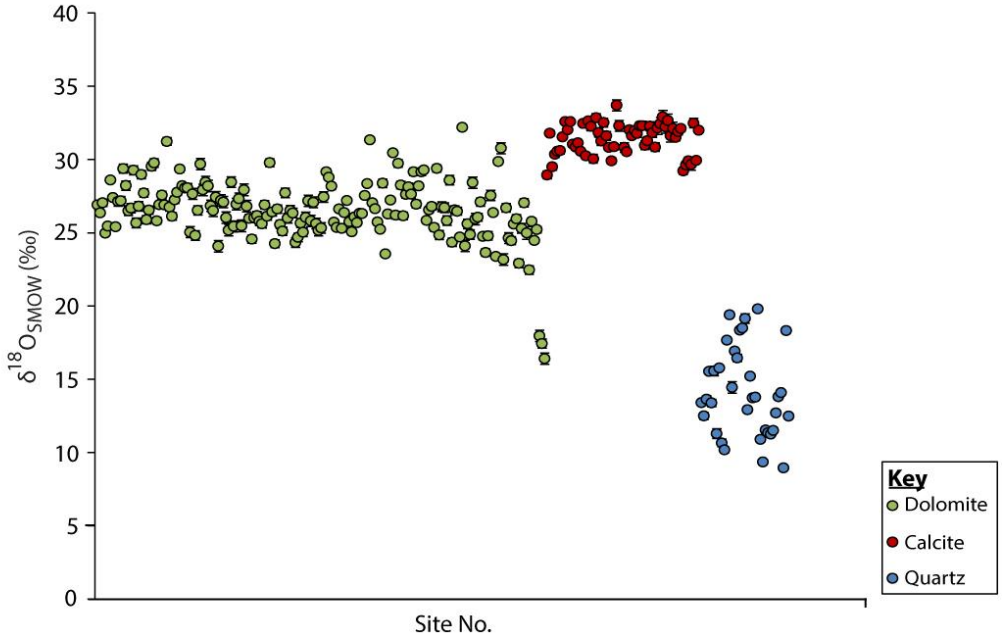

Figure 5.9 - Plot of all grain- scale oxygen stable isotope data collected by SIMS. Calcite, dolomite and quartz are plotted separately for comparison. Oxygen isotope data is reported relative to VSMOW. Error bars show precision, reported as 2 standard deviations. Where error bars do not appear present, they are smaller than the data point marker.

The oxygen isotopic composition of quartz is not discussed in detail in this thesis. Data inadvertently collected during this study is plotted for comparison with measurements for carbonate minerals. The range of $\delta^{18}O$ values for quartz is larger than those measured for calcite or dolomite, even though fewer analyses were conducted on quartz (quartz range: 10.9 ‰; calcite range: 8.8‰; dolomite range: 9.7‰) [when anomalies are removed].

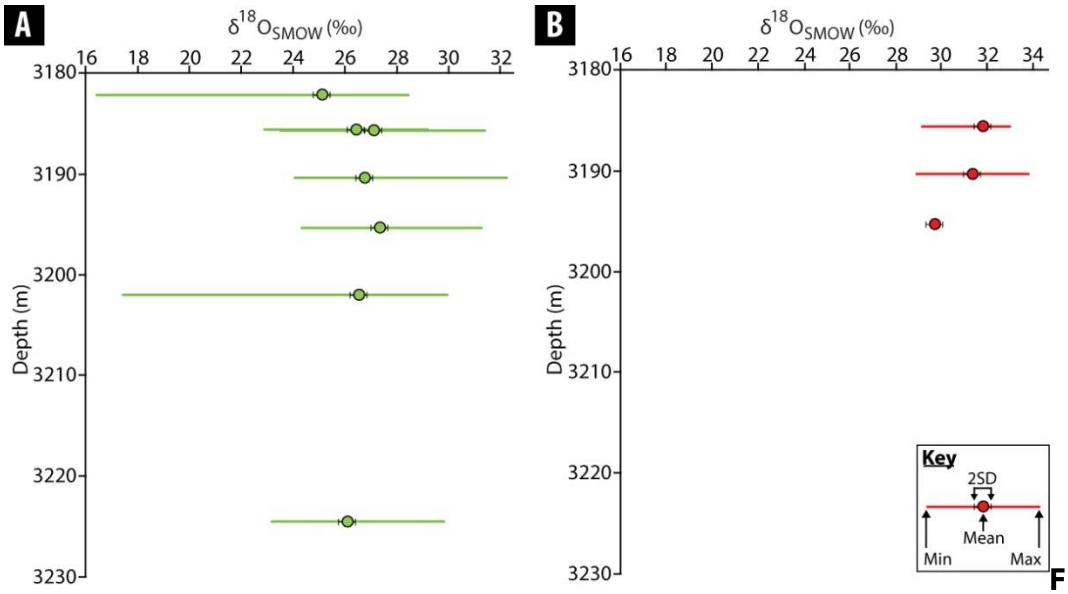

Figure 5.10 - $\delta^{18}O$ against depth. Range of values is shown by the light coloured line. Where no range is shown, then the range is smaller than the data point. Measurements for A) dolomite B) calcite.

Measurements of the $\delta^{18}O$ value of calcite by bulk analysis show that calcite is isotopically heavier than in measurements obtained by SIMS (Figure 5.10a). The difference between the average $\delta^{18}O$ of calcite obtained by bulk analysis and SIMS is 5.9‰ ± 0.2 (1SD). The bulk calcite data has similar $\delta^{18}O$ ratios to some dolomite crystals, measured by SIMS. For dolomite, there is no significant or systematic difference between the range of $\delta^{18}O$ value of dolomite obtained by bulk measurement vs SIMS.

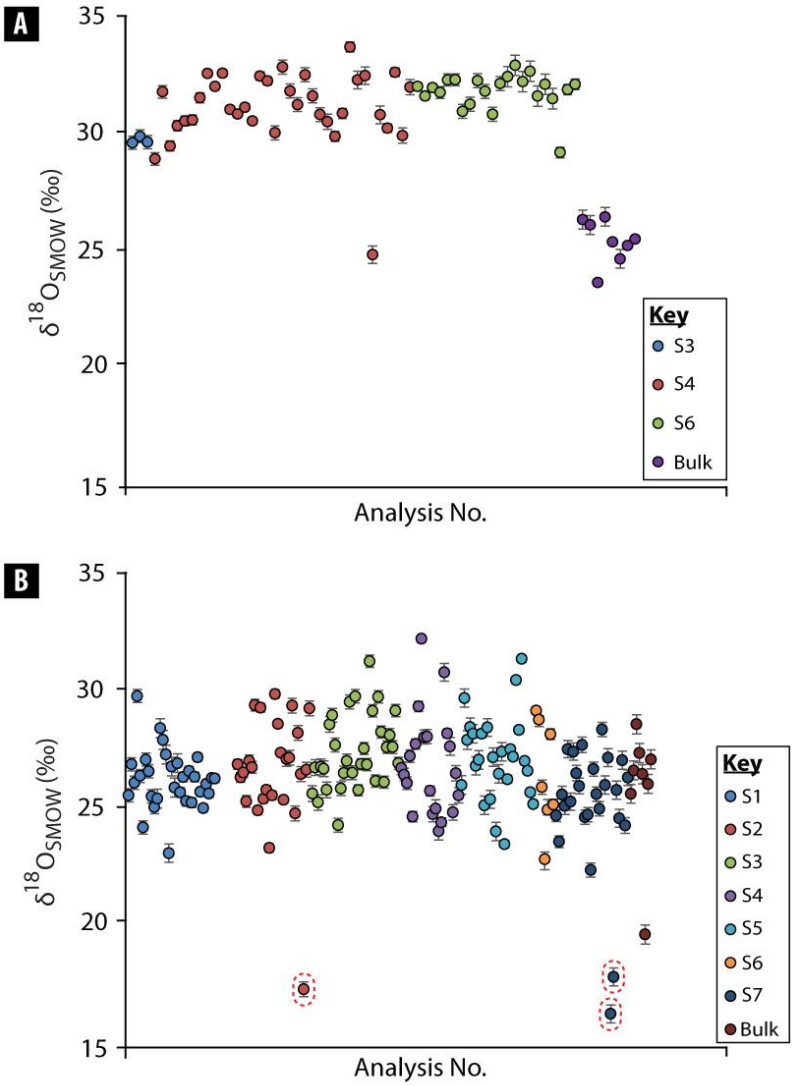

Figure 5.11 - Plot of grain- scale oxygen stable isotope data collected by SIMS from calcite grains. a) Calcite by sample b) Dolomite by sample. Anomalies identified above, circled with red dashed lines. Sx = sample number, e.g. S1 = sample 1.

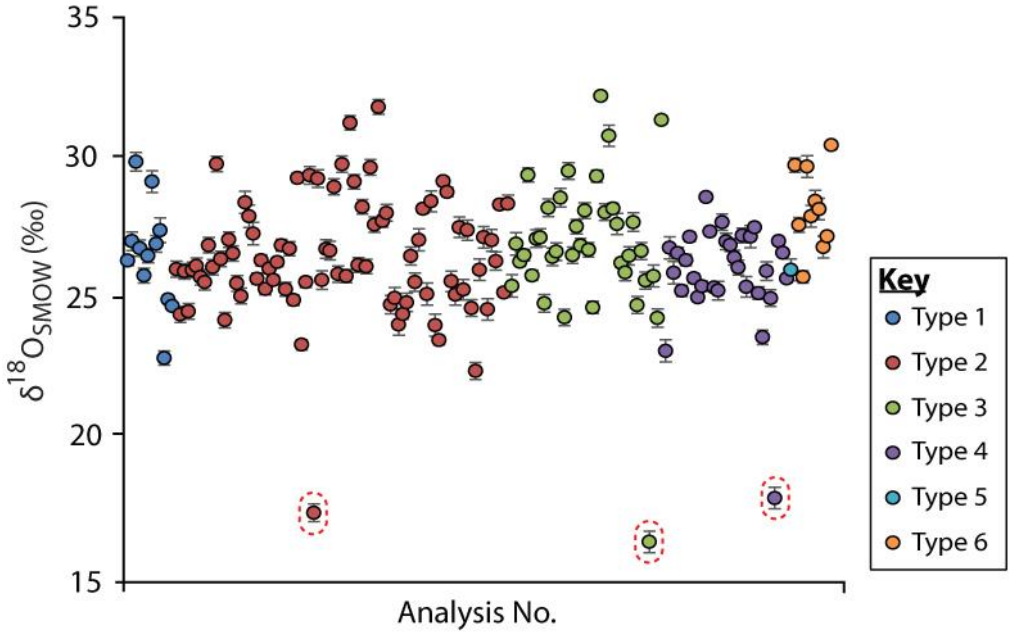

Figure 5.12 - Oxygen stable isotope data collected by SIMS on individual dolomite crystals and sorted by textural type. Anomalous values identified above, circled with red dashed lines.

Figure 5.11 shows there is no systematic variation in the mean $\delta^{18}O$ value between facies for both calcite and dolomite. The $\delta^{18}O$ values in dolomite show no correlation with textural type. Individual, anomalous values exist for type 2, 3 & 4 dolomite morphologies, Figure 5.12. The $\delta^{18}O$ values for different morphologies of dolomite are both of similar values but are also found to be over a similar range.

Formation temperature

The calcite paleothermometer proposed by O'Neil et al. (1969) was used to determine the calcite formation temperature. Assuming a $\delta^{18}O$ of water = -1.5‰ yields a temperature range of 8 - 51°C, with a mean formation temperature of 18°C. Similarly, dolomite formation temperatures determined using the method of Vasconcelos et al., (2007) were calculated to be between 5 - 64°C with a mean formation temperature of 33°C, Figure 5.13.

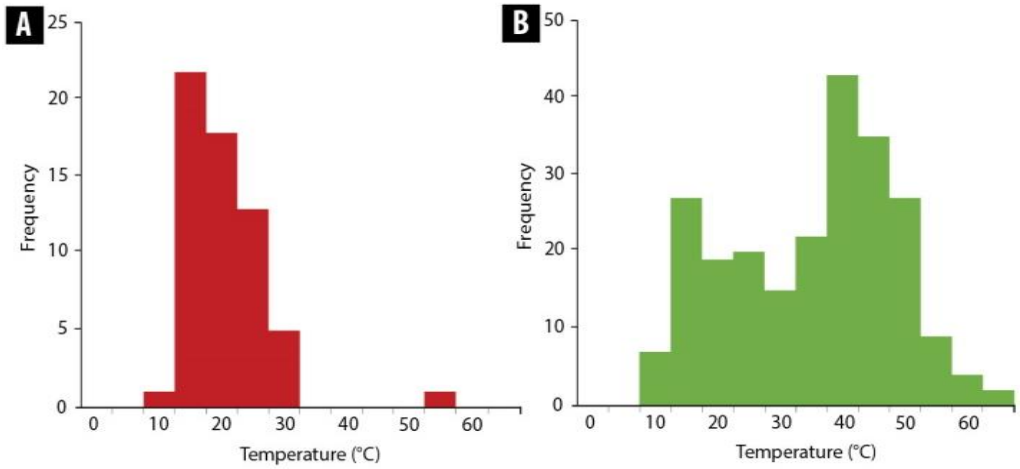

Figure 5.13 – Histogram of calculated precipitation temperatures from SIMS $\delta^{18}O$ values for a) Calcite b) Dolomite. Assuming the $\delta^{18}O_{water}$ = -1.5‰.

Histograms of calculated formation temperatures for calcite and dolomite provide an insight into the precipitation history of calcite and dolomite, Figure 5.13. At the lowest temperatures and therefore shallowest burial depths, calcite precipitation reaches a peak. With increasing temperature and therefore burial, dolomite precipitation increases and calcite precipitation decreases. Calcite occurs over a smaller temperature range than dolomite. The overlap in formation temperatures of the precipitation of calcite and dolomite suggests that dolomite precipitation commenced during calcite precipitation.

The modal formation temperature calculated for calcite is 15°C and 40°C for dolomite, where the $\delta^{18}O$ of seawater is assumed to be -1.5‰. The lowest values appear anomalous and/or difficult to explain as they suggest calcite formed at temperatures below expected paleoclimate temperatures of ~25°C, expected during the time of middle Bakken deposition, as proposed by Staruiala et al., (2013). There is no correlation between the morphological type and the calculated formation temperature for either dolomite or calcite (Figure 5.14).

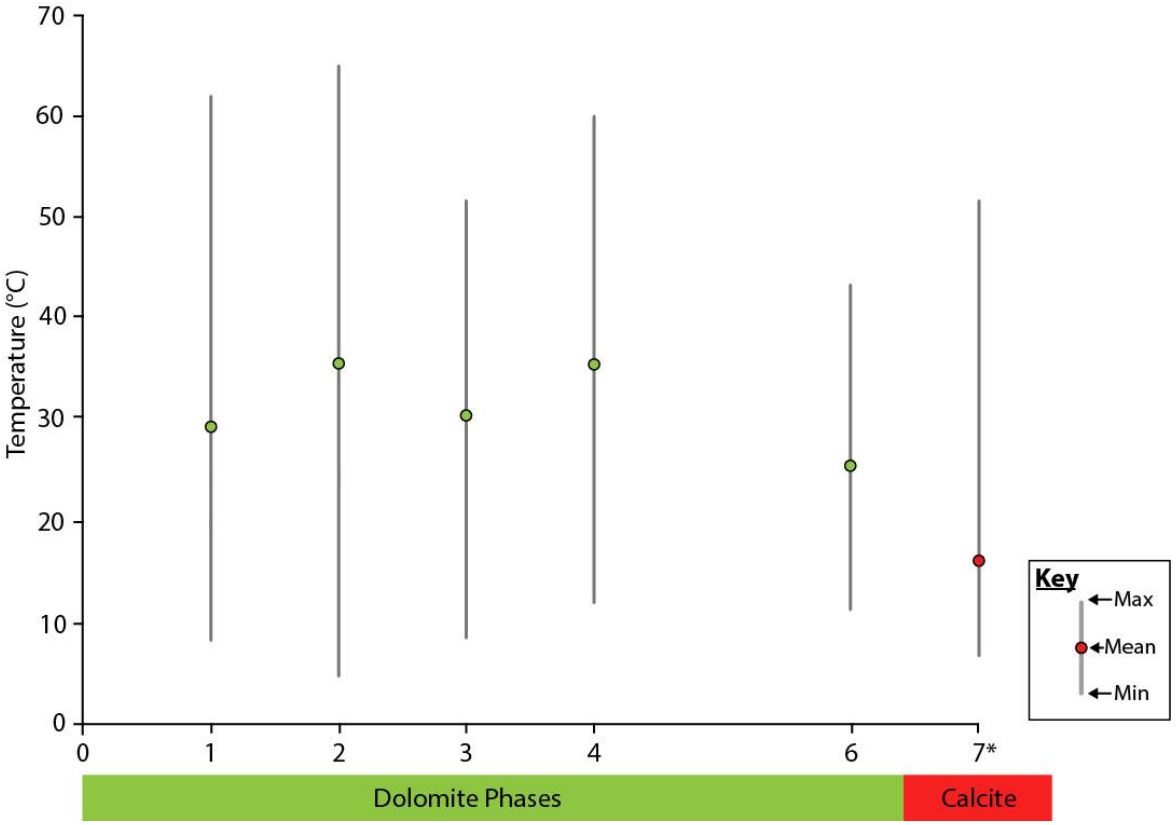

Figure 5.14 – Variations in the mean calculated paleo-formation temperatures for calcite and dolomite from oxygen stable isotope measurements by SIMS. Data is plotted by morphological type for dolomite. Grey lines show the range of temperatures calculated for each phase. $\delta^{18}O_{water}$ assumed to be -1.5‰. Where the 2SD value is not visible, it is smaller than the data point.

Discussion

Un-mixing Carbonate Phases

One of the challenges identified by previous workers on fine-grained mixed carbonate phases, is in separating individual minerals for isotopic analysis. Isolating different morphologies of the same carbonate phase is even more difficult. The use of sequential acid dissolution enabled us to obtain separate carbon and oxygen stable isotope ratios for very fine calcite and dolomite phases from bulk samples. This technique was used to investigate whether the apparent cluster of data observed in Karasinski's (2006) study was due to calcite and dolomite having the same isotope ratios or alternatively was the homogenisation of the isotopic signature of different carbonate minerals. Our results show that homogenisation of calcite and dolomite in bulk analysis has played a role in the

clustering of the results. Results obtained by separating calcite and dolomite occur over a much larger range of $\delta^{18}O$ than those in earlier studies which have not used acid dissolution to separate individual carbonate phases.

The isotopic compositions of calcite show a much larger spread of $\delta^{18}O$ values than those reported in both the studies of Pitman et al. (2001) and Karasinski (2006). The Pitman study was conducted on fracture fill cement whereas the Karasinski study was performed on samples of undifferentiated carbonate. Building on the work of Karasinski; our results differentiating calcite and dolomite, suggest there may have been multiple carbonate precipitation events.

Going further, the work by Pitman et al., (2001) suggests there have been multiple phases of calcite cementation; those in fracture fills and those not in fracture fills. We postulate that the large variations in $\delta^{18}O$ values in our study compared to Pitman's, and comparatively similar $\delta^{13}C$ values to Pitman et al., indicate the differences in calcite phases may be related to changes in fluid chemistry (discussed below).

These conclusions are however in the context of differences in geographical locations of these studies. The Bakken-Sorenson well of this study is close to the depocentre of the middle Bakken member in the Williston basin, whereas Karasinski's study focusses on samples taken from much further west, near the basin margins, Figure 3.1.

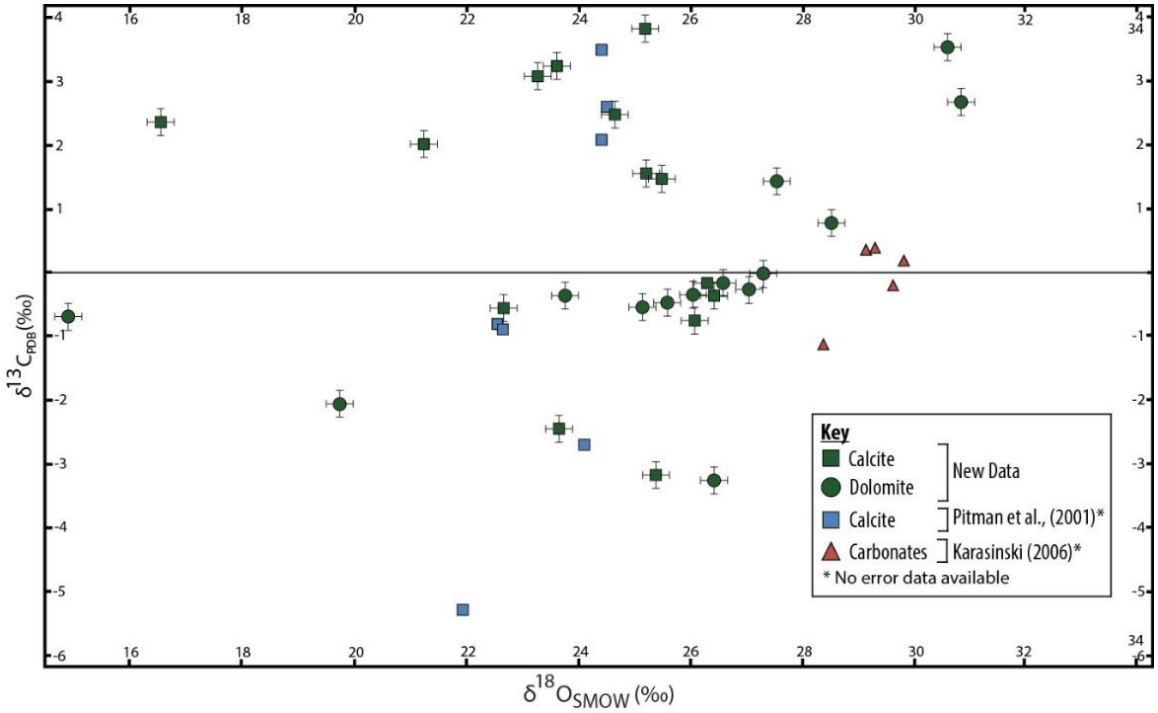

Figure 5.15 - Cross-plot showing the bulk carbon and oxygen stable isotope compositions of samples from the Bakken Formation and Three Forks Formation from previous studies, Pitman et al., (2001) and Karasinski (2006). Also shown is new bulk isotope data of middle Bakken member samples.

Whilst the use of sequential acid dissolution has allowed us to progress the study of middle Bakken member carbonates by separating the carbon and oxygen stable isotope signature for calcite and dolomite, there is some uncertainty to the effectiveness and reliability of this technique (Walters et al., 1972; Videtich, 1981; Al-Aasm et al., 1990). Within the study we note a difference between the average oxygen stable isotope composition obtained by SIMS (Calcite: 31.3‰ Dolomite: 26.5‰) and sequential acid dissolution of the bulk sample (Calcite: 26.7‰, Dolomite: 27.0‰) (Figure 5.11). This is particularly prevalent for bulk calcite measurement which has a $\delta^{18}O$ value similar to that measured by SIMS for dolomite.

The work of Al-Aasm (1990) considered the effect of sequential acid dissolution on carbonate minerals using phosphoric acid, as conducted in this study. In their study they found that CO_2 evolved during the calcite dissolution stage could be contaminated by dissolution of dolomite. They showed that contamination by dolomite was a function of dolomite abundance and the relative difference in the isotopic composition of the two

carbonate minerals. They suggest that the application of a standard method without specific consideration for dolomite abundance and the isotopic composition of the two minerals may increase the probability of contamination during dissolution. The explanation of Al-Aasm (1990) seems the most likely reason for the difference in calcite values obtained by bulk and SIMS measurements (Figure 5.11); it could be attributable to dissolution of dolomite during the calcite dissolution stage. Furthermore, using sequential leaching we were unable to separate different morphologies of dolomite and carbonate. To do this we used SIMS analysis. This protocol is however a significant improvement on bulk analysis on mixed calcite and dolomite without sequential dissolution.

Detrital Mineralogy

Quartz

Whilst not a principle target of this study, the oxygen isotope composition of quartz was measured by SIMS. The oxygen stable isotope composition of quartz overgrowth has been measured in several previous studies outside of the Bakken Formation. In these studies, it was used to determine the temperature and timing of authigenic quartz precipitation (Graham et al., 1996; Girard et al., 2001; Hiatt et al., 2007; Harwood et al., 2013). The thin nature (0.5-5 µm) of quartz overgrowths present in the middle Bakken member [see Chapter 3] and the comparatively large beam size used with SIMS (ellipse of 10 x 13 µm) means it was impossible, to have obtained a measurement from an overgrowth. Instead, we suggest quartz measurements represent analysis of detrital quartz. SEM-CL imaging on a selection of quartz grains (post-SIMS analysis) showed authigenic quartz rims have been 'breached' by ablation pits during isotopic analysis. This may in part explain the relatively large variations in $\delta^{18}O$ observed in quartz due to homogenisation of the isotopic signature of authigenic and detrital quartz. Where a solely detrital grain has been analysed differences may reflect different detrital sources of quartz; a conclusion which has been drawn in Chapter 3.

Dolomite

Textural analysis in Chapter 3, characterised dolomites with an anhedral, rounded morphology, to be 'type 1' dolomites. This morphology has previously been documented as a product of late stage, high temperature diagenesis (Gregg & Sibley, 1984; Warren,

2000). Early laboratory work to understand the origin of anhedral dolomite by Land (1967) found anhedral dolomite could be precipitated at a temperature of 300°C, in a hydrothermal bomb, therefore potentially of authigenic origin. Dolomites of the study by Land (1967) are neat, perfect, rounded, dolomite cement; quite unlike the anhedral dolomites of this study. Later work found that the recrystallization of dolomite from euhedral to anhedral forms could occur at temperatures as low as 50°C (Gregg & Sibley, 1984 and Sibley & Gregg, 1987). Similarly, recrystallised dolomites in these studies are homogeneous, perfect rounded crystals, unlike the ragged and rough anhedral dolomite crystals observed in this study. The maximum temperatures reached in the Bakken Formation were ~130°C, during the Eocene (Kuhn et al., 2012). From this it is possible that that the anhedral nature of type 1 dolomite is recrystallization of an earlier formed dolomite crystal. The exact source of this morphology of dolomite remained unclear from the evidence provided in Chapter 1.

In this chapter geochemical tools add new insights into the genetic history of this phase. The characteristics of this phase are quite different to that of phases 2-6 both in shape (from SEM imaging) (Figure 5.2) and in SEM-CL emission character, Figure 5.5. Simple, SEM-CL zonation has previously been attributed to a change in bulk-fluid properties (Boggs & Krinsley, 2006). The almost gradational change in CL intensity in 'type 1' dolomite suggests the inferred fluid change occurred as a continuous process and not a single event, which is quite different to the CL character of phases 2-6, which are composed of very uniform concentric layers, Figure 5.5. This would largely discount the idea of recrystallisation as one would expect to see simpler, more homogeneous CL emission spectra and therefore unlikely to have formed such complex CL characteristics.

Clastic inputs into the middle Bakken member were considered in a study by Henderson (2015), in which they dated detrital clastic material using zircon geochronology and conodont colour alteration index. They concluded the inputs were from four distinct age groups from middle Palaeozoic (middle Devonian) to Archean in age. They postulate that the clastic input was derived by long distance sediment transport from the Franklinian mobile belt to the North of the Williston Basin (Mohammed, 2015).

If the oldest ages are considered, then the likely source of detrital dolomite would be from the basin margins. Whilst the ages reported by Henderson (2015) are useful, we are

cautious when applying their suggestion of such long distances of transport to the deposition of detrital dolomite. It is challenging to envisage that dolomite would potentially survive such long distances of transport. The exact nature of which formations outcropped at the margin of the Williston basin during middle Bakken member deposition is not clear. This is in part due to the lack of clear evidence of the existence of tectonic relief during the deposition of the middle Bakken member (Pitman et al., 2001). If, alternatively we use the younger ages proposed by Henderson (2015), the detrital dolomite can be interpreted as evidence for reworking of sediment in the basin. Several of the formations underlying the Bakken Formationare dolomitic including the Three Forks, Birdbear, Duperow or Souris River Formations (Kent, 1967). The Three Forks being stratigraphically directly below the Bakken Formation is a potential source of detrital dolomite.

Comparing this to phases identified by other workers we find these crystals are similar in nature to 'phase D' crystals described by Staruiala et al., (2013) which they attribute to be of detrital origin, however they are also unclear as to the exact mechanism of formation or the source of such dolomites. They postulate, that this phase could represent reworked penecontemporaneous dolomite or dolomite derived from the erosion of pre-Bakken Formation dolomite, though they are uncertain as to which is most likely (Staruiala et al., 2013).

From the combined evidence of an apparent lack of 'cloudy crystals' in this phase (Chapter 3), a complex SEM-CL signature unlike the other dolomite phases in the middle Bakken member and the rounded, abraded nature of type 1 dolomites, we interpret this phase as detrital dolomite which was deposited into the middle Bakken member. The exact detrital source is unclear however from the clastic age dates of Henderson, (2015), we speculate that there may have been several sources of detrital dolomite.

Diagenetic Mineralogy

Authigenic phases of calcite and dolomite were differentiated from detrital calcite and dolomite petrographically; discussed above and in Chapter 3.

Diagenetic Regime

The carbon stable isotope composition of the middle Bakken member carbonates varies little from the PDB standard. Low ratios of $\delta^{13}C$ (+2 to -2) relative to the PDB standard are associated with carbonate and bicarbonate of marine origin (Rollinson, 2014). Seawater has a $\delta^{13}C$ value of ~0‰. In contrast sedimentary organic carbon and biomass typically have $\delta^{13}C$ values of -25 to -37 and -18 to -32 respectively, (Rollinson, 2014).

Positive values of $\delta^{13}C_{PDB}$ have previously been attributed to the process of methanogenesis (Irwin et al., 1977). Methanogenesis is the process of formation of methane methanogenic bacteria. Methanogens are observed in anoxic geological environments, contributing to the degradation of organic matter in ocean bottom sediments (Katz, 2011). From this, we suggest that middle Bakken member carbonates are of marine origin.

The bulk $\delta^{13}C$ values measured in this study are similar (maximum 2‰ lower) than those reported for estimates of dolomite derived from Devonian and Mississippian seawater (Amthor et al., 1993; White and Al-Aasm, 1997; van Geldern et al., 2006). They are also very similar to those reported in other studies of the carbon stable isotope composition of middle Bakken member carbonates (Pitman et al., 2001; Karasinski, 2006; Staruiala et al., 2013). Dissolved inorganic carbon sourced from oxidised organic matter is thought to have extreme negative $\delta^{13}C$ values (Sharp, 2007). The $\delta^{13}C$ of both calcite and dolomite are similar to each other. The carbon system is dominated by marine carbon with relatively little organic matter.

Several studies investigating diagenetic processes in carbonates have used carbonate concretions to track variations in $\delta^{13}C$ values (e.g. Irwin et al., 1977; Curtis et al., 1986, Mozley & Burns, 1993). One study suggests they are akin to a 'time-capsule'; recording changes in geochemical environments (Dale et al., 2014). Mozley and Burns (1993) suggest the large variations of $\delta^{13}C_{PDB}$ (range of 60‰) observed in their study reflect the movement of reservoir fluids through the organic rich mud rocks which the concretions are formed in. From this we suggest that the small range of values ($\delta^{13}C_{PDB}$ ~10‰) represents the $\delta^{13}C$ signature of fluid which has not moved through organic rich materials such as the underlying lower Bakken member and therefore represents the signature of infiltrating ocean water.

Mozely & Burns (1993) postulate a link between dolomite and calcite-dolomite formation and the rate of organic-carbon oxidation. They assert that in sediments where the rate of oxidation of organic-carbon is relatively slow (but high enough for carbonate precipitation), calcite is more likely to form, resulting in calcite with negative carbon isotope ratios and by return the opposite is also true. In this study $\delta^{13}C$ values vary between negative and positive values, and are similar for both calcite and dolomite. This is a complex relationship which is difficult to explain. We suggest this may represent changing conditions and lend support to our tentative suggestion that calcite cementation continued during dolomite replacement.

Formation Temperature

The formation temperature of calcite and dolomite was calculated using measured oxygen isotope ratios from crystals of these minerals. We found that the oxygen stable isotope composition of middle Bakken member calcite and dolomite are similar to values of early diagenetic marine Mississippian carbonates (Table 5.5).

Study	Formation	Age	Mineral	Type	Average $\delta^{18}O_{VSMOW}$	Range
Choquette & Steinen, 1980	Genevieve Limestone	Mississippian	Dolomite	Mixed water burial	32.7	30.1 - 35.0
Budai & Lohmann, 1984	Madison Limestone	Mississippian	Dolomite	RP	26.6	21.0-29.6
Budai & Lohmann, 1984	Madison Limestone	Mississippian	Calcite	Cement	22.6	21.0-24.4
Meyers & Lohmann, 1985	New Mexico Skeletal Limestones	Mississippian	Calcite	Cement	28.2	27.1 -29.6

Table 5.5 – Comparison of the oxygen isotope composition of Mississippian calcite and dolomite reported in earlier studies. For comparison, results from this study show, middle Bakken member calcite values vary from 16.5 - 33.7‰ and dolomite from 14.9 - 32.2‰ [Bulk & SIMS]. RP - replacement dolomitisation.

Whilst in broad agreement with the values above, the range of our data is larger and our average values are higher than those reported in Table 5.5. Differences in $\delta^{18}O$ ratios are a function of temperature and $\delta^{18}O$ water (Sharp, 2007).

Calcite

Throughout this thesis we have asserted that cementational porosity loss, indicates that calcite cementation occurred early in the diagenetic history of the middle Bakken mekmber. By implication it must have occurred at low, near surface temperatures. Surface paleo-temperatures were thought to be around 25°C (Stariuiala et al., 2013).
Calculated paleo-formation temperatures for calcite obtained by both bulk and grain scale analysis vary significantly. The mean temperature calculated from SIMS data is ~18°C whereas the mean temperature obtained by bulk analysis was ~49°C. Maximum calculated formation temperatures by SIMS and bulk analysis are relatively similar at 52°C/59°C, respectively.

Assuming an ocean temperature of ~25°C and a geothermal gradient of 25°C per km, the proposed maximum formation temperatures represent burial to a depth of the order of 1km. Comparing this with the Williston basin burial model of Kuhn (2012), these values seem reasonable. The mean SIMS temperature (~18°C) is however below that of the surface temperature. We propose several potential explanations for this:

a) Contamination of the analysis site: Contamination of the analysis site by other minerals/breaches of the analysis pit could explain apparently anomalous temperature values, however these crystals were painstakingly, repeatedly and systematically viewed and imaged at the grain-scale (imaged by SEM and position-referenced prior to analysis > imaged at acquisition (using pre-defined position-reference) > pit identified (using position reference and acquisition images) and integrity checked using secondary electron imaging > pit viewed in BSE mode and chemistry analysed by SEM-WDS). From this, we strongly assert that any contamination, heterogeneity in the crystal, boundary breaches or other inconsistency in the method would have been identified. We have shown this method to be robust; where anomalies have been identified, imaging has indicated the likely cause of such inconsistency.

b) Disequilibrium precipitation: It is assumed in this study that calcite precipitated in equilibrium with the formation fluid. Some studies have reported cases where this is the not the case in modern carbonate forming regimes (e.g. Fronval et al., 1995; Pentecost et al., 2006). Without knowing absolute $\delta^{18}O$ values for seawater or ocean temperatures it is

difficult to be certain whether disequilibrium precipitation has occurred, however it is prudent to acknowledge this possibility and highlight the importance of this, an assumption in this study, that disequilibrium precipitation did not occur.

c) Fluid Composition: To calculate the temperature of calcite formation we have assumed that the $\delta^{18}O$ of the precipitating fluid was both constant and of a value of -1.5‰. This may not be the case. The oxygen stable isotope composition of the current reservoir fluid of the middle Bakken member was determined by Rostron & Holmden (2000) and was found to be very saline with a $\delta^{18}O_{SMOW}$ value of between 5.0-5.6‰ with an average value of 5.3‰. This was taken from a reservoir sample at Midale, Saschatewan, approximately 170 km NW from where the samples were obtained from for this study.

Devonian seawater composition in the Williston basin was calculated by Staruiala et al., (2013), and found to have a $\delta^{18}O_{SMOW}$ value of between -7.1 and -5.3‰. In their work they concede this is unlikely to be the actual value of Devonian seawater and reflects either an altered $\delta^{18}O$ signature due to the effects of diagenesis or by the influx of meteoric water into the basin Staruiala et al., (2013). The study of Staruiala et al., (2013) draws attention to the uncertainty over whether the isotopic composition of seawater has changed over geological time scales (Muehlenbachs & Clayton, 1976; Gregory & Taylor, 1981; Walker and Lohmann, 1989 Kasting et al., 2006). These studies do however provide a range of isotope compositions of the reservoir fluid and as such are assumed to be end-members in this study. Lower $\delta^{18}O$ values of Devonian seawater is something previously considered by other workers (e.g. Fritz, 1971; Veizer et al., 1986).

Saline, evaporated seawater such as that reported by Rostron & Holmden (2000) for current middle Bakken member reservoir fluid is thought to have more positive $\delta^{18}O$ values (Emery & Robinson, 1993). The addition of saline fluid, and mixing with reservoir fluids would increase the $\delta^{18}O$ of the precipitating fluid and therefore the recalculated paleotemperature would be higher.

To investigate this, we have plotted oxygen isotope composition of calcite (Figure 5.16) as a function of both the isotopic composition of water and temperature. Average $\delta^{18}O$ of calcite is 31.3‰ for SIMS, and would therefore require a fluid with a $\delta^{18}O$ of ~0.1‰ to obtain a minimum near surface temperature of 25°C. At the extreme, for the lowest

temperature value to be 25°C, a fluid composition would have to be ~+3‰, likely achievable with the addition of saline fluid, Figure 5.16.

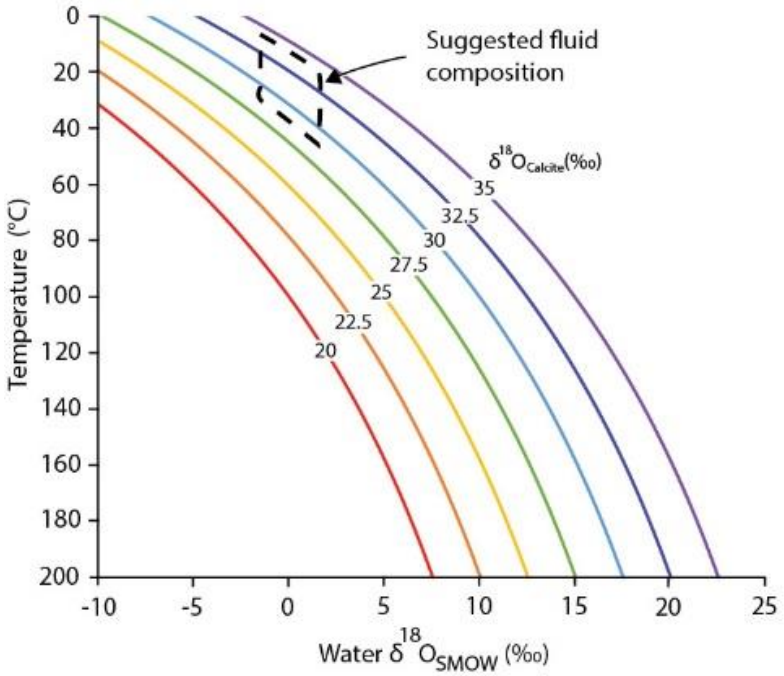

Figure 5.16 - Oxygen stable isotope composition of calcite as a function of temperature and the $\delta^{18}O$ of the fluid from which it precipitated from. Using the calcite paleothermometer of O'Neil et al., (1969). Black dashed box shows the region of the suggested fluid composition.

We observed no systematic difference between the precipitation temperature for type 2 and type 3 calcite. This is a due to no systematic difference in the $\delta^{18}O$ ratio of either phase. Combing this observation and the conclusion drawn from analysis of petrographic images of both calcite phases in Chapter 3 we suggest that type 3 calcite is an under-developed form of type 2 calcite.

Stable oxygen isotope ratios obtained by SIMS analysis, shows only a small range of $\delta^{18}O$ values (2.71‰) which corresponds to an estimated formation temperature range of 8°C - 52°C. Temperature values are predominantly between 10 - 40°C (Figure 5.13a), only 1 value is lower than this range and only one value is higher than this range. This supports the earlier suggestion from textural analysis that calcite cementation occurred early in the diagenetic history of the middle Bakken member but also suggests that cementation continued during the early stages of burial. The range in temperature suggests that calcite precipitation continued for a period of time after the peak of precipitation.

Dolomite

Temperature calculations for dolomite suggest it precipitated over a large range, in a similar manner to calcite. Whilst dolomite has previously been reported to have formed over a large temperature range of 20 - 300°C (Bush, 1973; Sibley et al., 1994), the highest formation temperature calculated from grain-scale data (64°C) is well within the maximum reservoir temperature modelled in the middle Bakken member reservoir (130°C) [Kuhn et al., 2012]. Figure 5.13b, shows that that calculated dolomite paleo-temperatures are predominantly between 15 - 55°C and the most frequent formation temperature which would correspond to ~45°C, which would correspond to precipitation at an estimated depth of ~800 m [assuming surface temperature of 25°C, a linear geothermal gradient of 25°C/km and a $\delta^{18}O_{H2O}$ of -1.5‰]. This also corresponds well to the mean formation temperature of 33°C calculated from the bulk sample.

Whilst the average formation temperature for dolomite is higher than that of calcite, the range of formation temperatures calculated for dolomite appear to overlap with those reported for calcite. This suggests that dolomite formation commenced prior to the completion of calcite precipitation.

Apparently anomalous $\delta^{18}O$ values identified correspond to the highest temperature values (60°C, 61°C and 64°C). These values are not unreasonable. That said, they are outliers in the dataset. There are four potential explanations to explain low $\delta^{18}O$ values and corresponding high postulated formation temperatures:

a) Contamination/method errors: Discussed in detail above with respect to calcite and similarly concluded as highly unlikely.

b) Disequilibrium Precipitation: In a similar manner to that discussed for calcite, disequilibrium precipitation of dolomite must be a consideration. It is assumed in this study that dolomite precipitated in equilibrium with the formation fluid.

c) High precipitation temperature: It has previously been proposed that dolomite can precipitate at temperatures up to 300°C (Bush, 1973; Sibley et al., 1994). This is possible, however does not account for calculated temperatures which are almost double that of

the maximum burial temperatures proposed in the burial model of Kuhn et al., (2012), a model proposed for a position closer to the depocentre of the basin than the middle Bakken member in the well of this study. Therefore it is easy to dismiss this possibility.

d) Fluid composition: One possibility is that the assumed oxygen isotope composition of the dolomitising fluid is a little too high. A lower assumed $\delta^{18}O$ value of -4 (Figure 5.17), would bring the outlying 3 crystals into formation temperatures <50°C. It is also possible that these 3 crystals represent isotopically evolving fluids due to the introduction of an isotopically different fluid during dolomitisation.

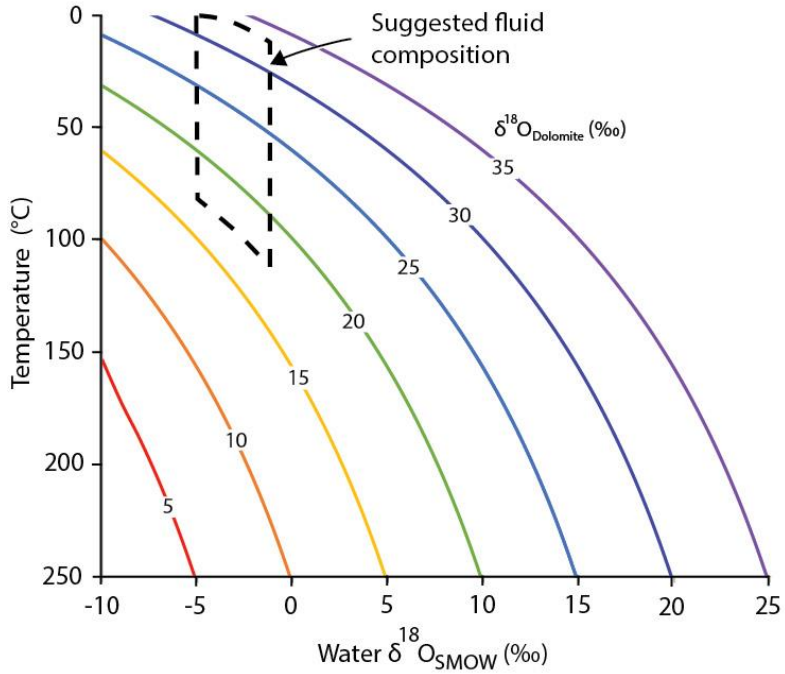

Figure 5.17 – Oxygen stable isotope composition of dolomite as a function of temperature and the $\delta^{18}O$ of the fluid from which it precipitated from. Using the dolomite paleothermometry equation of Vasconcelos et al., (2005).

One source of fluid which is isotopically light is meteoric water. Fritz (1971) suggests that since it is difficult to assign $\delta^{18}O$ ratios to past marine waters, most previous workers have attributed low $\delta^{18}O$ values to percolating meteoric waters. This is particularly prevalent in this system as the suggestion that the reservoir fluid most likely had a higher $\delta^{18}O$ composition to precipitate the pre-cursor calcite cement. Therefore, we suggest that this was lowered due to the introduction of meteoric water into the basin during

dolomitisation. Meteoric water in the Williston during the late Devonian is estimated to have a $\delta^{18}O$ value of ~-8 and -9‰ which has the potential to reduce the $\delta^{18}O$ of the dolomitising fluid (Carpenter et al., 1991). In order for meteoric to gain access to the reservoir a mechanism is required. At a regional scale it is thought the middle Bakken member has been exposed at the basin margins (Webster, 1984). It has been suggested that this unconformity resulted in the loss of 230 Ma of the rock record (Mageau et al., 2001). During such a long period of time, significant volumes of meteoric fluid could have penetrated into the middle Bakken member, mixed with the reservoir fluid and lowered the $\delta^{18}O$ of the dolomitising fluid. Furthermore, Berwick (2009) reports evidence from sedimentary structures which suggests that the middle Bakken member was frequently exposed during it is deposition so may have been exposed to meteoric water.

One way of directly measuring temperature of formation is by analysis of mineral fluid inclusions. We are aware of only one study which reports the homogenisation temperatures obtained from fluid inclusions for middle Bakken member carbonates and these values are both limited in number and reliability; something recognised by the author (Staruiala et al., 2013). The homogenisation temperatures reported by Staruiala et al., (2013) are higher than mean values calculated in our study. We support the authors caution to the accuracy of these values. This withstanding, homogenisation values of 74°C, 76°C, 110°C and 114°C were reported. The authors postulate the higher values are due to post-trapping stretching of the fluid inclusions; however, the lower values are tentatively interpreted as representing the upper temperature limits of dolomite precipitation.

Crystal Chemistry

Dolomite morphologies 2-6 detailed in Chapter 1 show very similar geochemical signatures in the analyses of this study so are discussed together. Whilst very small absolute differences in chemistry are likely to have been the cause of differences in the CL emission character in other previous studies, this seems unlikely in these dolomites as the compositional variation within each textural type is large, Table 5.3 & Figure 5.4. The elemental composition of individual dolomite crystals shows no relationship with morphological type. This may simply be because the dolomites were formed from the same or similar fluid and the variations in dolomite chemistry reflect very small, localised changes in fluid chemistry due to other diagenetic reactions (see Chapter 3). This idea is

supported by the simple SEM-CL signature observed in phases 2-6. Simple but discrete zonation in SEM-CL has been used by other workers to suggest these crystals have not been recrystallized and therefore are early diagenetic dolomites (Reinhold, 1998; Kupezs and Land, 1994; Montanaz and Read, 1992).

The chemistry of most of these dolomites is non-stoichiometric; with calcium magnesium ratios varying from 0.4 - 1.96, whereas stoichiometric dolomite has a calcium magnesium ratio of 1. The ordering of dolomite crystals is thought to increase with age, with deeply buried dolomite being the most stoichiometric, (McKenzie, 1981; Mazzullo, 1992; Boggs and Krinsley, 2006). The change from non-stoichiometric dolomite which has a poorly ordered atomic structure to stoichiometric dolomite which has better order is reported to occur via dissolution - re-precipitation reactions after multiple recrystallization events (In: Al-Aasm, 2000; from Land, 1980; Montanez and Read, 1992; Kupecz and Land, 1994; Malone et. al., 1996). The non-stoichiometric composition of middle Bakken member dolomites is similar to that of early diagenetic, marine, low-temperature dolomites, e.g., sabkha type dolomites (e.g. Geske et al., 2012).

The composition and large range in the elemental abundance found in dolomite phases 2 - 6 is similarly variable to those observed in previous studies of late-Devonian to Mississippian early diagenetic dolomites, Table 5.6. The range of values is large. The range of dolomite compositions reported by Reinhold (1998) is similarly very large.

Study	Type	$CaCO_3$ (mol%)	$MgCO_3$ (mol%)	$FeCO_3$ (ppm)
This study (T2-T6)	Cement (RP)	**50.5** (28.7 - 76.9)	**48.1** (22.2 - 89.6)	**121 ppm** (0 - 1720)
Mountjoy et al., 1999	Cement (RP)	**49.7** (49.3 - 49.7)	**49.8** (46.2 - 51.5)	**898.9** (60 - 1797)
Reinhold, 1998	Matrix & Cement	**NA** (48.3 - 62.1)	**NA** (37.8 - 51.7)	**NA** (BDL - 4700)
Al-Aasm, 2000 (micro-dolomites)	Primary - Evaporitic	**58** (54.1 – 61.4)	**NA**	**125** (112 - 1243)
Al-Aasm, 2000 (meso-dolomites)	Primary - Sabkha	**61.4** (56.9 - 67.4)	**NA**	**3493** (0 - 3006)
Mattes & Mountjoy, 1980	Various - Summary	**53.7** (48.1 - 60.2)	**46.5** (43.8 - 50.3)	**NA** (90 - 841)

Table 5.6 – Composition of early diagenetic dolomite from the late Devonian to early Mississippian in previous studies. Mean value is given in bold and the range of values is shown in parentheses. NA – values not published, RP - Replacive, BDL – Below detection limits.

Other workers, found such a large range of elemental compositions are present in and attributable to replacement dolomitisation (Katz, 1971; Searl, 1992; Carmichael et al., 2008). This finding is logical and builds on the petrographic observation of 'cloudy cores', present in some crystals due to the incomplete replacement of calcite. During calcite replacement conversion to dolomite will occur at slightly different rates; combined with the analytical practice of measuring the chemistry of the crystal at it's very centre, irrespective of crystal size, then it follows there will be varying quantities of both the precursor elements in the crystals. Other evidence for replacement includes:

1) Luminescence in the red spectrum (Amthor et al., 1993); whilst not exclusive to replacement dolomite, this is commonly a feature of replacement dolomite.

2) Presence of cloudy core and clear rim dolomites textures (Scholle & Ulmer-Scholle, 2003). Where the core represents the initial growth phase rich in unrecrystallised host-rock mineral inclusions and/or early precipitates and the edge is a more stoichiometric dolomite (Sibley, 1982; Budd, 1997; Kyser et al., 2002; Scholle & Ulmer-Scholle, 2003) (Chapter 3).

3) Medium to coarsely crystalline (10-100 µm, euhedral to subhedral mosaics of planar crystals, typical of replacement dolomite (Amthor et al., 1993; Warren, 2000), whereas finer grained (<10 µm) dolomites are typically thought to be formed by syn-depositional mechanisms (Chapter 3).

4) Vuggy porosity, thought to be formed in part due to the replacement of larger calcium atoms with smaller magnesium atoms (Weyl, 1960; Scholle & Ulmer-Scholle, 2003).

Reservoir Fluid Composition

Reservoir fluid composition can significantly affect the composition of the carbonate minerals from which they precipitate. Simple, concentrically zoned SEM-CL character that has been observed in diagenetic middle Bakken member dolomites has previously been attributed to a change in bulk-fluid properties (Boggs & Krinsley, 2006). The discrete change in CL emission intensity in each zone, suggests the inferred fluid change occurred as a single punctuated event, rather than a continuous and gradational process which we suggest would lead to multiple layers and a gradual change in luminescence intensity. That said, a large change in fluid chemistry is not necessarily required to change the very sensitive luminescence character of the dolomite, but would result in the same outcome. In SEM-CL images all diagenetic dolomites showed 2 red-luminescing zones. The apparent variation between apparent zones observed in BSE images and SEM-CL images has been reported in previous studies. Jones (2004) showed that apparently dull zones in SEM-CL had subtle zones caused by very small variations in the calcium-magnesium ratio within individual crystals. Such small variations in chemistry cannot simply be resolved using a BSE detector (Jones, 2004).

The red CL emissions found in middle Bakken member dolomites has previously been attributed to the high concentration of manganese in the dolomitising fluid which is thought to activate the luminescence (Richter et al., 2003). The red luminescence covers a range of 620–750 nm. It has been reported that when luminescence occurs most strongly in dolomite at 655 nm, then this is due to the presence of manganese in the magnesium position of the dolomite crystal lattice (El Ali et al., 1993). However, it has been shown that Mn^{2+} concentrations as low as 1 ppm can activate CL-emissions in iron poor carbonates (Habermann et al., 1998).

Direct compositional analysis of diagenetic dolomite crystals by SEM-WDS did not find a significantly high abundance of manganese in diagenetic dolomite relative to Mississippian dolomite compositions reported by other studies (Table 5.3), however 1ppm is significantly lower than the resolution of the grain-scale techniques used in this study. Other workers have suggested it is not the absolute concentration of an activator but in fact the ratio of the abundance of the activator to quencher ions which control the luminescence (Marshall, 1988).

If red wavelength emissions are attributable to small compositional changes, we postulate it is due to the ratio of activator to quencher elements and not the absolute concentration of either element. We suggest the new or evolved formation fluid introduced either had a depletion of Mn^{2+} (activator) ions or a relative enrichment in the proportion of Fe^{2+} ions (quencher ions).

Comparing the abundance of iron, magnesium or calcium with textural type we found significant variations in calcium in 'type 6' dolomites. Whilst it may be suggested this is an analytical artefact; due to the fine grained nature (<5 μm) of type 6 dolomite, we suggest this may be related to the mechanism of dolomitisation. We propose the variation in calcium content is a relic of growth due to the crystal not completely equilibrating with the surrounding fluid. Alternatively, it has been suggested that when the calcium concentration is high it may be due to incomplete dolomitisation from calcite during replacement (Warren, 2000).

Hydrogeology

Understanding the basin scale hydrogeology allows us to propose likely sources of dolomitising fluid within the Williston basin based on fluid composition, volume and source rock. There are several studies which have sought to trace local and aquifer specific fluid movements within the Bakken Formation (e.g. Grasby et al., 2000; Rostron & Holmden, 2003; Ferguson et al., 2007; Hendry et al., 2013). However, at the basin scale, fluid movement within the Williston basin are not well constrained (Bachu and Hitchon, 1996). Specific studies specifically referring to fluid movement in late Devonian to early Mississippian strata and the associated aquifers are limited.

At the basin scale fluid is thought to flow from the South West to the North East (Downey et al., 1985; Hannon, 1987; Le Fever, 1998). The Bakken Formation forms an aquiclude separating the underlying Devonian aquifer system and overlying Mississippian aquifer system (Bachu and Hitchon, 1996). These aquifers are sealed by the Praire aquiclude (underlying the Devonian aquifer) and the Mississippian-Jurassic Aquitard system (overlying the Mississippian aquifer system). The Bakken Formation does not outcrop in the Williston basin (Doughty et al., 2014), therefore the only potential large scale fluid sources entering the middle Bakken member are the Devonian aquifer system and Mississippian aquifer system, which must be accessed through the low permeability lower Bakken member and upper Bakken member.

The underlying Devonian aquifer system is composed of the Beaverhill Lake Group, Woodbend Group, Winterburn Group and Wabamun Group. This aquifer is regarded as open system; so can be recharged and discharge at the surface. The salinity of this aquifer is thought to reach a maximum of ~ 300,000 mg/L (Bachu & Hitchon, 1996). The Mississippian aquifer system is made up of the Lodgepole Formation and Mission Canyon Formation. This system is regarded by Bachu & Hitchon (1996) as a semi-open system as it can be recharged by exposure at the surface, but does not however outcrop downstream to allow discharge. In this aquifer system the salinity reaches a maximum of ~310,000 mg/L, (Bachu & Hitchon, 1996), which compared to current seawater (35,000 mg/L) makes the basin fluids very saline. The differences in salinity between the underlying Devonian aquifer system and the Mississippian aquifer have been used to suggest the Bakken Formation is a tight, effective aquiclude (Bachu & Hitchon, 1996). From this discussion of bulk fluid flow within the middle Bakken member it appears that the Bakken Formation is an effective aquitard, in a largely closed hydrogeological system where there is only limited fluid communication between the underlying and overlying aquifers.

It seems unlikely that there was any introduction of bulk fluids into the middle Bakken member by ingress post-consolidation as mercury intrusion porosimetry data [additional to Chapter 4, see Appendix 5] suggests the upper and lower Bakken members have a very low porosity and permeability. Possibilities of introduced or altered fluids include:

a) meteoric fluid during sedimentation and/or the post-Mississippian Bakken exposure (discussed above).

b) introduction of saline fluid into the basin, common in continental sag basin such as this.

c) ingress of fluid related to the dissolution of salt in the underlying Prairie Evaporite (LeFever and LeFever, 2005) d) evolution of diagenetic fluid.

We use this conclusion to support our assertion that dolomitisation occurred early in the diagenetic history of the middle Bakken member, prior to significant burial, consolidation and lithification of the upper and lower Bakken member which reduced their porosity and permeability. At shallow depths, where the sediment was less consolidated and later diagenetic minerals had not developed; the porosity and permeability of the unit would be greater and the effectiveness of the Bakken Formation aquitard would be less, allowing greater fluid communication into, out of and within the middle Bakken member. Therefore, we suggest that fluid introduced into the basin occurred early in the diagenetic history of the rock and was derived from both meteoric sources and evaporated seawater.

Conclusions

The oxygen isotope composition of middle Bakken member carbonate minerals was successfully measured at the grain scale by SIMS. Calcite, dolomite and quartz have a distinctly different oxygen isotope signature. Middle Bakken member calcites were found to have $\delta^{18}O$ values of 24.9 - 33.7‰, whereas dolomite has values of between 16.4 - 32.2‰. Measured $\delta^{18}O$ values for type 2 and type 3 calcite are very similar which we suggest indicates that these phases are the same. For dolomite we found no relationship between oxygen isotope composition with texture, facies, or depth. The similarity in $\delta^{18}O$ values of different morphologies of dolomite suggests that differences in morphology do not reflect fundamental differences in growth conditions.

From this work we suggest, the formation of diagenetic carbonate minerals calcite and dolomite occurred early in the diagenetic history of the middle Bakken member. Calcite formed at near-surface burial temperatures calculated to be between 8 - 51°C. The lowest temperature values are lower than predicted Devonian ocean water temperatures. During calcite precipitation it is suggested that the ocean water had a heavier oxygen isotope composition than previously reported.

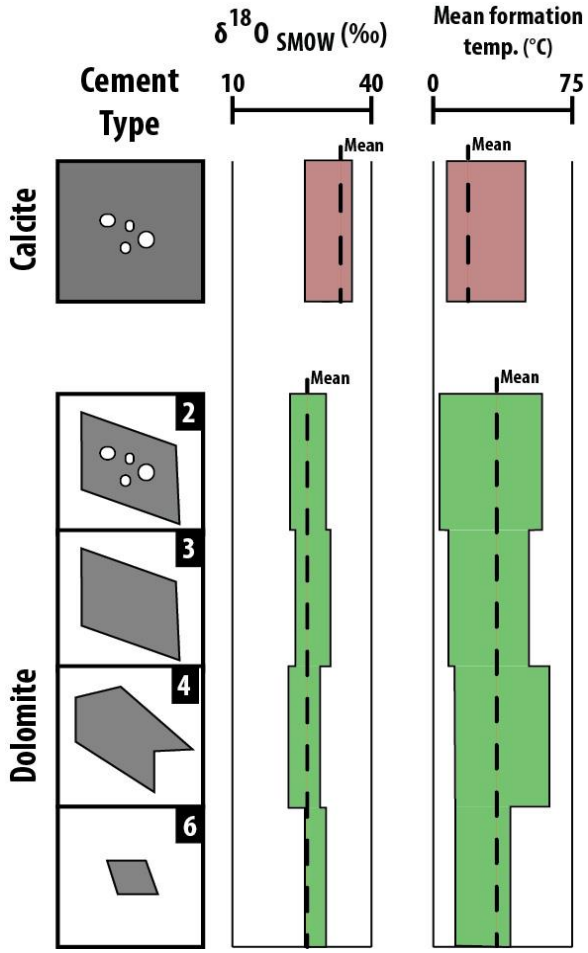

Figure 5.18 – Schematic summarising the differences in oxygen isotope composition and calculated formation temperature in different textures of carbonate phases calcite and dolomite.

This was followed by the replacement of the earlier formed calcite by dolomite at temperatures of between 5 - 64°C. Formation temperatures indicate calcite proceeded during the early stages of dolomite formation. During dolomite formation it is thought exposure of the middle Bakken member may have resulted in the introduction of meteoric water which decreased the $\delta^{18}O$ of the reservoir fluid.

We identified one detrital dolomite phase in the middle Bakken member; type 1. This phase has a rounded, abraded morphology and complex SEM-CL signature quite unlike that of diagenetic dolomite in this study. The exact source of detrital dolomite is however unclear. It is thought they could be either reworked dolomite from underlying formations or washed in from older underlying formations transported from the Bakken Formation's hinterland.

We suggest the remaining phases and the bulk of middle Bakken member dolomite, precipitated shortly after the precipitation of calcite. Dolomite formed by replacement of calcite during shallow burial.

References

Al-Aasm, I. S. (2000). Chemical and isotopic constraints for recrystallization of sedimentary dolomites from the Western Canada sedimentary basin. Aquatic Geochemistry 6, p. 227-248.

Al-Aasm, I. S., Taylor, B. & South, B. (1990). Stable isotope analysis of multiple carbonate samples using selective acid extraction. Chemical Geology: Isotope Geoscience Section 80, p. 119-125.

Amthor, J. E., Mountjoy, E. W. & Machel, H. G. (1993). Subsurface dolomites in Upper Devonian Leduc formation buildups, central part of Rimbey-Meadowbrook reef trend, Alberta, Canada. Bulletin of canadian petroleum geology 41, p. 164-185.

Bachu, S. & Hitchon, B. (1996). Regional-scale flow of formation waters in the Williston Basin. AAPG Bulletin 80, p. 248-264.

Bemis, B. E., Spero, H. J., Bijma, J. & Lea, D. W. (1998). Re-evaluation of the oxygen isotopic composition of planktonic foraminifera: Experimental results and revised paleotemperature equations. Paleoceanography 13, p. 150-160.

Berwick, B., (2009). Depositional Environment, Mineralogy, and Sequence Stratigraphy of the Late Devonian Sanish Member (Upper Three Forks Formation), Williston Basin, North Dakota: Master's Thesis, Colorado School of Mines, 263 p.

Boggs, S. and Krinsley, D., 2006. Application of cathodoluminescence imaging to the study of sedimentary rocks. Cambridge University Press.

Budd, D. (1997). Cenozoic dolomites of carbonate islands: their attributes and origin. Earth-Science Reviews 42, p. 1-47.

Bush, P. (1973). Some aspects of the diagenetic history of the sabkha in Abu Dhabi, Persian Gulf. The Persian Gulf: Springer, p. 395-407.

Carmichael, S. K., Ferry, J. M. & McDonough, W. F. (2008). Formation of replacement dolomite in the Latemar carbonate buildup, Dolomites, northern Italy: Part 1. Field relations, mineralogy, and geochemistry. American Journal of Science 308, p. 851-884.

Carpenter, S. J., Lohmann, K. C., Holden, P., Walter, L. M., Huston, T. J. & Halliday, A. N. (1991). $\delta^{18}O$ values, $^{87}Sr^{86}Sr$ and Sr/Mg ratios of Late Devonian abiotic marine calcite: Implications for the composition of ancient seawater. Geochimica et Cosmochimica Acta 55, p. 1991-2010.

Cavosie, A., Valley, J. & Wilde, S. (2005). Magmatic δ 18 O in 4400–3900 Ma detrital zircons: a record of the alteration and recycling of crust in the Early Archean. Earth and Planetary Science Letters 235, p. 663-681.

Curtis, C.D., Coleman, M.L. and Love, L.G., (1986). Pore water evolution during sediment burial from isotopic and mineral chemistry of calcite, dolomite and siderite concretions. Geochimica et Cosmochimica Acta, 50(10), p.2321-2334.

Dale, A., John, C.M., Mozley, P.S., Smalley, P.C. and Muggeridge, A.H., (2014). Time-capsule concretions: unlocking burial diagenetic processes in the Mancos Shale using carbonate clumped isotopes. Earth and Planetary Science Letters, 394, pp.30-37.

Doughty, T. (2014). Developing an Outcrop Reservoir Analog for the Williston Basin Bakken Formation with the Sappington Formation of South-Central Montana. Unconventional Resources Technology Conference (URTEC).

Downey, J., Busby, J. & Dinwiddie, G. (1985). Regional aquifers and petroleum in Williston Basin region of US. Am. Assoc. Pet. Geol., Bull. (United States) 69, 845.

Edwards, P & Lee, M. (2014) *Cathodoluminescence hyperspectral imaging in geoscience.* In: Cathodoluminescence and its Application to Geoscience. Short Course Series. Mineralogical Association of Canada, Québec, p. 29-45.

El Ali, A., Barbin, V., Calas, G., Cervelle, B., Ramseyer, K. & Bouroulec, J. (1993). Mn^{2+}-activated luminescence in dolomite, calcite and magnesite: quantitative determination of manganese and site distribution by EPR and CL spectroscopy. Chemical Geology 104, p. 189-202.

Emery, D. & Robinson, A. (2009). Stable Isotopes. Inorganic Geochemistry: Blackwell Scientific Publications, p. 73-100.

Epstein, S., Buchsbaum, R., Lowenstam, H. A. & Urey, H. C. (1953). Revised carbonate-water isotopic temperature scale. Geological Society of America Bulletin 64, p. 1315-1326.

Ferdous, H., (2001). Regional sedimentology and diagenesis of the Middle Bakken Member: implications for reservoir rock distribution in southern Saskatchewan. Unpublished thesis, Department of Geological Sciences: University of Saskatchewan, p. 467.

Ferguson, G. A., Betcher, R. N. & Grasby, S. E. (2007). Hydrogeology of the Winnipeg formation in Manitoba, Canada. Hydrogeology journal 15, p. 573-587.

Friedman, I. & O'Neil, J. R. (1977). Data of geochemistry: Compilation of stable isotope fractionation factors of geochemical interest: US Government Printing Office.

Fritz, P. (1971). Geochemical characteristics of dolomites and the ^{18}O content of Middle Devonian oceans. Earth and Planetary Science Letters 11, p. 277-282.

Fritz, P. and Smith, D.G.W., (1970). The isotopic composition of secondary dolomites. Geochimica et Cosmochimica Acta, 34(11), pp.1161-1173.

Fronval, T., Jensen, N.B. and Buchardt, B., (1995). Oxygen isotope disequilibrium precipitation of calcite in Lake Arresø, Denmark. Geology, 23(5), pp.463-466.

Geske, A., Goldstein, R. H., Mavromatis, V., Richter, D. K., Buhl, D., Kluge, T., John, C. M. & Immenhauser, A. (2015). The magnesium isotope ($\delta^{26}Mg$) signature of dolomites. Geochimica et Cosmochimica Acta 149, p. 131-151.

Girard, J.-P., Munz, I. A., Johansen, H., Hill, S. & Canham, A. (2001). Conditions and timing of quartz cementation in Brent reservoirs, Hild Field, North Sea: constraints from fluid inclusions and SIMS oxygen isotope microanalysis. Chemical Geology 176, p. 73-92.

Graham, C. M., Valley, J. W. & Winter, B. L. (1996). Ion microprobe analysis of $^{18}O/^{16}O$ in authigenic and detrital quartz in the St. Peter Sandstone, Michigan Basin and Wisconsin Arch, USA: contrasting diagenetic histories. Geochimica et Cosmochimica Acta 60, p. 5101-5116.

Grasby, S., Osadetz, K., Betcher, R. & Render, F. (2000). Reversal of the regional-scale flow system of the Williston basin in response to Pleistocene glaciation. Geology 28, 635-638.

Gregg, J. M. & Sibley, D. F. (1984). Epigenetic dolomitization and the origin of xenotopic dolomite texture. Journal of Sedimentary Research 54, p. 908-931.

Gregory, R. T. & Taylor, H. P. (1981). An oxygen isotope profile in a section of Cretaceous oceanic crust, Samail Ophiolite, Oman: Evidence for $\delta^{18}O$ buffering of the oceans by deep (>5 km) seawater-hydrothermal circulation at mid-ocean ridges. Journal of Geophysical Research: Solid Earth 86, p. 2737-2755.

Habermann, D., Neuser, R. D. & Richter, D. K. (1998). Low limit of Mn 2+-activated cathodoluminescence of calcite: state of the art. Sedimentary Geology 116, p. 13-24.

Hannon, N. (1987). Subsurface water flow patterns in the Canadian sector of the Williston Basin. Williston Basin: anatomy of a cratonic oil province. Edited by JA Peterson, DM Kent, SB Anderson, RH Pilatske, and MW Longman. Rocky Mountain Association of Geologists, Denver, Colo, p. 313-322.

Hardie, L. A. (1987). Dolomitization: A Critical View of some Current Views: Perspectives. Journal of Sedimentary Research 57, p. 166-183.

Harwood, J., Aplin, A. C., Fialips, C. I., Iliffe, J. E., Kozdon, R., Ushikubo, T. & Valley, J. W. (2013). Quartz cementation history of sandstones revealed by high-resolution SIMS oxygen isotope analysis. Journal of Sedimentary Research 83, p. 522-530.

Henderson, C. (2015) Sequence Model for the Bakken Formation in Southeast Alberta, Southwest Saskatchewan. Master's Thesis. University of Calgary.

Hendry, M. J., Barbour, S. L., Novakowski, K. & Wassenaar, L. I. (2013). Paleohydrogeology of the Cretaceous sediments of the Williston Basin using stable isotopes of water. Water Resources Research 49, p. 4580-4592.

Hiatt, E. E., Kyser, T. K., Fayek, M., Polito, P., Holk, G. J. & Riciputi, L. R. (2007). Early quartz cements and evolution of paleohydraulic properties of basal sandstones in three Paleoproterozoic continental basins: Evidence from in situ $\delta^{18}O$ analysis of quartz cements. Chemical Geology 238, p. 19-37.

Hudson, J. & Anderson, T. (1989). Ocean temperatures and isotopic compositions through time. Transactions of the Royal Society of Edinburgh: Earth Sciences 80, p. 183-192.

Irwin, H., Curtis, C. and Coleman, M., 1977. Isotopic evidence for source of diagenetic carbonates formed during burial of organic-rich sediments. Nature 269, p. 209-213

Jones, B. (2004). Petrography and significance of zoned dolomite cements from the Cayman Formation (Miocene) of Cayman Brac, British West Indies. Journal of Sedimentary Research 74, p. 95-109.

Karasinski, D. R. (2006). Sedimentology and Hydrocarbon Potential of the Devonian Three Forks and Mississippian Bakken Formations, Sinclair Area, Southeast Saskatchewan-southwest Manitoba. Master's Thesis. University of Manitoba (Canada).

Kasting, J. F., Howard, M. T., Wallmann, K., Veizer, J., Shields, G. & Jaffrés, J. (2006). Paleoclimates, ocean depth, and the oxygen isotopic composition of seawater. Earth and Planetary Science Letters 252, p. 82-93.

Katz, A. (1971). Zoned dolomite crystals. The Journal of Geology, p. 38-51.

Katz, B.J., (2011). Microbial processes and natural gas accumulations. Open Geol. J, 5(75), p.83.

Kent, D. M. (1987). Paleotectonic Controls on Sedimentation in the Northern Williston Basin, Saskatchewan. In: Longman, M. (ed.) Williston Basin: Anatomy of a Cratonic Oil Province. Denver: The Rocky Mountain Association of Geologists, p. 44-55.

Kita, N. T., Ushikubo, T., Fu, B. & Valley, J. W. (2009). High precision SIMS oxygen isotope analysis and the effect of sample topography. Chemical Geology 264, p. 43-57.

Kozdon, R., Ushikubo, T., Kita, N., Spicuzza, M. & Valley, J. (2009). Intratest oxygen isotope variability in the planktonic foraminifer N. pachyderma: Real vs. apparent vital effects by ion microprobe. Chemical Geology 258, p. 327-337.

Kuhn, P. P., di Primio, R., Hill, R., Lawrence, J. R. & Horsfield, B. (2012). Three-dimensional modeling study of the low-permeability petroleum system of the Bakken Formation. AAPG Bulletin 96, p. 1867-1897.

Kupecz, J. & Land, L. (1994). Progressive recrystallization and stabilization of early-stage dolomite: Lower Ordovician Ellenburger Group, west Texas. Dolomites: A volume in Honour of Dolomieu. B. Purser, M., Tucker, D. Zenger (eds.). International Association of Sedimentology Special Publication, p. 255-279.

Land, L.S., 1967. Diagenesis of skeletal carbonates. Journal of Sedimentary Research, 37(3), p. 914-930.

Land, L. S. (1980). The isotopic and trace element geochemistry of dolomite: the state of the art. SEPM Special Publication No. 28, p. 87-110.

Last, W. & Edwards, W. (1991). Petrology of the Middle Bakken Member in the Daly Field, southwestern Manitoba. Williston Basin Symposium, p. 64-69.

Le Fever, R. D. (1998). Hydrodynamics of formation waters in the North Dakota Williston Basin. Williston Basin Symposium, p. 229-231.

Lee, M. R. (2000). Imaging of calcite by optical and SEM cathodoluminescence. Microscopy and Analysis 70, p. 15-16.

Machel, H. G. (2004). Concepts and models of dolomitization: a critical reappraisal. Geological Society, London, Special Publications p. 235, p. 7-63.

Mageau, K.R., Leckie, D. and Maguire, R., (2001). The Bakken Formation of West-Central Saskatchewan and East-Central Albert: A Depositional History, Stratigraphy and Facies Distribution of Bakken Shelf Sand Ridges Using the Cactus Lake Field as a Working Model.

Malone, M. J., Baker, P. A. & Burns, S. J. (1996). Recrystallization of dolomite: An experimental study from. Geochimica et Cosmochimica Acta 60, p. 2189-2207.

Marshall, D. J. & Mariano, A. N. (1988). Cathodoluminescence of geological materials: Taylor & Francis, Geological Journal 26, p. 351.

Matthews, A. & Katz, A. (1977). Oxygen isotope fractionation during the dolomitization of calcium carbonate. Geochimica et Cosmochimica Acta 41, p. 1431-1438.

Mattes, B. W., and E. W. Mountjoy, (1980). Burial dolomitization of the Upper Devonian Miette Buildup, Jasper National Park, Alberta, in Concepts and models of dolomitization: SEPM Special Publication 28, p. 259-297.

Mazzullo, S. (1992). Geochemical and neomorphic alteration of dolomite: a review. Carbonates and evaporites 7, p. 21-37.

McBride, E. F. (1989). Quartz cement in sandstones: a review. Earth-Science Reviews 26, p. 69-112.

McCrea, J. M. (1950). On the isotopic chemistry of carbonates and a paleotemperature scale. The Journal of Chemical Physics 18, p. 849-857.

McKenzie, J. A. (1981). Holocene dolomitization of calcium carbonate sediments from the coastal sabkhas of Abu Dhabi, UAE: a stable isotope study. The Journal of Geology, p. 185-198.

Meyers W. J. and Lohmann K. C. (1985) Isotope geochemistry of regionally extensive calcite cement zones and marine components in Mississippian limestones, New Mexico. In Carbonate Cements; Sot. Econ. Paleont. Mineral. Spec. Publ. 36, p. 223-240.

Michalowski, T. & Asuero, A. G. (2012). Thermodynamic Modelling of Dolomite Behavior in Aqueous Media. Journal of Thermodynamics 2012. p. 1-12.

Mohamed, T.I., (2015). Sequence Stratigraphy and Provenance of the Bakken Formation in Southeast Alberta and Southwest Saskatchewan (Doctoral dissertation, University of Calgary).

Montanez, I. P. & Read, J. F. (1992). Fluid-rock interaction history during stabilization of early dolomites, upper Knox Group (Lower Ordovician), US Appalachians. Journal of Sedimentary Research 62. p. 753-778.

Moore, C. H. (1989). Carbonate diagenesis and porosity. Vol. 46. Elsevier.

Morrow, D. (1982). Diagenesis 1. Dolomite-Part 1: the chemistry of dolomitization and dolomite precipitation. Geoscience Canada 9. p. 113-123.

Mountjoy, E. W., Machel, H. G., Green, D., Duggan, J. & Williams-Jones, A. E. (1999). Devonian matrix dolomites and deep burial carbonate cements: a comparison between the Rimbey-Meadowbrook reef trend and the deep basin of west-central Alberta. Bulletin of canadian petroleum geology 47, p. 487-509.

Mozley, P.S. and Burns, S.J., (1993). Oxygen and carbon isotopic composition of marine carbonate concretions: an overview. Journal of Sedimentary Research, 63(1).

Muehlenbachs, K. & Clayton, R. N. (1976). Oxygen isotope composition of the oceanic crust and its bearing on seawater. Journal of Geophysical Research 81, p. 4365-4369.

O'Neil, J. R., Clayton, R. N. & Mayeda, T. K. (1969). Oxygen isotope fractionation in divalent metal carbonates. Journal of Chemical Physics 51, p. 5547-5558.

Pentecost, A., Andrews, J.E., Dennis, P.F., Marca-Bell, A. and Dennis, S. (2006). Charophyte growth in small temperate water bodies: extreme isotopic disequilibrium and implications for the palaeoecology of shallow marl lakes. Palaeogeography, Palaeoclimatology, Palaeoecology, 240(3), p.389-404.

Pitman, J. K., Price, L. C. & LeFever, J. A. (2001). Diagenesis and fracture development in the Bakken Formation, Williston Basin: Implications for reservoir quality in the middle member: US Department of the Interior, US Geological Survey Professional Paper 1653.

Reed, R. M. & Milliken, K. L. (2003). How to overcome imaging problems associated with carbonate minerals on SEM-based cathodoluminescence systems. Journal of Sedimentary Research 73, p. 328-332.

Reinhold, C. (1998). Multiple episodes of dolomitization and dolomite recrystallization during shallow burial in Upper Jurassic shelf carbonates: eastern Swabian Alb, southern Germany. Sedimentary Geology 121, p. 71-95.

Richter, D. K., Götte, T., Götze, J. & Neuser, R. D. (2003). Progress in application of cathodoluminescence (CL) in sedimentary petrology. Mineralogy and Petrology 79, p. 127-166.

Rollinson, H. R. (2014). Using geochemical data: evaluation, presentation, interpretation: Routledge. p. 384.

Rollion-Bard, C., Erez, J. & Zilberman, T. (2008). Intra-shell oxygen isotope ratios in the benthic foraminifera genus Amphistegina and the influence of seawater carbonate chemistry and temperature on this ratio. Geochimica et Cosmochimica Acta 72, p. 6006-6014.

Rostron, B. & Holmden, C. (2000). Fingerprinting formation-waters using stable isotopes, Midale area, Williston Basin, Canada. Journal of Geochemical Exploration 69, p. 219-223.

Sayani, H. R., Cobb, K. M., Cohen, A. L., Elliott, W. C., Nurhati, I. S., Dunbar, R. B., Rose, K. A. & Zaunbrecher, L. K. (2011). Effects of diagenesis on paleoclimate reconstructions from modern and young fossil corals. Geochimica et Cosmochimica Acta 75, p. 6361-6373.

Scholle, P. A. & Ulmer-Scholle, D. S. (2003). A Color Guide to the Petrography of Carbonate Rocks: Grains, Textures, Porosity, Diagenesis, AAPG Memoir 77: AAPG.

Searl, A. (1992). Dolomite-carbonate replacement textures in veins cutting Carboniferous rocks in East Fife. Sedimentary Geology 77, p. 1-14.

Sharp, Z. (2007). Principles of stable isotope geochemistry: Pearson Education Upper Saddle River, NJ. Prentice Hall, New York, 360.

Sibley, D. F. & Gregg, J. M. (1987). Classification of dolomite rock textures. Journal of Sedimentary Research 57, p. 967-975.

Sibley, D. F., Nordeng, S. H. & Borkowski, M. L. (1994). Dolomitization kinetics in hydrothermal bombs and natural settings. Journal of Sedimentary Research 64A, p. 630-637.

Śliwiński, M. G., Kitajima, K., Kozdon, R., Spicuzza, M. J., Fournelle, J. H., Denny, A. & Valley, J. W. (2015). Secondary Ion Mass Spectrometry Bias on Isotope Ratios in Dolomite–Ankerite, Part I: $\delta^{18}O$ Matrix Effects. Geostandards and Geoanalytical Research, 40, p. 157–172.

Sperber, C. M., Wilkinson, B. H. & Peacor, D. R. (1984). Rock composition, dolomite stoichiometry, and rock/water reactions in dolomitic carbonate rocks. The Journal of Geology, p. 609-622.

Staruiala, A. (2013). Diagenesis of the Bakken Formation, Southeastern Saskatchewan. Williston Basin Symposium. Twenty-first Williston Basin Petroleum Conference: Core Workshop Volume, p. 25-44.

Tarutani, T., Clayton, R. N. & Mayeda, T. K. (1969). The effect of polymorphism and magnesium substitution on oxygen isotope fractionation between calcium carbonate and water. Geochimica et Cosmochimica Acta 33, p. 987-996.

Urey, H. C. (1947). The thermodynamic properties of isotopic substances. Journal of the Chemical Society (Resumed), p. 562-581.

Valley, J. W. & Kita, N. T. (2009). In situ oxygen isotope geochemistry by ion microprobe. Mineralogical Association of Canada Short Course 41, p. 19-63.

Van Geldern, R., Joachimski, M., Day, J., Jansen, U., Alvarez, F., Yolkin, E. & Ma, X.-P. (2006). Carbon, oxygen and strontium isotope records of Devonian brachiopod shell calcite. Palaeogeography, Palaeoclimatology, Palaeoecology 240, p. 47-67.

Vasconcelos, C., McKenzie, J. A., Warthmann, R. & Bernasconi, S. M. (2005). Calibration of the δ18O paleothermometer for dolomite precipitated in microbial cultures and natural environments. Geology 33, p. 317-320.

Veizer, J., Fritz, P. & Jones, B. (1986). Geochemistry of brachiopods: Oxygen and carbon isotopic records of Paleozoic oceans. Geochimica et Cosmochimica Acta 50, p. 1679-1696.

Videtich, P.E., 1981. A Method for Analyzing Dolomite for Stable Isotopic Composition: Research-Method Paper. Journal of Sedimentary Research, 51(2), 661.

Walderhaug, O. & Bjørkum, P. (1998). Calcite cement in shallow marine sandstones: growth mechanisms and geometry. Carbonate Cementation in Sandstones: Distribution Patterns and Geochemical Evolution, p. 179-192.

Walker, J. C. G. & Lohmann, K. C. (1989). Why the oxygen isotopic composition of sea water changes with time. Geophysical Research Letters 16, 323-326.

Walters LJ, Claypool GE, Choquette PW. (1972). Reaction rates and δ18O variation for the carbonate-phosphoric acid preparation method. Geochimica et Cosmochimica Acta 36(2), p. 129–40.

Wardlaw, N. (1976). Pore geometry of carbonate rocks as revealed by pore casts and capillary pressure. AAPG Bulletin 60, p. 245-257.

Warren, J. (2000). Dolomite: occurrence, evolution and economically important associations. Earth-Science Reviews 52, p. 1-81.

Weyl, P. K. (1960). Porosity through dolomitization: conservation-of-mass requirements. Journal of Sedimentary Research 30 (1), p. 85-90.

White, T. & Al-Aasm, I. S. (1997). Hydrothermal dolomitization of the Mississippian Upper Debolt Formation, Sikanni gas field, northeastern British Columbia, Canada. Bulletin of canadian petroleum geology 45, p. 297-316.

Chapter 6

Conclusions & Further Work

Conclusions

The best reservoir quality within the middle Bakken member is found in facies with low carbonate mineral abundance. Carbonate minerals calcite and dolomite make up on average 49% of the middle Bakken member. Calcite is observed as 3 different textures. Dolomite is present in 6 different textural forms; five of which are thought to be of diagenetic origin. Diagenetic carbonate minerals formed early in the diagenetic history of the middle Bakken member. This early cementation event filled much of the depositional pore space and inhibited the effects of compaction. The presence and thickness of carbonate cemented bands occurs at a scale smaller than that of individual facies.

To better understand the origin of these carbonate minerals, sequential acid leaching was used to measure the carbon and oxygen isotope composition of calcite and dolomite. It seems likely that there was some contamination of the calcite measurements by inadvertent dissolution of dolomite. In order to analyse individual textural phases of these minerals and to be confident of the mineral being measured Secondary Ion Mass Spectrometry (SIMS) was used to measure the oxygen isotope composition at the grain scale. Comparison of $\delta^{18}O$ values obtained by SIMS with those obtained by sequential acid dissolution mass spectrometry found bulk calcite values were similar to SIMS dolomite. This suggests calcite measurements had been contaminated by dolomite. This finding reinforces the importance of grain-scale measurements by SIMS in complex mixed carbonate phase samples such as these.

Calcite in the middle Bakken member was found to have $\delta^{18}O$ values of between 24.9 - 33.7‰. Using these values formation temperatures of calcite were calculated. These temperatures suggest calcite formed at near-surface burial temperatures calculated to be between 8 - 51°C. Similarities in the calculated formation temperatures and therefore $\delta^{18}O$ values for type 2 and type 3 calcite lead us to suggest that type 3 calcite are an under-developed crystals of type 2 calcite cement.

In contrast, dolomite was found to have $\delta^{18}O$ values of between 16.4 -32.2‰. From which formation temperatures of between 5 - 64°C were calculated; indicative of relatively shallow burial depths. Measurements of the elemental composition of dolomites by SEM-WDS vary over a large range, though the average value for each textural type is close to stoichiometric dolomite.

Diagenetic dolomite is thought to have formed after calcite due to the replacement of the early calcite cement. Overlapping calculated formation temperatures for calcite and dolomite in conjunction with observations of textural relationships between the two minerals suggest calcite precipitation continued during the initial stage of dolomitisation.

The middle Bakken member is a low porosity, and very low permeability formation. The highest porosity regions in the middle Bakken member are found in facies D1 and the lowest in facies B. Different technqiues were used to measure the porosity of the middle Bakken member. The differences in values represent both the differences in the resolution of individual techniques but also variations in lithology which occur within the middle Bakken member. All of the techniques concur that porosity in the middle is low.

Porosity and permeability measurements indicate that these are low permeability, low porosity rocks composed of small pores. Differences between measurements of connected porosity (helium and mercury porosity) and total porosity (density porosity) suggest a large proportion of the porosity of the middle Bakken member is connected.

Gas sorption isotherms showed that the middle Bakken member is a mesoporous unit. Pores of the middle Bakken member have pore throats with radii which are < 100 nm; they are small. Only in facies D2 are pore throats with a radii >100 nm found. Pore bodies are all < 135 nm but predominantly between 5 - 20 nm in size.

Intergranular pores are associated with clay rich zones. Intragranular pore space makes up a significant component of the pore system of the middle Bakken member. Intragranular porosity is predominantly found in quartz, calcite and dolomite. Intra - granular porosity in quartz is thought to be a product of dissolution, whereas the inter-granular pore space in calcite is thought to be due to incomplete cementation, creating framework-pores. Porosity in dolomite is postulated to be a product of the process of calcite replacement. Type 2 dolomites which have vuggy intragranular porosity are thought to be a due to volume reduction during mole-for-mole replacement of calcite by dolomite.

In this study we have shown that diagenesis has significantly affected the reservoir quality of the Bakken Formation. Cementation by calcite and replacement by dolomite during diagenesis are the principle controls on reservoir quality in the middle Bakken member. The prescence, abundance and distribution of these minerals explain the challenges for

hydrocarbon production in the middle Bakken member. By improving our understanding of pore geometry and diagenesis, specific regions ofmore preferable reservoir quality can be targeted and exploited.

Further Work

Pico-scale Pores

This study has shown that much of the porosity is made up of pores which are at their largest mesoporous. Pores >4 nm have been measured using low pressure gas sorption, with nitrogen at 77k in this study. A significant number of pores were found to have sizes, close to this, the lower limit of resolution of this technique. One method of measuring pore size distributions <4 nm is to obtain isotherms using carbon dioxide as the adsorptive gas, at a temperature of 273K. The higher adsorption temperatures, compared with N_2 at 77K, results in CO_2 molecules having a larger kinetic energy, meaning these gas molecules are able to enter into the narrow pores, avoiding the diffusional problems. This would enable the presence of smaller pores to be determined and quantified. Alternatively, small angle x-ray scattering (SAXS) would allow the detection and measurement of pores as small as ~1 nm.

Pore Connectivity

Quantitative analysis of pore morphology in 2D has been successfully undertaken in this study. The techniques used in this study, do not however indicate the nature or location of connected porosity. We are unable to comment on the contribution of intergranular and intragranular pores on the connected pore network. By analysing the pore system in 3D these questions could be addressed. Our attempts to quantify pore systems in 3D have been less successful. Gas sorption analyses conducted in this study suggest that a significant component of porosity is at the nano-scale. The implementation of nano-CT may be more appropriate. Either way, the advantage of x-ray scanning techniques is large and therefore representative sample volumes can be analysed. Until very recently sub-micron scans were not routinely possible. Furthermore, challenges in accurately thresholding both FIB-SEM and micro-CT data sets without manual tracing, in a reproducible way continues to present challenges in complex, heterogeneous samples such as those from the middle Bakken member. The application of the latest nano-CT scanning and image analysis techniques would provide useful insights into the 3D pore morphology on representative volumes.

Permeability

We found measurements of permeability vary significantly. Whilst all of the techniques generate results which suggest permeability is low in the middle Bakken member, an exact value of permeability is difficult to determine, yet would be very important for models of fluid flow, particularly hydrocarbon movement in the middle Bakken member. Understanding the variability in permeability and the principle controls on permeability within the middle Bakken member could be used to further improve the producibility of this low permeability unit.

Chapter 7

Appendicies

Appendix 1

Detailed facies descriptions. From Simenson (2010).

Facies B: Bioturbated, Argillaceous, Calcareous, Very Fine-Grained Siltstone/Sandstone.

Facies B consists of bioturbated, argillaceous, calcareous sandstones and siltstones. Strong bioturbation makes identification of many trace fossils difficult but some common *Helminthopsis*/*Sclarituba* burrow traces have been identified. Some calcite filled vertical fractures are present and local calcareous concretions are found within the facies. Intergranular and micro-fracture porosity are present with calcite cement and some pyrite cement. The facies shows up on wireline logs as a thick section of shaly sand. Core porosity values for this interval range from 2.2% - 9.8% and average 5.7%. Permeability values range from 0.0001 mD – 0.03 mD and average 0.0015 mD. The porosity values are favourable for a target zone but because of the homogeneous nature of this highly bioturbated section permeability measurements are extremely low.

Facies C: Planar to Undulose Laminated, Shaly, Very Fine-Grained Siltstone/Sandstone.

Facies C1 mainly consists of finely laminated shaly sandstone and siltstone. These laminations are on the millimeter and centimeter scale. There are some wavy laminated sections which could possibly be microbial influence (or colonization) of the sediment; however the section is dominated by continuous planar laminations. Intergranular and minimal amounts of inter-crystaline porosity are present. On well logs this interval is identified by convergence of the neutron porosity and density porosity curves and by clean (low) gamma ray readings. Core porosity values for this interval range from 2.5% - 10.3% and average 6.3%. Permeability values range from 0.0001 mD – 0.01 mD and average 0.0026 mD.

Facies D1: Contorted to Massive, Fine-Grained Sandstone.

Facies D1 consists of a muddy, contorted to massive, fine-grained sandstone that has common micro-faults, micro-fractures, and slumps representing soft sediment deformation. Some localized microbial influenced (or colonized) sections have been found in this facies. On well logs, this facies appears just below the cleanest gamma ray readings of facies D2 but are still cleaner than the underlying facies C2. Core porosity values range from 2.0% - 2.6%, averaging 2.3%. Permeability in this facies ranges from 0.0003 mD – 0.0012 mD and average 0.0008 mD.

Facies D2: Low Angle, Planar to Slightly Undulose, Cross-Laminated Sandstone with Thin Discontinuous Shale Laminations.

Facies D2 consists of a light brown to light grey, parallel to undulating laminated, low angle cross-laminated sandstone. This facies lacks bioturbation and can be highly cemented by calcite. Some calcite filled fractures are also present. This facies is present in only four of the cores described. Intergranular porosity is abundant with calcite as the dominant cement. This facies has the cleanest signature on the gamma ray reading from wireline logs (it has been called the “clean bench”) and the neutron and density come together. Core porosity values range from 2.5% - 12.8%, averaging 4.3% and permeability ranges from 0.0001 mD – 0.055 mD, averaging 0.0042 mD. This facies is considered to be included as a target interval for horizontal drilling in the Bakken but is mostly absent in the Parshall Field area.

Facies E: Finely Inter-Laminated, Bioturbated, Dolomitic-Mudstone and Dolomitic Siltstone/Sandstone.

Facies E consists of an interbedded dark grey, highly bioturbated siltstone, and light grey, very fine grained, thin parallel laminated sandstone. Locally strong and moderate bioturbation and microbial influence of the sediment is present. At the base of this facies there is a thin organic-rich mudstone which can be clearly seen on the gamma ray log as a high gamma ray value and a low bulk density. Core porosity ranges from 0.5% - 11.3% with an average of 5.7% for this facies. Permeability values range from 0.0001 mD – 0.083 mD and has an average permeability of 0.0062 mD. This interval is the most dolomitic zone of the Bakken and is one of the main targets for drilling.

Appendix 2

Lithology log of the Charlie Sorenson core log (Hart, 2014 pers. comm., 15th January). Facies are those proposed by Simenson (2010).

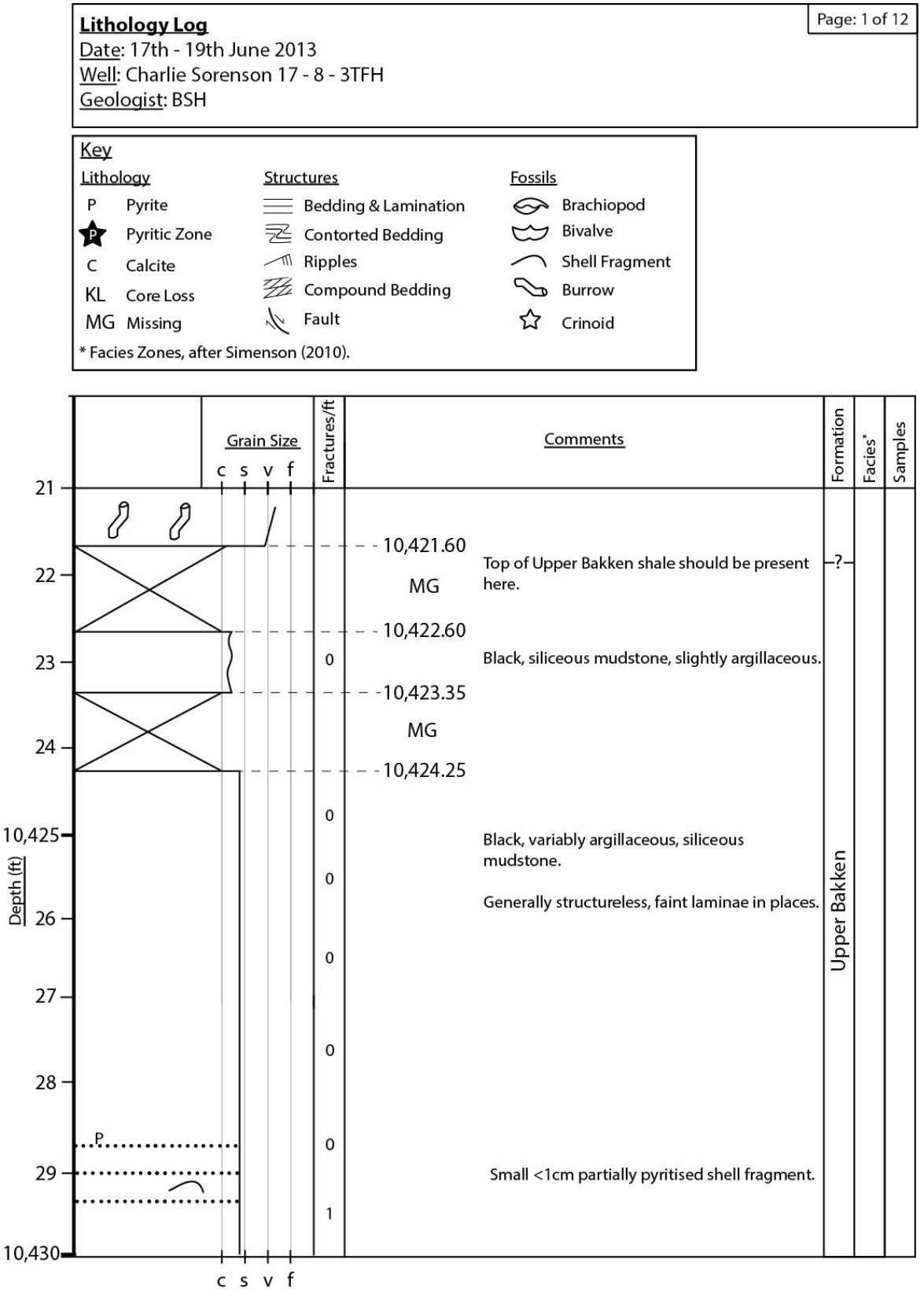

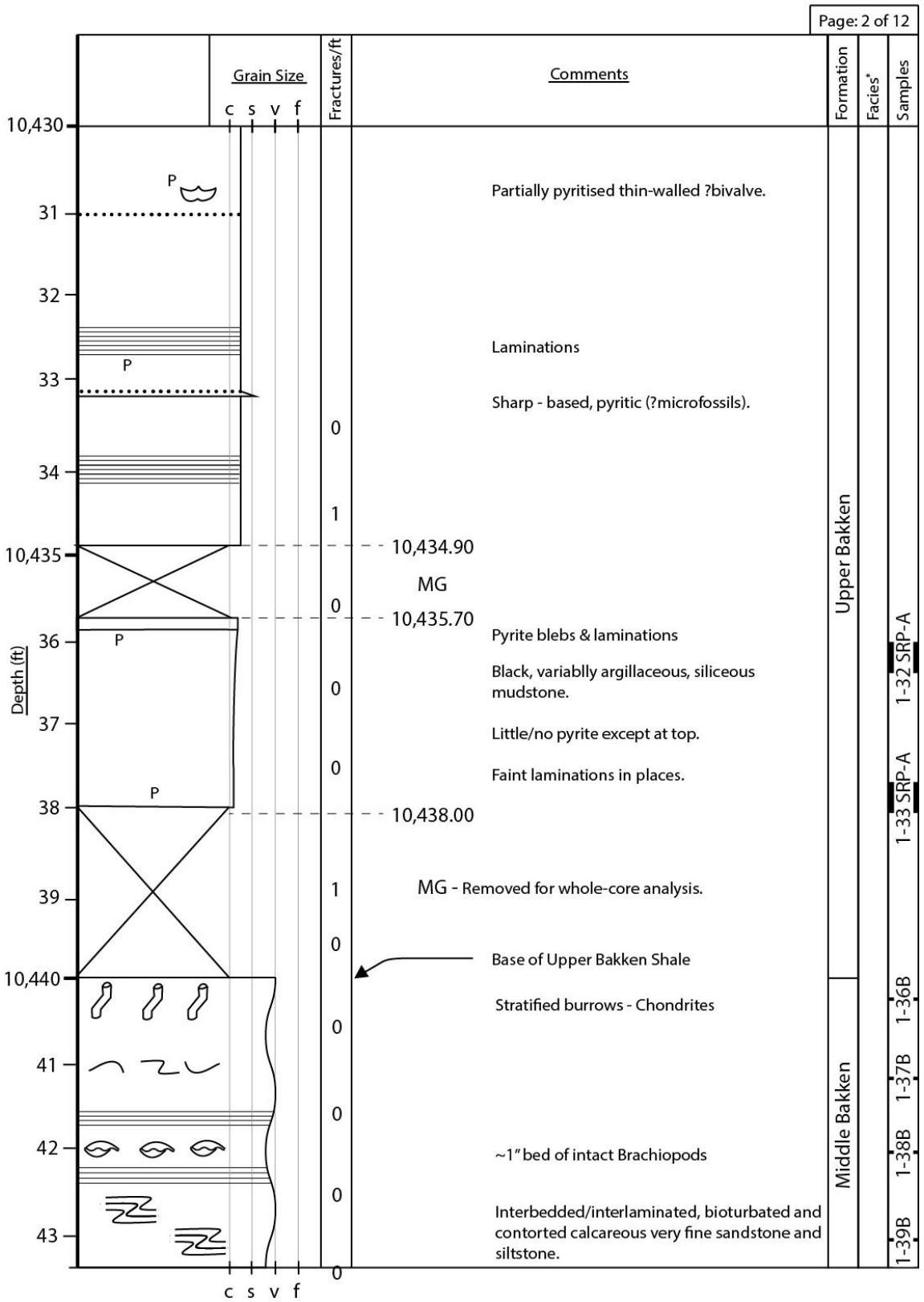
Grain Size
c s v f
Fractures/ft
Comments
Formation
Facies*
Samples
Depth (ft)
10,430
31
32
33
34
10,435
36
37
38
39
10,440
41
42
43
P
Partially pyritised thin-walled ?bivalve.
Laminations
Sharp - based, pyritic (?microfossils).
10,434.90
MG
10,435.70
Pyrite blebs & laminations
Black, variablly argillaceous, siliceous mudstone.
Little/no pyrite except at top.
Faint laminations in places.
10,438.00
MG - Removed for whole-core analysis.
Base of Upper Bakken Shale
Stratified burrows - Chondrites
~1" bed of intact Brachiopods
Interbedded/interlaminated, bioturbated and contorted calcareous very fine sandstone and siltstone.
Upper Bakken
Middle Bakken
1-32 SRP-A
1-33 SRP-A
1-36B
1-37B
1-38B
1-39B

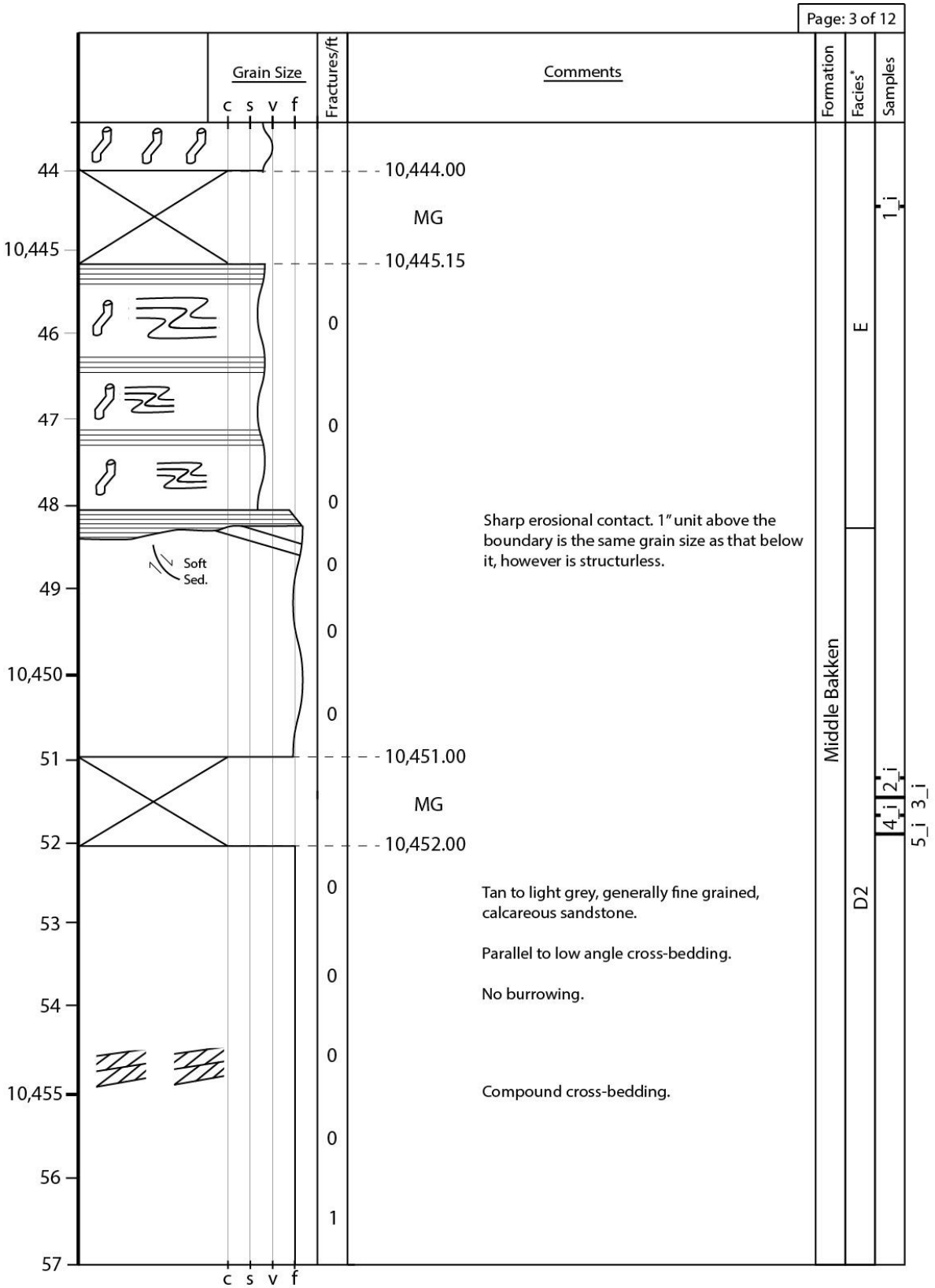
Grain Size
c s v f
Fractures/ft
Comments
Formation
Facies*
Samples
44
10,445
46
47
48
49
10,450
51
52
53
54
10,455
56
57
10,444.00
MG
10,445.15
0
0
0
0
0
0
10,451.00
MG
10,452.00
0
0
0
0
1
Soft Sed.
Sharp erosional contact. 1" unit above the boundary is the same grain size as that below it, however is structurless.
Tan to light grey, generally fine grained, calcareous sandstone.
Parallel to low angle cross-bedding.
No burrowing.
Compound cross-bedding.
Middle Bakken
E
D2
1_i
2_i
3_i
4_i
5_i

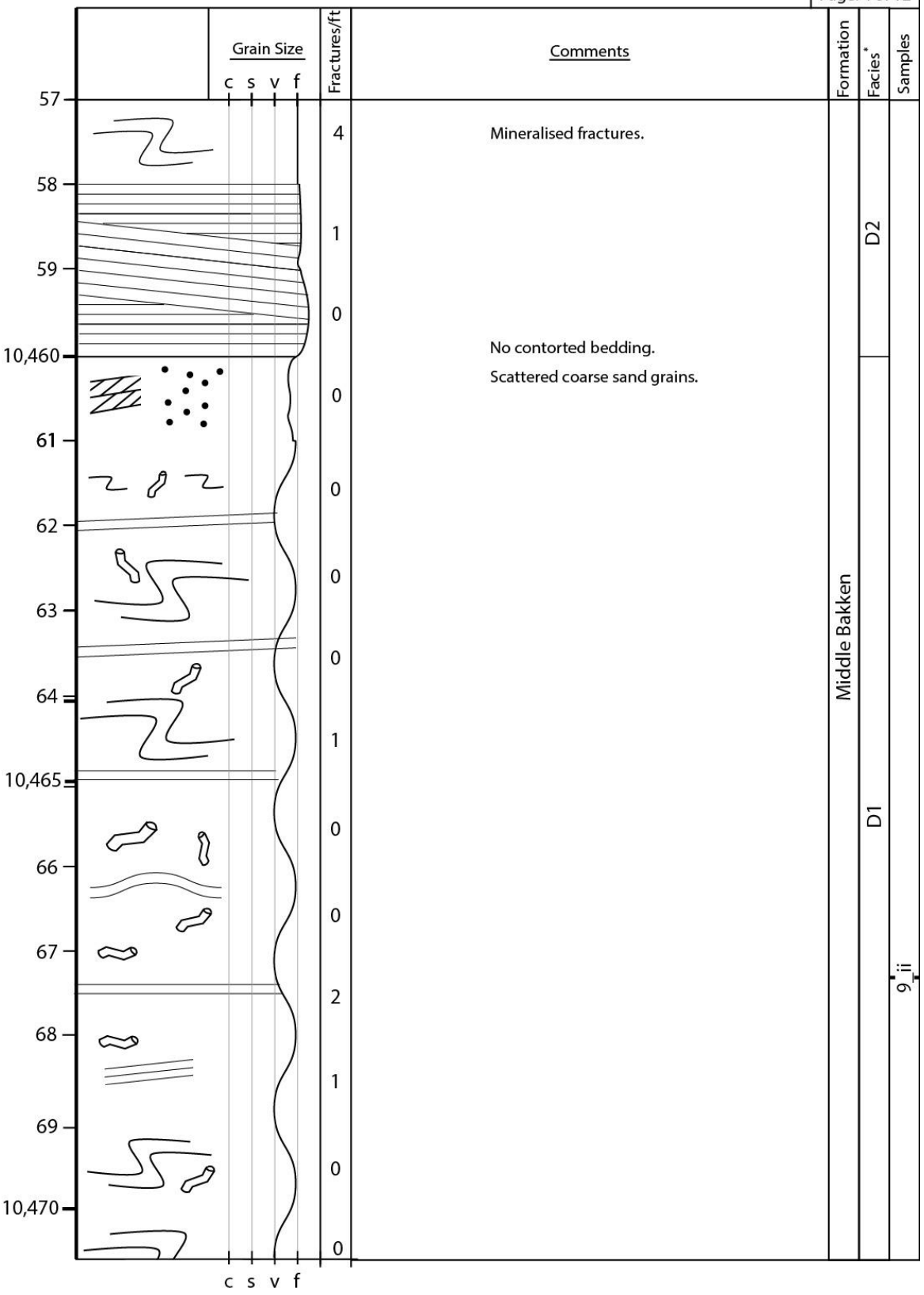
Grain Size
c s v f
Fractures/ft
Comments
Formation
Facies*
Samples
57
58
59
10,460
61
62
63
64
10,465
66
67
68
69
10,470
4
1
0
0
0
0
0
1
0
0
0
2
1
0
0
Mineralised fractures.
No contorted bedding.
Scattered coarse sand grains.
Middle Bakken
D2
D1
9_ii
c s v f

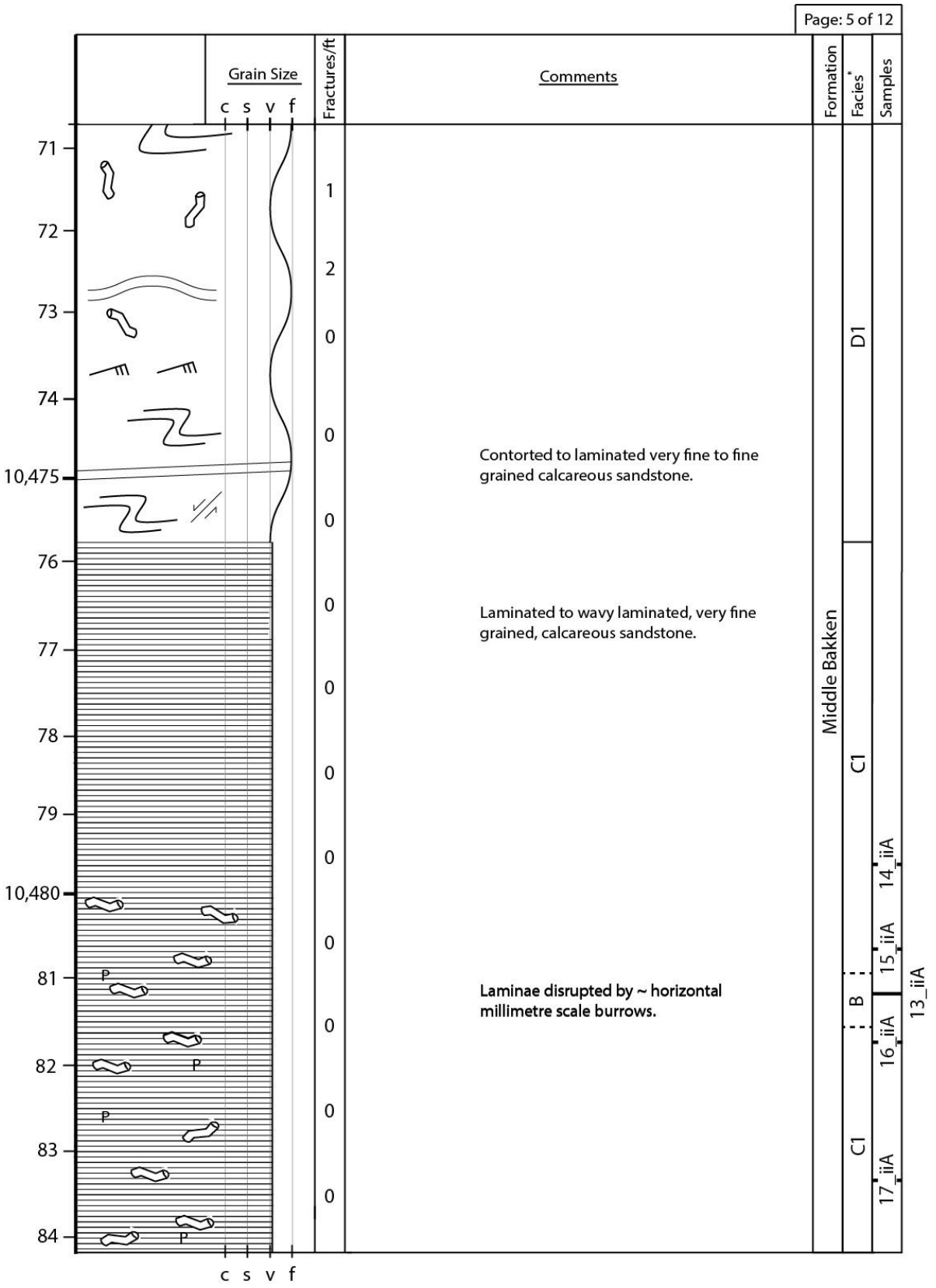
Grain Size
c s v f
Fractures/ft
Comments
Formation
Facies
Samples
71
72
73
74
10,475
76
77
78
79
10,480
81
82
83
84
1
2
0
0
0
0
0
0
0
0
0
0
0
0
Contorted to laminated very fine to fine grained calcareous sandstone.
Laminated to wavy laminated, very fine grained, calcareous sandstone.
Laminae disrupted by ~ horizontal millimetre scale burrows.
P
Middle Bakken
D1
C1
B
C1
14_iiA
15_iiA
13_iiA
16_iiA
17_iiA

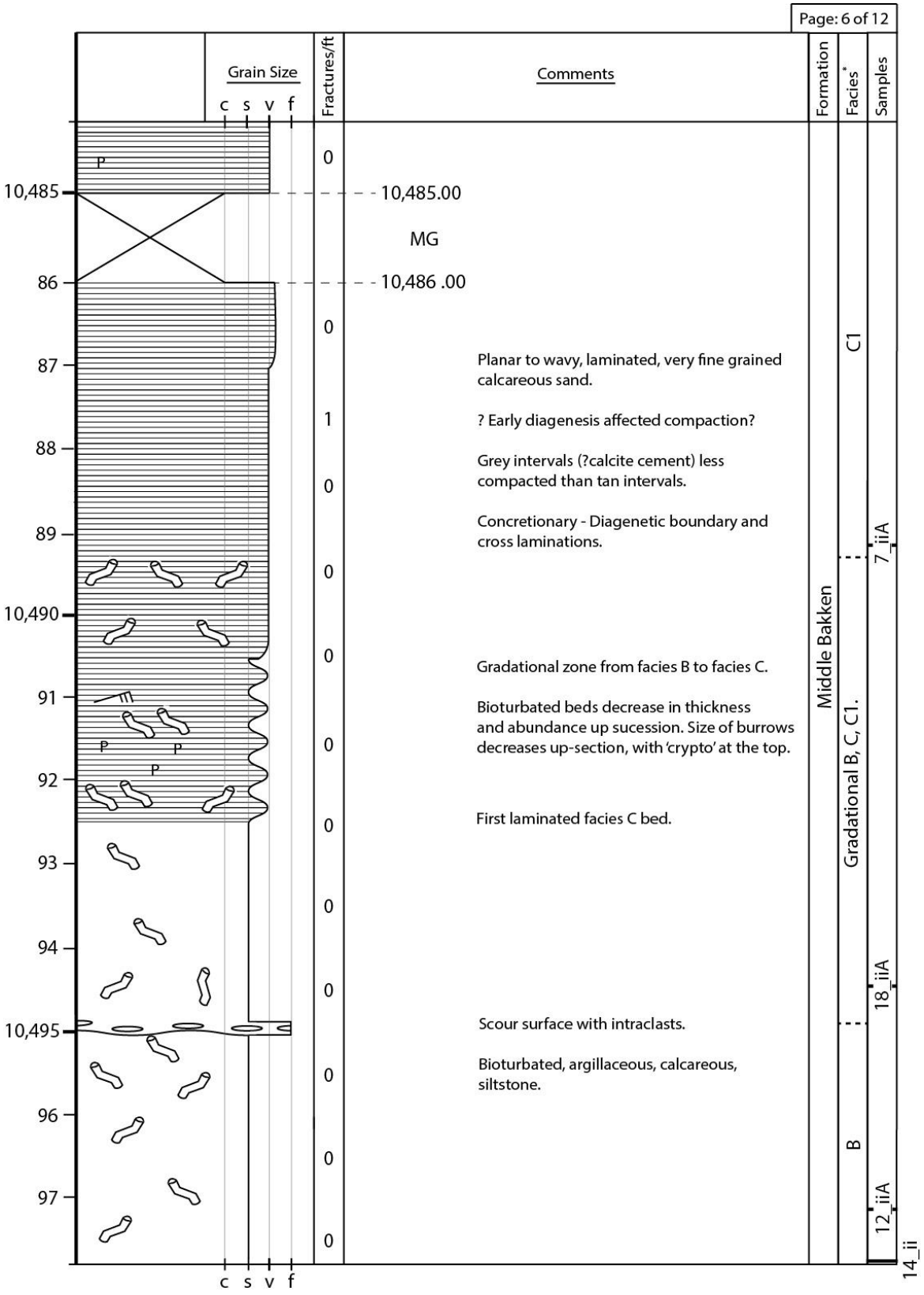
Grain Size
c s v f
Fractures/ft
Comments
Formation
Facies*
Samples
10,485
86
87
88
89
10,490
91
92
93
94
10,495
96
97
10,485.00
MG
10,486 .00
Planar to wavy, laminated, very fine grained calcareous sand.
? Early diagenesis affected compaction?
Grey intervals (?calcite cement) less compacted than tan intervals.
Concretionary - Diagenetic boundary and cross laminations.
Gradational zone from facies B to facies C.
Bioturbated beds decrease in thickness and abundance up sucession. Size of burrows decreases up-section, with 'crypto' at the top.
First laminated facies C bed.
Scour surface with intraclasts.
Bioturbated, argillaceous, calcareous, siltstone.
Middle Bakken
Gradational B, C, C1.
C1
B
7_iiA
18_iiA
12_iiA
14_ii

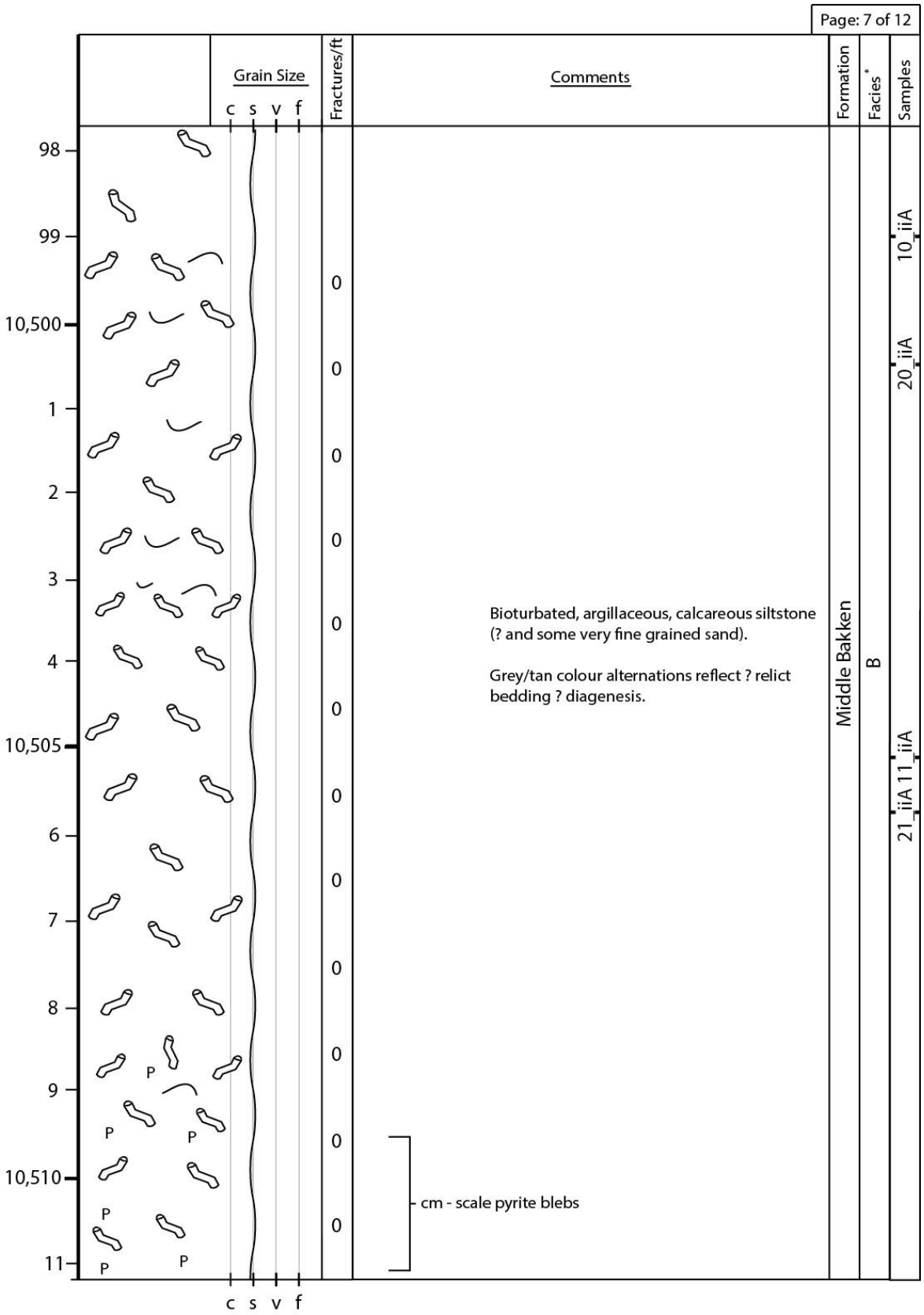
Grain Size
c s v f
Fractures/ft
Comments
Formation
Facies*
Samples
98
99
10,500
1
2
3
4
10,505
6
7
8
9
10,510
11
0
Bioturbated, argillaceous, calcareous siltstone
(? and some very fine grained sand).
Grey/tan colour alternations reflect ? relict
bedding ? diagenesis.
Middle Bakken
B
10_iiA
20_iiA
21_iiA 11_iiA
P
cm - scale pyrite blebs

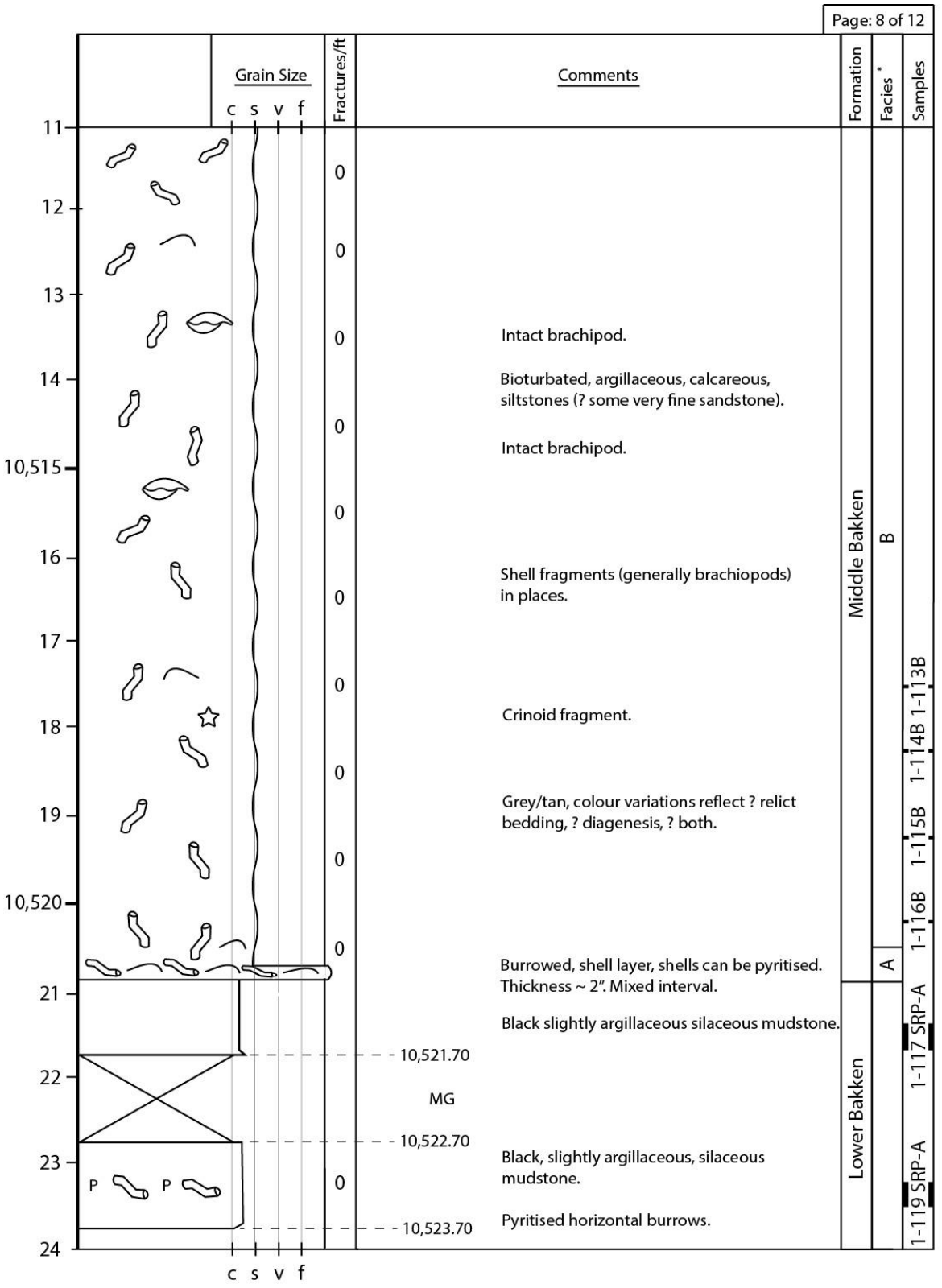
Grain Size
c s v f
Fractures/ft
Comments
Formation
Facies *
Samples
11
12
13
14
10,515
16
17
18
19
10,520
21
22
23
24
0
Intact brachipod.
Bioturbated, argillaceous, calcareous, siltstones (? some very fine sandstone).
Intact brachipod.
Shell fragments (generally brachiopods) in places.
Crinoid fragment.
Grey/tan, colour variations reflect ? relict bedding, ? diagenesis, ? both.
Burrowed, shell layer, shells can be pyritised. Thickness ~ 2". Mixed interval.
Black slightly argillaceous silaceous mudstone.
10,521.70
MG
10,522.70
Black, slightly argillaceous, silaceous mudstone.
Pyritised horizontal burrows.
10,523.70
P
P
Middle Bakken
Lower Bakken
B
A
1-113B
1-114B
1-115B
1-116B
SRP-A
1-117
SRP-A
1-119

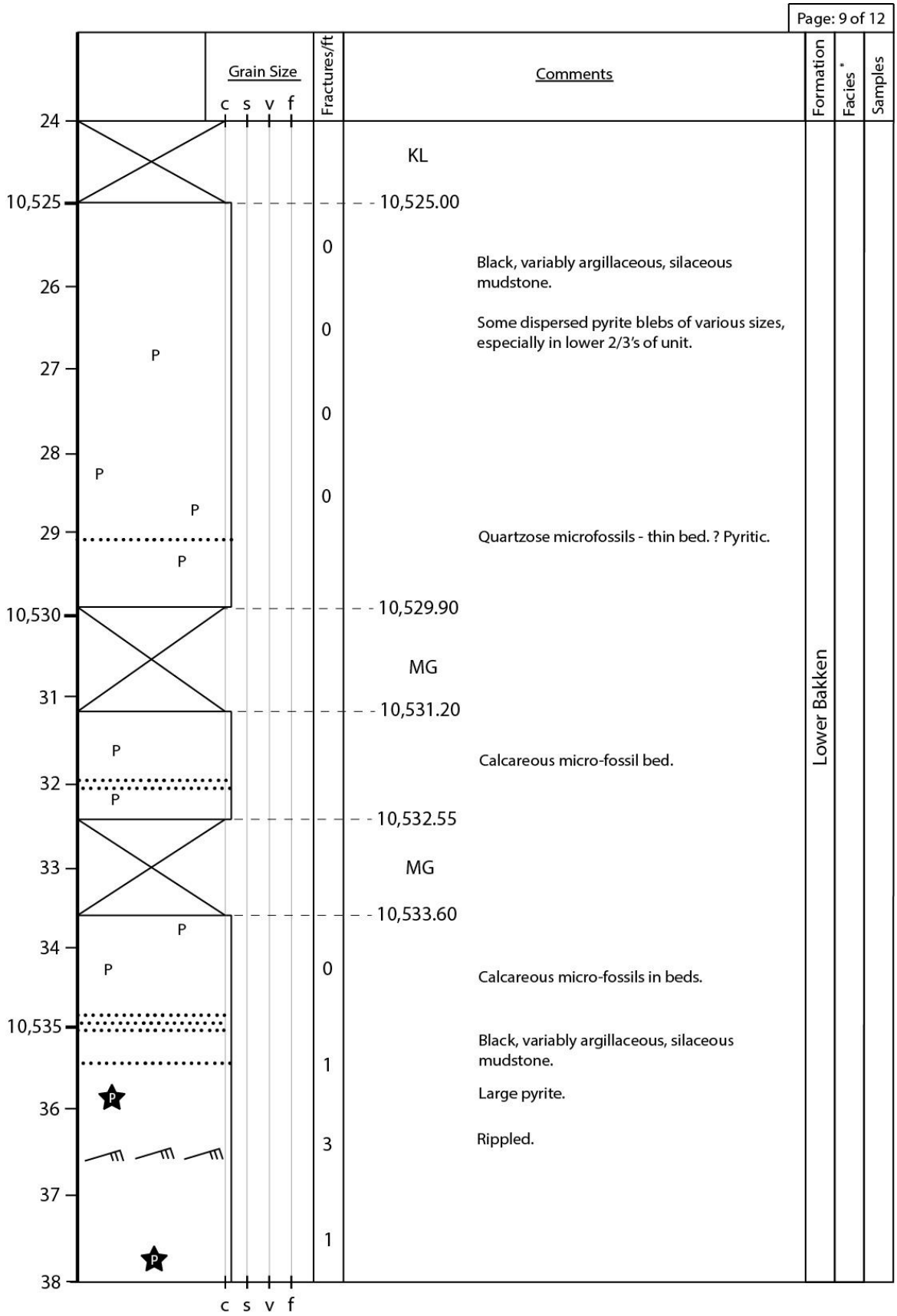
Grain Size
c s v f
Fractures/ft
Comments
Formation
Facies *
Samples
24
10,525
26
27
28
29
10,530
31
32
33
34
10,535
36
37
38
KL
10,525.00
0
Black, variably argillaceous, silaceous mudstone.
0
Some dispersed pyrite blebs of various sizes, especially in lower 2/3's of unit.
0
0
Quartzose microfossils - thin bed. ? Pyritic.
10,529.90
MG
10,531.20
Calcareous micro-fossil bed.
10,532.55
MG
10,533.60
0
Calcareous micro-fossils in beds.
1
Black, variably argillaceous, silaceous mudstone.
Large pyrite.
3
Rippled.
1
Lower Bakken
P

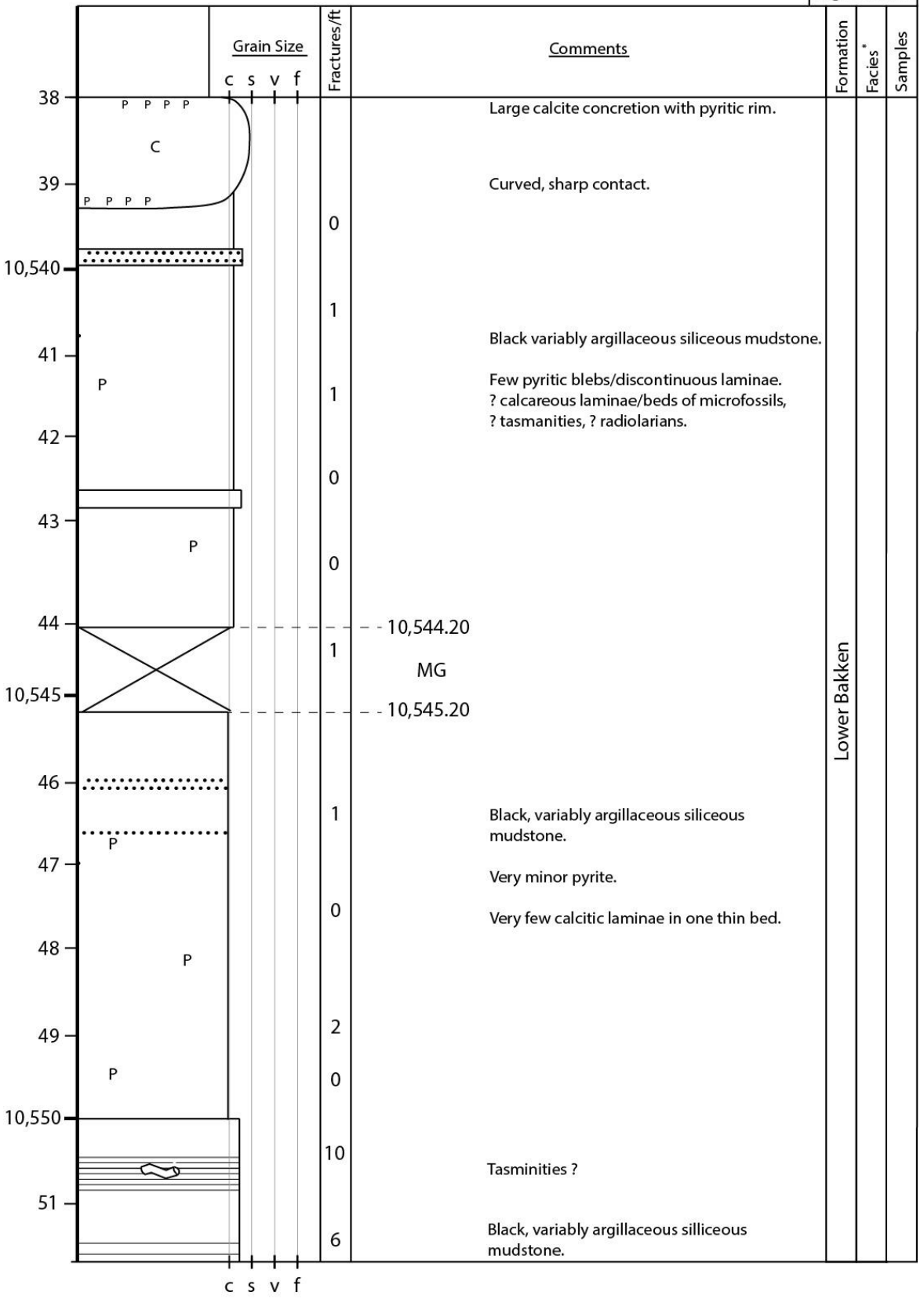
Grain Size
c s v f
Fractures/ft
Comments
Formation
Facies*
Samples
38
39
10,540
41
42
43
44
10,545
46
47
48
49
10,550
51
P P P P
C
P P P P
P
P
P
P
P
P
0
1
1
0
0
1
1
0
2
0
10
6
10,544.20
MG
10,545.20
Large calcite concretion with pyritic rim.
Curved, sharp contact.
Black variably argillaceous siliceous mudstone.
Few pyritic blebs/discontinuous laminae.
? calcareous laminae/beds of microfossils,
? tasmanities, ? radiolarians.
Black, variably argillaceous siliceous
mudstone.
Very minor pyrite.
Very few calcitic laminae in one thin bed.
Tasminities ?
Black, variably argillaceous silliceous
mudstone.
Lower Bakken
c s v f

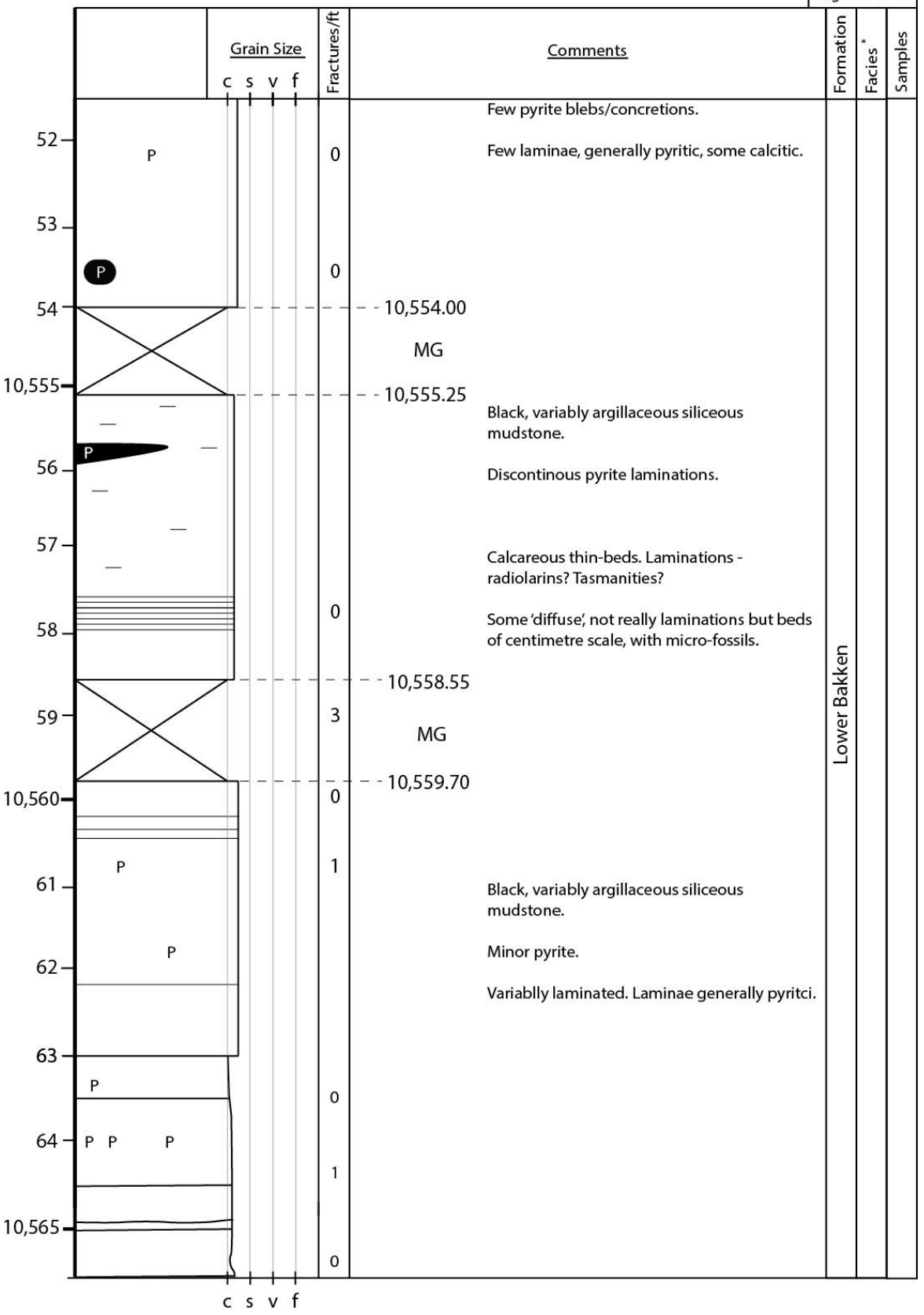
Grain Size
c s v f
Fractures/ft
Comments
Formation
Facies*
Samples
52
53
54
10,555
56
57
58
59
10,560
61
62
63
64
10,565
P
0
10,554.00
MG
10,555.25
Few pyrite blebs/concretions.
Few laminae, generally pyritic, some calcitic.
Black, variably argillaceous siliceous mudstone.
Discontinous pyrite laminations.
Calcareous thin-beds. Laminations - radiolarins? Tasmanities?
Some 'diffuse', not really laminations but beds of centimetre scale, with micro-fossils.
10,558.55
3
MG
10,559.70
1
Black, variably argillaceous siliceous mudstone.
Minor pyrite.
Variablly laminated. Laminae generally pyritci.
Lower Bakken

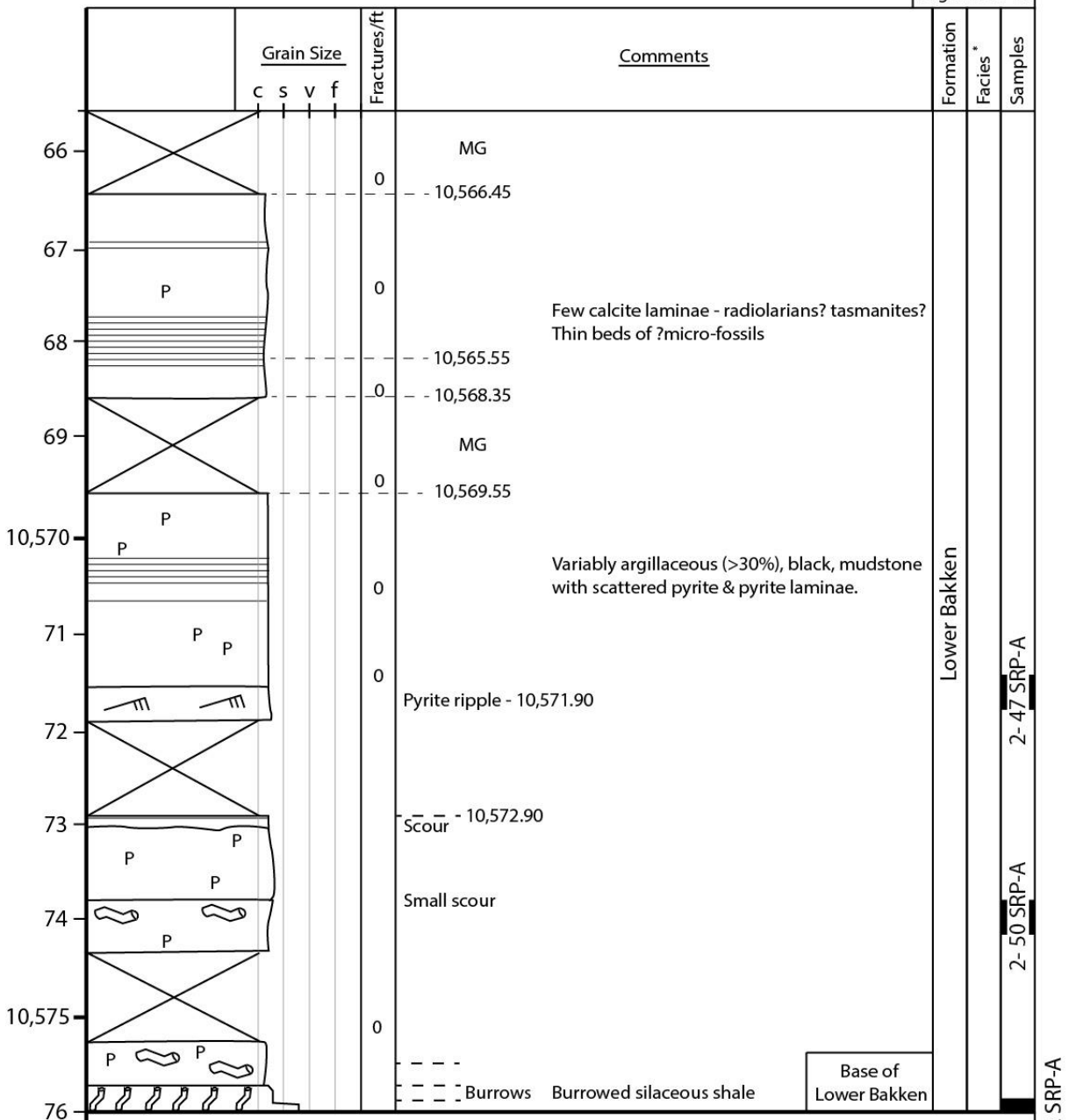

Notes:

Natural fractures in the Upper Bakken:

- Compacted mineralised fractures are present but rare in UBS.
- Mineralisation mostly pyrite with some calcite.
- Would be near vertical if uncompacted.
- Uncompacted lengths range from 2cm (largest) to 3mm (smallest).

- Fractures in the Middle Bakken are primarily in facies D, with minor (1 fracture) in facies C. They tend to bed-bound in the grey (?calcitic) layers and terminate at the bed boundaries. They are steeply dipping but not vertical. Not exactly planar. Calcite vein fill in most smaller fractures which have apertures <1mm.

Appendix 3

Details of samples of this study from the Charlie Sorensen well.

Sample	Depth (m)	Formation	Facies
1-36B	3182.17	MB	E
1-37B	3182.48	MB	E
1-38B	3182.74	MB	E
1-39B	3183.09	MB	E
1_iiA	3183.48	MB	E
2_ii	3185.62	MB	D2
3_ii	3185.65	MB	D2
4_ii	3185.70	MB	D2
5_ii	3185.74	MB	D2
1-55B	3187.99	MB	D2
1-58B	3188.86	MB	D1
9_ii	3190.40	MB	D1
14_iiA	3194.2	MB	D1
15_ii	3194.55	MB	D1
13_ii	3194.67	MB	D1
16_ii	3194.87	MB	D1
8_ii	3195.25	MB	D1
17_ii	3195.37	MB	D1
7_ii	3197.11	MB	C
1-87B	3197.72	MB	Grad
18_ii	3198.76	MB	Grad
12_ii	3199.55	MB	Grad
19_ii	3199.71	MB	Grad
10_ii	3200.14	MB	Grad
20_ii	3200.55	MB	Grad
11_ii	3201.95	MB	Grad
21_ii	3202.12	MB	Grad
1-112B	3205.34	MB	Grad
1-113B	3205.76	MB	B
1-114B	3206	MB	B
1-115B	3206.25	MB	B
1-116B	3206.56	MB	B

Appendix 4

Visual estimates of mineral abundances, estimated by transmitted light microscopy.

Sample	Depth (m)	Quartz	K-Feldspar	Plagioclase Feldspar	Calcite	Dolomite	Matrix - Clays & Organics	Pyrite	Mica
1-36B	3182.17	35	0	0	20	0	15	10	20
1-37B	3182.48	30	0	0	10	5	50	5	0
1-38B	3182.74	25	0	5	25	5	30	10	0
1-39B	3183.09	35	5	0	20	15	20	5	0
1_iiA	3183.48	30	5	0	25	20	15	5	0
2_iiA	3185.62	25	0	0	35	20	10	5	5
3_iiA	3185.65	40	0	0	25	25	5	5	0
4_i	3185.70	40	0	0	20	20	10	5	5
5_i	3185.74	30	5	0	20	10	25	0	10
1-55B	3188.00	35	0	0	20	5	30	10	0
1-58B	3188.86	15	0	0	45	20	15	5	0
9_iiA	3190.40	65	0	0	2.5	2.5	25	5	0
14_iiA	3194.21	40	0	0	20	10	20	5	5
15_iiA	3194.55	50	0	0	5	15	30	0	0
13_iiA	3194.67	40	0	0	5	10	35	5	5
16_iiA	3194.87	60	0	0	5	10	20	0	5
8_iiA	3195.25	40	0	0	25	15	10	5	5
17_iiA	3195.37	60	0	0	10	10	5	5	10
7_iiA	3197.11	30	0	0	10	20	30	10	0
1-87B	3197.72	30	0	0	15	15	30	5	5
18_iiA	3198.76	25	0	0	10	20	40	3	2
12_iiA	3199.55	30	0	0	15	15	30	10	0
19_iiA	3199.71	35	5	0	20	10	25	5	0
10_iiA	3200.14	30	5	0	20	15	25	4	1
20_iiA	3200.55	35	0	0	30	15	15	5	0
11_iiA	3201.95	30	5	5	25	15	15	5	0
21_iiA	3202.12	40	5	5	25	10	15	0	0
1-112B	3205.34	20	5	0	20	30	10	5	10
1-113B	3205.76	25	0	0	25	30	10	0	10
1-114B	3205.95	30	5	0	20	15	15	10	5
1-115B	3206.25	35	0	0	20	5	25	5	10
1-116B	3206.56	15	0	0	20	0	60	5	0

Appendix 5

SEM-WDS analysis of carbonate standards.

Analysis	Calcite ($CaCO_3$)		
	C (wt%)	Ca (wt%)	O (wt%)
Reported	11.9	40.3	47.8
1	12.8	40.0	47.3
2	10.3	44.2	45.5
3	12.3	40.4	47.4
4	12.4	41.2	46.4
5	12.2	41.3	46.5
6	12.3	40.5	47.3
7	12.6	39.9	47.5
8	13.2	37.3	49.5
9	13.4	36.4	50.2
10	13.2	38.2	48.6
Average	12.5	39.9	47.6
Accuracy	0.5	0.3	0.2
Precision	3.2	7.8	4.7

Analysis	Dolomite ($CaMg[CO_3]_2$)				
	C (wt%)	Mg (wt%)	Ca (wt%)	Fe (wt%)	O (wt%)
Reported	12.9	11.3	23.6	0.8	51.4
1	11.5	13.0	25.0	0.7	49.8
2	12.1	13.8	22.9	1.0	50.2
3	12.9	13.2	21.8	0.9	51.2
4	10.9	14.9	24.2	1.0	49.1
5	10.8	13.8	26.3	1.0	48.1
6	10.7	13.7	26.1	0.9	48.7
7	10.8	14.1	26.6	1.0	47.5
8	13.6	12.7	20.8	0.7	52.3
9	11.3	13.5	23.0	0.7	51.5
10	11.1	14.2	25.3	1.0	48.5
Average	11.6	13.7	24.2	0.9	49.7
Accuracy	1.3	2.3	0.6	0.1	1.7
Precision	2.2	2.8	5.9	0.4	4.8

Analysis	Ankerite ($Ca[Fe^{2+}, Mg][CO_3]_2$)					
	C (wt%)	Mg (wt%)	Ca (wt%)	Mn (wt%)	Fe (wt%)	O (wt%)
Reported	12.4	3.6	21.6	2.1	12.2	48.1
1	11.3	4.1	21.8	2.3	14.0	46.4
2	11.8	4.0	21.1	2.2	13.7	47.3
3	11.2	4.1	21.7	2.1	13.8	47.2
4	11.4	3.7	21.1	2.5	13.8	47.5
5	11.7	3.7	20.9	2.3	13.8	47.6
6	11.6	3.7	21.6	2.3	14.1	46.7
7	11.8	3.7	21.5	2.4	14.0	46.6
8	11.9	4.5	20.9	2.1	13.7	46.9
9	11.4	4.1	21.7	2.3	13.7	46.9
10	11.9	4.2	21.0	2.2	13.6	47.2
Average	11.6	4.0	21.3	2.3	13.8	47.0
Accuracy	0.8	0.3	0.3	0.1	1.6	1.0
Precision	0.7	0.9	0.9	0.4	0.5	1.2

Analysis	Siderite ($Fe^{2+}CO_3$)					
	C (wt%)	Mg (wt%)	Ca (wt%)	Mn (wt%)	Fe (wt%)	O (wt%)
Reported	11.8	0.6	0.3	2.3	40.7	44.3
1	13.1	0.6	0.1	1.8	36.9	47.4
2	13.2	0.7	0.2	2.0	36.7	47.3
3	13.1	0.6	0.2	2.1	36.7	47.4
4	13.0	0.7	0.2	1.8	36.6	47.8
5	13.1	0.7	0.2	2.0	36.5	47.6
6	13.3	0.6	0.2	2.0	35.9	48.0
7	12.8	0.6	0.1	2.0	36.1	48.3
8	13.6	0.6	0.2	2.1	36.3	47.3
9	13.2	0.6	0.2	2.1	36.3	47.7
10	13.1	0.7	0.2	1.9	36.4	47.8
Average	13.1	0.6	0.2	2.0	36.4	47.7
Accuracy	1.4	0.0	0.2	0.3	4.3	3.4
Range	0.5	0.1	0.1	0.2	1.0	0.9

Appendix 6

Pore throat size distributions of samples of the upper and lower Bakken shale. Obtained by mercury intrusion porosimetry (MICP.

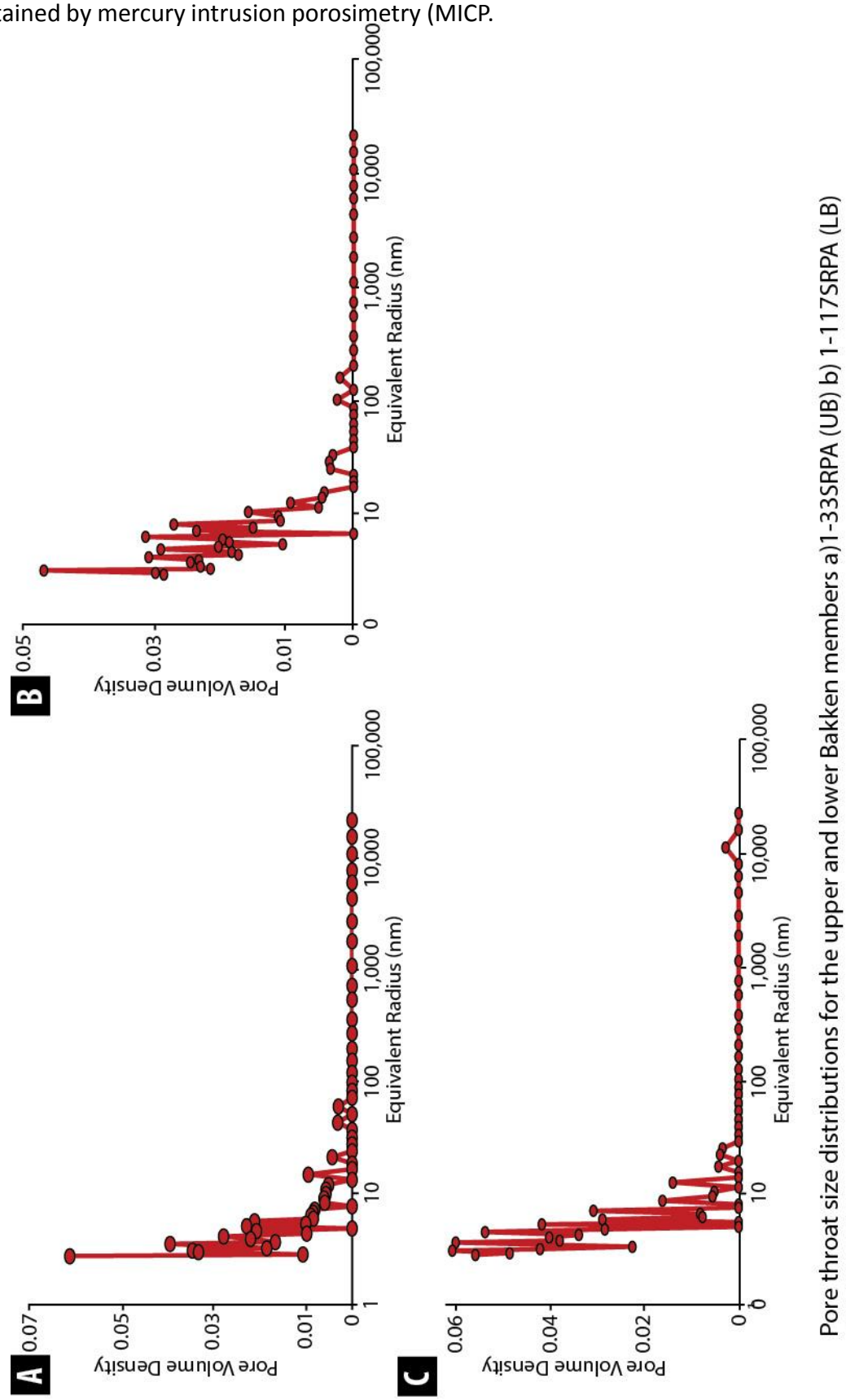

Pore throat size distributions for the upper and lower Bakken members a)1-33SRPA (UB) b) 1-117SRPA (LB) c) 1-119SRPA

Appendix 7

Table of bulk carbon and oxygen isotope data collected by sequential acid dissolution.

Sample	Mineral	Yield	$\delta^{13}C$ (‰)VPDB	$\delta^{18}O$ (‰) VPDB	$\delta^{18}O$ (‰) VSMOW
1-36B	Calcite	1.44	-0.17	-4.41	26.36
1-37B	Calcite	1.26	-0.77	-4.63	26.14
1-38B	Calcite	1.06	-2.48	-7.00	23.69
1-39B	Calcite	3.03	-0.38	-4.29	26.48
1-113B	Calcite	6.16	-3.22	-5.32	25.42
1-114B	Calcite	3.10	2.51	-6.03	24.70
1-115B	Calcite	2.03	1.58	-5.48	25.26
1-116B	Calcite	5.43	1.48	-5.21	25.54
2_iiA	Calcite	3.21	3.07	-4.99	25.77
4_iiA	Calcite	3.20	3.83	-3.72	27.08
9_iiA	Calcite	6.07	3.25	-4.78	25.99
11_iiA	Calcite	0.99	-0.54	-5.40	25.34
17_iiA	Calcite	14.88	2.04	-6.35	24.37
1-36B	Dolomite	1.74	-0.48	-5.09	25.66
1-37B	Dolomite	2.60	-0.17	-4.14	26.65
1-38B	Dolomite	4.91	0.78	-2.25	28.59
1-39B	Dolomite	0.82	-0.03	-3.43	27.38
1-113B	Dolomite	3.46	-3.30	-4.29	26.49
1-114B	Dolomite	0.55	-2.10	-10.83	19.75
1-115B	Dolomite	0.75	-0.33	-4.69	26.08
1-116B	Dolomite	1.02	-0.26	-3.69	27.11
2_iiA	Dolomite	0.15	1.46	-2.16	28.69
4_iiA	Dolomite	0.86	2.71	0.01	30.92
9_iiA	Dolomite	1.07	3.58	-0.13	30.78
11_iiA	Dolomite	4.05	-0.50	-3.76	27.03
17_iiA	Dolomite	19.10	-0.32	-4.68	26.09

Appendix 8

(a) Plot relating the SIMS $\delta^{18}O$ bias (‰) to the cation composition of the dolomite–ankerite solid solution series [Fe# = Fe/(Mg+Fe)] for a typical calibration using a 10µm diameter spot size. The sample matrix effect can be accurately estimated using the Hill equation, which is commonly employed to describe relations of 'concentration'
versus 'measured effect' type, especially in systems that behave non-linearly and reach saturation. (b) Plot of the calibration residual. For most reference materials in the suite, the averaged measured value of $\delta^{18}O$ bias*(RMUW6220) differs by < 0.3‰ from the value predicted by the calibration (depicted by solid lines). Modified from Sliwinski et al., (2015). Figure from Orland et al., pers. com. (2015).

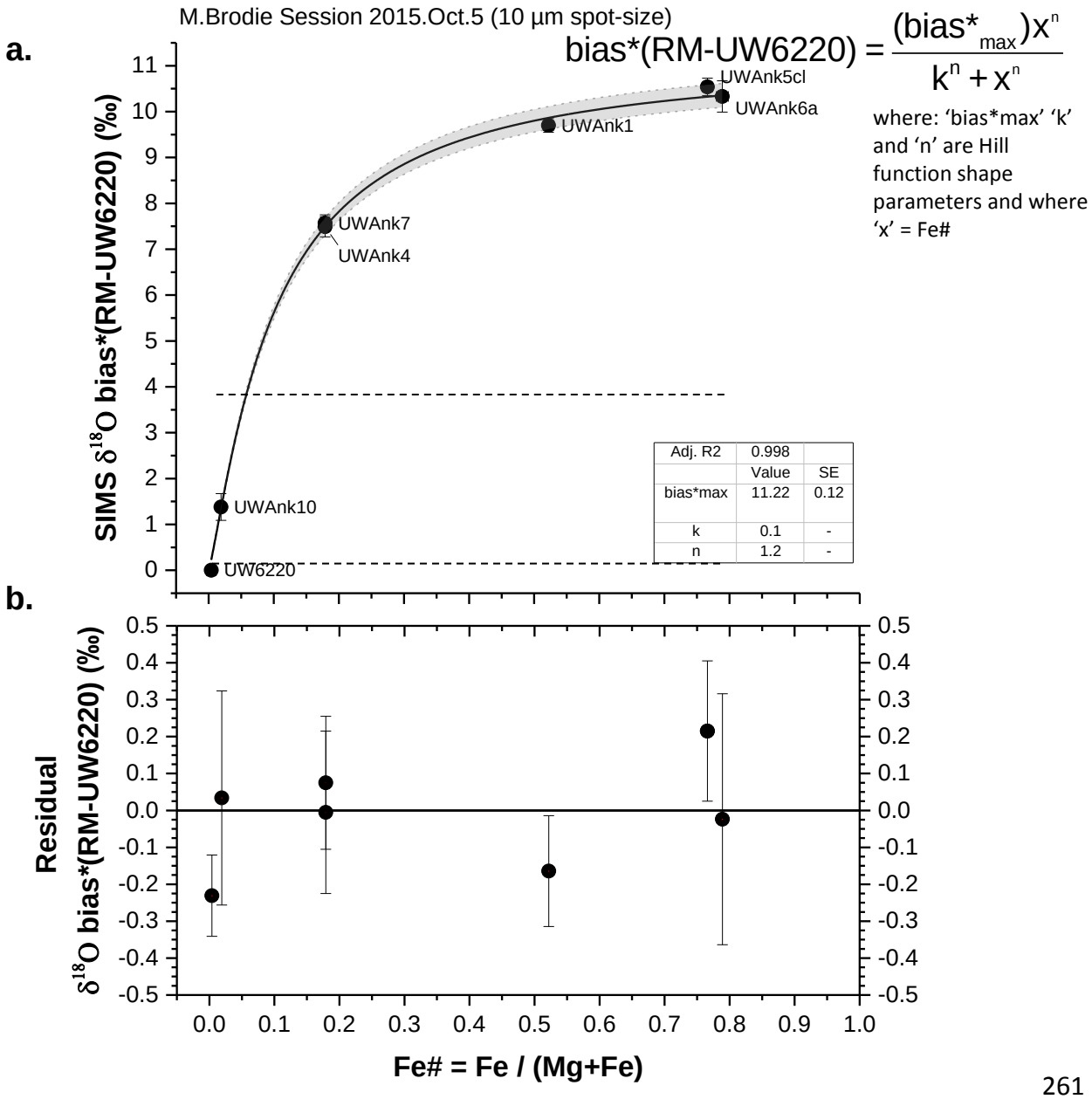

Appendix 9

SIMS Data – corrected for iron – instrumental bias.

Analysis ID	$\delta^{18}O$ ‰ VSMOW	2SD (ext.)	Mass Bias (‰)	2SE (int.)	^{16}O (Gcps)	IP (nA)	Yield (Gcps/nA)	Relative Yield	Mineral	Dolomite Type
2-006	26.36	0.21	-12.28	0.46	3.011	1.135	2.654	1.074	Dolomite	1
2-012	27.05	0.25	-12.30	0.71	3.075	1.192	2.580	1.043	Dolomite	1
3-010	26.80	0.33	-12.29	0.54	2.969	1.142	2.599	1.063	Dolomite	1
3-024	26.54	0.29	-12.19	0.39	2.867	1.172	2.447	0.995	Dolomite	1
3-098	29.16	0.26	-12.19	0.47	3.288	1.215	2.706	1.103	Dolomite	1
3-099	26.95	0.26	-12.19	0.54	3.233	1.212	2.669	1.088	Dolomite	1
5-100a	27.43	0.39	-12.57	0.41	2.952	1.170	2.524	1.034	Dolomite	1
1-051b	25.98	0.28	-12.61	0.47	3.096	1.224	2.529	1.058	Dolomite	2
1-053	24.56	0.28	-12.61	0.47	3.147	1.264	2.490	1.041	Dolomite	2
1-054	26.03	0.28	-12.61	0.41	3.276	1.273	2.573	1.076	Dolomite	2
1-054a	26.18	0.28	-12.61	0.50	3.229	1.257	2.568	1.074	Dolomite	2
1-054b	25.78	0.28	-12.61	0.44	3.196	1.249	2.558	1.070	Dolomite	2
1-054c	25.60	0.28	-12.61	0.46	3.162	1.220	2.592	1.084	Dolomite	2
1-054d	26.91	0.28	-12.61	0.46	3.106	1.205	2.577	1.078	Dolomite	2
1-067	26.13	0.28	-12.52	0.59	3.335	1.336	2.495	1.032	Dolomite	2
1-067a	29.78	0.28	-12.52	12.49	2.873	1.272	2.259	0.934	Dolomite	2
1-067b	26.42	0.28	-12.52	0.66	3.086	1.232	2.504	1.036	Dolomite	2
1-067c	24.25	0.28	-12.52	0.51	3.091	1.213	2.549	1.054	Dolomite	2
1-067e	26.61	0.28	-12.52	0.45	3.087	1.226	2.518	1.041	Dolomite	2
1-067f	25.56	0.28	-12.52	0.49	3.072	1.218	2.522	1.043	Dolomite	2
1-067g	25.11	0.28	-12.52	0.50	3.118	1.196	2.608	1.078	Dolomite	2
1-071b	27.93	0.39	-12.56	0.34	3.170	1.302	2.436	1.016	Dolomite	2
1-072	27.32	0.39	-12.56	0.51	3.068	1.203	2.549	1.063	Dolomite	2
1-084	25.72	0.20	-12.35	0.60	2.797	1.109	2.522	1.038	Dolomite	2
1-085	25.35	0.20	-12.35	0.52	2.842	1.105	2.572	1.059	Dolomite	2
1-108	26.08	0.16	-12.39	0.44	2.927	1.142	2.564	1.053	Dolomite	2
1-109	25.68	0.16	-12.39	0.46	2.934	1.141	2.571	1.056	Dolomite	2
1-113	26.31	0.16	-12.39	0.38	2.837	1.130	2.510	1.031	Dolomite	2
2-004	26.90	0.21	-12.28	0.47	3.144	1.183	2.658	1.076	Dolomite	2
2-013	26.78	0.25	-12.30	0.45	3.049	1.201	2.538	1.026	Dolomite	2
2-022a	24.96	0.18	-12.33	0.43	3.170	1.200	2.641	1.077	Dolomite	2
2-022b	29.28	0.18	-12.33	0.49	3.035	1.190	2.551	1.041	Dolomite	2
2-043a	29.37	0.31	-12.32	0.39	3.032	1.187	2.554	1.040	Dolomite	2
2-081	29.26	0.31	-12.32	0.49	2.721	1.142	2.382	0.970	Dolomite	2
3-004	25.67	0.33	-12.29	0.44	2.940	1.167	2.518	1.030	Dolomite	2
3-018	28.97	0.29	-12.19	0.41	3.190	1.194	2.672	1.086	Dolomite	2
3-023	25.88	0.29	-12.19	0.53	2.937	1.175	2.500	1.016	Dolomite	2
3-027	29.77	0.29	-12.19	0.42	2.722	1.095	2.485	1.010	Dolomite	2
3-028	25.82	0.23	-12.21	0.54	3.059	1.214	2.520	1.025	Dolomite	2
3-080b	31.23	0.26	-12.19	0.39	3.031	1.120	2.707	1.104	Dolomite	2
3-083	29.15	0.26	-12.19	0.45	2.922	1.141	2.562	1.044	Dolomite	2
3-084b	26.20	0.26	-12.09	0.46	3.027	1.154	2.623	1.069	Dolomite	2
3-088	28.26	0.26	-12.19	0.57	3.056	1.189	2.571	1.048	Dolomite	2
3-089	26.15	0.26	-12.19	0.45	3.036	1.193	2.545	1.037	Dolomite	2
3-097	27.63	0.27	-12.20	0.55	2.867	1.103	2.598	1.060	Dolomite	2
4-015	27.76	0.22	-12.41	0.44	3.115	1.236	2.520	1.043	Dolomite	2
4-031	28.05	0.30	-12.33	0.42	3.027	1.208	2.506	1.047	Dolomite	2
4-042	24.81	0.32	-12.33	0.59	3.268	1.288	2.538	1.061	Dolomite	2

Analysis ID	$\delta^{18}O$ ‰ VSMOW	2SD (ext.)	Mass Bias (‰)	2SE (int.)	^{16}O (Gcps)	IP (nA)	Yield (Gcps/nA)	Relative Yield	Mineral	Dolomite Type
4-058	25.04	0.38	-12.32	0.41	3.232	1.288	2.509	1.039	Dolomite	2
4-082a	26.52	0.32	-12.33	0.57	3.260	1.289	2.528	1.057	Dolomite	2
5-023	27.09	0.39	-12.47	0.35	3.116	1.246	2.500	1.030	Dolomite	2
5-072	28.19	0.16	-12.49	0.37	3.207	1.206	2.660	1.078	Dolomite	2
5-078	25.18	0.39	-12.47	0.56	2.903	1.130	2.569	1.058	Dolomite	2
5-080	28.45	0.37	-12.43	0.47	2.926	1.179	2.483	1.017	Dolomite	2
5-099	24.08	0.39	-12.47	0.53	3.193	1.258	2.538	1.045	Dolomite	2
5-102	23.55	0.16	-11.98	0.53	2.990	1.199	2.493	1.011	Dolomite	2
6-005a	29.16	0.16	-12.38	0.41	3.050	1.175	2.595	1.057	Dolomite	2
6-007	28.78	0.16	-12.38	0.46	3.162	1.167	2.710	1.104	Dolomite	2
7-030	25.63	0.36	-12.50	0.45	3.137	1.269	2.472	1.040	Dolomite	2
7-037	25.15	0.36	-12.50	0.47	3.235	1.283	2.522	1.061	Dolomite	2
7-038	25.33	0.36	-12.501	0.63	3.242	1.28	2.524	1.062	Dolomite	2
7-038a	27.44	0.36	-12.501	0.51	3.328	1.28	2.592	1.090	Dolomite	2
7-051	24.68	0.30	-12.213	0.52	3.077	1.22	2.523	1.050	Dolomite	2
7-073	26.04	0.38	-12.246	0.35	3.136	1.20	2.603	1.083	Dolomite	2
7-074	27.18	0.38	-12.246	0.53	3.089	1.21	2.554	1.062	Dolomite	2
7-081a	27.08	0.38	-12.25	0.49	3.078	1.209	2.545	1.059	Dolomite	2
7-100	26.34	0.33	-12.43	0.44	2.943	1.188	2.478	1.044	Dolomite	2
5-113	28.35	0.14	-12.52	0.47	3.053	1.149	2.657	1.074	Dolomite	2
5-122	25.23	0.14	-12.52	0.39	2.828	1.107	2.554	1.032	Dolomite	2
7-070	28.37	0.30	-12.21	0.55	2.758	1.103	2.501	1.041	Dolomite	2
1-071	25.46	0.39	-12.56	0.47	3.139	1.224	2.565	1.070	Dolomite	3
1-079	26.95	0.39	-12.56	0.33	2.997	1.225	2.447	1.020	Dolomite	3
1-110	26.32	0.16	-12.39	0.48	2.886	1.145	2.522	1.036	Dolomite	3
2-008	26.56	0.21	-12.28	0.53	2.909	1.099	2.647	1.071	Dolomite	3
2-025	25.83	0.18	-12.33	0.50	3.053	1.177	2.594	1.058	Dolomite	3
2-040	27.13	0.31	-12.32	0.52	3.124	1.207	2.588	1.053	Dolomite	3
2-042	27.18	0.31	-12.32	0.52	3.113	1.182	2.634	1.072	Dolomite	3
2-046	28.22	0.31	-12.32	0.43	2.952	1.157	2.551	1.038	Dolomite	3
2-047	26.49	0.31	-12.32	0.42	3.035	1.147	2.645	1.077	Dolomite	3
2-049	26.68	0.31	-12.32	0.58	3.034	1.143	2.654	1.080	Dolomite	3
3-026	29.53	0.29	-12.19	0.54	2.651	1.125	2.356	0.958	Dolomite	3
3-080	27.57	0.26	-12.19	0.57	2.983	1.132	2.635	1.074	Dolomite	3
3-080a	26.89	0.26	-12.19	0.50	2.849	1.126	2.530	1.032	Dolomite	3
3-093	28.13	0.27	-12.20	0.48	3.004	1.118	2.687	1.096	Dolomite	3
4-005	26.74	0.26	-12.30	0.56	2.972	1.185	2.507	1.029	Dolomite	3
4-016	29.34	0.22	-12.41	0.57	3.316	1.251	2.651	1.097	Dolomite	3
4-034	28.07	0.30	-12.33	0.46	3.083	1.233	2.499	1.045	Dolomite	3
4-074a	28.21	0.18	-12.45	0.35	3.437	1.321	2.601	1.095	Dolomite	3
4-078	27.65	0.38	-12.32	0.50	3.280	1.295	2.533	1.049	Dolomite	3
5-103	26.28	0.16	-12.13	0.45	3.056	1.192	2.564	1.040	Dolomite	3
7-041	26.53	0.33	-12.43	0.44	2.994	1.211	2.472	1.042	Dolomite	3
7-048	27.72	0.33	-12.43	0.55	3.152	1.219	2.585	1.089	Dolomite	3
7-054b	25.65	0.30	-12.21	0.39	2.738	1.091	2.51	1.04	Dolomite	3
7-080	25.82	0.38	-12.25	0.45	3.073	1.21	2.53	1.05	Dolomite	3
7-099	24.33	0.33	-12.43	0.57	3.028	1.19	2.53	1.07	Dolomite	3
5-114	31.34	0.14	-12.52	0.37	3.012	1.15	2.63	1.06	Dolomite	3

Analysis ID	$\delta^{18}O$ ‰ VSMOW	2SD (ext.)	Mass Bias (‰)	2SE (int.)	^{16}O (Gcps)	IP (nA)	Yield (Gcps/nA)	Relative Yield	Mineral	Dolomite Type
1-074	26.81	0.39	-12.56	0.51	3.243	1.32	2.46	1.027	Dolomite	4
1-101	26.62	0.20	-12.35	0.58	2.762	1.101	2.509	1.033	Dolomite	4
1-102	25.29	0.20	-12.35	0.42	2.763	1.105	2.501	1.030	Dolomite	4
1-103	26.37	0.20	-12.35	0.50	2.809	1.102	2.548	1.049	Dolomite	4
1-105	27.20	0.16	-12.39	0.40	2.994	1.155	2.591	1.064	Dolomite	4
1-106	25.74	0.16	-12.39	0.44	2.956	1.155	2.559	1.051	Dolomite	4
1-107	25.06	0.16	-12.39	0.57	2.952	1.149	2.569	1.055	Dolomite	4
2-024	25.46	0.18	-12.33	0.43	3.057	1.182	2.587	1.055	Dolomite	4
2-033	28.60	0.14	-12.28	0.39	3.120	1.200	2.599	1.062	Dolomite	4
2-036a	27.39	0.14	-12.28	0.42	2.953	1.168	2.528	1.032	Dolomite	4
2-039	25.41	0.14	-12.28	0.52	3.017	1.151	2.620	1.070	Dolomite	4
3-021	27.71	0.29	-12.19	0.44	2.984	1.184	2.521	1.025	Dolomite	4
3-032	26.91	0.23	-12.21	0.53	3.235	1.200	2.695	1.096	Dolomite	4
4-009	26.11	0.26	-12.30	0.58	2.943	1.167	2.523	1.035	Dolomite	4
4-010	27.25	0.26	-12.30	0.63	3.034	1.166	2.601	1.067	Dolomite	4
5-081	25.43	0.37	-12.43	0.46	3.002	1.172	2.562	1.049	Dolomite	4
5-098	27.21	0.39	-12.47	0.50	3.125	1.259	2.482	1.022	Dolomite	4
5-107	27.54	0.16	-12.49	0.54	2.942	1.185	2.482	1.006	Dolomite	4
7-047	25.99	0.33	-12.43	0.48	3.100	1.210	2.561	1.079	Dolomite	4
7-055	25.03	0.30	-12.21	0.48	2.848	1.104	2.579	1.074	Dolomite	4
5-115	27.05	0.14	-12.52	0.42	2.967	1.147	2.586	1.045	Dolomite	4
5-117	26.63	0.14	-12.52	0.55	2.959	1.121	2.639	1.066	Dolomite	4
5-118	25.73	0.14	-12.52	0.41	2.923	1.120	2.608	1.054	Dolomite	4
5-004	26.03	0.39	-12.47	0.57	3.311	1.227	2.698	1.111	Dolomite	5
3-086	29.74	0.26	-12.19	0.54	3.192	1.175	2.716	1.107	Dolomite	6
3-090	27.62	0.26	-12.19	0.44	3.191	1.195	2.670	1.088	Dolomite	6
5-015	29.69	0.39	-12.57	0.21	3.039	1.205	2.522	1.033	Dolomite	6
5-015a	27.92	0.39	-12.57	0.45	3.202	1.216	2.634	1.078	Dolomite	6
5-015b	28.46	0.39	-12.57	0.37	3.121	1.209	2.582	1.057	Dolomite	6
5-015c	28.19	0.39	-12.57	0.46	3.185	1.208	2.637	1.080	Dolomite	6
5-015d	26.84	0.39	-12.57	0.62	3.164	1.199	2.640	1.081	Dolomite	6
5-108	27.22	0.14	-12.29	0.35	2.860	1.164	2.457	0.993	Dolomite	6
5-109	30.44	0.14	-12.48	0.40	3.148	1.165	2.703	1.092	Dolomite	6
6-068	28.17	0.22	-12.25	0.34	2.846	1.138	2.502	1.026	Dolomite	
3-016	25.83	0.33	-11.63	0.50	3.029	1.154	2.623	1.073	Dolomite	1
7-004	24.75	0.25	-11.79	0.45	3.247	1.268	2.561	1.071	Dolomite	1
1-051	26.06	0.28	-11.96	0.55	3.060	1.235	2.479	1.037	Dolomite	2
1-067d	27.10	0.28	-11.86	0.45	3.066	1.218	2.518	1.041	Dolomite	2
1-071a	28.42	0.39	-11.90	0.48	3.101	1.276	2.430	1.013	Dolomite	2
1-084a	26.37	0.20	-11.69	0.64	2.880	1.105	2.605	1.073	Dolomite	2
2-011	25.35	0.25	-11.64	0.39	3.095	1.178	2.627	1.062	Dolomite	2
3-005	26.77	0.33	-11.63	0.33	2.984	1.151	2.593	1.060	Dolomite	2
3-015	26.72	0.33	-11.63	0.77	2.942	1.159	2.539	1.038	Dolomite	2
4-061	24.10	0.38	-11.66	0.43	3.223	1.291	2.495	1.033	Dolomite	2
4-082	24.88	0.32	-11.67	0.58	3.306	1.279	2.584	1.080	Dolomite	2
4-089	25.60	0.32	-11.67	0.49	3.534	1.427	2.476	1.035	Dolomite	2
7-037a	27.54	0.36	-11.843	0.40	3.288	1.29	2.556	1.075	Dolomite	2
2-017	29.39	0.25	-11.64	0.45	2.894	1.205	2.401	0.971	Dolomite	3

Analysis ID	$\delta^{18}O$ ‰ VSMOW	2SD (ext.)	Mass Bias (‰)	2SE (int.)	^{16}O (Gcps)	IP (nA)	Yield (Gcps/nA)	Relative Yield	Mineral	Dolomite Type
2-044	24.84	0.31	-11.66	0.58	3.119	1.183	2.636	1.073	Dolomite	3
3-017	28.59	0.33	-11.63	0.49	3.003	1.148	2.615	1.069	Dolomite	3
3-022	24.35	0.29	-11.53	0.43	2.982	1.178	2.532	1.029	Dolomite	3
3-026a	26.55	0.29	-11.53	0.45	2.827	1.111	2.545	1.035	Dolomite	3
4-012	24.71	0.22	-11.75	0.44	3.106	1.200	2.588	1.071	Dolomite	3
4-024	32.18	0.15	-11.81	0.48	3.046	1.330	2.291	0.959	Dolomite	3
7-052	24.79	0.30	-11.56	0.49	3.125	1.224	2.554	1.063	Dolomite	3
1-075	25.93	0.39	-11.90	0.51	3.314	1.333	2.487	1.037	Dolomite	4
4-007	26.47	0.26	-11.64	0.33	3.116	1.175	2.652	1.088	Dolomite	4
7-005	23.65	0.25	-11.79	0.46	3.208	1.302	2.464	1.030	Dolomite	4
2-029	29.86	0.18	-10.93	0.49	3.012	1.161	2.595	1.059	Dolomite	1
2-026	23.38	0.18	-10.93	0.45	3.109	1.175	2.646	1.080	Dolomite	2
7-081	24.64	0.38	-10.842	0.51	3.010	1.21	2.491	1.036	Dolomite	2
4-070	30.77	0.38	-10.92	0.52	3.017	1.302	2.317	0.959	Dolomite	3
7-054a	26.70	0.30	-10.81	0.43	1.850	1.103	1.678	0.699	Dolomite	3
1-073	23.17	0.39	-11.16	0.52	3.108	1.22	2.56	1.07	Dolomite	4
1-051a	24.46	0.28	-10.50	0.48	3.084	1.213	2.543	1.063	Dolomite	2
6-037	22.91	0.30	-9.76	0.48	3.268	1.231	2.656	1.087	Dolomite	1
2-028	25.60	0.18	-9.57	0.53	3.203	1.168	2.744	1.119	Dolomite	2
6-036	25.94	0.30	-9.76	0.48	3.359	1.235	2.720	1.113	Dolomite	3
6-040a	24.99	0.43	-9.06	0.44	3.271	1.200	2.727	1.124	Dolomite	1
3-009	25.30	0.33	-8.93	0.45	2.988	1.143	2.615	1.069	Dolomite	4
3-025	27.04	0.29	-8.83	0.45	3.069	1.152	2.664	1.083	Dolomite	4
7-054	22.46	0.30	-7.839	0.50	2.790	1.082	2.578	1.073	Dolomite	2
4-039	25.78	0.21	-6.37	0.53	2.893	1.247	2.321	0.962	Dolomite	6
4-066	24.46	0.18	-5.80	0.48	2.917	1.317	2.215	0.933	Dolomite	2
6-075	25.21	0.22	-5.60	0.55	2.749	1.162	2.366	0.971	Dolomite	4
7-079	17.96	0.38	-2.20	0.44	2.802	1.217	2.303	0.958	Dolomite	4
2-048	17.44	0.31	-2.21	0.43	2.978	1.148	2.594	1.056	Dolomite	2
7-075	16.41	0.38	-1.82	0.45	3.086	1.21	2.55	1.06	Dolomite	3
3-096	29.66	0.27	-12.20	0.51	2.600	1.106	2.351	0.959	Calcite	
4-006	31.79	0.26	-12.30	0.56	2.724	1.183	2.303	0.945	Calcite	
3-087	29.63	0.26	-12.19	0.61	2.723	1.183	2.301	0.938	Calcite	
3-091	29.91	0.26	-12.19	0.54	2.817	1.200	2.348	0.957	Calcite	
4-004	28.94	0.26	-12.30	0.54	2.870	1.182	2.429	0.997	Calcite	
4-013	29.50	0.22	-12.41	0.45	2.903	1.214	2.391	0.990	Calcite	
4-014	30.35	0.22	-12.41	0.53	2.808	1.222	2.298	0.951	Calcite	
4-017	30.56	0.22	-12.41	0.71	2.843	1.263	2.251	0.932	Calcite	
4-018	30.60	0.22	-12.41	0.54	2.942	1.288	2.285	0.946	Calcite	
4-018a	31.54	0.22	-12.41	0.59	2.996	1.308	2.290	0.948	Calcite	
4-019	32.58	0.15	-12.46	0.52	3.036	1.295	2.344	0.982	Calcite	
4-020	32.03	0.15	-12.46	0.53	2.979	1.297	2.296	0.962	Calcite	
4-021	32.58	0.15	-12.46	0.51	2.948	1.304	2.261	0.947	Calcite	
4-022	31.05	0.15	-12.46	0.57	2.801	1.310	2.137	0.895	Calcite	
4-023	30.85	0.15	-12.46	0.46	3.086	1.315	2.348	0.983	Calcite	
4-025	31.14	0.15	-12.46	0.58	3.079	1.334	2.309	0.967	Calcite	
4-026	30.56	0.15	-12.46	0.46	3.136	1.349	2.325	0.973	Calcite	
4-027	32.46	0.18	-12.45	0.51	2.965	1.316	2.253	0.948	Calcite	

Analysis ID	$\delta^{18}O$ ‰ VSMOW	2SD (ext.)	Mass Bias (‰)	2SE (int.)	^{16}O (Gcps)	IP (nA)	Yield (Gcps/nA)	Relative Yield	Mineral	Dolomite Type
4-028	32.26	0.18	-12.45	0.49	3.128	1.341	2.332	0.982	Calcite	
4-029	30.05	0.30	-12.33	0.56	2.894	1.212	2.387	0.998	Calcite	
4-030	32.85	0.30	-12.33	0.44	2.814	1.210	2.326	0.972	Calcite	
4-032	31.83	0.30	-12.33	0.54	2.700	1.213	2.227	0.931	Calcite	
4-033	31.25	0.30	-12.33	0.47	2.823	1.217	2.320	0.970	Calcite	
4-035	32.51	0.30	-12.33	0.49	2.913	1.244	2.342	0.979	Calcite	
4-035a	31.61	0.30	-12.33	0.53	2.734	1.256	2.177	0.910	Calcite	
4-036	30.82	0.30	-12.33	0.51	2.857	1.265	2.259	0.944	Calcite	
4-043	30.53	0.32	-12.33	0.59	2.930	1.263	2.320	0.969	Calcite	
4-048	29.90	0.21	-12.23	0.46	2.894	1.248	2.320	0.961	Calcite	
4-051	30.88	0.21	-12.23	0.48	2.745	1.189	2.308	0.956	Calcite	
4-056	33.70	0.21	-12.23	0.54	2.380	1.017	2.341	0.970	Calcite	
4-057	32.29	0.38	-12.32	0.53	2.984	1.283	2.326	0.963	Calcite	
4-059	32.48	0.38	-12.32	0.58	2.979	1.289	2.310	0.956	Calcite	
4-069a	24.88	0.38	-12.32	0.46	3.225	1.292	2.495	1.033	Calcite	
4-072	30.82	0.38	-12.32	0.55	3.024	1.299	2.327	0.963	Calcite	
4-074	30.25	0.18	-12.45	0.45	2.950	1.313	2.247	0.946	Calcite	
4-074b	32.62	0.18	-12.45	0.46	3.074	1.327	2.316	0.975	Calcite	
4-097	29.94	0.32	-12.33	0.53	3.169	1.370	2.313	0.966	Calcite	
4-097a	31.99	0.32	-12.33	0.52	3.107	1.403	2.214	0.925	Calcite	
6-005	32.02	0.16	-12.38	0.63	2.758	1.177	2.343	0.954	Calcite	
6-009	31.62	0.16	-12.38	0.53	2.743	1.165	2.355	0.959	Calcite	
6-010	31.97	0.16	-12.38	0.55	2.832	1.151	2.461	1.003	Calcite	
6-029	31.77	0.25	-12.42	0.53	2.617	1.113	2.351	0.958	Calcite	
6-030	32.30	0.25	-12.42	0.55	2.667	1.106	2.410	0.982	Calcite	
6-031	32.31	0.25	-12.42	0.64	2.594	1.103	2.352	0.958	Calcite	
6-032	30.97	0.30	-12.53	0.46	2.772	1.237	2.241	0.917	Calcite	
6-033	31.27	0.30	-12.53	0.48	2.939	1.242	2.367	0.969	Calcite	
6-034	32.27	0.30	-12.53	0.55	2.864	1.237	2.315	0.948	Calcite	
6-035	31.81	0.30	-12.53	0.57	2.910	1.241	2.344	0.960	Calcite	
6-038	30.84	0.30	-12.53	0.54	2.865	1.226	2.338	0.957	Calcite	
6-039	32.14	0.30	-12.53	0.49	2.881	1.225	2.351	0.963	Calcite	
6-040	32.44	0.43	-12.42	0.48	2.866	1.207	2.374	0.978	Calcite	
6-059	32.91	0.43	-12.42	0.48	2.832	1.198	2.363	0.974	Calcite	
6-059a	32.22	0.43	-12.42	0.60	2.819	1.197	2.355	0.971	Calcite	
6-059b	32.66	0.43	-12.42	0.53	2.758	1.188	2.323	0.957	Calcite	
6-062	31.62	0.43	-12.42	0.48	2.812	1.184	2.374	0.978	Calcite	
6-063	32.11	0.43	-12.42	0.53	2.801	1.190	2.355	0.970	Calcite	
6-064	31.51	0.43	-12.42	0.52	2.834	1.188	2.386	0.983	Calcite	
6-071	29.22	0.22	-12.25	0.37	3.178	1.140	2.787	1.144	Calcite	
6-074	31.89	0.22	-12.25	0.57	2.748	1.164	2.361	0.969	Calcite	
1-111	19.81	0.16	-5.50	0.21	2.009	1.140	1.762	0.724	Quartz	
2-007	13.41	0.21	-5.40	0.27	2.006	1.118	1.793	0.726	Quartz	
2-009	12.50	0.25	-5.41	0.22	2.146	1.190	1.803	0.729	Quartz	
2-009-2	13.63	0.25	-5.41	0.30	2.044	1.177	1.737	0.702	Quartz	
2-009-3	15.54	0.25	-5.41	0.23	2.117	1.172	1.806	0.730	Quartz	
2-018	13.38	0.25	-5.41	0.29	2.066	1.205	1.714	0.693	Quartz	
2-028a	12.48	0.18	-5.45	0.22	2.094	1.170	1.790	0.730	Quartz	

Analysis ID	$\delta^{18}O$ ‰ VSMOW	2SD (ext.)	Mass Bias (‰)	2SE (int.)	^{16}O (Gcps)	IP (nA)	Yield (Gcps/nA)	Relative Yield	Mineral	Dolomite Type
3-006	15.56	0.33	-5.40	0.28	2.084	1.143	1.823	0.746	Quartz	
3-011	11.28	0.33	-5.40	0.29	2.087	1.155	1.806	0.739	Quartz	
3-029	15.77	0.23	-5.32	0.30	2.127	1.218	1.746	0.710	Quartz	
3-084a	8.95	0.26	-5.30	0.29	2.087	1.163	1.795	0.732	Quartz	
3-092	18.32	0.27	-5.31	0.25	2.092	1.128	1.854	0.756	Quartz	
4-008	10.65	0.26	-5.41	0.21	2.105	1.166	1.806	0.741	Quartz	
4-038	10.18	0.21	-5.34	0.23	2.163	1.239	1.746	0.723	Quartz	
4-069	17.66	0.38	-5.43	0.23	2.272	1.286	1.768	0.732	Quartz	
4-086	19.40	0.38	-5.43	0.28	2.285	1.290	1.772	0.733	Quartz	
5-005	14.44	0.39	-5.58	0.30	2.184	1.207	1.810	0.745	Quartz	
5-082	16.93	0.37	-5.54	0.25	2.104	1.166	1.804	0.739	Quartz	
5-104	10.89	0.16	-5.60	0.28	2.141	1.192	1.796	0.728	Quartz	
5-105	9.35	0.16	-5.60	0.28	2.083	1.186	1.757	0.712	Quartz	
5-106	11.54	0.16	-5.60	0.25	2.129	1.183	1.799	0.729	Quartz	
5-110	11.34	0.14	-5.63	0.23	2.082	1.156	1.801	0.728	Quartz	
5-111	11.26	0.14	-5.63	0.25	2.081	1.157	1.799	0.727	Quartz	
5-112	11.50	0.14	-5.63	0.27	2.080	1.153	1.804	0.729	Quartz	
5-116	12.70	0.14	-5.63	0.26	2.041	1.121	1.821	0.736	Quartz	
6-004	13.78	0.16	-5.49	0.26	2.117	1.176	1.800	0.733	Quartz	
6-077b	13.81	0.22	-5.36	0.27	2.068	1.146	1.805	0.741	Quartz	
6-077c	14.10	0.22	-5.36	0.30	2.062	1.143	1.805	0.740	Quartz	
7-020	16.46	0.25	-5.56	0.23	2.362	1.357	1.741	0.728	Quartz	
7-024	18.35	0.25	-5.56	0.32	2.325	1.342	1.732	0.724	Quartz	
7-040	19.15	0.33	-5.54	0.37	2.090	1.194	1.751	0.738	Quartz	
7-053	15.21	0.30	-5.32	0.27	1.992	1.146	1.739	0.724	Quartz	
7-060	18.50	0.25	-5.56	0.28	2.361	1.351	1.748	0.731	Quartz	
7-082	13.73	0.38	-5.36	0.32	2.146	1.202	1.785	0.743	Quartz	
7-098	12.91	0.33	-5.54	0.25	2.133	1.200	1.778	0.749	Quartz	

Appendix 9

Table of SEM-WDS crystal composition data.

Sample	SIMS No	Mineral	CaO	MgO	FeO	SrO	MnO	BaO
1	1-110	Dolomite	47.52	52.20	0.00	0.07	0.10	0.11
1	1-51b	Dolomite	46.87	52.91	0.06	0.00	0.00	0.16
1	1-51a	Dolomite	45.65	52.04	1.85	0.00	0.33	0.13
1	1-51	Dolomite	46.85	52.51	0.48	0.00	0.17	0.00
1	1-67d	Dolomite	46.65	52.61	0.64	0.00	0.10	0.00
1	1-53	Dolomite	47.17	52.52	0.21	0.00	0.10	0.00
1	1-67b	Dolomite	47.01	52.54	0.40	0.00	0.05	0.00
1	1-71a	Dolomite	46.14	53.36	0.28	0.00	0.17	0.05
1	1-73	Dolomite	47.27	51.19	0.95	0.00	0.59	0.00
1	1-75	Dolomite	45.20	54.14	0.63	0.00	0.00	0.03
1	1-84a	Dolomite	46.62	52.51	0.49	0.00	0.38	0.01
2	2-48	Dolomite	37.81	59.63	0.52	1.24	0.00	0.80
2	2-49	Dolomite	38.96	60.86	0.08	0.00	0.10	0.00
2	2-17	Dolomite	39.17	59.80	0.55	0.00	0.48	0.00
2	2-009	Dolomite	39.20	60.63	0.08	0.00	0.10	0.00
2	2-33	Dolomite	41.09	58.56	0.10	0.00	0.18	0.07
2	2-12	Dolomite	38.40	61.51	0.00	0.00	0.00	0.09
2	2-22a	Dolomite	41.07	58.80	0.13	0.00	0.00	0.00
2	2-081	Dolomite	38.83	61.01	0.00	0.00	0.16	0.00
2	2-024	Dolomite	38.73	60.88	0.14	0.00	0.14	0.11
2	2-026	Dolomite	42.81	55.68	1.10	0.00	0.41	0.00
2	2-011	Dolomite	36.14	63.56	0.20	0.00	0.00	0.10
2	2-025	Dolomite	37.37	62.54	0.09	0.00	0.00	0.00
2	2-36a	Dolomite	41.76	56.53	1.62	0.00	0.09	0.00
2	2-006	Dolomite	50.40	48.69	0.66	0.00	0.25	0.00
2	2-004	Dolomite	37.37	62.28	0.11	0.00	0.24	0.00
2	2-11	Dolomite	36.41	62.83	0.45	0.00	0.20	0.11
2	2-39	Dolomite	35.92	63.73	0.00	0.00	0.00	0.36
2	2-44	Dolomite	40.33	59.06	0.61	0.00	0.00	0.00
2	2-43a	Dolomite	36.87	62.92	0.10	0.00	0.06	0.05
2	2-004	Dolomite	50.24	49.76	0.00	0.00	0.00	0.00
2	2-042	Dolomite	36.09	63.64	0.25	0.00	0.02	0.00
2	2-046	Dolomite	36.19	63.61	0.01	0.00	0.16	0.03
2	2-47	Dolomite	36.63	63.32	0.00	0.00	0.00	0.05
2	2-40	Dolomite	39.20	60.36	0.18	0.00	0.18	0.08
2	2-29	Dolomite	38.38	60.20	0.95	0.00	0.40	0.06
2	2-28	Dolomite	35.19	61.61	2.58	0.00	0.56	0.06
7	7-052	Dolomite	51.94	47.07	0.34	0.00	0.35	0.30
7	7-005	Dolomite	50.97	48.26	0.60	0.00	0.08	0.10
7	7-081	Dolomite	49.96	49.28	0.24	0.00	0.24	0.29
7	7-004	Dolomite	49.81	49.73	0.31	0.00	0.00	0.15
7	7-037a	Dolomite	52.98	46.48	0.42	0.06	0.06	0.00
7	7-038a	Dolomite	53.23	45.90	0.23	0.00	0.62	0.02
7	7-037	Dolomite	49.91	49.68	0.20	0.00	0.00	0.21
7	7-038	Dolomite	50.46	49.14	0.09	0.00	0.31	0.00
7	7-052	Dolomite	51.94	47.07	0.34	0.00	0.35	0.30
7	7-054a	Dolomite	50.55	48.28	0.81	0.00	0.34	0.02
7	7-055	Dolomite	49.99	49.84	0.04	0.00	0.05	0.09
7	7-054b	Dolomite	50.41	49.53	0.00	0.00	0.06	0.00

Sample	SIMS No	Mineral	CaO	MgO	FeO	SrO	MnO	BaO
7	7-054	Dolomite	54.95	41.87	3.05	0.00	0.07	0.06
7	7-099	Dolomite	51.70	48.02	0.00	0.00	0.29	0.00
7	7-051	Dolomite	51.37	47.85	0.00	0.00	0.52	0.26
7	7-081a	Dolomite	53.08	46.83	0.00	0.00	0.00	0.09
7	7-074	Dolomite	50.68	48.74	0.10	0.00	0.24	0.24
4	4-004	Calcite	99.41	0.59	0.00	0.00	0.00	0.00
4	4-005	Dolomite	29.43	70.27	0.08	0.00	0.00	0.22
4	4-074b	Calcite	93.79	5.55	0.00	0.00	0.00	0.66
4	4-074a	Dolomite	28.67	71.13	0.00	0.00	0.20	0.00
4	4-074	Calcite	90.74	7.40	0.00	0.00	1.10	0.76
3	3-004	Dolomite	52.21	47.58	0.00	0.00	0.18	0.03
3	3-005	Dolomite	51.58	47.65	0.72	0.00	0.00	0.05
3	3-009	Dolomite	54.03	43.47	2.33	0.00	0.16	0.02
3	3-010	Dolomite	51.27	48.18	0.18	0.00	0.18	0.19
3	3-015	Dolomite	52.43	47.13	0.24	0.00	0.18	0.02
3	3-016	Dolomite	51.47	48.11	0.41	0.00	0.00	0.01
3	3-017	Dolomite	50.52	48.66	0.40	0.00	0.25	0.17
3	3-018	Dolomite	50.43	49.35	0.13	0.00	0.09	0.00
3	3-023	Dolomite	50.67	48.86	0.01	0.00	0.46	0.00
3	3-021	Dolomite	53.07	46.68	0.06	0.00	0.06	0.13
3	3-022	Dolomite	50.62	48.67	0.38	0.00	0.33	0.00
3	3-024	Dolomite	51.87	48.13	0.00	0.00	0.00	0.00
3	3-025	Dolomite	53.25	44.48	2.23	0.00	0.00	0.04
3	3-026a	Dolomite	50.88	48.50	0.62	0.00	0.00	0.00
4	4-015	Dolomite	42.07	57.42	0.19	0.00	0.17	0.15
4	4-014	Calcite	96.59	1.76	0.26	0.00	1.04	0.35
4	4-017	Calcite	95.99	3.09	0.62	0.00	0.31	0.00
4	4-016	Dolomite	42.18	56.96	0.29	0.00	0.39	0.19
4	4-018a	Calcite	94.85	4.37	0.00	0.00	0.00	0.78
4	4-018	Calcite	94.80	2.96	0.99	0.22	0.47	0.56
4	4-019	Calcite	95.82	3.60	0.09	0.01	0.00	0.49
4	4-020	Calcite	96.78	3.21	0.00	0.00	0.01	0.00
4	4-021	Calcite	96.92	3.04	0.00	0.03	0.00	0.01
4	4-022	Calcite	95.89	3.70	0.40	0.00	0.00	0.00
4	4-025	Calcite	95.20	4.29	0.00	0.00	0.33	0.18
4	4-026	Calcite	95.01	4.50	0.00	0.00	0.14	0.35
4	4-012	Dolomite	39.99	59.15	0.57	0.00	0.29	0.00
4	4-010	Dolomite	41.54	57.84	0.20	0.11	0.00	0.31
4	4-011	Calcite	95.24	3.47	0.84	0.00	0.35	0.10
4	4-013	Calcite	96.75	0.90	1.14	0.22	0.77	0.22
4	4-006	Calcite	96.35	3.51	0.00	0.04	0.10	0.00
4	4-072	Calcite	95.30	2.89	1.29	0.00	0.00	0.53
4	4-069a	Dolomite	37.77	61.62	0.38	0.00	0.23	0.00
4	4-070	Calcite	95.85	3.77	0.06	0.32	0.00	0.00
4	4-061	Dolomite	38.46	59.92	0.64	0.00	0.98	0.00
4	4-066	Dolomite	35.94	50.78	8.30	0.00	0.00	4.98
4	4-036	Calcite	99.77	0.00	0.00	0.00	0.23	0.00
4	4-035	Calcite	97.34	2.59	0.00	0.07	0.00	0.00
4	4-035a	Calcite	97.37	2.21	0.00	0.00	0.28	0.14

Sample	SIMS No	Mineral	CaO	MgO	FeO	SrO	MnO	BaO
4	4-033	Calcite	97.46	2.03	0.27	0.00	0.00	0.25
4	4-032	Calcite	95.69	4.27	0.00	0.03	0.00	0.01
4	4-009	Dolomite	41.98	57.62	0.00	0.00	0.40	0.00
4	4-007	Dolomite	43.44	56.09	0.34	0.00	0.04	0.09
4	4-031	Dolomite	43.07	56.83	0.01	0.00	0.09	0.00
4	4-030	Calcite	95.32	4.66	0.00	0.02	0.00	0.00
4	4-029	Calcite	96.71	2.65	0.24	0.00	0.12	0.28
4	4-028	Calcite	98.04	1.63	0.09	0.14	0.00	0.10
4	4-027	Calcite	96.55	3.24	0.00	0.00	0.00	0.21
4	4-034	Dolomite	42.60	54.70	0.00	0.00	0.80	1.90
4	4-039	Calcite	95.85	3.56	0.43	0.00	0.00	0.17
4	4-042	Dolomite	41.23	58.37	0.26	0.00	0.00	0.14
4	4-043	Calcite	94.38	4.75	0.00	0.00	0.74	0.13
4	4-058	Dolomite	41.34	58.65	0.01	0.00	0.00	0.00
4	4-059	Calcite	96.40	2.72	0.36	0.15	0.00	0.37
4	4-057	Calcite	96.17	3.33	0.00	0.00	0.37	0.13
4	4-056	Calcite	95.46	3.98	0.20	0.05	0.00	0.31
4	4-048	Calcite	98.46	0.88	0.48	0.00	0.18	0.00
4	4-051	Calcite	98.11	1.40	0.47	0.00	0.00	0.02
4	4-024	Dolomite	52.90	46.39	0.56	0.00	0.08	0.07
4	4-043	Calcite	96.18	3.52	0.19	0.12	0.00	0.00
4	4-023	Calcite	97.29	2.68	0.02	0.01	0.00	0.00
4	4-097a	Calcite	96.34	3.05	0.20	0.00	0.42	0.00
4	4-097	Calcite	98.37	1.44	0.15	0.00	0.04	0.00
4	4-092	Calcite	96.30	3.60	0.00	0.10	0.00	0.00
4	4-089	Dolomite	40.24	58.70	0.41	0.00	0.61	0.04
4	4-082	Dolomite	39.55	60.14	0.31	0.00	0.00	0.00
4	4-082a	Dolomite	39.01	60.86	0.00	0.02	0.00	0.11
4	4-078	Dolomite	40.07	59.87	0.00	0.00	0.06	0.00
6	6-005	Calcite	97.14	2.27	0.46	0.00	0.00	0.13
6	6-005a	Dolomite	45.88	53.85	0.27	0.00	0.00	0.00
6	6-062	Calcite	97.72	2.06	0.07	0.07	0.09	0.00
6	6-063	Calcite	98.02	1.98	0.00	0.00	0.00	0.00
6	6-064	Calcite	99.10	0.90	0.00	0.00	0.00	0.00
6	6-029	Calcite	97.63	2.12	0.06	0.19	0.00	0.00
6	6-030	Calcite	96.77	2.60	0.37	0.00	0.27	0.00
6	6-031	Calcite	97.88	1.73	0.00	0.00	0.28	0.11
6	6-032	Calcite	96.53	2.66	0.22	0.00	0.00	0.59
6	6-034	Calcite	97.40	2.43	0.11	0.00	0.00	0.06
6	6-035	Calcite	97.12	2.68	0.00	0.00	0.20	0.00
6	6-040	Calcite	97.66	1.73	0.42	0.00	0.01	0.18
6	6-040a	Dolomite	43.41	53.79	2.59	0.00	0.21	0.00
6	6-037	Dolomite	45.35	52.54	2.07	0.04	0.00	0.00
6	6-039	Calcite	98.58	1.34	0.08	0.00	0.00	0.00
6	6-036	Dolomite	42.99	54.48	2.09	0.04	0.34	0.06
6	6-038	Calcite	96.80	2.83	0.00	0.00	0.27	0.11
6	6-071	Calcite	96.91	2.45	0.16	0.00	0.48	0.00
6	6-068	Dolomite	41.67	58.10	0.00	0.00	0.16	0.07
6	6-074	Calcite	97.28	2.47	0.01	0.00	0.24	0.00

Sample	SIMS No	Mineral	CaO	MgO	FeO	SrO	MnO	BaO
6	6-075	Calcite	97.00	2.19	0.37	0.00	0.39	0.05
6	6-010	Calcite	96.31	3.06	0.34	0.00	0.25	0.04
1	1-074	Dolomite	48.55	50.13	0.76	0.00	0.01	0.55
1	1-072	Dolomite	49.16	49.96	0.65	0.00	0.24	0.00
1	1-071	Dolomite	49.56	50.18	0.00	0.00	0.26	0.00
1	1-067e	Dolomite	46.91	50.69	1.84	0.00	0.05	0.51
1	1-067f	Dolomite	49.04	50.61	0.27	0.00	0.08	0.00
1	1-067c	Dolomite	48.28	51.50	0.00	0.00	0.00	0.22
1	1-067a	Dolomite	49.26	50.46	0.16	0.00	0.12	0.00
1	1-108	Dolomite	47.77	51.92	0.15	0.00	0.15	0.01
1	1-109	Dolomite	44.74	53.60	1.29	0.00	0.26	0.12
1	1-113	Dolomite	47.91	51.72	0.00	0.00	0.26	0.12
1	1-054a	Dolomite	48.75	50.44	0.54	0.00	0.26	0.01
1	1-054b	Dolomite	41.63	57.84	0.30	0.00	0.00	0.23
1	1-054c	Dolomite	72.01	26.63	1.36	0.00	0.00	0.00
1	1-054d	Dolomite	62.92	35.64	0.66	0.00	0.77	0.00
1	1-101	Dolomite	48.97	50.26	0.65	0.00	0.00	0.12
1	1-103	Dolomite	50.00	49.84	0.16	0.00	0.00	0.00
1	1-102	Dolomite	45.18	53.19	1.35	0.00	0.09	0.19
1	1-079	Dolomite	48.69	47.70	1.58	0.00	0.50	1.53
1	1-084	Dolomite	49.03	50.81	0.02	0.00	0.14	0.00
1	1-085	Dolomite	49.85	49.74	0.00	0.00	0.35	0.06
1	1-071b	Dolomite	48.09	51.09	0.72	0.00	0.10	0.00
1	1-067	Dolomite	47.10	51.68	0.85	0.00	0.37	0.00
1	1-107	Dolomite	47.75	51.89	0.19	0.00	0.02	0.16
1	1-105	Dolomite	48.26	51.73	0.01	0.00	0.00	0.00
1	1-106	Dolomite	48.67	50.18	0.98	0.00	0.05	0.12
3	3-032	Dolomite	50.12	49.30	0.51	0.00	0.07	0.00
3	3-026	Calcite	98.25	1.33	0.18	0.00	0.25	0.00
3	3-028	Dolomite	52.48	47.49	0.00	0.00	0.00	0.03
3	3-027	Dolomite	54.06	44.01	1.49	0.00	0.43	0.00
3	3-089	Dolomite	64.04	35.67	0.15	0.00	0.13	0.01
3	3-088	Dolomite	53.56	43.02	2.97	0.00	0.44	0.00
3	3-087	Calcite	97.89	1.31	0.40	0.21	0.00	0.20
3	3-086	Dolomite	53.49	44.34	1.88	0.00	0.29	0.00
3	3-081	Dolomite	49.15	49.94	0.50	0.00	0.32	0.10
3	3-083	Dolomite	50.76	48.51	0.55	0.00	0.12	0.06
3	3-080	Dolomite	51.14	48.84	0.02	0.00	0.00	0.00
3	3-080b	Dolomite	53.26	43.85	2.78	0.00	0.07	0.04
3	3-080a	Dolomite	53.99	45.73	0.10	0.00	0.18	0.00
3	3-084b	Dolomite	52.22	47.32	0.46	0.00	0.00	0.00
3	3-093	Dolomite	52.33	46.79	0.88	0.00	0.00	0.00
3	3-091	Calcite	97.20	2.54	0.10	0.00	0.00	0.16
3	3-090	Dolomite	50.91	47.78	1.12	0.00	0.19	0.00
3	3-096	Calcite	98.28	1.16	0.23	0.00	0.21	0.12
3	3-097	Dolomite	51.56	44.79	3.33	0.00	0.32	0.00
3	3-098	Dolomite	53.43	41.44	4.53	0.00	0.53	0.07
3	3-099	Dolomite	50.37	47.50	1.66	0.00	0.34	0.13
5	5-023	Dolomite	51.09	48.88	0.02	0.00	0.00	0.01

Sample	SIMS No	Mineral	CaO	MgO	FeO	SrO	MnO	BaO
5	5-081	Dolomite	51.76	47.46	0.51	0.00	0.21	0.06
5	5-080	Dolomite	50.62	48.67	0.33	0.00	0.38	0.00
5	5-078	Dolomite	50.88	48.68	0.20	0.00	0.24	0.00
5	5-072	Dolomite	50.53	48.01	0.95	0.00	0.45	0.06
5	5-103	Dolomite	50.57	48.88	0.00	0.00	0.35	0.20
5	5-102	Dolomite	50.71	48.69	0.52	0.00	0.08	0.00
5	5-107	Dolomite	50.73	48.98	0.29	0.00	0.00	0.00
5	5-115	Dolomite	52.10	47.79	0.11	0.00	0.00	0.00
5	5-113	Dolomite	52.08	44.34	3.20	0.00	0.38	0.00
5	5-114	Dolomite	49.97	49.55	0.29	0.00	0.19	0.00
5	5-118	Dolomite	50.39	48.78	0.50	0.00	0.31	0.02
5	5-122	Dolomite	50.16	49.24	0.39	0.00	0.17	0.05
5	5-117	Dolomite	51.22	48.54	0.09	0.00	0.15	0.00
5	5-109	Dolomite	48.54	44.47	6.60	0.00	0.38	0.00
5	5-108	Dolomite	51.50	48.03	0.30	0.00	0.09	0.08
5	5-004	Dolomite	50.53	47.42	1.80	0.00	0.26	0.00
5	5-015	Dolomite	52.12	46.51	1.16	0.00	0.21	0.00
5	5-015	Dolomite	50.74	48.01	0.99	0.00	0.26	0.00
5	5-015	Dolomite	50.20	48.25	1.04	0.00	0.34	0.18
5	5-015	Dolomite	51.14	47.62	1.07	0.00	0.17	0.00
5	5-015	Dolomite	42.38	55.65	1.64	0.00	0.33	0.00
5	5-100a	Dolomite	50.17	48.01	1.32	0.00	0.39	0.11
5	5-098	Dolomite	53.72	45.99	0.00	0.00	0.22	0.07
5	5-099	Dolomite	51.45	48.52	0.03	0.00	0.00	0.00
5	5-100	Dolomite	52.05	47.27	0.03	0.00	0.66	0.00
6	6-033	Calcite	97.04	2.62	0.25	0.00	0.09	0.00
6	6-007	Dolomite	44.72	51.23	3.43	0.00	0.48	0.13
6	6-009	Calcite	97.25	2.32	0.43	0.00	0.00	0.00
6	6-059a	Calcite	98.57	1.32	0.00	0.00	0.00	0.11
6	6-059	Calcite	97.72	2.05	0.09	0.00	0.15	0.00
6	6-059b	Calcite	98.85	0.73	0.28	0.00	0.14	0.00
6	6-028	Dolomite	43.66	56.13	0.00	0.00	0.00	0.21
7	7-075	Dolomite	47.47	52.44	0.00	0.01	0.00	0.08
7	7-070	Dolomite	50.11	49.19	0.58	0.00	0.12	0.00
7	7-073	Dolomite	47.21	49.46	0.87	0.00	1.65	0.81
7	7-029	Dolomite	52.90	46.71	0.22	0.00	0.04	0.13
7	7-030	Dolomite	51.87	47.69	0.11	0.00	0.20	0.13
7	7-041	Dolomite	51.78	48.08	0.05	0.00	0.09	0.00
7	7-048	Dolomite	52.23	45.46	1.54	0.00	0.77	0.00
7	7-047	Dolomite	51.37	48.28	0.23	0.00	0.11	0.01
7	7-100	Dolomite	50.83	49.17	0.00	0.00	0.00	0.00
7	7-081a	Dolomite	51.91	46.70	0.69	0.00	0.70	0.00
7	7-079	Calcite	95.50	3.75	0.23	0.44	0.08	0.00
7	7-080	Dolomite	41.84	38.10	19.95	0.00	0.12	0.00
3	3-087	Calcite	97.89	1.31	0.40	0.21	0.00	0.20
3	3-088	Dolomite	53.56	43.02	2.97	0.00	0.44	0.00
3	3-089	Dolomite	51.98	47.73	0.15	0.00	0.13	0.01
3	3-083	Dolomite	50.76	48.51	0.55	0.00	0.12	0.06
3	3-084b	Dolomite	52.22	47.32	0.46	0.00	0.00	0.00

Sample	SIMS No	Mineral	CaO	MgO	FeO	SrO	MnO	BaO
3	3-086	Dolomite	53.49	44.34	1.88	0.00	0.29	0.00
3	3-090	Dolomite	50.91	47.78	1.12	0.00	0.19	0.00
3	3-091	Calcite	97.20	2.54	0.10	0.00	0.00	0.16
3	3-093	Dolomite	52.33	46.79	0.88	0.00	0.00	0.00
3	3-097	Dolomite	51.56	44.79	3.33	0.00	0.32	0.00
3	3-098	Dolomite	53.43	41.44	4.53	0.00	0.53	0.07
3	3-099	Dolomite	50.37	47.50	1.66	0.00	0.34	0.13
4	4-059	Calcite	93.53	5.48	0.50	0.29	0.19	0.01
4	4-097	Calcite	93.53	5.48	0.50	0.29	0.19	0.01
4	4-097a	Calcite	93.53	5.48	0.50	0.29	0.19	0.01
5	5-109	Dolomite	48.54	44.47	6.60	0.00	0.38	0.00
5	5-108	Dolomite	51.50	48.03	0.30	0.00	0.09	0.08
5	5-103	Dolomite	50.57	48.88	0.00	0.00	0.35	0.20
5	5-102	Dolomite	50.71	48.69	0.52	0.00	0.08	0.00
7	7-070	Dolomite	51.64	48.10	0.00	0.00	0.00	0.26
2	2-008	Dolomite	38.85	60.66	0.00	0.00	0.49	0.00
2	2-013	Dolomite	36.78	62.92	0.18	0.00	0.00	0.12
2	2-025	Dolomite	38.79	60.82	0.14	0.00	0.14	0.11

Appendix 10

Backscatter electron image maps of samples analysed by SIMS. Images show the regions analysed by SIMS. FOV = 5mm (analysis sweet spot) for all the samples.

Sample 1

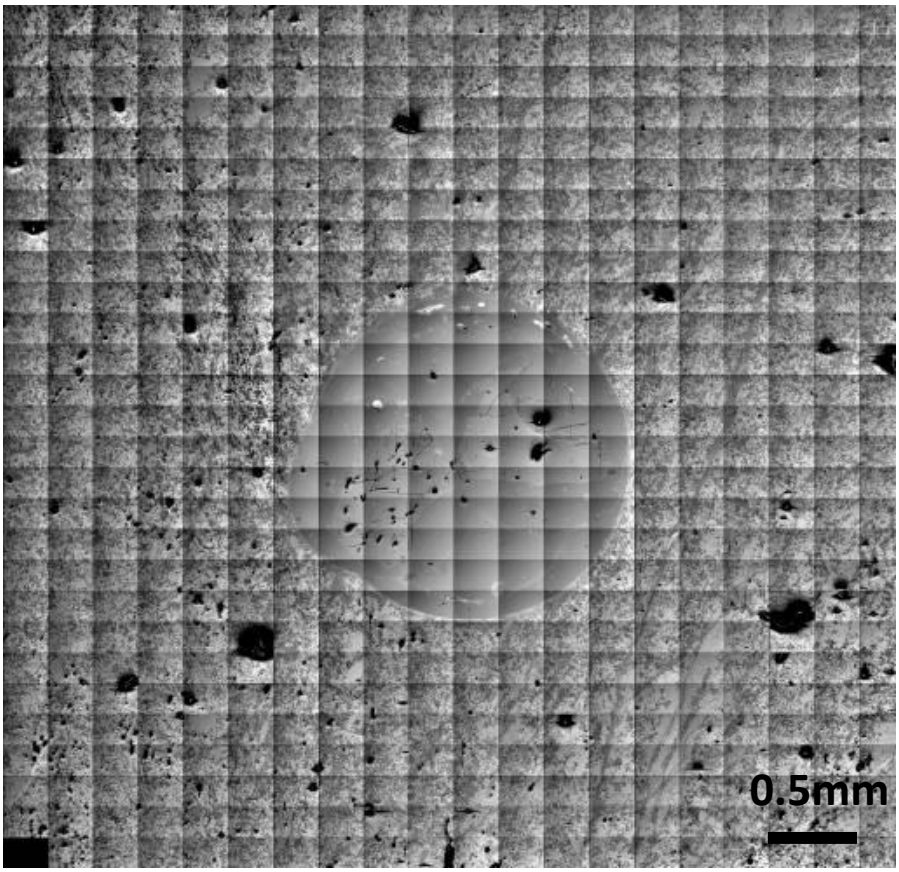

Sample 2

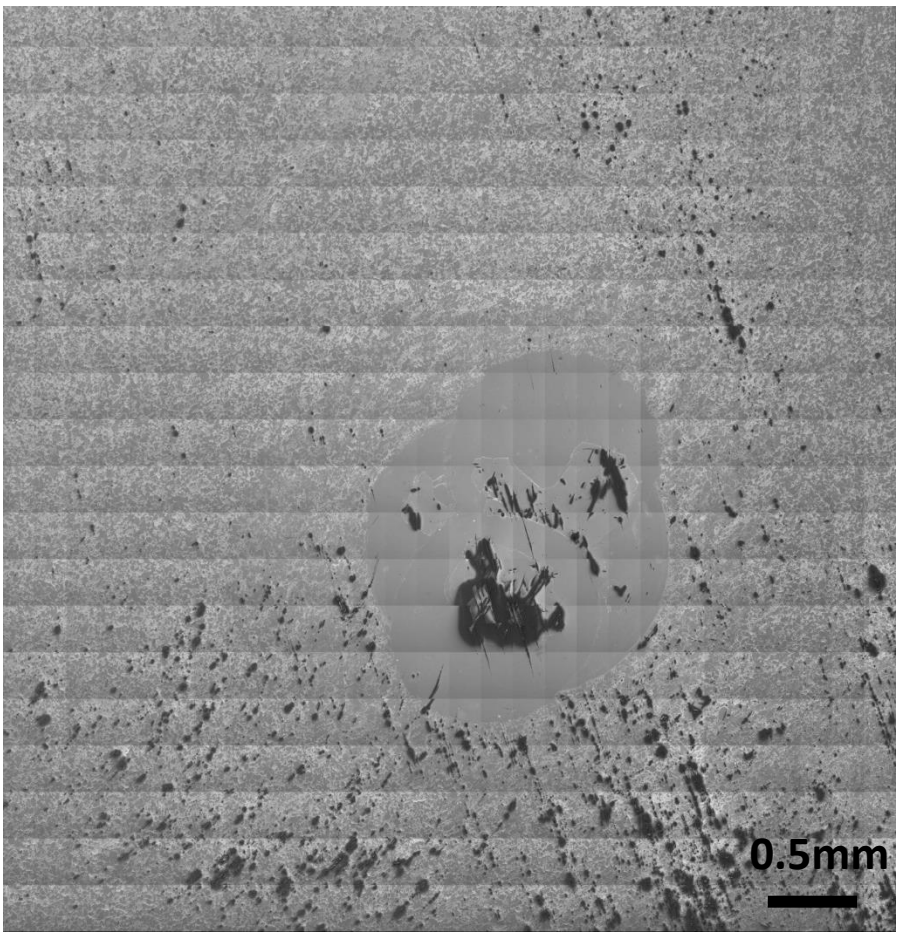

Sample 3

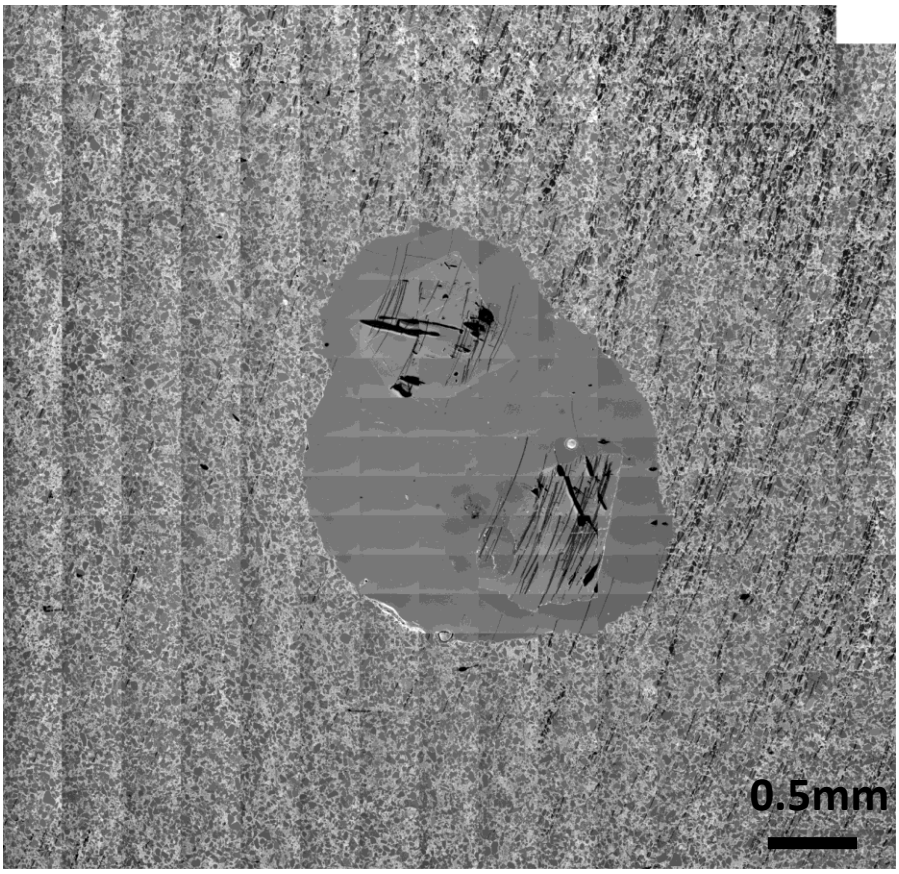

Sample 4

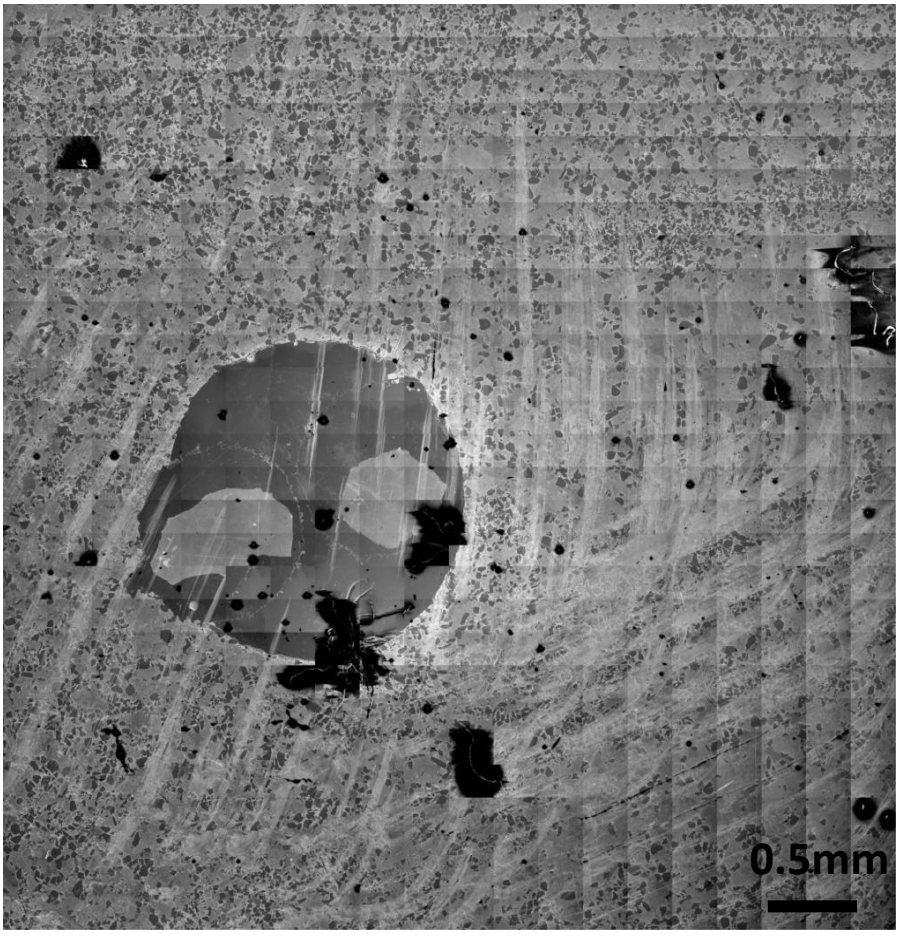

Sample 5

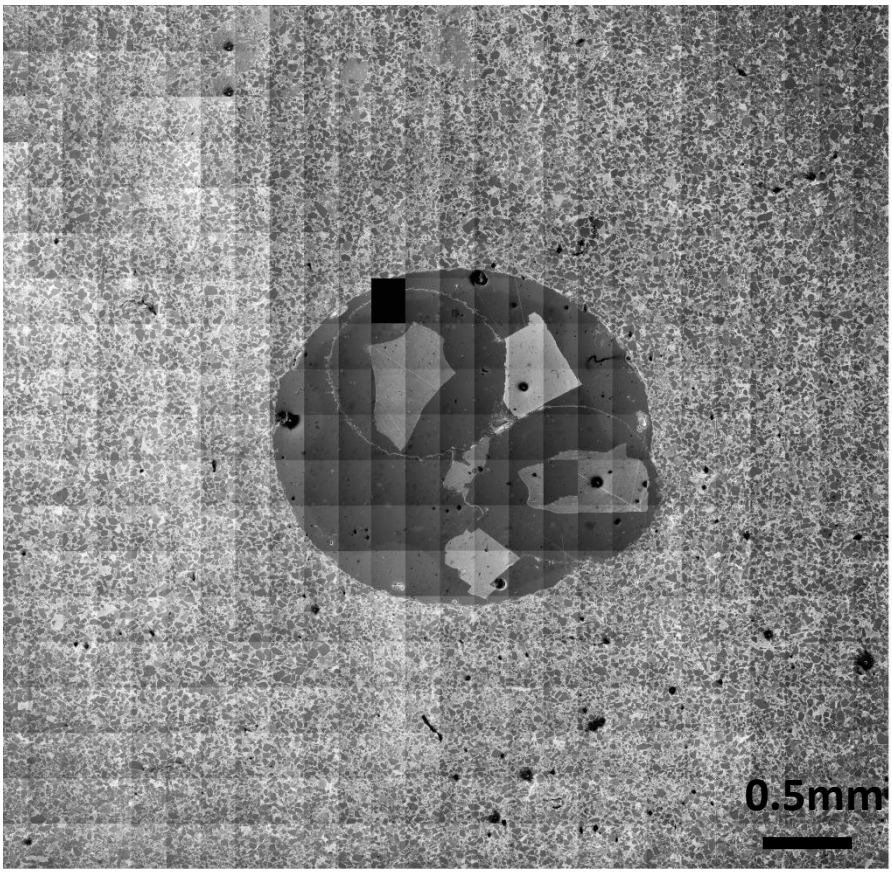

Sample 6

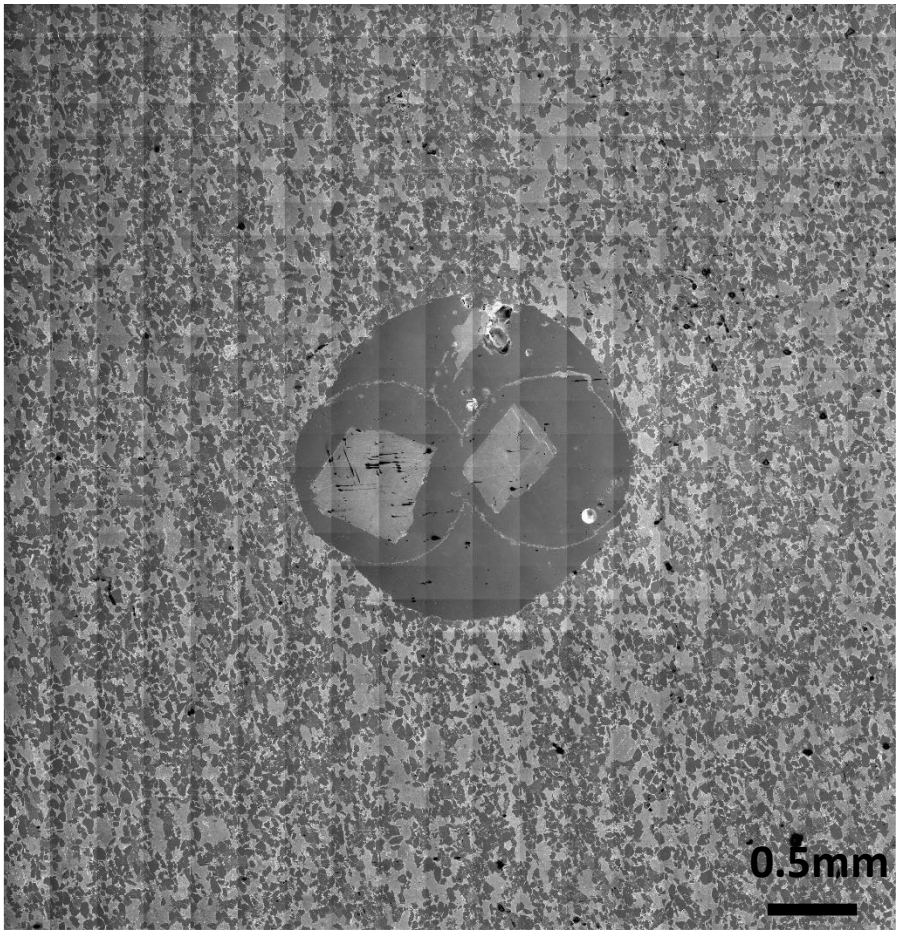

Sample 7